INFLUENCE OF RIPARIAN VEGETATION ON NEAR-BANK FLOW STRUCTURE AND RATES OF EROSION ON A LARGE MEANDERING RIVER

BY

KORY MATTHEW KONSOER

DISSERTATION

Submitted in partial fulfillment of the requirements
for the degree of Doctor of Philosophy in Geography
in the Graduate College of the
University of Illinois at Urbana-Champaign, 2014

Urbana, Illinois

Doctoral Committee:

Professor Bruce Rhoads, Chair
Professor James Best
Professor Gary Parker
Professor Marcelo Garcia

ABSTRACT

The dynamic process of meandering in alluvial rivers occurs through complex interactions among autogenic processes such as three-dimensional flow structure, channel planform geometry, and sediment transport. These internal processes can be strongly influenced by the geotechnical properties of the channel banks and floodplains, as well as riparian and in-channel vegetation, modifying rates of erosion and mechanism of bank retreat, often leading to complex planform geometries. While extensive research has been conducted on each of these processes independently, few studies have examined through detailed field measurements the combined effects and interactions between the internal processes and external forcings driving channel migration. Furthermore, most of the studies investigating the influence of bank material properties and vegetation have been conducted on small and moderately sized rivers with relatively simple planform geometry, or using simplified experimental flumes and numerical models. Thus, the influence of these external forcings on the meander dynamics of large rivers remain poorly understood.

This dissertation research is organized into three separate investigations from two elongate meander loops with different riparian vegetation on a large river. The first study focuses on the spatial patterns of three-dimensional flow structure throughout these meander loops and examined the effects of near-bank large woody debris (LWD) on near-bank flow structure and boundary shear stress, and how the hydrodynamics varied during different hydrologic conditions. Data consist of time-averaged three-dimensional velocity measurements, which were obtained using a boat-mounted acoustic Doppler current profiler (ADCP) during varying hydrologic conditions. Patterns of depth-averaged velocity through the meander loop without near-bank LWD are fairly consistent with previous investigations of flow through elongate meander loops,

however, LWD near the outer bank of the forested loop has a strong influence on the near-bank flow field. Specifically, the LWD produces a zone of low velocity against the outer bank that extends up to 40 m into the channel and over the entire flow depth, and creates several streamwise-oriented secondary cells. These effects from the LWD on the near-bank flow field prevent advection of high momentum fluid against the outer bank. In contrast, the roughness elements along the outer bank of the unforested bend are primarily large-scale topographic irregularities that are not effective at reducing flow velocities near the bank toe.

The second study explores the various scales of outer bank form roughness produced from large-scale bankline irregularities and small-scale surface roughness, the influence of bank material properties and vegetation on scales of roughness, and how scales of roughness differ during variable discharge conditions and through time. Detailed morphology of the outer banks was obtained using terrestrial LiDAR during low flow conditions and multi-beam echo sounding (MBES) during near-bankfull conditions, and scales of roughness were evaluated using Hilbert-Huang Transform spectral analysis and root-mean-square analysis. Results show that scales of roughness along banks composed primarily of non-cohesive sediment vary as bank elevation increases and show a tendency for a dominant length scale of roughness, whereas banks composed of fine-grained silt and clay increase the resistance properties of the banks and promote uniform roughness vertically over the bank face and do not appear to have a dominant scale of roughness through the bend. Additionally, comparison between small-scale surface roughness obtained during subaerial and subaqueous conditions shows that bank roughness is considerably reduced during high flow conditions when the banks are inundated, most likely related to the removal of small woody and leafy vegetation during subaqueous and eradication of small-scale erosional features in non-cohesive bank materials.

The third study examined the lateral and vertical heterogeneities in bank material properties and riparian vegetation between these two bends using various geotechnical tests, and a numerical model of bank retreat and repeat terrestrial LiDAR surveys to evaluate the capacity of bank material properties to modify the rates and mechanisms of bank retreat. Results show substantial differences in the characteristic grain size of the bank materials, soil cohesion, and critical shear stress necessary for sediment entrainment between the forested and unforested bends, and are highly variable within each bend, both laterally and vertically. Results also reveal that riparian trees are capable of enhancing bank stability through increased cohesion due to root-reinforcement, and that bedrock outcrops within the downstream limbs of both of these bends that are highly resistant to erosion. The findings from the model simulations of bank retreat show that the variations in bank material properties and riparian vegetation greatly contribute to rates of erosion and the style of bank failure, and suggest that hydrologic variability is an important factor influencing the erodibility of cohesive banks.

For the unforested bend, the non-cohesive bank materials, lack of riparian and in-channel vegetation, and limited influence of the bank roughness elements produce high rates channel migration near the bend apex. However, on the downstream limb of this bend, the platform of bedrock exposed within the channel is strongly influencing patterns of near-bank flow and shear stress, leading to a small zone of deposition along the outer bank downstream of the bedrock. In contrast, at the forested bend, the high resistance of bank materials, stabilizing effects of riparian trees, and reduction of near-bank shear stress from increased flow resistance by LWD, limit extension of this bend near the apex. On the downstream limb where the highest shear stresses occur, the channel is confined by bedrock from the upland valley, restricting the downstream translation of the bend.

In conclusion, the results from this research advance knowledge and understanding of how the interactions and feedbacks among three-dimensional flow structure, material properties of the banks and floodplains (sediment and bedrock), and vegetation characteristics near the outer bank influence the morphodynamics of meandering rivers. The findings also provide an empirical foundation for the refinement and calibration of numerical models aimed at predicting these morphodynamics in complex natural settings.

To my family with love:

Samantha, William and Kaylee

and my mother and father

Mary and William Konsoer

ACKNOWLEDGMENTS

The work leading toward the completion of my dissertation has been one of the most exciting and rewarding endeavors of my life, and there are many people that I would like to thank for contributing to such a positive experience.

I would first like to thank my advisor, Prof. Bruce Rhoads, for his insight into the design of this research project, careful guidance through the data analysis and writing stages, and support and encouragement. He has continued to challenge me to think critically about the interactions driving complex process-response dynamics in geomorphic systems, and how to best convey findings from scientific research – a topic that required a considerable amount of effort and patience through many discussions and edits. Thank you for seeing the talent in me during my campus visit and pushing me towards success.

I am very grateful to my committee members: Prof. Jim Best, Prof. Gary Parker, and Prof. Marcelo Garcia. I have been extremely fortunate during my tenure at the University of Illinois to work in a highly collaborative environment and be involved in a large interdisciplinary research project. This experience has enabled me to work closely with my all of my committee members, and many of their students, and I have benefited greatly from these interactions. I would like to give special thanks to Prof. Jim Best for funding me as a research assistant during this project, and for trusting me with expensive state-of-the-art survey equipment despite limited initial training – I am now hooked on this technology.

The work presented in this dissertation would not have been possible without the technical support and expertise of Dr. Eddy Langendoen and Mick Ursic. They provided many hours in the field, laboratory, and over the phone helping with data acquisition, analysis, and interpretation. I would also like to acknowledge the many people that helped with various

aspects of field work associated with this project: David Fazio, Kevin Johnson, Ron Cash, Jessica Zinger, Jorge Abad, Christian Frias, Frank Engel, David Waterman, Quinn Lewis, Alex Bryk, Dan Parsons, Jacqueline Costello, and Michael Brown. I am especially grateful for the friendship and support of everyone in the UIUC Earth Surface Processes (ESP) group, and in particular, Jess Zinger, Frank Engel, and Quinn Lewis.

I would like to thank the faculty in the geology department at Grand Valley State University. If it were not for your enthusiasm and dedication to undergraduate research and education, I certainly would not have developed such a deep interest in Earth systems. My sincerest thanks and I look forward to seeing you at the Annual Geological Society of America Meetings every fall.

I owe endless gratitude to my loving wife, Samantha, who has been a source of steadfast encouragement, support, and patience throughout my entire academic career as a graduate student, and has always been in favor of me pursuing my academic and professional goals. I am truly blessed to have a wonderful family that has always been my biggest fans, holding up banners and signs even when I beg them not to. I happily share this accomplishment with you.

This research was funded by grants from the National Science Foundation (EAR – 0952242 and SBE – 1129889), Geological Society of America Graduate Student Research Grant, and grants from the University of Illinois Graduate College and Department of Geography and Geographic Information Science. Lastly, I would like to acknowledge Dr. Roscoe Jackson for his continued support of the UIUC-ESP group, and the many hours with me spent talking about the wild Wabash River.

TABLE OF CONTENTS

LIST OF FIGURES

LIST OF TABLES

CHAPTER 1

INTRODUCTION

1.1 Motivation

Meandering rivers are prominent physical features on Earth's surface and have received much attention across disciplines because of their political, economic, and environmental importance as they often form boundaries between states and countries, are used as traffic ways for goods, and provide a vast range of aquatic habitats. The process of meandering in alluvial rivers occurs through dynamic interactions among channel planform, three-dimensional flow structure, sediment transport, and the geotechnical characteristics of the channel banks and floodplains. A necessary component of meander migration in alluvial channels is bank retreat, which mobilizes stored floodplain sediments through fluvial entrainment and mass bank failure with subsequent removal of the failed material (Thorne, 1982, 1992; Rhoads and Welford, 1991). The introduction of large amounts of sediment to the fluvial system can have great impacts on downstream patterns of river erosion and deposition, water quality, and riverine ecosystems (Rinaldi and Darby, 2007). Rates of bank erosion are influenced by the near-bank turbulent flow field, mechanical properties of the bank sediments, and the presence of in-channel and riparian vegetation. Extensive research has been conducted on each on these processes independently (Simon and Collison, 2002; Frothingham and Rhoads, 2003; Daniels and Rhoads, 2003), yet few studies have examined their combined effects and interactions in detail. Moreover, most of these studies have been conducted on small and moderately sized rivers with relatively simple planform geometry, or using simplified experimental flumes and numerical models. Detailed field studies of near-bank flow structure, geotechnical bank properties, and the influence of near-

bank large woody debris (LWD) are necessary to improve current theoretical models of meander evolution.

Forested riverbanks and other types of riparian vegetation can greatly reduce the rate of bank retreat through root-reinforcement (root tensile strength) and increase flow resistance near the bank. Forested banks can also provide LWD to the channel, and if located near the outer bank, can act to armor the bank and redirect flow away from the bank toe, the locus of erosion in meandering rivers. The effects of vegetation on turbulent flow structure and sediment transport in open-channel flow are well documented. Vegetation within river channels can reduce flow velocities through increased form drag (Daniels and Rhoads, 2003; Bennett, 2004), alter profiles of turbulence intensities and shear stresses (Lopez and Garcia, 1998; Majoribanks *et al*., 2012) and promote deposition of sediment within patches of vegetation (Zong and Nepf, 2011; Gorrick and Rodriguez, 2012). However, despite the prevalence of in-channel vegetation, our knowledge of the interactions between vegetation, flow structure, and sediment transport has been limited to arrays of simplified plant geometries in small natural rivers, experimental channels, and numerical models (Garcia *et al*., 2004; Sukhodolov and Sukhodolova, 2011; Majoribanks *et al*., 2012). To date, no such studies have examined in detailed the flow structure around complex plant geometries such as LWD and submerged trees, and how the alteration of the three-dimensional flow field influences bank erosion and sediment transport in large rivers.

Traditional theoretical models for long-term river migration define bend migration as a function of local and upstream channel curvature (Guneralp and Rhoads, 2009), relating the rate of migration to the near-bank excess velocity and a dimensionless coefficient calibrated against field data (Hasegawa, 1977; Ikeda *et al*., 1981). These models have provided much insight into the process dynamics and behavior of meandering in alluvial rivers, but have had limited success

in simulating processes of complex channel planform evolution because they operate under the assumption that channel width is constant and that channel curvature is the primary factor influencing bend migration. Although channel curvature has been shown to influence three-dimensional flow structure (Rhoads and Welford, 1991; Whiting and Dietrich, 1993a,b), an important limiting factor to these models is that they do not incorporate detailed near-bank processes of sediment transport, bank erosion, and turbulence characteristics. In particular, current models fail to include the influences of bank morphology, mechanical properties of the bank, bank heterogeneity, and near-bank LWD on flow velocities and boundary shear stresses. Meander migration models are further oversimplified by using depth and time-averaged flow, most often the bankfull discharge (Abad *et al*., 2008), and therefore do not consider seasonal stage variability, a factor known to have influence on subaerial bank preparation and erosion (Luppi *et al*., 2009; Simon and Rinaldi, 2006; Lawler, 1992; Pizzuto, 2009; Wynn and Mostaghimi, 2006). Alternatively, models of localized bank retreat are more physically-based, incorporating vertical heterogeneity of the bank material, processes of mass-wasting, ground water pore pressures, and flow-stage variability (Darby and Thorne, 1996a,b; Simon *et al*., 2003; Rinaldi and Darby, 2007; Langendoen and Simon, 2008). However, recent work has focused on developing more physically-based channel planform models by incorporating detailed subroutines for bank stability (Darby *et al*., 2002; Rinaldi *et al*., 2008; Parker *et al*., 2011; Güneralp and Rhoads, 2011; Motta *et al*., 2012). These advanced morphodynamic models are much more successful than their predecessors at producing realistic channel planforms, yet still do not incorporate any influence exerted by in-channel vegetation. Furthermore, the effects of LWD are likely scale dependent, since the relative size of LWD remains constant while channel

dimensions increase, and it is therefore important to understand how these processes operate over large and small scales.

The purpose of this research is to examine the complex near-bank flow structure of forested and non-forested meander bends in a large river to elucidate the influence of near-bank large woody debris and the bank material properties on the mechanisms of bank retreat and overall rates of channel planform migration. Through detailed field measurements and analyses of bank morphology and flow structure around near-bank LWD, this research provides invaluable information about the hydrodynamics and morphodynamics of large meandering rivers. As investigations of this type are rare for large rivers, the results provide detailed field data that can be incorporated into short and long-term planform evolution models and computational fluid dynamics models, allowing for more accurate simulations of meander processes and forms, a topic that requires more attention in the literature.

1.2 Research Objectives/Questions

The main objectives of this research are to explore the complex interactions among near-bank flow structure, bank material properties, near-bank large woody debris, and riparian vegetation in meander bends on a large river and the influence of these interactions on meander migration and planform dynamics. These issues will be addressed through the following research questions:

1) What are the dominant scales of near-bank form roughness for forested and unforested bends, how do these scales of roughness vary spatially throughout these bends, and what is the effect of variable discharge and progressive bank retreat on scales of roughness?

2) How do the spatial patterns of three-dimensional flow structure differ for forested and unforested elongate meander loops, and what effect do near-bank large-scale roughness elements, such as LWD and topographic irregularities, have on the near-bank flow structure and boundary shear stress in elongate meander loops?
3) How do the geotechnical properties (e.g. grain size, cohesion, bank height, root tensile strength) vary laterally and vertically throughout forested and unforested bends, and how much effect do riparian trees have on increasing bank stabilization on large meandering rivers?
4) What effect does spatial heterogeneity of the bank material properties have on the dominant processes of bank erosion operating in forested and unforested bends (e.g. fluvial entrainment, mass failure, subaerial preparation)?
5) How do the interactions between near-bank shear stress, bank material properties, and vegetation relate to patterns of short-term rates of erosion and long-term rates of channel migration in forested and unforested bends?

By examining these questions, this research will improve understanding of the process mechanics driving riverbank erosion and planform dynamics on large meandering rivers. Additionally, this research provides detailed field measurements of the dynamic interactions between near-bank turbulent flow fields, complex vegetation geometries (i.e. LWD), and bank erosion, offering a means to improve upon and evaluate predictive 2D and 3D models of meander dynamics. Results from this research will also provide a means to evaluate the scale dependence of riparian vegetation on meander migration by comparing the large river findings to previous research on smaller rivers.

1.3 Research Organization

The process of bank erosion in meandering rivers occurs through the complex interactions among channel planform geometry, mean and turbulent flow fields, sediment transport, and the material properties of the channel banks and floodplains. Much research has been devoted to improving our understanding of dynamic fluvial processes in meandering rivers that operate over a range of spatial and temporal scales. Chapter 2 provides an overview of the extant literature pertaining to river morphodynamics in the context of the research objectives and questions outlined above. The chapter begins with an overview of river planform geometry and a review of mean and turbulent flow structure through curved channels and relates the hydrodynamic boundary shear stresses to sediment transport and erosion. The chapter continues by reviewing the influence of vegetation on turbulent flow fields and sediment transport through vegetated reaches. Next, a review is given on the influence of geotechnical properties of channel banks and floodplains, the role of riparian vegetation on bank stability, and mechanical processes of bank retreat. The reviews presented in this chapter are also discussed within the context of theoretical and numerical models of river morphodynamics, and knowledge gaps in current understanding of fluvial dynamics related to the outlined research questions are addressed.

Chapter 3 examines the three-dimensional flow structure within two different elongate meander loops on the lower Wabash River: 1) a ~4 km long bend with agricultural fields along majority of the outer bank (Maier Bend) and 2) a ~3 km long bend with riparian forests along the entirety of its outer bank (Horseshoe Bend). This chapter presents detailed field measurements investigating the secondary flow structures produced through interactions with near-bank LWD, shear stresses acting upon the channel boundary, and the spatial evolution of near-bank flow structure through both bends at different flow discharge and stage conditions.

Chapter 4 examines the scales of outer bank roughness for Maier and Horseshoe bends through detailed measurements of bank topography using subaerial and subaqueous field techniques. Large-scale topographic irregularities at different elevations around each bend are explored through the use of the Hilbert-Huang Transform, a spectral method valid for non-stationary and nonlinear signals. Small-scale form roughness is estimated at various locations around each bend through statistical analysis for both subaerial and subaqueous conditions. Results from the investigations of bank roughness are compared to patterns of near-bank flow structure measured in the field, and discussed within the context of short-term bank erosion and long-term planform evolution.

Chapter 5 investigates the spatial variability in channel bank and floodplain resistance between Maier and Horseshoe bend with an emphasis on how riparian vegetation influences the mechanical strength of riverbanks. Field measurements focus on characterizing the geotechnical properties of the banks through grain size distributions, evaluation of critical shear stress necessary for sediment entrainment, cohesive strength of bank materials, and the additional resistance offered by forested riparian zones. The results from these analyses are used to inform a physically-based model of bank retreat and are compared to spatial patterns of long-term planform migration through GIS-based analysis of historical aerial photography from 1938 to present. Additionally, the role of bedrock outcrops exposed within the channel on the planform dynamics of a low gradient, large meandering river is discussed.

Chapter 6 summarizes the results from this research and integrates the topics covered in Chapters 3, 4 and 5 into an overview of the morphodynamics of the lower Wabash River. The specific findings related to the research questions and objectives are discussed, as well as additional findings that were not originally included in proposed research, namely the strong

influence of bedrock within the lower Wabash River valley. Limitations in the acquired field data, and challenges encountered through this research project are discussed. Lastly, although the findings from this research have provided much insight into the process dynamics of large meandering rivers, it has also revealed complexities beyond the scope of the research outlined herein, and thus the chapter closes with topics for future studies.

CHAPTER 2

PLANFORM DYNAMICS AND BANK EROSION – A CONCEPTUAL FRAMEWORK

2.1 Introduction

The process of meandering in alluvial rivers occurs through complex interactions and feedbacks among three-dimensional flow structure, channel planform geometry, and sediment transport. These three components are often referred to as the 'trinity' of fluvial dynamics (e.g. Leeder, 1983) and represent the key internal processes driving morphologic change in fluvial systems (Figure 2.1). However, it can be argued that a fourth component should be added to this commonly used diagram of fluvial dynamics, one that encompasses the geotechnical and resistance to erosion properties of the channel banks and floodplains. The characteristics of the banks and floodplains act as an external forcing affecting the feedbacks among the internal processes (Güneralp and Rhoads, 2011). It is the combination of these internal processes and external forcings, along with the fact that the process-response of each of these components occurs over a range of spatial and temporal scales, which results in nonlinear dynamic behavior that can produce complex fluvial landforms (Philips, 2003). In the following sections, individual attention will be given to each of these internal processes (e.g. flow and form) and external forcings (e.g. floodplain resistance and vegetation), to provide an overview of factors influencing river morphodynamics.

2.2 River planform geometry

River meanders are some of the most ubiquitous and easily recognizable landforms on Earth's surface. Furthermore, meander bends form across a range of spatial scales and are of fundamental interest to many scientific and applied research disciplines. However, despite the vast amount of research performed on meandering rivers, there remain many gaps in our

knowledge that are critical to understanding of the dynamics of rivers; perhaps most notably, *why* rivers meander and what gives rise to the numerous planform shapes observed in nature.

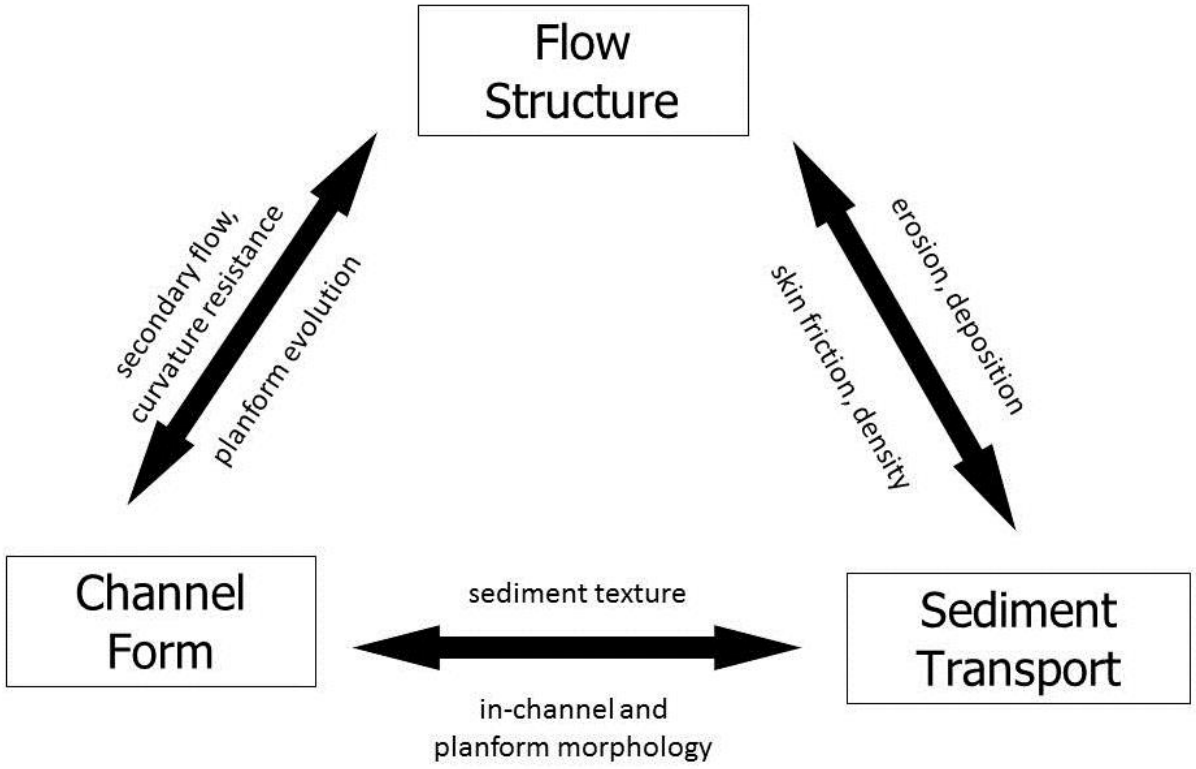

Figure 2.1 Theoretical ternary diagram of the "trinity" of fluvial dynamics representing the key internal processes driving morphologic change in rivers. Labels on the outside (inside) of the arrows give examples of factors influencing processes in a clockwise (counter-clockwise) direction. (After Leeder, 1983)

Before an overview can be given on the different types of river meanders, it is necessary to present some general geometric definitions used to characterize river planforms. The first approaches used to characterize bend geometry relied upon inscribing circles with various radii to fit the curvature of the bends (Leopold *et al*., 1964). The characteristic planform geometry of the meander bends are then described in terms of the radius of curvature r_c, a technique still commonly used. However, this over-simplified method is limited because it assumes channel curvature is constant throughout the bend and discontinuous between bends of opposite sinuosity

(Güneralp and Rhoads, 2008). Advances to this approach rely on a cylindrical coordinate system where *s* represents the streamwise distance along the channel centerline and *n* represents the orthogonal distance from the centerline, with *s* positive in the downstream direction and *n* positive toward the left bank (Langbein and Leopold, 1966; Ikeda *et al*., 1981) (Figure 2.2). In this frame of reference, the channel curvature *C* can be defined as the rate of change in the downstream channel direction relative to the down-valley gradient θ along the channel centerline (Langbein and Leopold, 1966),

$$C = \frac{\Delta\theta}{\Delta s} = r_c^{-1} \tag{2.1}$$

This definition allows for channel curvature to be estimated at discrete locations along the channel centerline, with the accuracy of this approach dependent upon the sampling distance Δs. Recent work has shown that meandering river planform geometry can be more accurately represented by fitting piecewise cubic splines to the channel centerline, thus allowing for a continuously differentiable value of curvature along an entire length of river (Güneralp and Rhoads, 2008). This approach allows values of channel curvature to be calculated at any location along the centerline *s* as a function of the first and second-order derivatives of the Cartesian coordinates (X, Y) of *s*,

$$C = \frac{X'Y'' - Y'X''}{[(X')^2 + (Y')^2]^{3/2}} \tag{2.2}$$

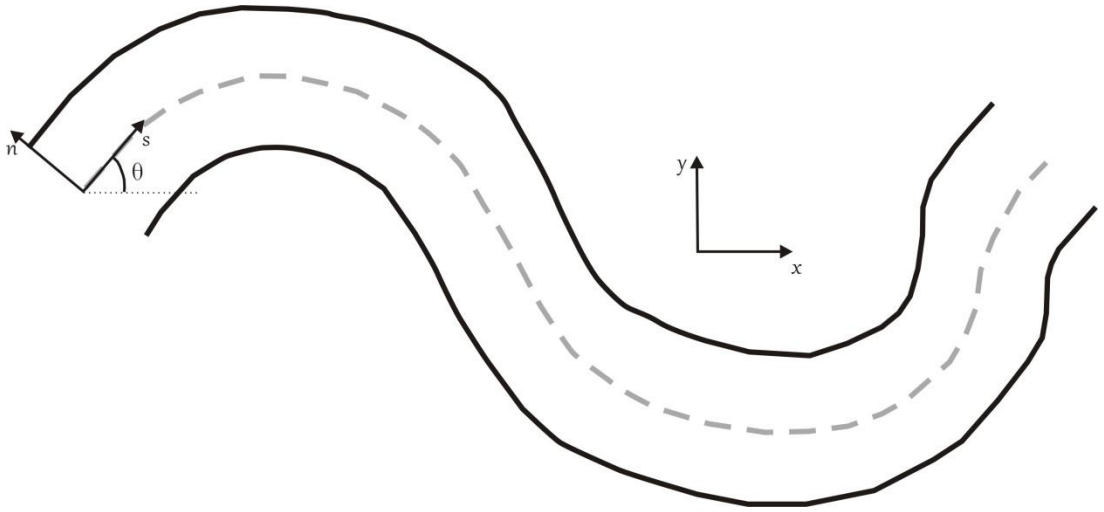

Figure 2.2 Streamwise coordinate system (*s*, *n*) for meandering rivers (After Ikeda *et al*., 1981).

Using these frames of reference and definitions of channel curvature, classification schemes of natural meander bends have been proposed that include four broad categories (Brice, 1974; Frothingham and Rhoads, 2003). The most basic planform geometry of sinuous channels is the simple bend, defined as a bend that can be characterized by a single radius of curvature and the sum of the absolute angles $|\theta|$ at the upstream and downstream inflection points of the bend is less than 180° (Frothingham and Rhoads, 2003) (Figure 2.3A). If the sum of $|\theta|$ is greater than or equal to 180° and the chord length (straight-line distance between inflection points) is less than radius of curvature, then the planform geometry can be classified as an elongate meander loop (Figure 2.3B). A meander loop can further be classified as compound if it contains more than one offset lobes, and can be either symmetrical or asymmetrical if the lobes have similar or different radii of curvature, respectively (Brice, 1974) (Figure 2.3C-D). The complex interactions between internal processes and external forcings often tend to produce asymmetrical compound meander loops with either upstream or downstream valley oriented skewness (Kinoshita, 1961;

Hickin, 1974; Hickin and Nanson, 1975; Hooke, 1995; Hooke, 2003; Abad and Garcia, 2009a, b).

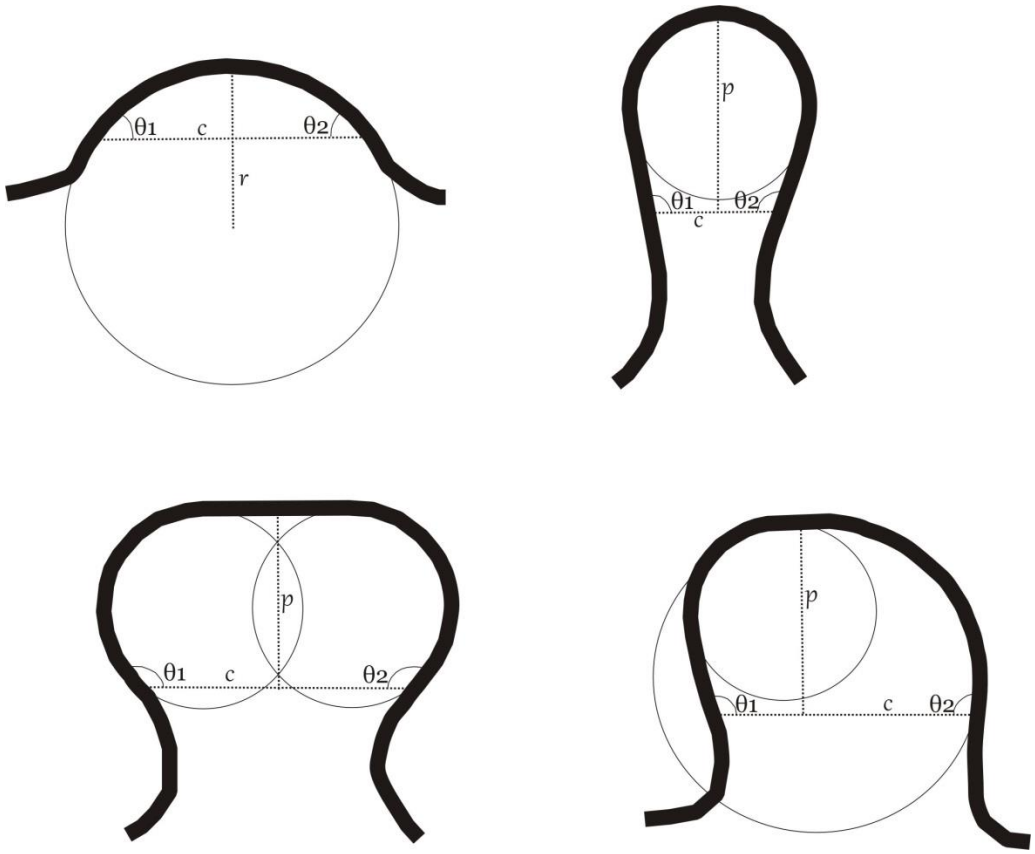

Figure 2.3 Classification scheme for natural meandering rivers. A) simple meander bend B) elongate meander loops C) symmetrical compound meander loop and D) asymmetrical compound meander loop (After Frothingham and Rhoads, 2003).

In addition to characterizing rivers based on planform geometry, metrics related to the bankfull channel dimensions have been used to classify rivers into general size categories. Although some research has attempted to distinguish between small and large rivers (Potter, 1978; Schumm and Winkley, 1994; Hovius, 1998; Gupta, 2007; Latrubesse, 2008; Ashworth and Lewin, 2012; Nicholas, 2013; Lewin and Ashworth, 2014), widespread agreement on what constitutes a large river has yet to be achieved. Various metrics have been proposed as bases for

classifying large rivers, such as drainage basin, channel width, water or sediment discharge, and the mainstem length of the river. Some common thresholds used to define large rivers are channel length greater than 1,000 km, drainage basin area greater than 100,000 km^2, or channel width greater than 1,000 m (Miall, 2014). As with many naturally occurring phenomena that vary over a continuous range of properties, the classification of rivers into discrete categories is somewhat subjective. Any particular river may perhaps satisfy some of Miall's (2014) criteria, but not others, and still be considered a large river.

The Wabash River, which drains an area of 103,500 km^2, satisfies the drainage basin criterion, yet has a channel length of only 810 km and a channel width of ~350 m, both of which do not satisfy Miall's (2014) criteria for large rivers. However, many of the world's largest rivers are multi-threaded channels (e.g. braided, anastomosing, anabranching) and have channel widths that are considerably greater than single-threaded rivers. Although many single-threaded rivers have channel widths greater than 1,000 m (e.g. Mississippi, Amazon, Ganges) (Ashworth and Lewin, 2012), a plot of channel width and depth for 231 river cross sections around the world show that the Wabash River has channel dimensions that are near the upper third of this distribution (Konsoer *et al*., 2013) (Figure 2.4). Thus, the research presented herein on the Wabash River will be cast in the context of a *large meandering* river.

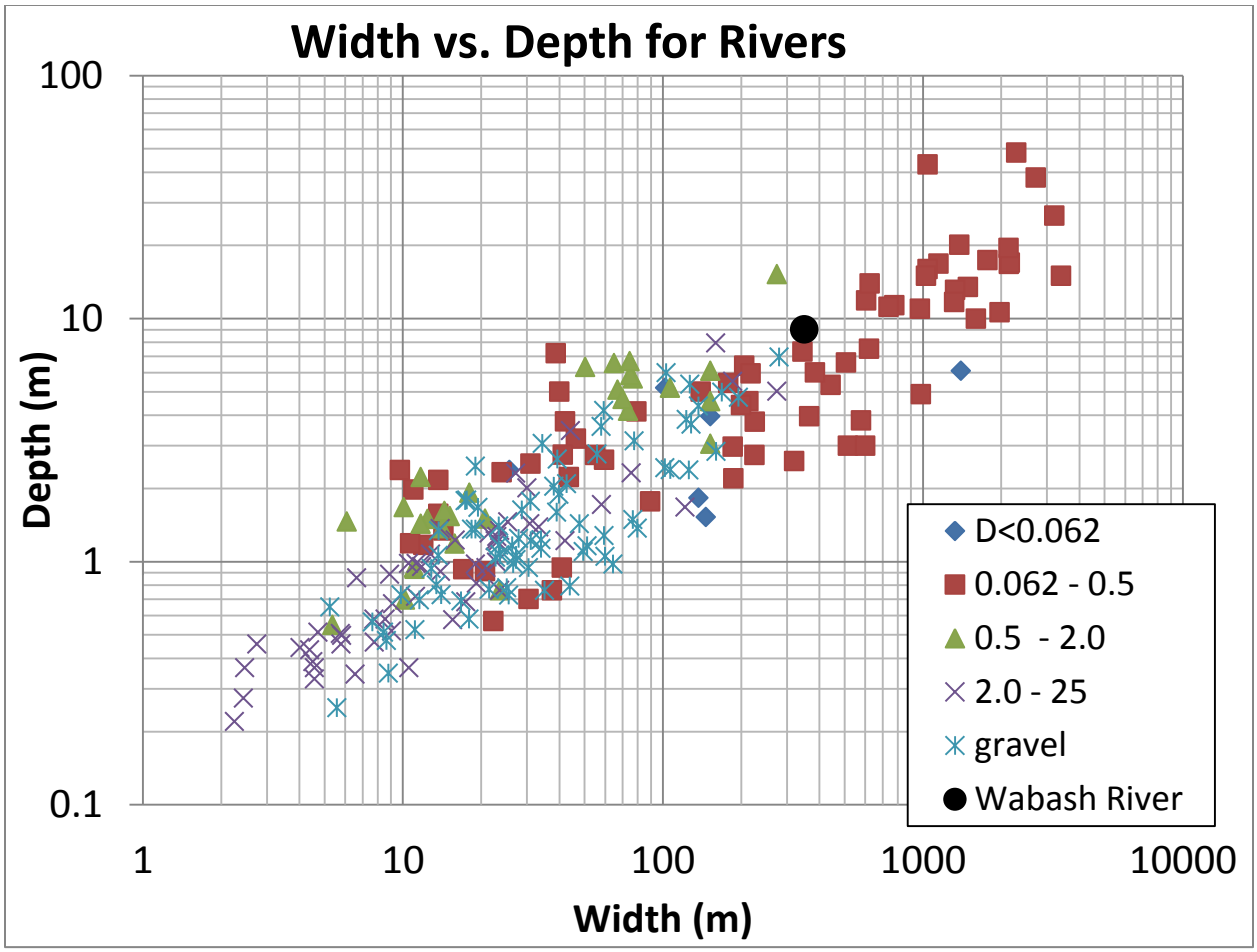

Figure 2.4 Plot of bankfull width against bankfull depth for 231 river cross sections sorted by median grain size. The Wabash River near Grayville, IL is shown for reference and plots roughly within the upper third of the largest channel dimensions (After Konsoer *et al.*, 2013).

2.3 Time-averaged flow through curved channels and characteristic bed morphology

As flow enters the upstream reach of a bend, centrifugal forces cause super-elevation of the water surface towards the outer bank which produces an opposing pressure gradient force oriented roughly perpendicular to the channel centerline. This inward directed, cross-channel gradient opposes the outward-directed centrifugal forces. As a result of the increase frictional resistance at the channel bed, the pressure gradient force is stronger than centrifugal force and flow near the bed is directed inward. Conversely, near the water surface centrifugal forces

dominant over the pressure gradient force and flow near the water surface is directed outward. This variation in the local forces acting upon the water column produces a secondary circulation that is imposed upon the downstream current resulting in large-scale helical motion as the flow travels through the bend (Figure 2.5). This idealized flow pattern has been well documented in numerous field studies (Jackson, 1975a, b; Frothingham and Rhoads, 2003), laboratory experiments (Whiting and Dietrich, 1993 a, b; Abad and Garcia, 2009a), and computational fluid dynamics models (Blanckaert, 2001; Blanckaert and de Vriend, 2003). Additionally, this pattern of helical motion is often accentuated through topographic steering by barforms (Blanckaert, 2010; Rhoads and Welford, 1991; Dietrich and Smith, 1983; Dietrich, 1987).

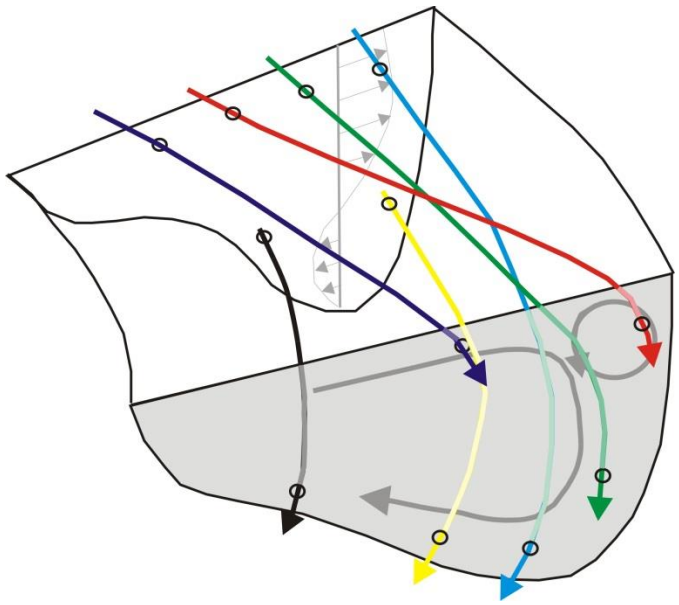

Figure 2.5 Diagram of time-averaged three-dimensional flow structure through curved channels showing super-elevation of the water surface near the outer bank and patterns of cross-stream circulation (After Blanckaert and de Vriend, 2004 and Frothingham and Rhoads, 2003).

In addition to the main curvature-induced secondary helical motion, which is present throughout most of the channel cross-section, a counter-rotating cell near the outer bank is often

observed (Thorne and Hey, 1979; Blanckaert and de Vriend, 2004) (Figure 2.5). These near-bank hydrodynamic features are smaller and commonly weaker than their curative-induced counterparts, and are produced through interactions between centrifugal forces and cross-stream turbulent stresses near the channel bed and bank (Blanckaert and de Vriend, 2004). These outer bank cells are typically restricted to the upper part of the water column, and evidence suggests that they are more pronounced in sharply curved channels with steep banks (Thorne *et al*., 1985; Bathurst *et al*., 1979). Recent experimental work has shown that increasing the outer bank roughness causes the outer bank cell to increase in both width and strength (Blanckaert *et al*., 2012). These outer bank cells have important morphological implications as they decrease near-bank velocity gradients and shear stresses acting on the outer bank, thus reducing bank erosion and stabilizing the outer bank (Thorne *et al*., 1985; Blanckaert *et al*., 2012). However, as the strength of the cell increases, these cells can advect high-momentum fluid near the surface toward the toe of the bank, increasing flow forcing and bank instability (Blanckaert *et al*., 2012).

In open-channel flows, such as rivers, the driving force acting on a control volume of water is the downslope component of the weight of the fluid. As a first-order approximation, the gravitational driving forces are balanced by flow resistance given by frictional forces at the channel boundary. Thus, if we consider a control volume with reach-averaged slope *S*, width *B*, depth *H*, streamwise length *L*, and density of water ρ (Figure 2.6), then the boundary shear stress τ_b is given as,

$$\tau_b = \rho g B H L sin\theta = \rho g A L S \tag{2.3}$$

Averaging the boundary shear stress over the streamwise distance gives the reach-averaged boundary shear stress,

$$\tau_b = \rho g A S = \rho g R S \tag{2.4}$$

where R is the hydraulic radius defined as the cross-sectional area divided by the wetted perimeter ($P_w = B + 2H$). However, in many natural rivers, the width:depth ratio is large enough that the hydraulic radius can be approximated as simply the flow depth H. As flow depth within a river varies spatially, this formulation can be applied to estimate the boundary shear stress at any location within the channel, and is commonly referred to as the depth-slope product.

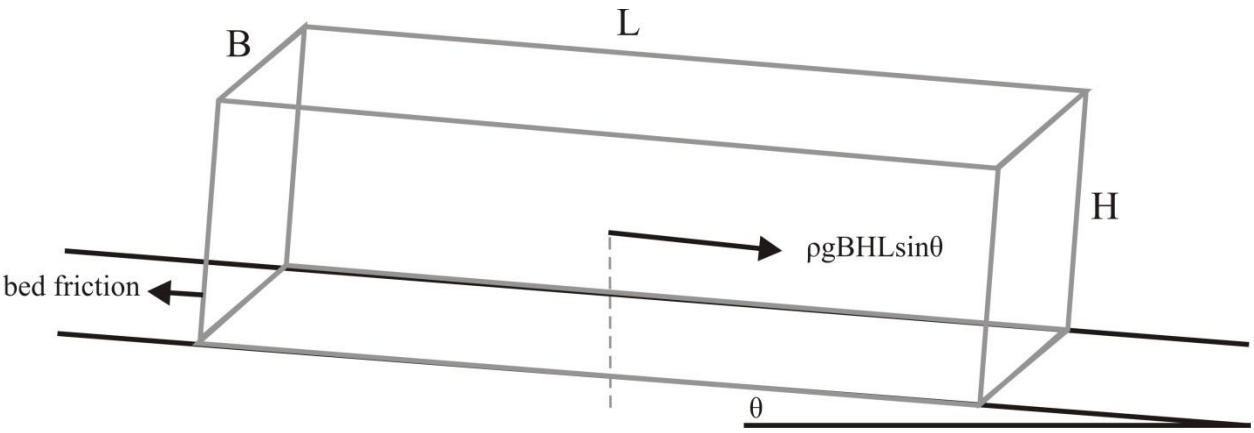

Figure 2.6 Force balance diagram for open-channel flow in a river. (After Konsoer *et al.*, 2013)

The distribution of the three-dimensional velocity field through the bend determines the distribution of boundary shear stresses which act upon the channel bed and banks (Jamieson *et al.*, 2010), thus affecting the spatial patterns of where sediment is eroded, transported and deposited downstream, influencing the overall morphology of the channel. This produces a characteristic bed morphology that can be described by the bar unit; a single bed form that consists of a pool-riffle-point bar sequence (Dietrich, 1987) (Figure 2.7A). The spatial patterns of erosion and deposition linked to the formation of the bar unit can be explained by the distribution of lateral (cross-channel) water surface gradients that influence the local driving force acting on the flow. As described above, centrifugal forces cause super-elevation of the water surface along

the outer banks of meander bends, with lower water surface elevations along the inner banks (Figure 2.7B). Thus, as water travels through the bend, the highest water surface gradients are along the outer bank downstream from the bend apex, resulting in a positive gradient in boundary shear stress, leading to erosion and the formation of a scour pool. In contrast, along the inner bank the boundary shear stress displays a negative gradient as a result of adverse water surface gradients, promoting deposition of sediment and the formation of a point bar (Figure 2.7B). Therefore, it is the gradients in boundary shear stress, not the overall magnitudes, which lead to variations in patterns of erosion and deposition within meandering rivers.

The above description of the spatial distribution of boundary shear stress and bed morphology represent the case of idealized simple bends. However, much research has been conducted on linking the spatial patterns of flow structure and bed morphology in more complex channel planforms. In high-amplitude loops, such as elongate meander bends, the bed morphology displays a series of overlapping bar units termed shingle bars (Whiting and Dietrich, 1993a). In contrast to the alternating pool-riffle-point bar sequence as observed in relatively simple bends (e.g. Figure 2.7), elongate loops typically display a series of symmetrical bar forms with multiple pools along the outer bank within the bend (Hooke and Harvey, 1983).

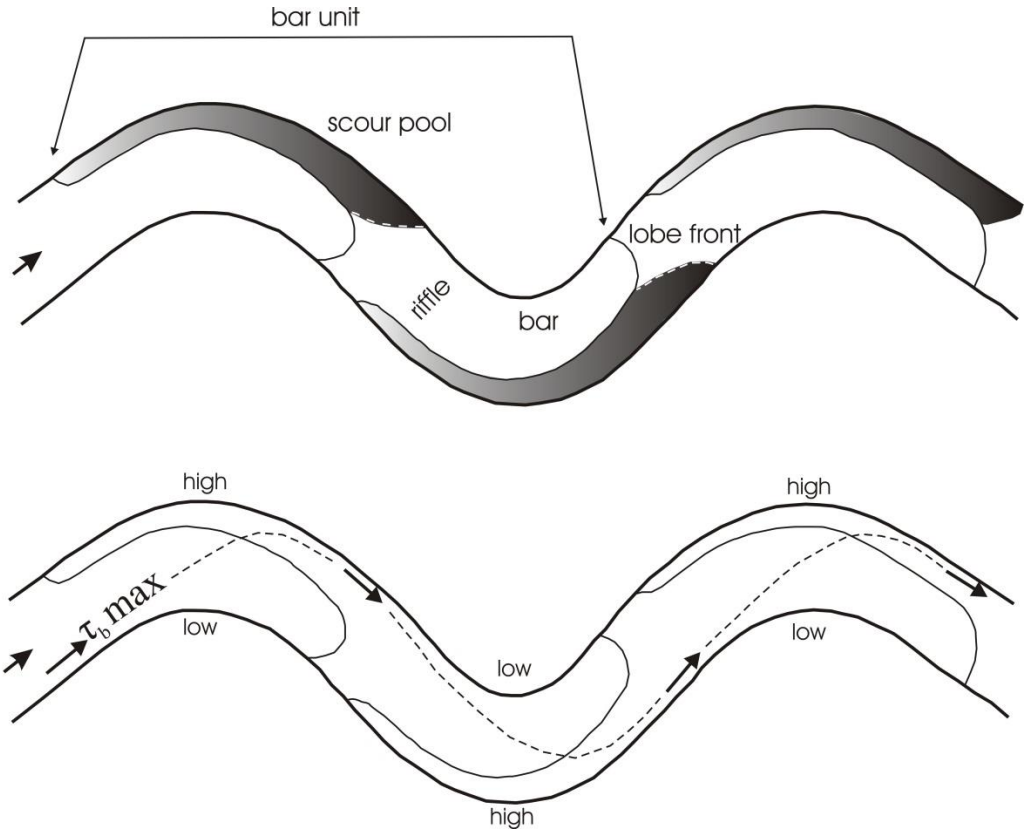

Figure 2.7 A) Spatial distribution of bed morphology within a series of meander bends and the bar unit. B) Spatial variations in water surface elevation and approximate maximum boundary shear stress. (after Dietrich, 1987).

Important to the formation of these complex planform geometries and the linked bed morphology is the "phase lag" of the three-dimensional flow structure through the bends, or the location within the bend where the high velocity core switches from the inner to outer bank. Investigations of three-dimensional flow through an asymmetrical elongate loop has shown that the spatial pattern of shear stresses acting upon the outer bank can result in the development of multiple lobes of curvature, with diverging migration of the lobes and the continued progression of complex channel geometry (Frothingham and Rhoads, 2003). The skewness of asymmetrical elongate loops (upstream or downstream valley) will also affect the phase lag of the flow through the bend, with downstream oriented bends displaying a hydraulic transition zone downstream of

the apex, resulting in deeper scour pools downstream of the apex and larger point bars upstream (Abad and Garcia, 2009a, b). Additionally, geometric parameters such as the ratio of radius of curvature to channel width (r_c/B) have been shown to effect the spatial extent of the hydraulic transition zone and the corresponding bed morphology and grain texture throughout the bend, thus influencing the depositional sequences and preservation potential of fluvial sediments (Jackson 1976).

2.4 Vegetation effects on flow structure

Riparian and in-channel vegetation has been shown to affect open-channel flows and sediment transport in four principal ways: 1) reduction of flow velocities and channel boundary shear stresses within vegetated zones by increasing flow resistance through form drag, 2) altering profiles of turbulence intensities and shear stresses, whereby the maximum values are shifted away from the channel boundary, 3) reducing the transport capacity of the flow, thus causing sorting and deposition of sediment, and 4) creating secondary circulation patterns and redirecting the primary flow direction (Thorne and Furbish, 1995; Bennett, 2004; Daniels and Rhoads, 2004; Garcia *et al*., 2004; Kean and Smith, 2004).

Early investigations concerning the increased resistance caused by vegetation on the mean flow relied on adjusting Manning's roughness coefficients, and often resulted in over predicting the roughness (Beven *et al*., 1979; Gregory *et al*., 1985). In cases of LWD, it is inappropriate to use the Manning equation to estimate roughness since it was developed to estimate roughness provided by skin friction from bed sediments, as opposed to form drag from large obstacles such as LWD (Gippel, 1995). A more appropriate approach is to account for the added resistance through a shear stress partitioning that allows for the skin friction, bed form drag, and resistance from LWD to be estimated separately (Magna and Kirchner, 2000) (Figure

2.8). Attempts at quantifying the effects of vegetation on flow structure have focused on modification of a drag coefficient through incorporation of vegetation parameters such as height, rigidity, density, cross-sectional area of individual vegetative elements, and the presence of leaves or branches. The drag force F_d per unit area A in vegetated flows can be estimated as,

$$\frac{F_d}{A} = \frac{1}{2}\rho C_d \alpha U^2 \qquad (2.5)$$

where C_d is the drag coefficient, U is the mean velocity, and α is a geometric term characterizing the size and spacing of the vegetation. The drag force acting upon any given vegetation element will depend upon Reynolds number, Froude number, the location of the vegetation within the channel, the geometry, orientation and rigidity (flexible vs. rigid) of the vegetation, and distribution of velocity within the cross section (Shields and Gippel, 1995; Nepf, 1999; Magna and Kirchner, 2000). However, it is common to assume that in-channel vegetation can be approximated by simple arrays of cylinders oriented either vertically (Nepf, 1999; Lopez and Garcia, 1998, 2001; Bennett *et al*., 2004) or horizontally in a spanwise direction across the channel (Shields and Gippel, 1995; Magna and Kirchner, 2000).

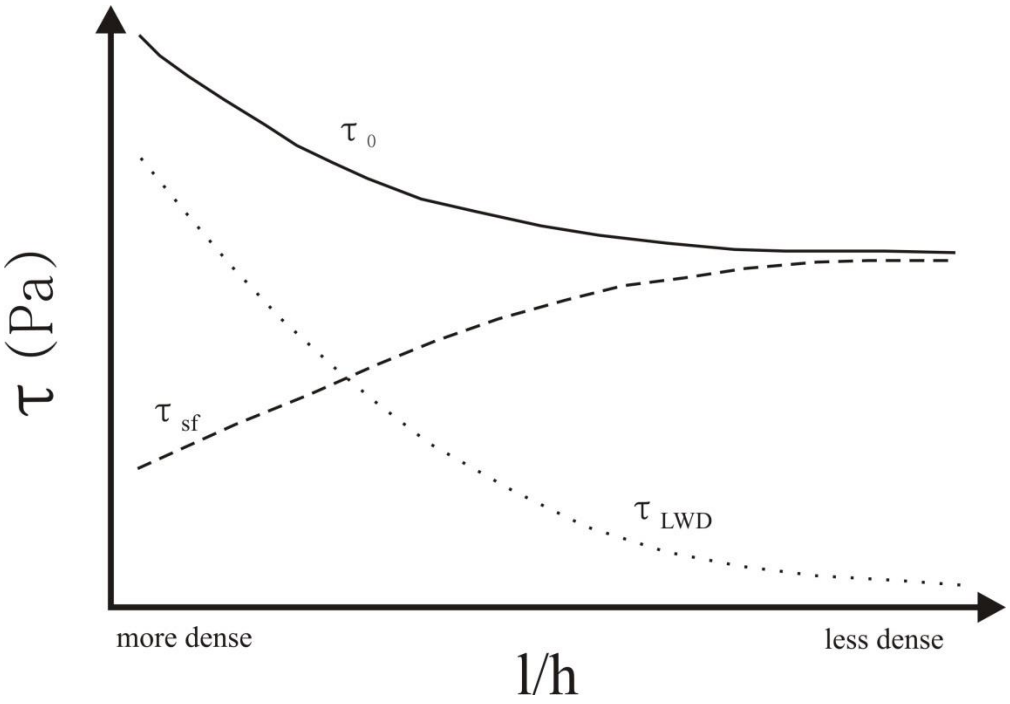

Figure 2.8 Theoretical shear stress partitioning of form drag due to large woody debris (LWD) τ_{LWD} and grain skin friction τ_{sf}. l is the mean streamwise distance between trees and h is the mean diameter of the trees. Note that as LWD density increases, the overall shear stress τ_0 increases, although there is a decrease in τ_{sf}. (After Magna and Kirchner, 2000).

Numerous experimental studies have been conducted in which the height (emergent vs submergent), rigidity (rigid vs flexible), and geometry/orientation of the vegetation are varied (Nepf and Vivoni, 2000; Jiménez-Hornero *et al*., 2007; Hopkinson and Wynn, 2009; Sukhodolov and Sukhodolova, 2010; Zong and Nepf, 2011; Gorrick and Rodríguez, 2012), and results from these types of studies show similar characteristic effects of in-channel vegetation on mean and turbulent flow, and patterns of sediment transport. As flow enters into the upstream region of vegetated flow, the increased drag and reduction of cross-sectional flow area decreases streamwise velocities, resulting in an increase in water surface elevation and an adverse pressure gradient on the leading edge of the vegetation, causing flow streamlines to be redirected around the vegetation (Zong and Nepf, 2011) (Figure 2.9A). The strong lateral gradient in streamwise

velocity from the non-vegetated flow into the zone of vegetation leads to the development of a vertically-oriented shear layer (Bennett *et al*., 2008; Zong and Nepf, 2011). For the case of submergent vegetation, a horizontally-oriented shear layer can also develop, resulting in peak turbulence intensities near the top of the vegetation canopy (Nepf and Vivoni, 2000; Lopez and Garcia, 2001; Garcia *et al*., 2004; Griffin *et al*., 2005) (Figure 2.9B). Lastly, the reduction in streamwise velocity, and thus shear stresses acting on the channel bed, within patches of vegetation promote the deposition of sediments, particularly fine sediment (Nepf and Vivoni, 2000; Zong and Nepf, 2011) (Figure 2.9C).

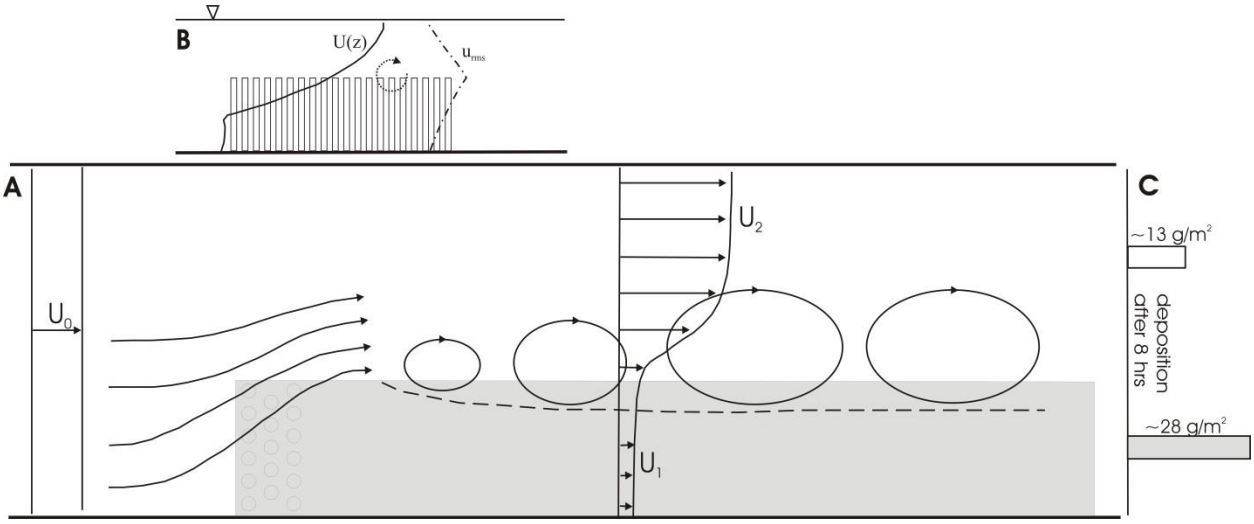

Figure 2.9 Conceptual diagram showing various effects of in-channel vegetation on flow and sediment transport in open-channel flows. A) Planview of experimental setup with zone of vegetation simulated as cylindrical rods (shaded area). B) Longitudinal cross-sectional view showing submergent vegetation as simulated cylindrical rods. C) Experimental results of sediment deposition within vegetation zone. (After Nepf and Vivoni, 2000 & Zong and Nepf, 2011).

The spatial patterns of mean flow, turbulence, and boundary shear stress can also be greatly influenced by LWD particularly through curved channels. Even relatively small percentages of LWD within a channel (2% of streambed) have been shown to provide roughly

half of the total flow resistance within a reach (Magna and Kirchner, 2000). LWD located along the outer banks of meander bends can yield lower velocities, redirect flow from the outer bank towards the center of the channel and significantly alter the secondary currents from that expected in the absence of vegetation (Thorne and Furbish, 1995; Daniels and Rhoads, 2003) (Figure 2.10). Spatial patterns of turbulence and shear stress within alluvial channels will vary depending upon the stage, location and orientation of the vegetation, size of the vegetation relative to the channel, and the spatial distribution and density of vegetation within channel reaches (Keller and Swanson, 1979; Robinson and Beschta, 2001; Young, 1991; Magna and Kirchner, 2000; Shields *et al*., 2001; Daniels and Rhoads, 2007). These interactions between vegetation and flow structure will influence the spatial pattern of erosion and deposition, leading to complex adjustments of the river planform (Beeson and Doyle, 1995; Abbe and Montgomery, 1996; Bennett *et al*., 2008).

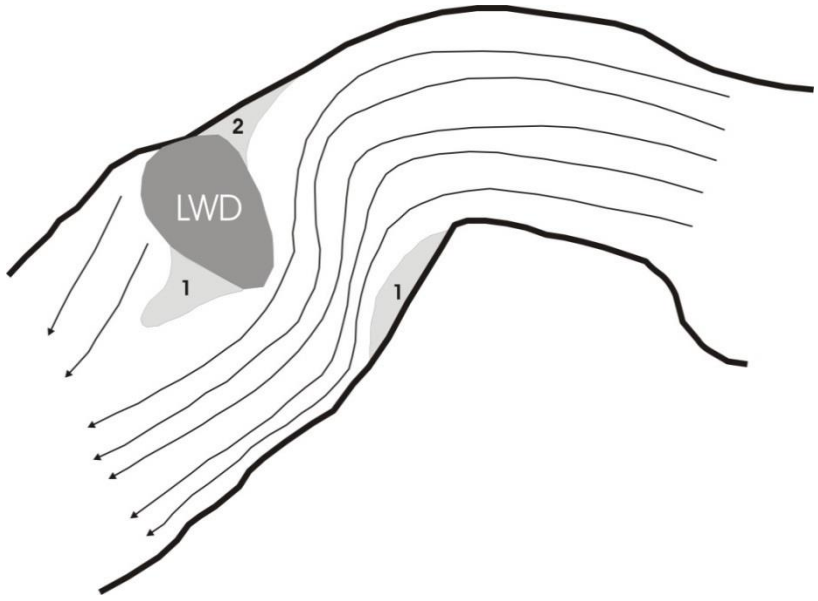

Figure 2.10 Flow redistribution caused by LWD obstruction in a small meander bend showing pattern of flow streamlines, regions of flow separation (1) and stagnation (2). (After Daniels and Rhoads, 2003).

2.5 Mechanisms of bank erosion and the influence of vegetation on bank stability

The process of bank erosion in alluvial rivers occurs most commonly through the process of fluvial entrainment at the bank toe and mass failure of the overlying bank material, with subsequent removal of the failed material (Thorne, 1982, 1992). Erosion of riverbanks through mass failure driven by gravity is responsible for the vast majority of fine-grained sediments to fluvial systems (Langendoen and Simon, 2008). The processes of mass failure in river systems are related to bank stability and typically discussed in terms of a *factor of safety*. The factor of safety for riverbanks is the ratio between the resisting and driving forces acting on a section of the bank as

$$f_s = \frac{\overrightarrow{F_c}+\overrightarrow{F_{c_r}}+\overrightarrow{F_{pw}}+\overrightarrow{F_f}+\overrightarrow{F_p}}{\overrightarrow{F_g}} \quad (2.6)$$

where f_s is the factor of safety, $\overrightarrow{F_c}$ is the cohesive resistance of the bank material (kPa),$\overrightarrow{F_{c_r}}$ is the additional cohesive resistance due to root-reinforcement, $\overrightarrow{F_w}$is the confining pressure from water within the channel, $\overrightarrow{F_{pw}}$ is the pore water pressure along the shear plane (kPa), $\overrightarrow{F_f}$ is the frictional force from the weight of soil acting along the failure plane (kN), $\overrightarrow{F_p}$ is the hydrostatic confining pressure from the water surface elevation of the streamflow (kN/m), and $\overrightarrow{F_g}$ is the gravitational force acting on the bank material (kN) (Figure 2.11).

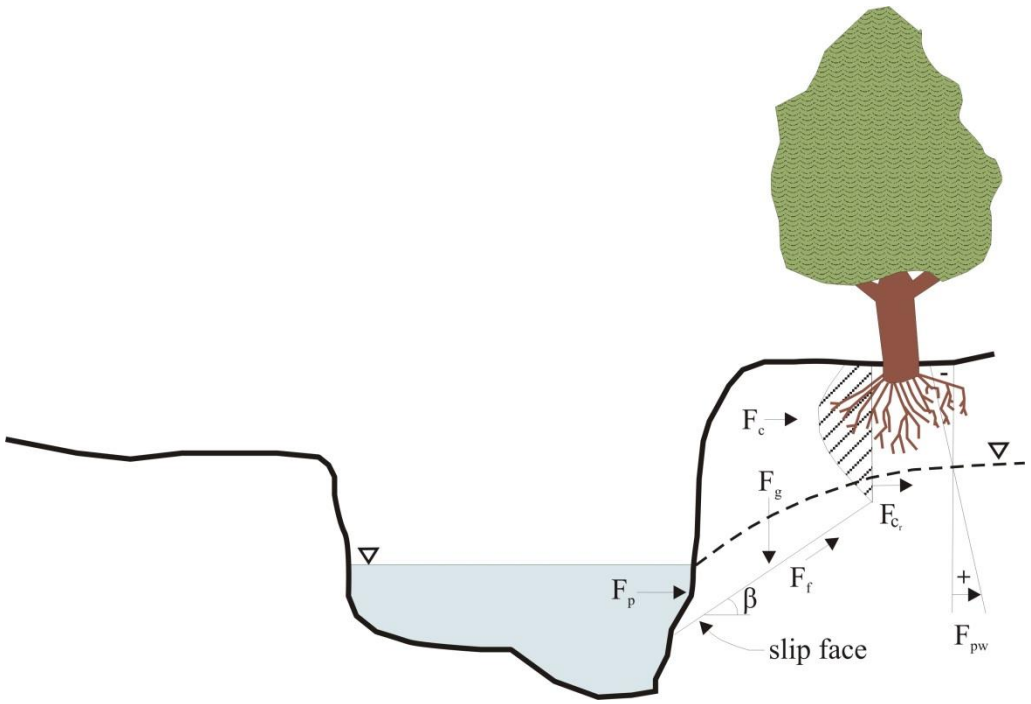

Figure 2.11 Conceptual diagram of the forces influencing stability in riverbanks. F_p is the confining pressure of the streamflow, F_g is the gravitational force acting on the bank sediments, F_{c_r} is the increased cohesion force due to vegetation roots, F_{pw} is the pore pressure, F_c is the cohesion of the bank sediment, F_f is the frictional resistance force along the slip face (After Langendoen *et al.*, 2009).

Depending upon the geotechnical properties of the banks and the vertical and lateral heterogeneities within the floodplain, multiple mechanisms of bank failure can occur. Four main mechanisms of mass failure have been identified for riverbanks and include: 1) planar failures, 2) rotational slumps, 3) cantilever failures, and 4) piping and sapping (Langendoen and Simon, 2008). The first three types of mass failure occur when over-steepening of the transverse bank slope through basal erosion causes gravitational forces to exceed resisting forces (e.g. friction, cohesion, root tensile strength), and are commonly enhanced by tension cracks within the top portion of the bank material (Thorne, 1982; Langendoen and Simon, 2008). The fourth type of failure mechanism occurs where exfiltration of groundwater at the bank face results in internal erosion (Fox *et al.*, 2006, 2007; Cancienne et al., 2008). The exact failure mechanism that occurs

is ultimately dependent upon the geotechnical properties of the channel banks and floodplains, and the presence of riparian vegetation.

One of the most significant properties affecting bank erosion is the texture of the bank material. The grain size distribution of the bank will determine the necessary fluid shear stress required to entrain and transport the sediment within the reach (Parker et al., 2008). Furthermore, the relative amount of fines, particularly clay sized particles, influences the amount of cohesion. Resistivity of the banks to fluvial entrainment is directly related to the cohesion of the bank material and increases with increasing cohesiveness (Pizzuto, 2009; Pizzuto *et al*., 2010). In highly cohesive sediments, cycles of wetting and drying, or freezing and thawing (commonly associated with seasonal variations) can have a substantial influence on the erodibility of the bank material and are referred to as *subaerial preparation* (Luppi *et al*., 2009; Simon and Rinaldi, 2006; Lawler, 1992; Pizzuto, 2009; Wynn and Mostaghimi, 2006). Particularly, in shrink-swell clays cycles of wetting and drying can cause tension cracks and loosening of bank materials. Likewise, during periods of freezing and thawing, the formation of needle ice can displace near-surface bank sediments making normally cohesive fine-grained sediments much more susceptible to fluvial entrainment (Lawler, 1993).

Another property known to influence bank erosion is pore water pressure, which has received much recent attention in the literature (Shields et al., 2009; Simon and Collison, 2001; Thorne, 1992). Shields et al. (2009) installed tensiometers at various depths within the bank and floodplain to measure the pore water pressure (kPa) during flooding events on an experimental stream in Mississippi. Their results indicate that the banks were more susceptible to mass failure under high positive pore pressures, most typically during the falling limb of the flood hydrograph, as the confining pressure from the flood decreased (Thorne, 1992). Conversely,

negative pore water pressures, termed matric suction, can dramatically increase the stability of channel banks. This effect mostly occurs during periods of high evapotranspiration within the riparian zone, as the vegetation extracts water from the floodplain (Simon and Collison, 2001; Shields et al., 2009). Also related to pore water pressure is the lateral flow path of groundwater within the floodplain. Lateral flow paths and groundwater seepage at the bank face have been shown to locally increase the erodibility of the bank through both fluvial entrainment and undercutting and cantilevering of the overhanging bank block (Fox *et al.*, 2006, 2007; Cancienne et al., 2008).

Perhaps the most controversial and still misunderstood factor affecting bank stability is riparian vegetation. Research in this topic is abundant; however, general agreement as to whether forested reaches are more stable than non-forested reaches has not yet been achieved, and is most likely related to a scale dependency (Eaton and Giles, 2009). Some researchers have suggested that riparian grasses result in less floodplain area being eroded compared to forested reaches, which have the tendency to mobilize sediment through wind-throw (trees felled from wind) and surcharge (tree slumping) from the mass of the trees (Trimble, 2004; Zimmerman et al., 1967). Further arguments against the role of riparian forests as stabilizing agents are that the forests are sources of LWD which have the potential to create LWD jams and cause localized scour (Trimble, 2004).

Although these arguments about the destabilizing effects of forest vegetation have conceptual merit, several studies have shown that forested reaches have lower rates of bank retreat than non-forested reaches (Abernethy and Rutherfurd, 1998; Pizzuto *et al.*, 2010; Tal and Paola, 2010). Beeson and Doyle (1995) performed statistical analyses of bank erosion following a flooding event in British Columbia, Canada. Using aerial photography before and after the

flood, a total of 748 bends were identified on four streams, and their results indicate that bank erosion is four times as likely to occur on bends without riparian vegetation when compared to vegetated bends. Many factors have been identified to explain the increase in bank stabilization of riparian vegetation. One of the most influential factors, depending on vegetation type and channel size, is mechanical root-reinforcement. Root networks not only provide mechanical reinforcement through increased tensile strength, they also affect the hydrologic and hydraulic processes acting on stream banks (Pollen-Bankhead and Simon, 2009, 2010; Pollen and Simon, 2005). Hydrologically, the root network allows for the riparian vegetation to remove water from the floodplains, thereby increasing matric suction. Hydraulically, as roots are exposed at the face of the bank, flow may be deflected away from the bank resulting in reduced shear stresses.

The increased tensile strength of bank materials is also important for failed bank slumps that accumulate near the bank toe. Micheli and Kirchner (2002) measured the effects of wet meadow vegetation on bank strength and failure mechanisms of a small montane meadow stream in California. Through field measurements and a geotechnical model, their results showed that the wet meadow vegetation increases the thickness, width, and cohesiveness of bank cantilevers which increase the time required to undermine, detach, and remove failed bank blocks. These larger block slumps provide additional protection from further bank erosion and can survive relatively infrequent flood flows.

2.6 Theoretical models of bank retreat and meander migration

Traditional theoretical models for long-term river migration rely on two-dimensional analytical treatments that relate the rate of migration to the near-bank excess velocity and a dimensionless coefficient calibrated against field data (Hasegawa, 1977; Ikeda *et al*., 1981). These types of models have provided much insight into the process dynamics and behavior of

meandering rivers (Motta *et al*., 2012), but are limited because they operate under the assumption that channel curvature is the primary factor influencing bend migration. Furthermore, these models assume a constant channel width and that bank retreat is a product solely of erosion of the bank toe material. Additionally, these types of models are only able to create relatively simple planform configurations prior to cutoff (Güneralp and Rhoads, 2011). However, similar models that incorporate a randomly generated floodplain resistivity throughout the simulation domain are capable of producing complex channel planforms that are comparable to those observed in nature, emphasizing the importance of spatial variability in floodplain resistivity on meander evolution (Güneralp and Rhoads, 2011; Motta *et al*., 2012).

Alternatively, models of localized bank retreat are more physically-based and incorporate vertical and horizontal heterogeneities, complex bank geometries, effects from floodplain vegetation, and ground water pore pressures (Darby and Thorne, 1996a,b; Simon *et al*., 2003; Rinaldi and Darby, 2007; Langendoen and Alonso, 2008; Langendoen and Simon, 2008). These models are capable of thus capturing the geotechnical processes that occur during bank erosion and retreat, such as basal undercutting, failure of overlying cohesive sediments including planar, rotational, and cantilever failures, and ground water sapping (Rinaldi *et al*., 2004; Fox *et al*., 2006; Cancienne *et al*., 2008; Langendoen *et al*., 2009; Pollen-Bankhead and Simon, 2009). However, despite the inclusion of detailed bank processes, many of these models still rely on an erosion coefficient to account for the critical shear stress (τ_c) necessary for entrainment of sediment. This is partly due to the difficulties in obtaining accurate measurements of cohesion and τ_c in the field. Furthermore, the use of an erosion coefficient provides a means to calibrate against field data without the need to partition between skin friction and near-bank form drag. Recent work has focused on developing more physically-based channel planform models by

incorporating detailed subroutines for bank stability (Darby *et al*., 2002; Rinaldi *et al*., 2008; Parker *et al*., 2011; Motta *et al*., 2012). These morphodynamic models are much more successful than their predecessors at producing realistic channel planforms, yet still do not incorporate any influence exerted by in-channel vegetation.

The issue of shear stress partitioning ($\tau_T = \tau_{sf} + \tau_d$) into skin friction ($\tau_{sf}$) and form drag ($\tau_d$) components has long been recognized for sediment transport within the main portion of river channels. However, more recent advancements have applied a shear stress partitioning to determine the skin friction acting on channel banks (Kean and Smith 2006a,b). In the method of Kean and Smith (2006a,b) form drag introduced by large-scale topographic irregularities of channel banks are approximated by Gaussian-shaped bumps allowing for relatively easy geometric characterization and estimation of the form drag forces. Darby *et al*. (2010) combine a physically-based model of bank stability and in situ measurements of bank erodibility parameters with the method of Kean and Smith (2006a,b) to estimate annual bank erosion on the Mekong River, providing the first predictions of hydraulic bank erosion without requiring calibration against an erosion coefficient.

2.7 Current remaining issues related to bank erosion and vegetation in large rivers

The above discussion highlights only a fraction of the substantial extant literature dedicated to advancing our understanding of the co-evolution of flow, sediment transport and morphologic change, and the influence of vegetation on meandering rivers. While our understanding of these processes has increased significantly over the past few decades, there still remain gaps in our current knowledge of how vegetation interacts with flow structure and short- and long-term patterns of bank erosion, particularly for large rivers.

Despite the prevalence of in-channel vegetation, our knowledge of the interactions between vegetation, flow structure, and sediment transport has been limited to arrays of simplified plant geometries in small or moderately sized rivers with relatively simple planform geometry, or using simplified experimental flumes and numerical models. To date, no such studies have examined in detail the flow structure around complex geometries such as LWD, and how this influences patterns of bank erosion in large rivers. This is, in part, due to the difficulties in obtaining high spatial and temporal measurements of the flow field and channel morphology around complex vegetation elements in large rivers. However, recent advances in hydroacoustic instrumentation now allow for a more thorough characterization of the flow structure in such environments.

The lack of detailed measurements from large rivers investigating the effects of vegetation on flow structure and bank erosion also limits our ability to accurately inform morphodynamic models of short- and long-term migration models. While recently proposed methods (e.g. Kean and Smith, 2006a, b) provide a means to estimate the form roughness of banks and vegetation, the complex geometry of LWD limits the ability to approximate these roughness elements as Gaussian shapes. Thus, despite the improvements in numerical modeling concerning bank erosion, the importance of near-bank vegetation is often neglected, limiting the predictive ability of these models.

The work presented herein begins to address some of the remaining gaps in our current understanding related to the influence of riparian and in-channel vegetation on flow structure and bank erosion on a large meandering river. The following chapters examine the near-bank flow structure of forested and non-forested meander bends to elucidate the influence of near-bank large woody debris on bank erosion and meander migration patterns in a large river. Through

detailed field measurements and analyses of bank morphology and flow structure around LWD, this research provides invaluable information about the process dynamics of complex meander bends of large rivers, and allows for detailed comparisons between laboratory and small river investigations to address the issue of scaling among vegetation and fluvial systems.

CHAPTER 3

COMPARISON OF NEAR-BANK HYDRODYNAMICS IN FORESTED AND UNFORESTED ELONGATE MEANDER LOOPS ON A LARGE RIVER

3.1 Introduction

Meandering in alluvial rivers is produced through complex interactions among three-dimensional flow structure, channel planform, sediment transport, and the geotechnical properties of the channel banks and floodplains. As flow enters the upstream reach of a bend, centrifugal forces cause super-elevation of the water surface towards the outer bank which produces an opposing pressure gradient force oriented roughly perpendicular to the channel centerline. This inward directed, cross-channel gradient opposes the outward-directed centrifugal forces and results in large-scale helical motion as flow travels through the bend (Frothingham and Rhoads, 2003). Secondary circulation associated with the helical motion advects high momentum near-surface fluid outward and downward within the curving channel, resulting in the development of a submerged high-velocity core near the base of the outer (concave) bank (Blanckaert, 2011). The development of a point bar within natural meandering channels modifies the lateral extent of secondary circulation, confining it through topographic steering effects to the channel thalweg (Dietrich and Smith, 1983; Rhoads and Welford, 1991; Blanckaert, 2010). The distribution of the three-dimensional velocity field determines the spatial pattern of boundary shear stresses that act upon the channel bed and banks (Jamieson *et al*., 2010), thus affecting rates of sediment transport and bank migration.

The spatial patterns of mean flow, turbulence, and boundary shear stress can also be greatly influenced by large woody debris (LWD) and other large-scale roughness elements,

particularly in curved channels. Even relatively small percentages of LWD within a channel (2% of streambed) have been shown to provide roughly half of the total flow resistance within a reach (Magna and Kirchner, 2000). LWD along the outer banks of meander bends can reduce velocities, redirect flow from the outer bank towards the inner bank, and significantly alter the pattern of secondary currents from that expected in the absence of vegetation (Thorne and Furbish, 1995; Daniels and Rhoads, 2003; Gorrick and Rodriguez, 2012). Redirection of the high-velocity core around LWD obstacles can locally increase curvature of the flow, enhance helicity, and lead to inward advective transport of high velocity flow toward the inner bank (Daniels and Rhoads, 2004), which, in turn, can shift the locus of maximum near-bed shear stress away from the outer bank toe where maximum rates of bank erosion typically occur (Thorne, 1992). The effect of vegetation on spatial patterns of turbulence and shear stress within meander bends will vary with flow stage, the location and orientation of the vegetation, the size of the vegetation relative to the channel dimensions, and the spatial distribution and density of vegetation within the channel (Keller and Swanson, 1979; Robinson and Beschta, 1990; Young, 1991; Shields *et al*., 2001; Daniels and Rhoads, 2007).

In addition to the main secondary helical motion, which is present throughout most of the channel cross-section, a counter-rotating cell near the outer bank is often observed (Thorne and Hey, 1979; Blanckaert and de Vriend, 2004). These small, weak near-bank cells are produced through interactions between centrifugal forces and cross-stream turbulent stresses near the channel boundary (Blanckaert and de Vriend, 2004). Such cells generally are confined to the upper part of the water column and tend to be most pronounced in sharply curved channels with steep banks (Thorne *et al*., 1985; Bathurst *et al*., 1979). Recent experimental work has shown that increasing the outer bank roughness causes the outer bank cell to increase both in width and

strength (Blanckaert *et al*., 2012). These outer bank cells have important morphological implications; by decreasing near-bank velocity gradients and shear stresses acting on the outer bank, such cells reduce bank erosion and stabilize the outer bank (Thorne *et al*., 1985; Blanckaert *et al*., 2012). However, as the strength of the cell increases, these cells can advect high-momentum fluid near the surface toward the toe of the bank, increasing near-bank shear stresses and bank instability (Blanckaert *et al*., 2012).

Although increasing bank roughness via grain size has been shown to strengthen and widen outer bank cells (Blanckaert *et al*., 2012), the effects of large scale roughness elements, such as LWD and slump blocks, on the near-bank flow structure (including outer bank cells) are not yet fully understood, particularly for large rivers. In contrast to the streamwise-oriented outer bank cells, other research suggests that in the presence of large-scale bank roughness vertically-oriented coherent structures become dominant (Kean and Smith, 2004, 2006a,b; Ferreira da Silva and Ahmari, 2009; Darby *et al*., 2010). In these situations, flow past a roughness element creates a pressure differential between the upstream and downstream sides of the element, resulting in flow separation and reattachment downstream of the element (Kean and Smith, 2006a). The resulting form drag stress is typically the dominant shear stress acting on the channel boundary. Thus, accurate quantification of the near-bank flow structure in the presence of LWD is vital for determining the appropriate shear stresses acting on the channel boundary.

While many studies have investigated the influence of LWD on flow structure and channel morphology (Young, 1991; Thorne and Furbish, 1995; Abbe and Montgomery, 1996; Daniels and Rhoads, 2007; Bennett *et al*., 2008; Zong and Nepf, 2011), few have examined in detail the influence of LWD on the near-bank three-dimensional flow structure in large rivers. Thus, the need exists for high-resolution measurements of the near-bank velocity field in large

rivers to develop an improved understanding of the feedbacks between near-bank large-scale roughness elements, three-dimensional flow structure, and rates of bank erosion. This chapter investigates the three-dimensional flow structure near the outer banks of two elongate bends with different types of vegetation cover along a large meandering river. The outer bank of one of the bends is heavily forested, whereas the outer bank of the other bend is unforested. Primary goals of the study are to examine differences in near-bank flow structure between the two bends, investigate the patterns of secondary currents that arise through interaction with near-bank LWD, estimate the shear stresses acting on the channel boundary, and explore the spatial patterns of near-bank secondary flow throughout these two bends. The results of the research have implications for rates of bank migration and channel planform evolution.

3.2 Field Site

The field site for this study consists of two elongate meander bends on the lower Wabash River, near Grayville, Illinois (Figure 3.1). At this location, the Wabash River has a bankfull width that ranges between 200-350 m, a bankfull depth between 4-8 m, and a drainage area of roughly 74070 km^2. Based on 85years of hydrologic data from a U.S. Geological Survey gaging station at Mt. Carmel, Illinois (~20 km upstream of Grayville), the mean annual discharge of the lower Wabash River is 881 m^3s^{-1}, whereas the mean annual peak discharge is 4112 m^3s^{-1}. The lower Wabash River meanders freely across its alluvial floodplains, except for a few locations where it erodes into Pleistocene glaciofluvial sediments or bedrock (Jackson, 1975a). Furthermore, the Wabash River is currently the only meandering river of its size in the conterminous United States that is unregulated, providing an ideal opportunity to study bank erosion and meander evolution on a large natural river. Bank cover along the river varies

spatially both within and between consecutive bends and includes riparian forests, grasses, and agricultural fields.

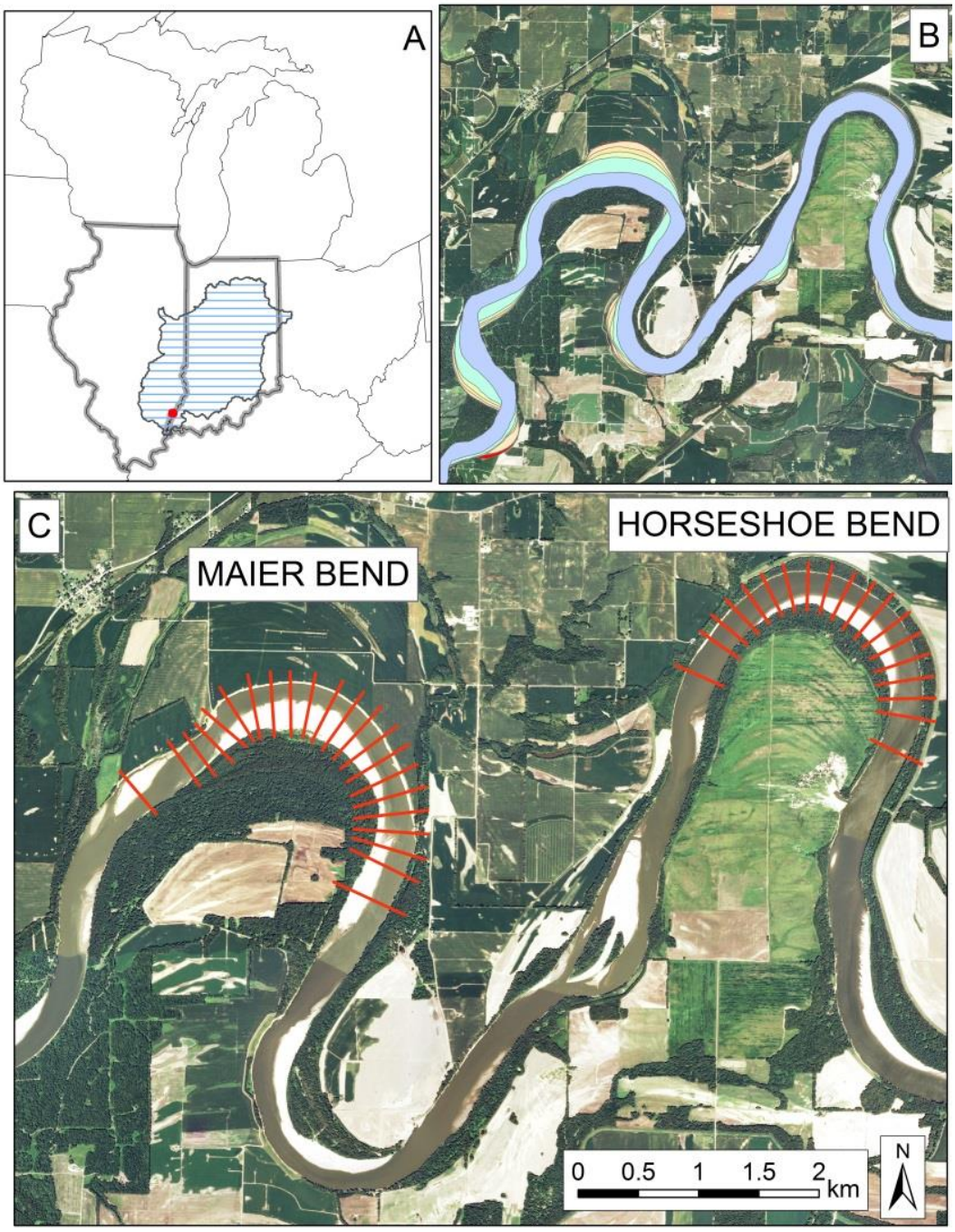

Figure 3.1: A) Location of field site within Wabash River basin shown by red dot. B) Digitized banklines from aerial photography (1938, 1980, 1988, 1998, 2012) showing patterns of channel migration at area of study. C) Location of Maier Bend and Horseshoe Bend shown with ADCP cross sections.

The upstream site, Horseshoe Bend, is an elongate meander bend ~3 km in length with riparian forest along the outer bank (Figure 3.2). Although bank composition varies slightly along the bend, bank materials at Horseshoe Bend are composed of a relatively thick layer (4-6 m) of cohesive fine sediments (> 70% silt and clay) underlain by a basal layer of coarse sand and fine gravel. The upper part of the banks, formed in the cohesive material, is nearly vertical, whereas the lower part of the banks tends to be at, or close to, the angle of repose. On the downstream limb of the bend, the channel erodes into Pennsylvanian shales of the Mattoon Formation (Illinois Basin Consortium – Study 5, 2001), restricting downstream migration of the bend (Figure 3.2B). Bank erosion processes along Horseshoe Bend result in the introduction of large trees to the channel near the outer bank. These trees are embedded in the base of the bank, and tend to become aligned roughly perpendicular to the local mean flow direction, and are present along the majority of the bend. Repeat surveys suggest individual LWD obstacles can have residence times greater than five years (see discussion in Chapter 4, section 4.5).

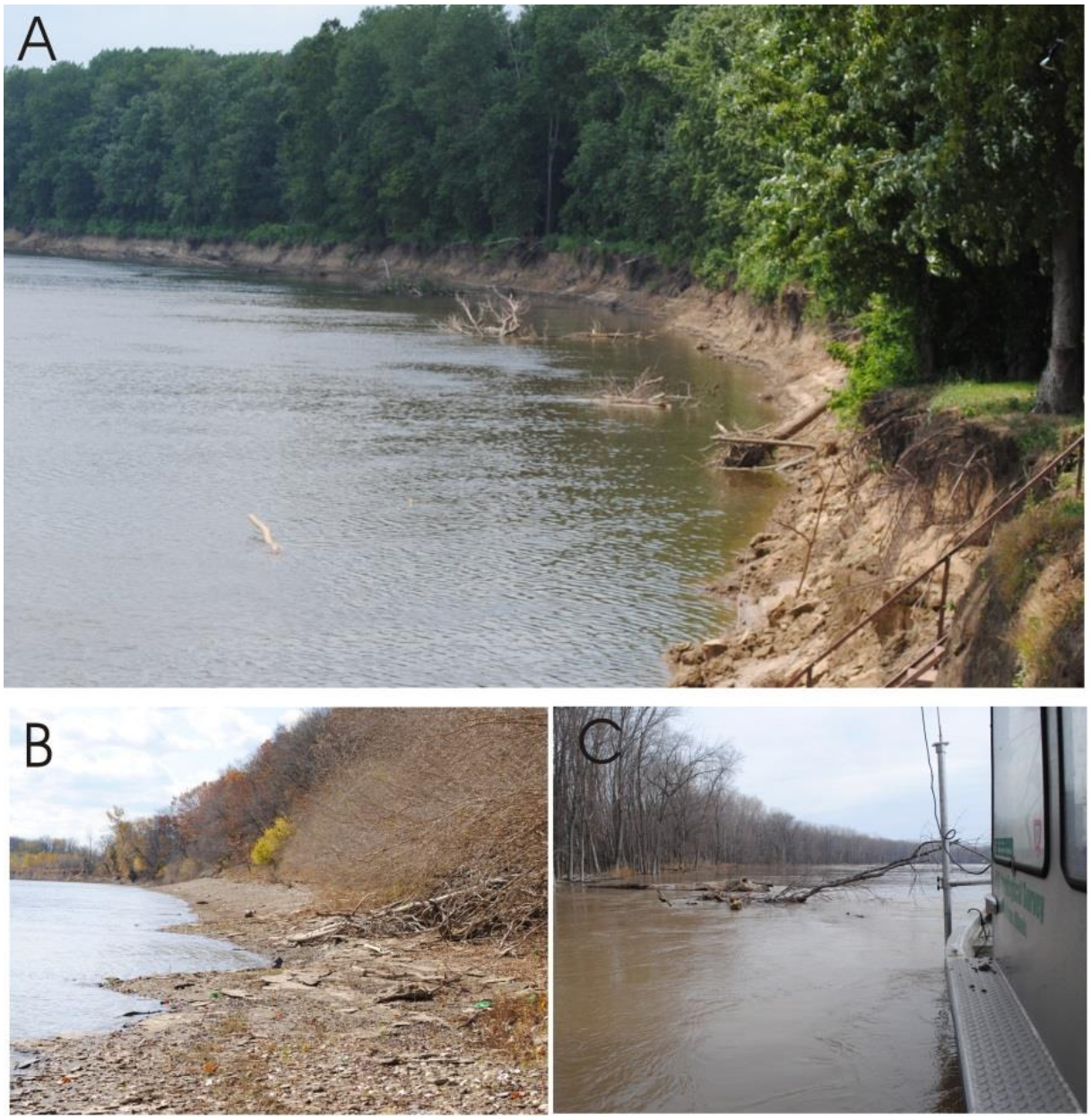

Figure 3.2: A) Near-bank LWD on Horseshoe Bend at low flow (looking downstream). B) Downstream bedrock outcrop along outer bank. C) Near-bank LWD at near-bankfull flow conditions (01/16/2013) at cross-section 73.50.

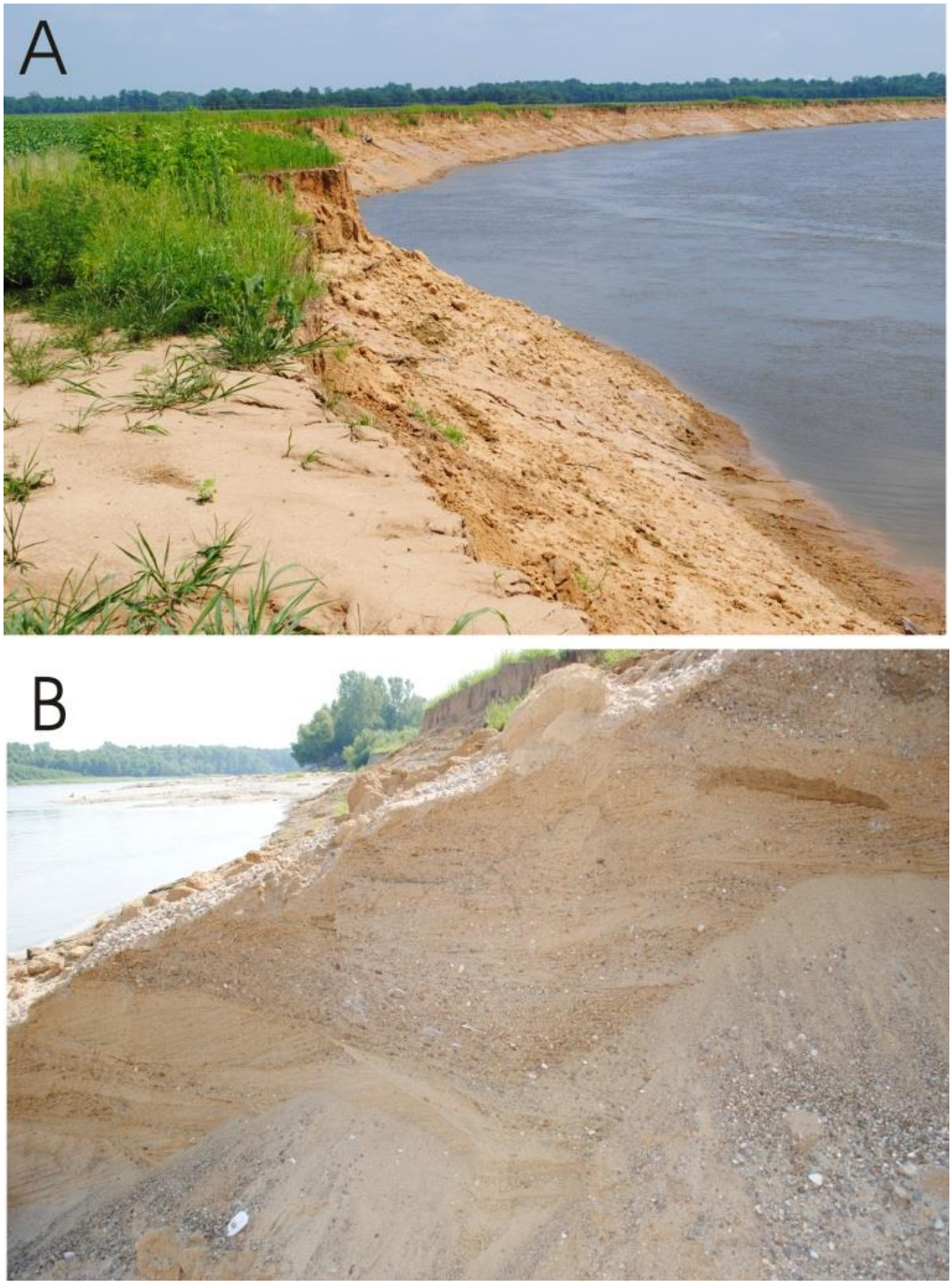

Figure 3.3: A) Agricultural floodplains on Maier Bend showing lack of vegetation on the banks and a ~30° transverse slope. B) Profile view of outer bank showing mixture of sand and gravel with cross-bedded stratigraphy.

The second site, Maier Bend, located ~12 km downstream of Horseshoe Bend, is also an elongate meander bend ~4 km in length flanked by an agricultural floodplain (Figure 3.3). No tributaries join the Wabash River between Horseshoe Bend and Maier Bend. Crops grown in the field along the outer bank of the bend include corn and soybeans. In contrast to Horseshoe Bend, the bank material at Maier Bend is composed of a lower layer consisting of 4-5 m of coarse sand and fine gravel. This part of the bank has a slope angle of about 30°. The upper part of the bank, which is nearly vertical, consists of a 1-2 m layer of fine sand and silt. Downstream of the bend apex, the channel erodes into a small outcrop of interbedded shales and sandstones of the Pennsylvanian Bond Formation (Illinois Basin Consortium – Study 5, 2001). Although Maier Bend lacks substantial in-channel and/or bank vegetation, the outer bank morphology consists of large-scale undulations (15-30 m) that occur periodically throughout the bend.

Time-series analysis of aerial photography reveals significant differences in the rates of bank erosion and planform migration between Maier and Horseshoe bends (Figure 3.1B). Over the time period of 1938 – 2012, Horseshoe Bend has been relatively stable, with an average rate of bank migration of ~0.75 myr^{-1}, and maximum rates occurring near the bend apex. By comparison, during the same period, rates of bank erosion over much of Maier Bend were on the order of 8-15 myr^{-1}. Patterns of bank migration for this bend vary spatially, with little or no bank erosion occurring at the entrance and exit of the bend and exposure of bedrock in the channel downstream of the apex constraining migration at this location, especially over the past 10-15 years. The net result is progressive extension of the bend laterally into the adjacent floodplain.

3.3 Methods

Flow measurements were obtained for three different flood events between spring 2011 and winter 2013. The first flow measurements (Campaign 1) were obtained on May 9-10, 2011

during a flood event with a peak discharge of approximately 7,650 m^3s^{-1} (05/03/2011) and a recurrence interval of about 15 years. The discharge at the time of data acquisition was 5,660 m^3s^{-1} – a magnitude that still produced substantial overbank flow along the Wabash River. The second set of flow measurements (Campaign 2) was collected on June 28-29, 2011, during peak flow of an event with a maximum discharge of 2450 m^3s^{-1} and a recurrence interval of 1.2 years. This event corresponds closely to the bankfull discharge along the lower Wabash River. The third set of flow measurements (Campaign 3) were obtained on January 15-16, 2013 at a discharge of 2380 m^3s^{-1} - a flow similar to that of Campaign 2.

Three-dimensional velocity measurements were collected along predetermined cross sections oriented perpendicular to the channel centerline using a boat-mounted Teledyne RDI 1200 kHz acoustic Doppler current profiler (ADCP) with an integrated Hemisphere A100 dGPS antenna located directly above the ADCP. The sampling frequency of the dGPS was ~1 Hz with an accuracy greater than 60 cm. At each cross section, four to six traverses were collected to improve time-averaging of the velocity fields (Szupiany *et al*., 2007). These ADCPs are 4-beam systems, with a 20° beam angle, possessing a bin size in profiling mode as low as 0.1 m. Velocity measurements were acquired with a sampling frequency ~1 Hz, with a resolution of roughly 0.01 ms^{-1} and an accuracy of +/- 0.25% of the water and boat speed. For Campaigns 1 and 2, velocity measurements were collected across the entire width of flow at an average streamwise distance of 150 m (Figure 3.1) During campaign 3, three cross sections on Maier Bend and five cross sections on Horseshoe Bend extended across the width of flow throughout the bend, but measurements focused mainly on numerous transects spaced at 40 m intervals along the channel that extended from the edge of water along the outer bank to the thalweg. The

purpose of these focused measurements was to characterize in detail near-bank velocity structure around the bends.

Cross sections within the series of meander bends near Grayville, IL were produced by digitizing banklines from NAIP 2011 orthophotography and using the Planform Statistics toolbar (J. Lauer – NCED http://www.nced.umn.edu/content/stream-restoration-toolbox) to calculate a channel centerline. Cross sections orthogonal to the centerline were established at a streamwise spacing of 150 m, corresponding to the channel half-width (Güneralp and Rhoads, 2008). These full cross sections are labelled by whole number increments, starting with the meander bend upstream of Horseshoe Bend and continuing downstream through Maier Bend. Thus, cross section 100 corresponds to a streamwise distance of 15,000 m (100 x 150m). The partial near-bank cross sections used for campaign 3 have a streamwise spacing of ~about 37.5 m, corresponding to $1/8^{th}$ of the channel width. To maintain consistency with the original cross-section numbering system, these near-bank sections are labelled with quarter divisions of whole numbers (e.g. 150, 150.25, 150.50, 150.75). Thus near-bank section 100.25 corresponds to a streamwise distance of approximately 15,037.5 m.

All velocity measurements were collected using RDI-WinRiver II, which resolves velocities into north, east, and vertical components. The data were exported to ASCII format and processed using the Velocity Mapping Toolbox (VMT), a suite of Matlab-based programs designed for processing and visualization of ADCP data (Parsons *et al*., 2013). VMT projects multiple ADCP traverses onto a common plane of intersection and spatially and temporally averages the data for visualization of the three-dimensional velocity field within cross sections. A major advantage of VMT is its ability to quickly decompose the velocity field using various frames of reference, such as streamwise – transverse (relative to the orientation of the cross

section measured in the field), zero net secondary discharge (relative to the plane of zero net discharge over the cross section), and the Rozovskii (1957) method (relative to local depth-averaged vector for each vertical profile of velocity measurements). The Rozovskii (1957) method has been shown to be particularly useful in conditions of converging and diverging flow streamlines (Rhoads and Kenworthy, 1998), flow conditions commonly observed in the presence of in-channel vegetation (Daniels and Rhoads, 2007; Sukhodolov and Sukhodolova, 2010). In this paper, the cross-sectional frame of reference and Rozovskii (1957) method are both used to visualize cross-sectional velocity fields.

To compare the near-bank velocity fields to bank morphology and roughness elements, detailed topographic data of the outer banks were obtained using a Topcon GLS-1500 laser scanner at a sampling frequency of 30 kHz with an accuracy of roughly 5 mm. Outer bank topographic surveys were conducted at each bend during low flow conditions in August 2011 by positioning the scanner at various locations along the point bar. A Topcon GR3 RTK-GPS with accuracy ~10 mm was used to establish three temporary benchmarks for georeferencing individual scan positions. A transformation was then applied to determine instrument location with subcentimetric accuracies. Scan point densities were roughly 5 cm covering ~2.5 km of Maier Bend and ~2 km of Horseshoe Bend, requiring about 15 different scan locations for each bend.

Fluid shear stresses acting along the channel bed can be estimated using a depth-averaged Chezy resistance equation as follows,

$$\tau = \rho g H S = \rho C_f U^2 \qquad (3.1)$$

where τ is shear stress (Pa), ρ is the fluid density of water (kg/m^3), g is the gravitational acceleration (ms^{-2}), H is flow depth (m), S is slope, C_f is the friction coefficient, and U is the

depth-averaged streamwise velocity (ms^{-1}). In Equation 1, τ represents the boundary shear stress resulting both from skin friction by grains of sediment and from form drag by bedforms. However, for estimating rates of sediment transport, and thereby morphological change, the component of shear stress due to skin friction is the relevant force acting on the channel boundary and thus must be partitioned from the total resistance. One common approach for shear stress decomposition is (Einstein 1950):

$$\tau = \tau_s + \tau_f \tag{3.2}$$

$$\tau_s = \rho g H_s S = \rho C_{fs} U^2 \tag{3.3}$$

$$\tau_{bf} = \rho g H_f S = C_{ff} U^2 \tag{3.4}$$

where τ_s is the shear stress due to skin friction and τ_f is the shear stress due to form drag from bedforms, C_{fs} is the friction coefficient associated with skin friction, C_{ff} is the friction coefficient associated with form drag, H_s is the flow depth from skin friction, and H_f is the form drag flow depth. To solve for shear stress due to skin friction, a Keulegan formulation for resistance can be used to estimate the skin friction coefficient,

$$C_{fs} = \left[\frac{1}{\kappa}\ln\left(11\frac{H_s}{k_s}\right)\right]^{-2} \tag{3.5}$$

where κ is the von Kármán constant 0.4, k_s is the roughness height associated with the median grain size, $k_s = 2D_{50}$, herein D_{50} estimated as 0.7 mm. Substituting Eq. 3.5 into Eq. 3.3, and iteratively solving for H_s yields an estimate of τ_s. The iterative method supplies an initial estimate of H_s and then progressively adjusts this value until the solution converges. Values of τ_s were estimated using the ADCP-measured values of depth-averaged streamwise velocity and a reach averaged slope of 0.0001 for each ensemble at all cross sections from campaigns 1 and 2. The reach averaged slope was estimated using water-surface elevation data from USGS gaging

stations at Mt. Carmel, IL and New Harmony, IN. The estimated values of τ_s along each cross section were imported into iRIC, a river flow and bed sediment analysis software package capable of producing curvilinear computational grids for meandering river channels. A TIN representation of the shear stress values and an inverse distance weighting interpolation scheme was used to estimate shear stress values between cross sections on a curvilinear grid with a 6 m streamwise spacing and a 1 m transverse spacing. These values were then imported into ArcGIS for visual display and comparison between flow events.

3.4 Results

3.4.1 Depth-averaged flow through meander bends

3.4.1.1 Maier Bend

The spatial pattern of depth-averaged velocity vectors for Campaign 1 along Maier Bend shows that on the upstream limb of this bend (cross-sections 135 – 141), the highest velocities (~ 1.75 ms^{-1}) are located near the inner bank and that depth-averaged velocities along the outer bank are relatively small (Figure 3.4A). As flow continues through the bend, the zone of highest depth-averaged velocities within the channel shifts toward the outer bank. Downstream of this location, within the bend apex region (cross sections 146-151), the pattern of depth-averaged velocities within each cross section is highly asymmetrical, with the highest velocities adjacent to the outer bank and reduced velocities along the inner bank over the point bar. Velocities near the outer bank are greatest (~1.75 ms^{-1}) immediately downstream of the bend apex (cross-sections 149-151). Farther downstream (cross-sections 152-153), the depth-averaged velocity vectors are directed away from the outer bank towards the center of the channel by a local bedrock outcrop. Downstream of the bedrock (cross-section 156), the depth-averaged velocities

attain the highest values within the bend (>2 ms^{-1}), but this high velocity core is located away from the outer bank with a shear layer existing between this core and the outer bank.

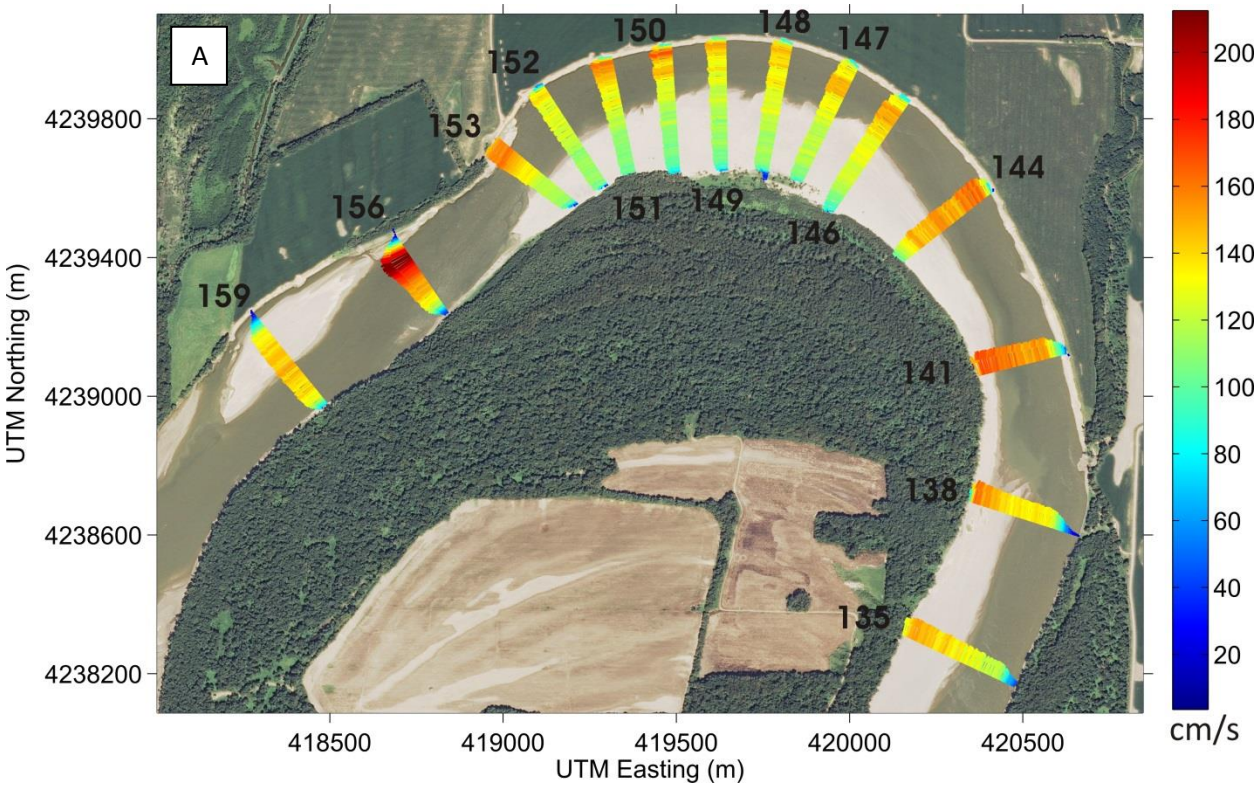

Figure 3.4: Depth-averaged velocity vectors along Maier Bend for Campaign 1 (A), Campaign 2 (B), and Campaign 3 (C).

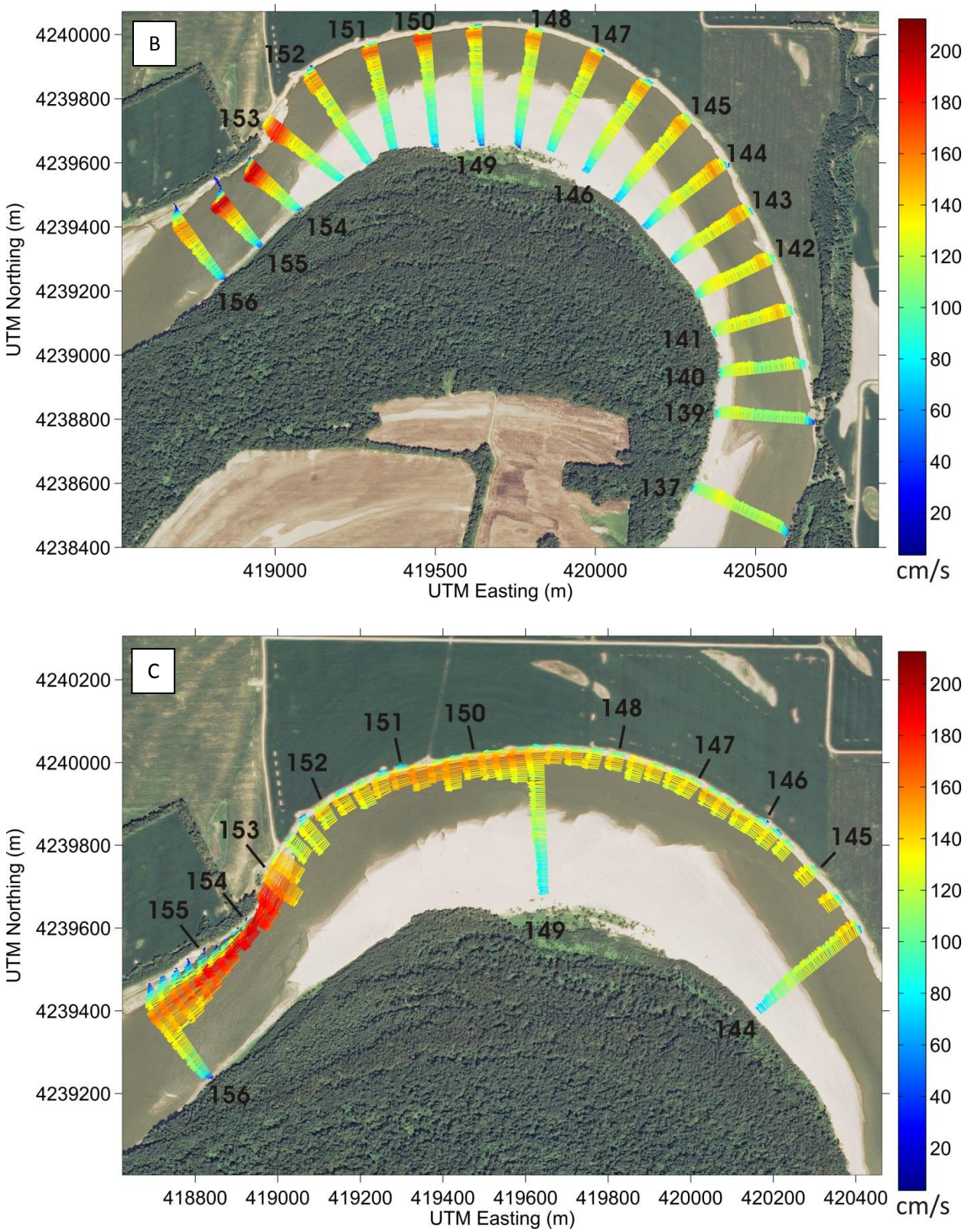

Figure 3.4: (cont.) Depth-averaged velocity vectors along Maier Bend for Campaign 1 (A), Campaign 2 (B), and Campaign 3 (C).

The spatial pattern of depth-averaged velocity vectors for Campaign 2 is slightly different from the pattern for Campaign 1 (Figure 3.4B). At the bend entrance, maximum velocities are located close to the inner bank, but are about 25% lower (1.3 ms^{-1}) than in Campaign 1. As flow moves into the bend, the high velocities quickly shift to the outer bank immediately downstream from the entrance (cross section 141). The zone of highest depth-averaged velocities remains adjacent to the outer bank and the magnitude of these velocities increases throughout the bend. As in campaign 1, the highest velocities occur downstream of the apex (cross-sections 149-151). Cross-stream patterns of depth-averaged velocity vectors are asymmetrical with low values (~0.7 ms^{-1}) near the inner bank and high values (~1.8 ms^{-1}) along the outer bank. Detailed measurements downstream of the bedrock outcrop (cross-sections 154-156) clearly show the redirection of the zone of high velocity away from the outer bank and the development of a zone of flow recirculation along the outer bank.

Because flow conditions for Campaign 3 are similar to those for Campaign 2, patterns of depth-averaged velocity vectors at cross sections from Campaign 3 that span the entire channel width are nearly identical to patterns at these same cross sections from Campaign 2 (Figure 3.4C). Depth-averaged velocities are low over the point bar and high near the outer bank for both campaigns. Moreover, the magnitudes of the depth-averaged velocities are nearly identical. The close spacing of transects near the outer bank show in detail how near-bank velocities vary throughout the bend. Within the apex region of the bend near-bank depth-averaged velocities are generally high (cross sections 149-151), but some locations (i.e. cross sections 146, 151.25, and 152.25) exhibit relatively small depth-averaged velocity immediately adjacent to the outer bank (Figure 3.4). The spatial pattern of depth-averaged velocity vectors downstream of the bedrock outcrop show that as flow is redirected away from the outer bank, a zone of flow recirculation

extends roughly 300 m downstream along the outer bank with near-bank depth-averaged velocities oriented in the upstream direction.

3.4.1.2 Horseshoe Bend

At the entrance to Horseshoe Bend (cross-section 60), the spatial pattern of depth-averaged velocity vectors shows an asymmetric distribution of velocity, with high velocities (~ 1.75 ms^{-1}) occurring near the inner bank and low velocities (~ 0.05 ms^{-1}) along the outer bank (Figure 3.5A). This pattern of asymmetry is observed well downstream of the bend entrance (i.e. cross-section 64). As flow continues downstream, the magnitudes of the velocity vectors become fairly uniform across each cross section. Near the outer bank, depth-averaged velocities are reduced to values ranging from 0.25 – 0.75 ms^{-1}. This pattern of reduced near-bank velocities persists downstream of the bend apex (i.e. cross-section 74). On the downstream limb of the bend, near-bank flow accelerates to nearly 2 ms^{-1} as it moves past the local outcrop of bedrock.

The velocity vectors from Campaign 2 show an overall increase in depth-averaged velocity around the bend (Figure 3.5B). At the entrance to the bend (cross sections 60-62), high velocities are located along the inner bank and low velocities near the outer bank. Just upstream of the bend apex, (cross-sections 65-66) the magnitude of velocities across the channel is fairly uniform (Figure 3.5). In contrast to Campaign 1, the spatial pattern of depth-averaged velocity vectors near the bend apex (cross sections 67-72) indicates that the largest velocities at this location occur close to the outer bank. However, this zone of high velocity is separated from the outer bank by a region of reduced velocities extending approximately 30 meters from the outer bank. Where flow is constricted and deflected laterally by the outcrop of bedrock along the outer bank at the downstream end of the bend, it accelerates, reaching velocities greater than 2 ms^{-1}.

The near-bank depth-averaged velocity vectors from Campaign 3 show that reduced near-bank velocities are present along the entire bend apex region (cross-sections 67-74) (Figure 3.5). Additionally, at many cross-sections throughout the bend, near-bank flow is nearly stagnant. The persistence of a near-bank region with reduced depth-averaged velocities contrasts with the intermittent and localized reduced near-bank velocities at Maier Bend.

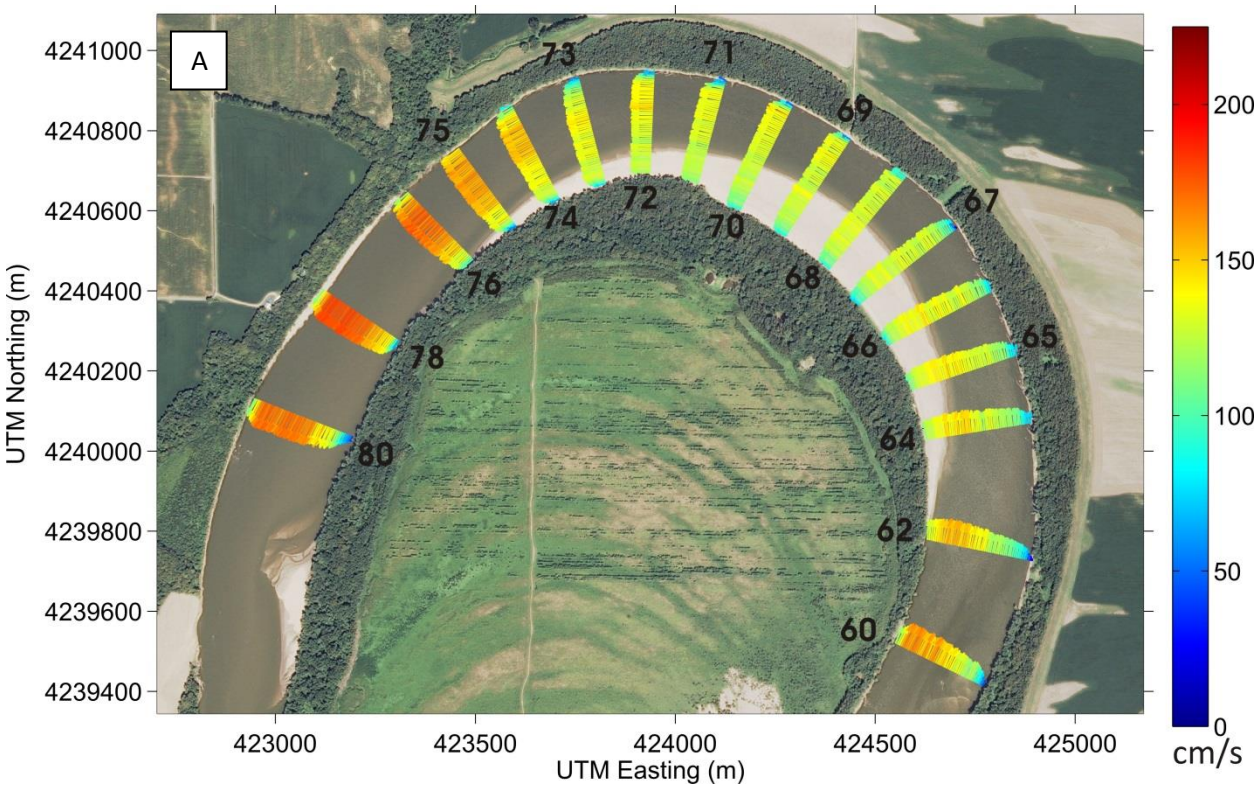

Figure 3.5: Depth-averaged velocity vectors at Horseshoe Bend for Campaign 1 (A), Campaign 2 (B), and Campaign 3 (C).

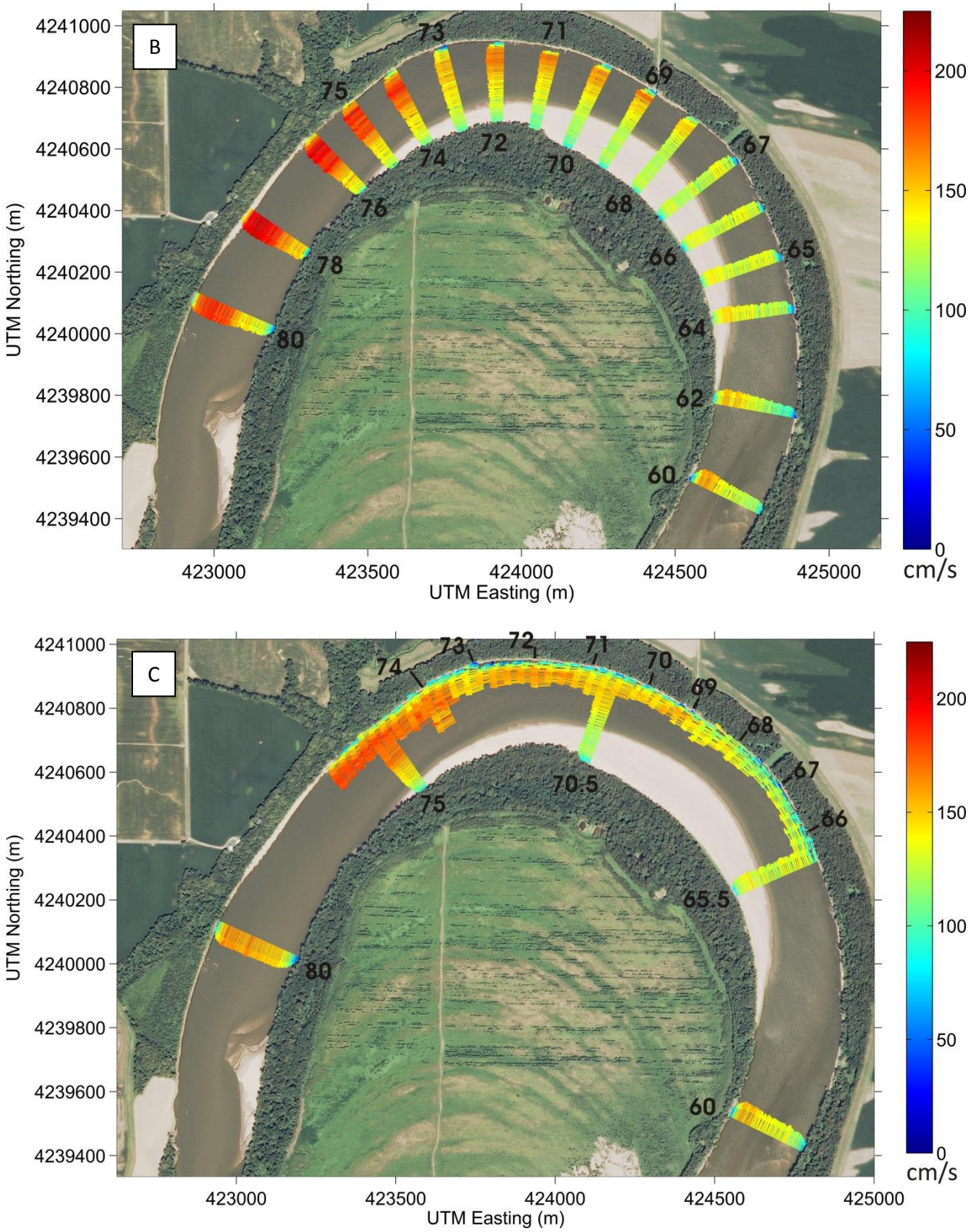

Figure 3.5: (cont.) Depth-averaged velocity vectors at Horseshoe Bend for Campaign 1 (A), Campaign 2 (B), and Campaign 3 (C).

3.4.2 Mean cross-sectional flow fields

3.4.2.1 Maier Bend

Within the apex region of Maier Bend, channel cross-sectional profiles are asymmetric with a broad transversely sloping point bar and relatively deep scour hole adjacent to the outer bank (Figures 3.6-3.7). For Campaign 1, primary velocities are greatest within the thalweg of the channel and in particular near the toe of the outer bank (Figure 3.6). During Campaign 1, the discharge exceeded ~5660 m^3s^{-1}, resulting in flow depths over the point bar of 2-3 meters with primary velocities ranging from ~ 1.0 – 1.5 ms^{-1} (Figure 3.6). Secondary velocity vectors show that helical motion is already established upstream of the bend apex (cross section 146) and that this motion increases in strength and coherence downstream through the bend apex. Upstream of the bend apex (cross sections 147-148), the local influence of bed forms can be seen on the secondary velocity vectors with large near-bed vectors curving downward into the channel bed (Figure 3.6).

During Campaign 2, the discharge (~2450 m^3s^{-1}) was much less than that of Campaign 1, resulting in flow depths over the point bar of about 0.5-2 m and flow velocities of about 0.3 – 1.0 ms^{-1}. (Figure 3.7). Upstream of the apex of Maier Bend (cross-section 146), primary velocities over the point bar are relatively large (~1.0 ms^{-1}). As the water flows downstream, high velocity fluid is advected outward, resulting in a reduction of velocities over the point bar at ~ 0.75 ms^{-1} (Figure 3.7). Lateral advection of momentum via topographic steering by the point bar, along with the effects of centrifugal acceleration, shifts the high velocity core to the thalweg, resulting in primary velocities of ~ 2.0 ms^{-1} along the outer bank from the bank toe to water surface. Secondary velocity vectors also show near-surface flow directed toward the outer bank and near-bed flow directed inward toward the point bar, indicating well-established helical motion

throughout the apex region. Additionally, the relatively large undulations seen in the bed profiles, interpreted to be dunes, appear to be altering local patterns of secondary velocity vectors at most cross sections within the bend apex region (Figure 3.7).

Comparison of the primary and secondary velocities derived from the Rozovskii decomposition with patterns of streamwise and transverse velocities, oriented perpendicular and parallel, respectively, to the plane of the cross section, suggest that the flow path may be influenced locally by topographic effects. At cross-sections 135 and 138 of Campaign 1 (Figure 3.8) and cross-section 137 of Campaign 2 (Figure 3.9), the pattern of transverse velocity vectors show flow directed toward the inner bank over the majority of the cross section. This pattern may reflect a slight difference between the path of the mean flow and the orientation of the cross section relative to this flow path. Farther downstream (cross-sections 139-147), the transverse velocity vectors show flow being directed toward the outer bank, perhaps as a result of topographic steering from the point bar. This effect is more pronounced during Campaign 2 when low flow depths limit the amount of flow across the top of the point bar compared to Campaign 1. For example, comparison of the transverse velocity vectors between Campaigns 1 and 2 for cross sections upstream of the bend apex (141, 144, 146) reveals that flow is directed outward over the point bar during Campaign 2 as the bed elevation progressively rises in the downstream direction, but that this effect is not noticeable during Campaign 1 (Figure 3.8 and 3.9). This difference suggests that topographic steering of the flow by the point bar may be more pronounced for the near-bankfull flow of Campaign 2 compared to the overbank flow of Campaign 1. Such steering could account for the higher streamwise velocities in the thalweg near the outer bank in Campaign 2 compared to Campaign 1 as the net cross-stream discharge toward the thalweg results in convective acceleration of streamwise flow to maintain continuity.

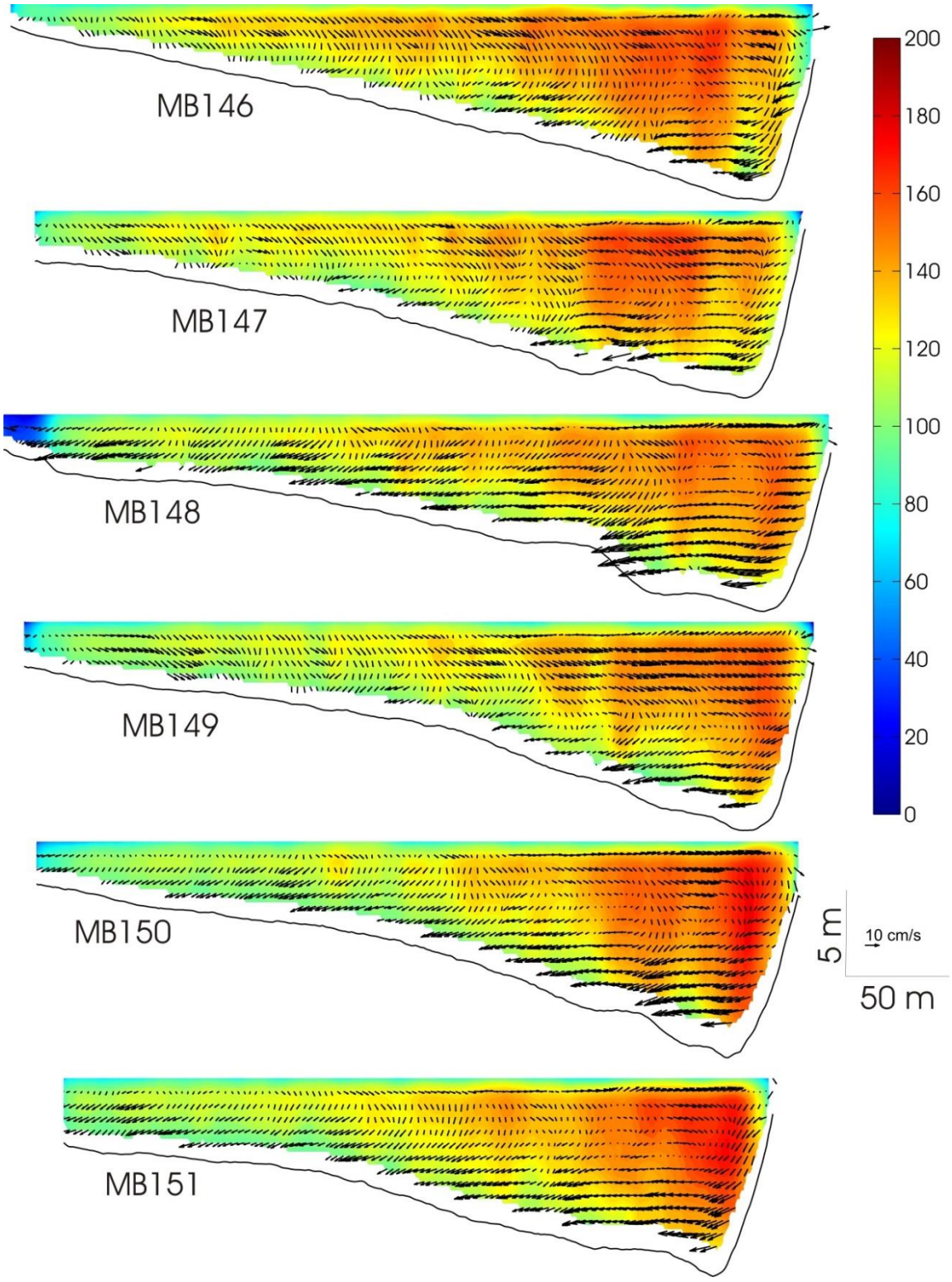

Figure 3.6: Cross-sectional flow fields at Maier Bend for Campaign 1 (05/09/2011) using Rozovskii (1957) frame of reference showing primary (contours) and secondary (vector) velocities.

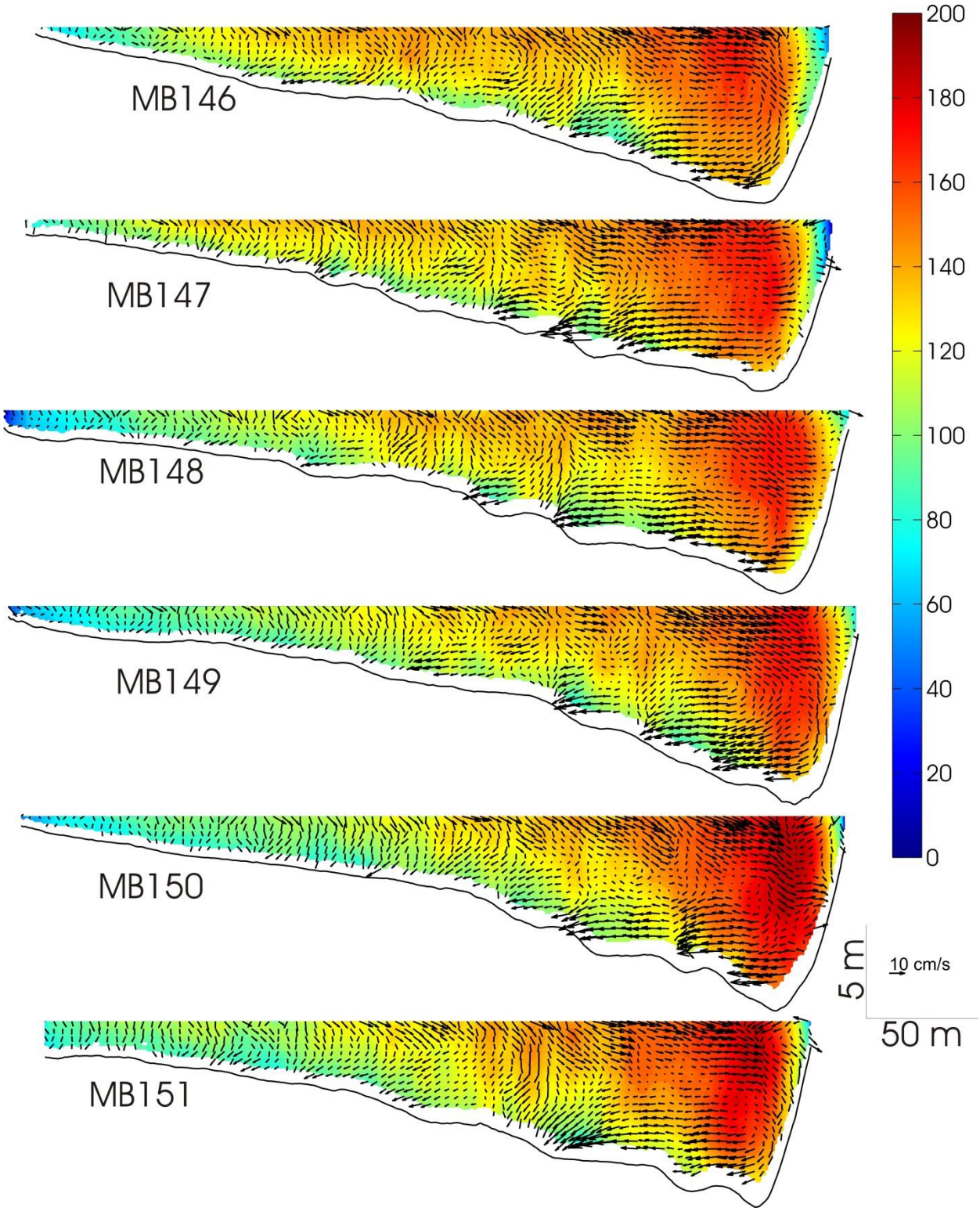

Figure 3.7: Cross-sectional flow fields at Maier Bend for Campaign 2 (06/28/2011) using Rozovskii (1957) frame of reference showing primary (contours) and secondary (vector) velocities.

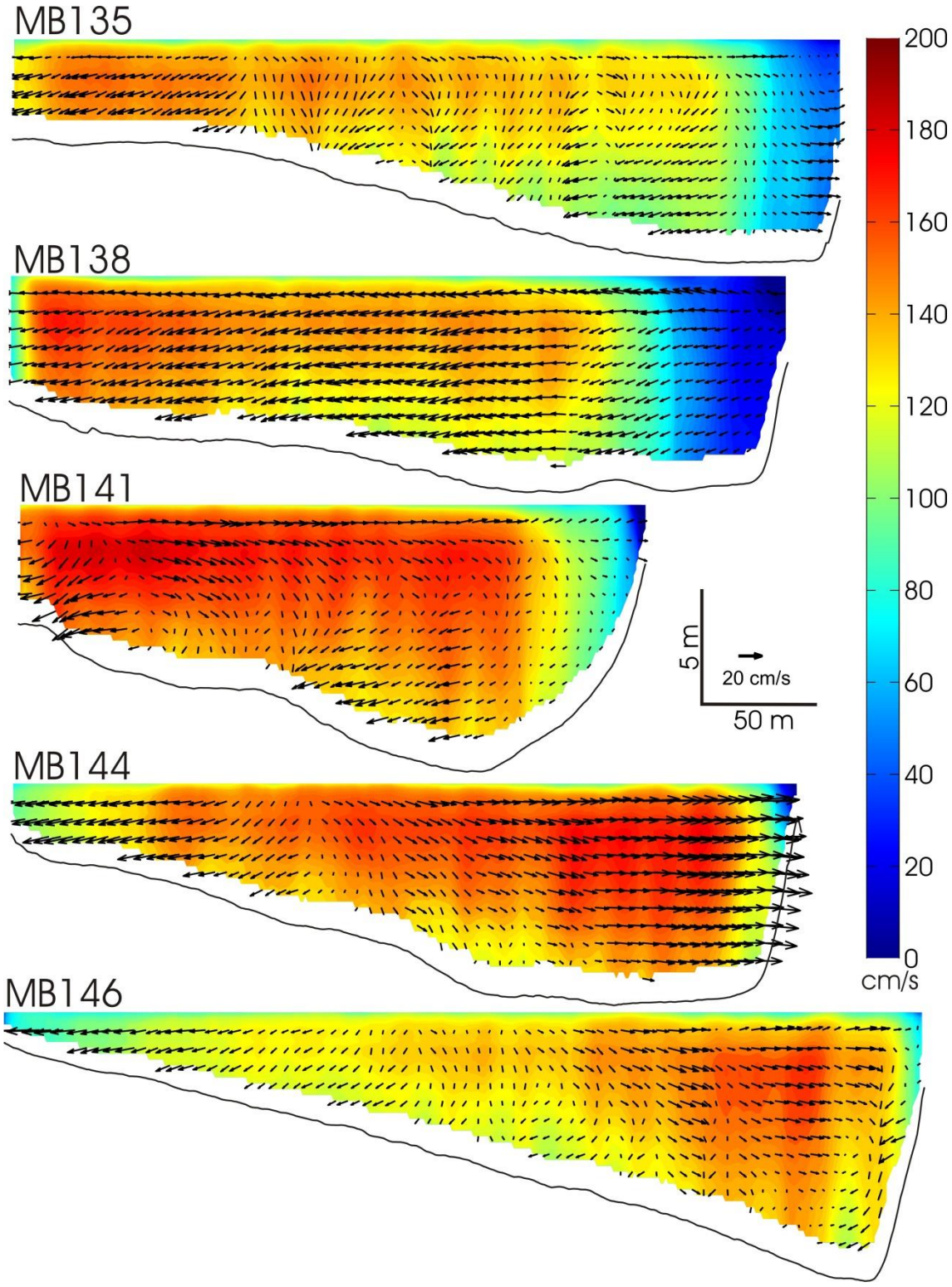

Figure 3.8 Cross-sectional flow fields at Maier Bend for Campaign 1 (05/09/2011) using a cross section frame of reference showing streamwise (contours) and transverse (vectors) velocities.

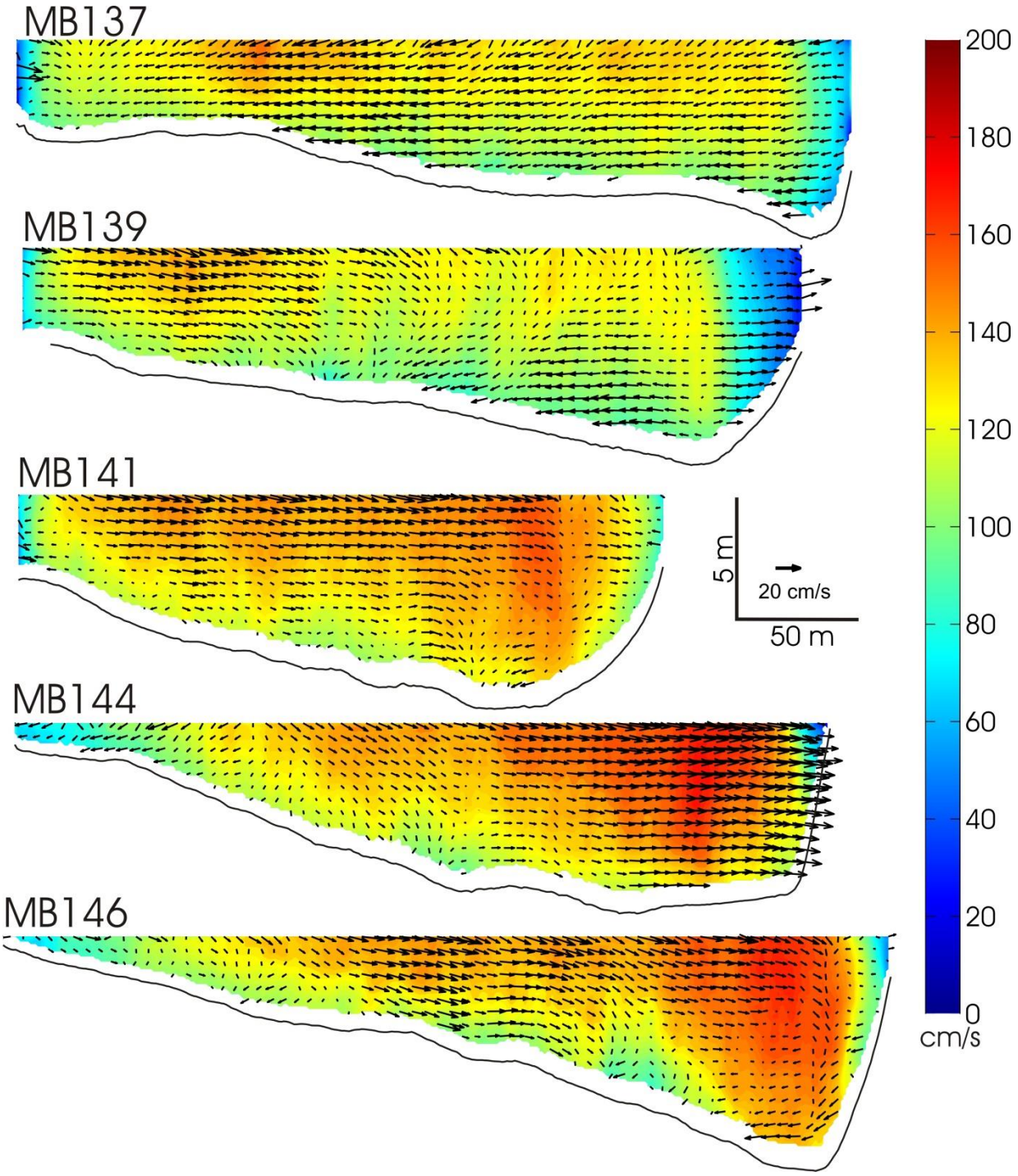

Figure 3.9 Cross-sectional flow fields at Maier Bend for Campaign 2 (06/28/2011) using a cross section frame of reference showing streamwise (contours) and transverse (vectors) velocities.

3.4.2.2 Horseshoe Bend

Channel cross-sectional profiles at Horseshoe Bend also display strong asymmetry within the apex region of the bend (Figures 3.10-3.11). The streamwise velocities for Campaign 1 show an area of substantially reduced velocities along the outer bank extending roughly 30 meters from the bank toward the channel thalweg – a distance equal to about four times the bank height (Figure 3.10). Secondary velocity vectors show outward directed near-surface flow and inward directed near-bed flow, indicating helical flow patterns over most of the channel cross-section, from the point bar to the thalweg, at all locations within the apex. However, patterns of secondary velocity vectors within the near-bank regions also show evidence of inward directed near-surface flow with outward directed flow below the water surface, suggesting the presence of a secondary outer bank cell of reversed orientation from the main helical cell (Figure 3.10). This pattern is most evident immediately upstream of the bend apex (cross sections 69-70) where the secondary outer bank cell extends from near the water surface to roughly 5 m below the water surface.

Velocities at Horseshoe bend for Campaign 2 overall are higher than velocities from Campaign 1, with the highest velocities occurring over the channel thalweg, perhaps as a result of enhanced topographic steering of the flow by the point bar during Campaign 2 (Figure 3.11). Although streamwise velocities are highest in the channel thalweg, a region of reduced velocities exists between the thalweg and the outer bank (Figure 3.11). Near the bend apex (cross-section 71), the apparent lack of a reduced velocity region near the outer bank is at least in part due to less extensive measurements near the outer bank in Campaign 2 compared to Campaign 1. Whereas during Campaign 1, the overbank flow allowed measurements up to and even slightly overtop, the outer bank, during Campaign 2 the proximity of measurements to the outer bank

was constrained by the presence of LWD and by confinement of flow within the channel. The more limited near-bank measurements during Campaign 2 compared to Campaign 1 can be seen by comparing the bed profiles near the outer bank for these two campaigns, which show that the profile is more truncated in Campaign 1 relative to Campaign 2 (i.e. cross-section 71) (Figures 3.10-3.11). Patterns of secondary velocity vectors display outward directed near-surface flow and inward directed near-bed flow, indicating helical motion from the point bar to the channel thalweg. However, the presence of a secondary outer bank cell is only observed near the bend apex (cross sections 69–71), where near-bank surface flow is directed inward and flow ~2 m below the surface is directed outward (Figure 3.11). At the other cross sections the pattern of near-bank secondary velocity vectors appears less coherent, displaying a wide range of orientations and magnitudes (Figure 3.11).

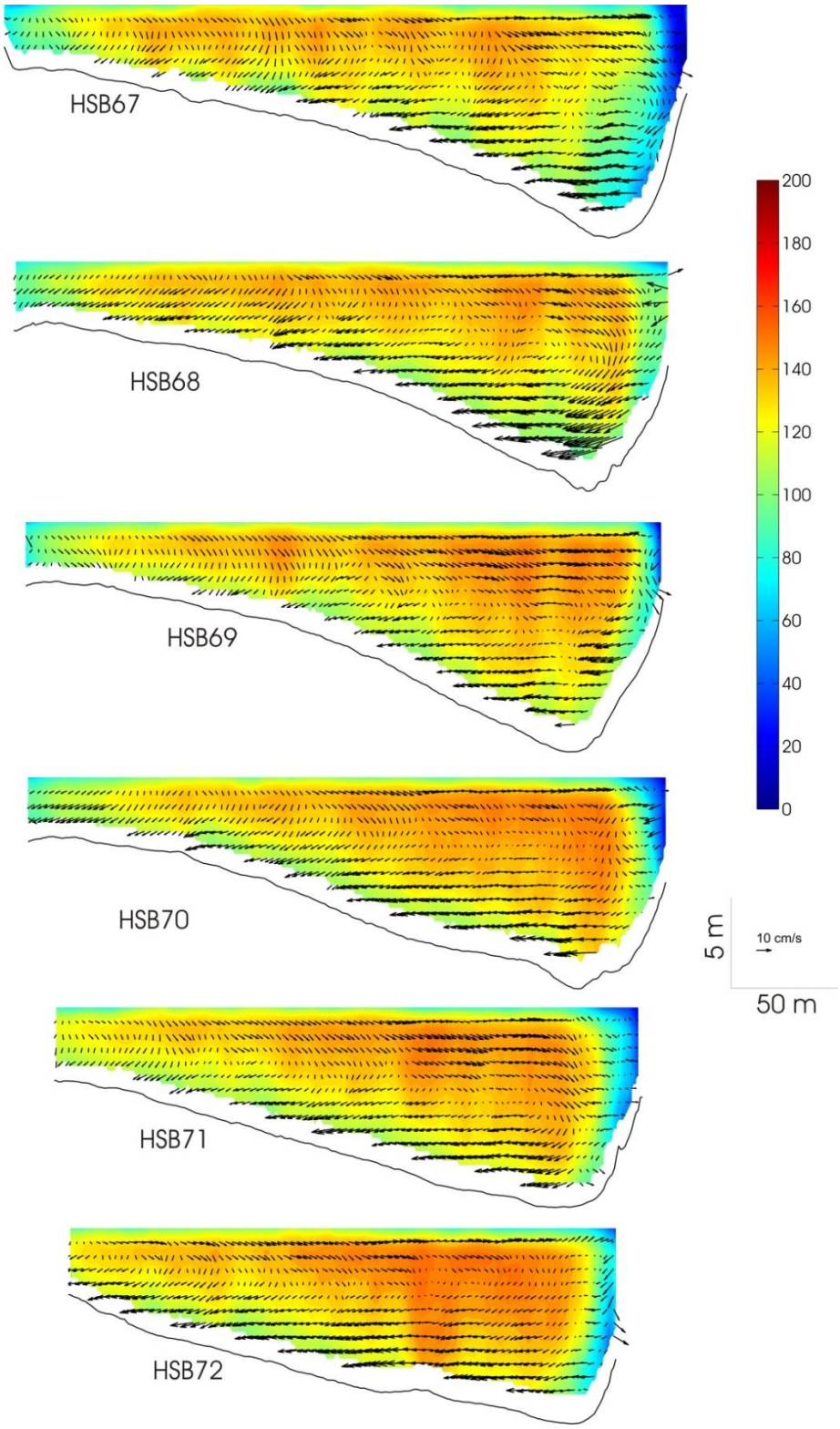

Figure 3.10: Cross-sectional flow fields at Horseshoe Bend for Campaign 1 (05/10/2011) using Rozovskii (1957) frame of reference showing primary (contours) and secondary (vector) velocities.

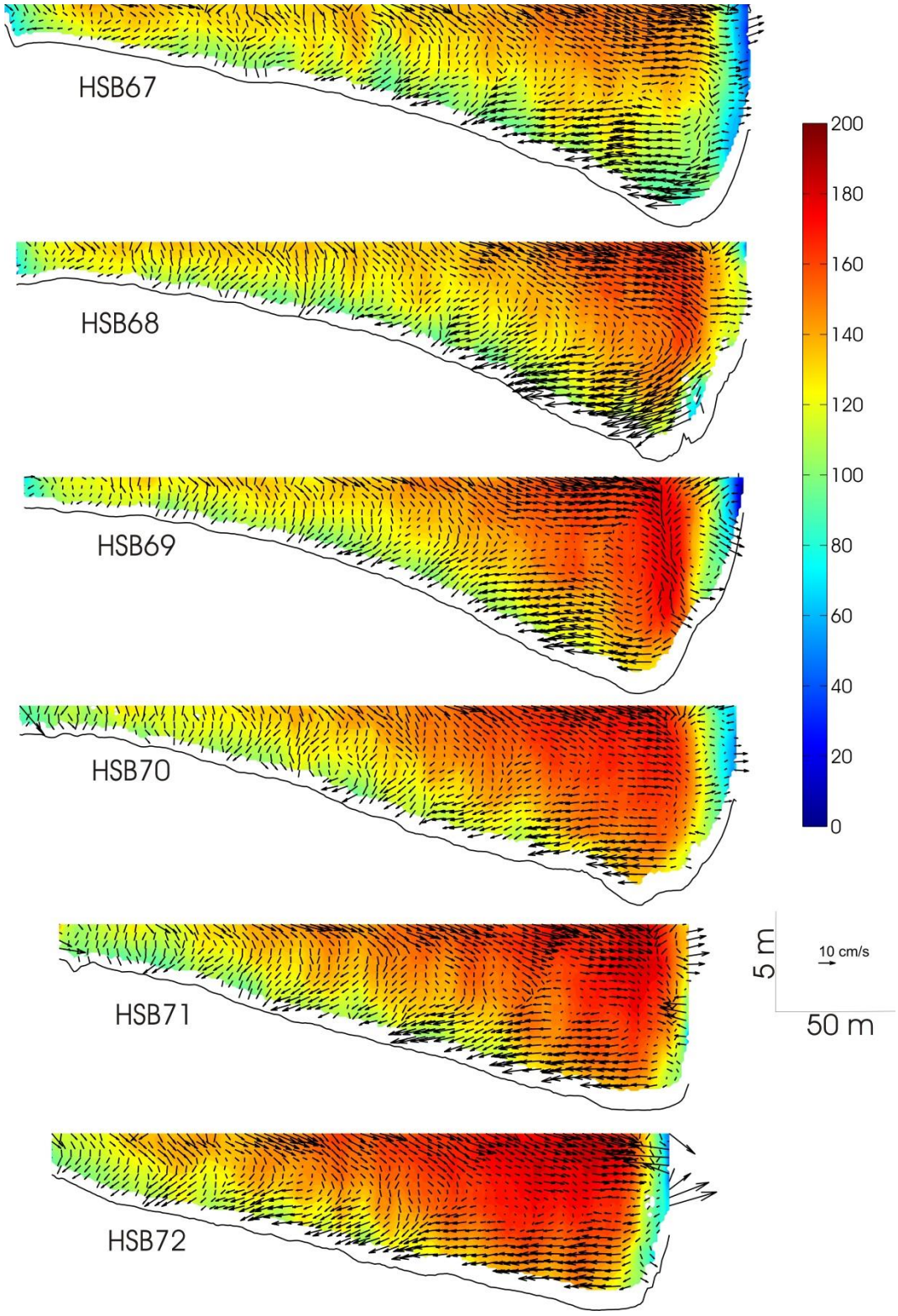

Figure 3.11: Cross-sectional flow fields at Horseshoe Bend for Campaign 2 (06/29/2011) using Rozovskii (1957) frame of reference showing primary (contours) and secondary (vector) velocities.

3.4.3 Near-bank velocity cross sections

Along the apex region of Horseshoe Bend (cross-sections 72.25 – 73.25), a region of low streamwise velocities (0.0 – 0.8 ms^{-1}) extends from 15 to 40 m from the outer bank (Figure 3.12). Immediately downstream of the bend apex (cross section 72.25) the width of this reduced velocity zone is roughly 20 m, and a pronounced secondary outer bank cell can be seen from the pattern of secondary velocity vectors with inward directed near-surface flow and flow below the surface directed toward the outer bank. At the next cross section downstream (cross-section 72.50), near-bank streamwise velocities have decreased, the width of the reduced velocity zone has increased, and the secondary outer bank cell has increased in strength and vertical extent. Near-bank streamwise velocities are close to 0 ms^{-1} at cross-section 72.75 and the zone of low velocities extends beyond the bank toe into the channel thalweg with an apparent decrease in the strength of the outer bank cell. Within cross section 73, the missing ensembles near the outer bank are the result of the ADCP measurements crossing directly over submerged LWD within the water column (Figure 3.12). The zone of low streamwise velocities at this cross section extends more than 40 meters from the outer bank and a small but strong rotational secondary cell, shown by inward directed near-surface flow and outward directed flow ~2 m below the water surface, exists near the water surface along the boundary between the low velocity zone and high velocities over the thalweg.

Downstream at cross-section 73.25, the near-bank streamwise velocities increase slightly and the width of the low velocity zone decreases. The pattern of secondary velocity vectors at this cross section define a rotational cell along the outer bank near the channel bed and extending to a height of ~4 m above the bed with outward directed near-surface flow and inward directed flow below the surface, similar in orientation to the main helical flow within the full cross

section. This cell is still present at cross-section 73.50, yet appears to dissipate downstream (before cross-section 73.75), where an outer bank cell of counter-clockwise rotation is observed.

Patterns of near-bank velocities along Maier Bend apex are much different than those at Horseshoe Bend. At Maier Bend, the influence of outer bank roughness appears to be localized and zones of low streamwise velocity do not persist along the outer bank for more than ~40 meters (Figure 3.13). At the upstream end of the bend apex region (cross-section 146), a zone of low streamwise velocity ($0.0 – 0.4\ ms^{-1}$) can be seen along the outer bank with a width of about 4 m and is confined to the upper portion of the outer bank. Additionally a small secondary outer bank cell is evident within this low velocity zone. However, ~40 m downstream (cross-section 146.25) velocities are high near the outer bank and no evidence exists of a secondary outer bank cell. Immediately downstream of the bend apex (cross-sections 150.75 – 152), high velocities exist along the outer bank, extending from the water surface to the toe of the bank (Figure 3.13). A secondary outer bank cell with counter-clockwise circulation may exist locally (cross-section 151), but it is small and relatively weak. At the other cross sections, the spatial pattern of near-bank secondary velocity vectors lack any significant coherency and instead comprise a region of disorganized motion that can clearly be distinguished from the main helical motion within the thalweg region.

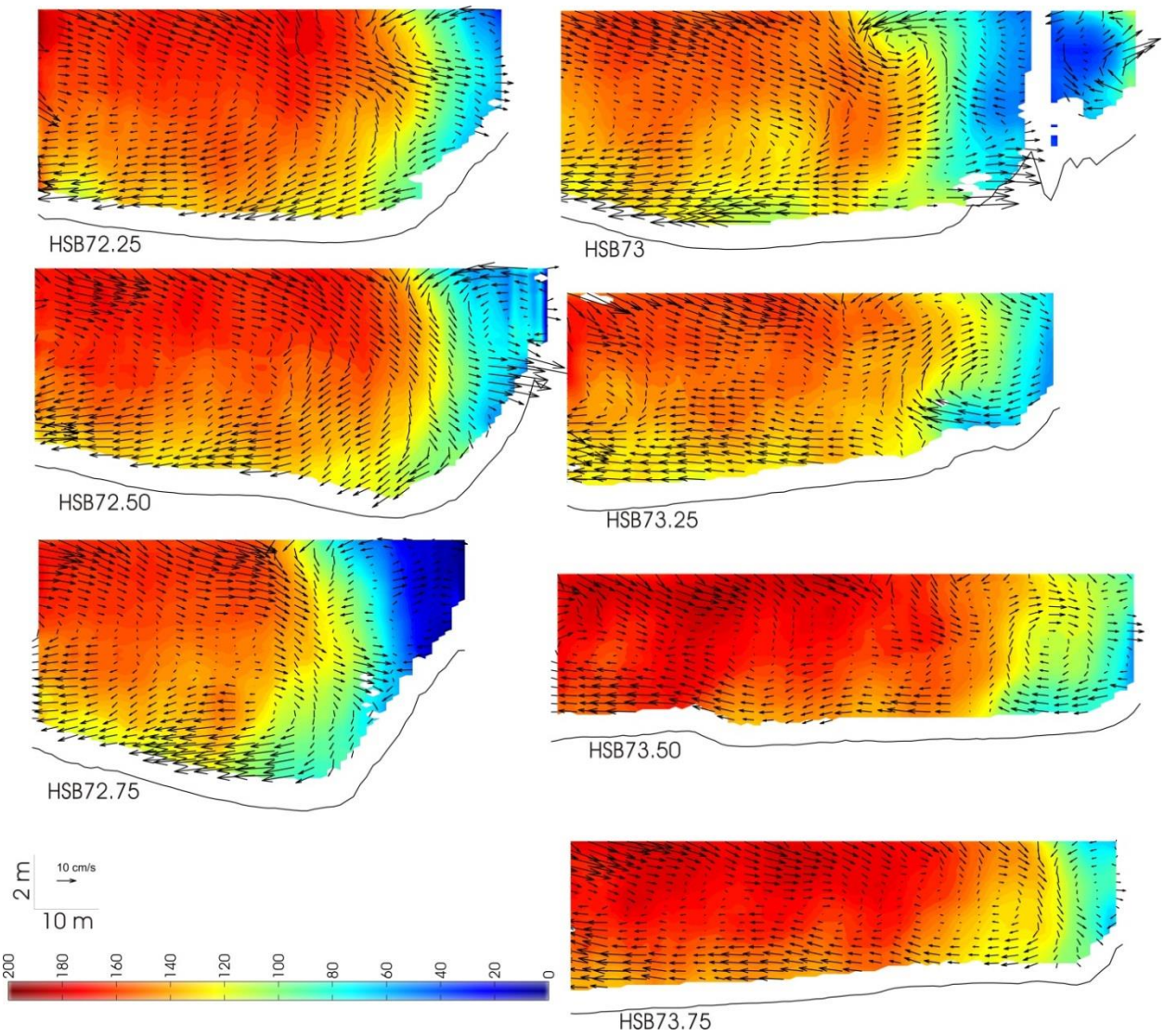

Figure 3.12: Near-bank velocity fields along Horseshoe Bend for Campaign 3 (01/16/2013) using Rozovskii (1957) frame of reference showing primary (contours) and secondary (vector) velocities. Note the influence of LWD producing a zone of low velocity adjacent to outer bank and complexity of secondary velocity vectors.

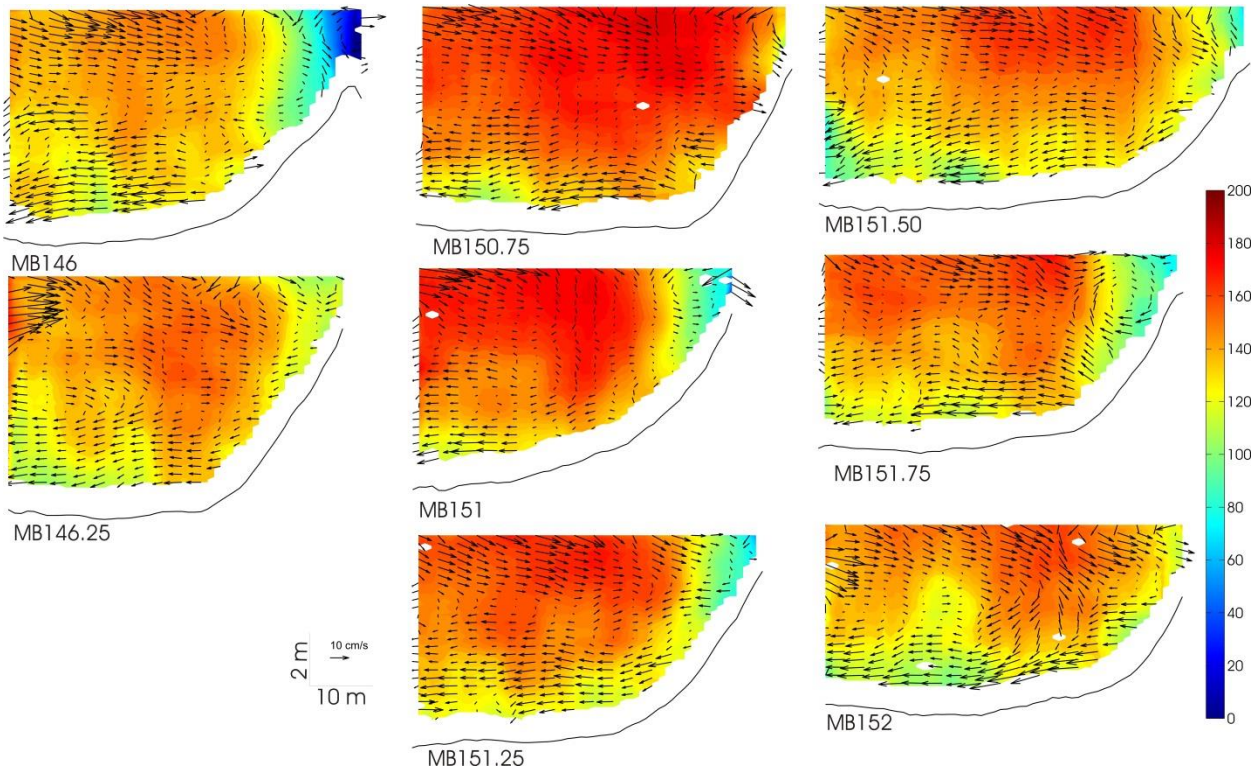

Figure 3.13: Near-bank velocity fields along Maier Bend for Campaign 3 (01/15/2013) using Rozovskii (1957) frame of reference showing primary (contours) and secondary (vector) velocities. Cross-section MB146 shows influence of outer bank roughness on near-bank flow structure but is confined within the upper ~3 m of flow. Patterns of near-bank velocity at all cross sections show high velocities near bank toe.

3.4.4 Patterns of shear stress

To investigate the influence of near-bank roughness elements on channel morphology and sediment transport along these bends, boundary shear stresses due to skin friction were estimated for Campaigns 1 and 2. Overall, values of shear stress around each bend were greater during Campaign 2 than during Campaign 1, despite the fact that the total discharge of Campaign 1 was over twice as large the discharge for Campaign 2 (Figure 3.14). For both bends, shear stresses are highest near exposures of bedrock in the downstream parts of the bends. At Horseshoe Bend, values of shear stress within the downstream limb increase from ~3 Pa for Campaign 1 to values between 5 – 6 Pa during Campaign 2. Shear stress values at Maier Bend

downstream of the bedrock outcrop increased from slightly ~4.5 Pa to 6 Pa, with a region of negative (upstream oriented) shear stress values within the recirculation zone along the outer bank (Figure 3.14).

Shear stresses along the outer bank of Maier Bend for Campaign 1 are typically less than 3.5 Pa, with a small gradient of decreasing shear stress from the thalweg to outer bank (Figure 3.15). For Campaign 2, values of outer bank shear stress increase to greater than 4.5 Pa and show a much larger gradient of decreasing shear stress than that for Campaign 1. Values of relatively high shear stress are observed within 20 meters from the outer bank, occurring beyond the toe of the bank and on the transverse sloping outer bank. At Horseshoe Bend, near-bank shear stresses are typically less than 2 Pa and these low values of shear stress extend from the outer bank to 30-40 meters away from this bank (Figure 3.15). Although values of shear stress over the channel thalweg increase during Campaign 2 relative to those for Campaign 1, the boundary between regions of high thalweg shear stresses and low near-bank shear stresses does not shift toward the outer bank.

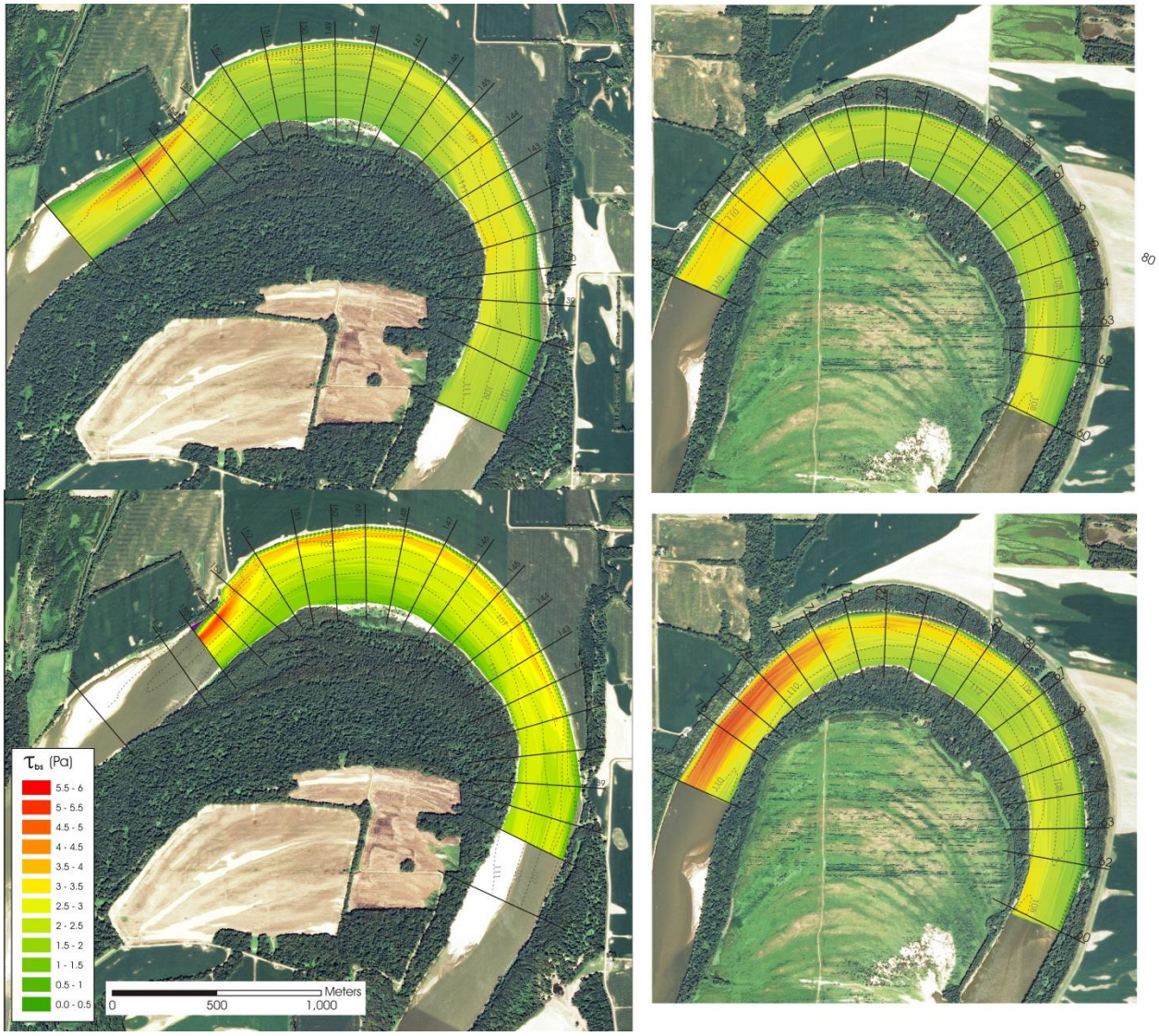

Figure 3.14: Estimated values of shear stress due to skin friction within Maier (left) and Horseshoe (right) bends for Campaigns 1 and 2 (top and bottom, respectively). Channel bathymetry shown in dashed contours.

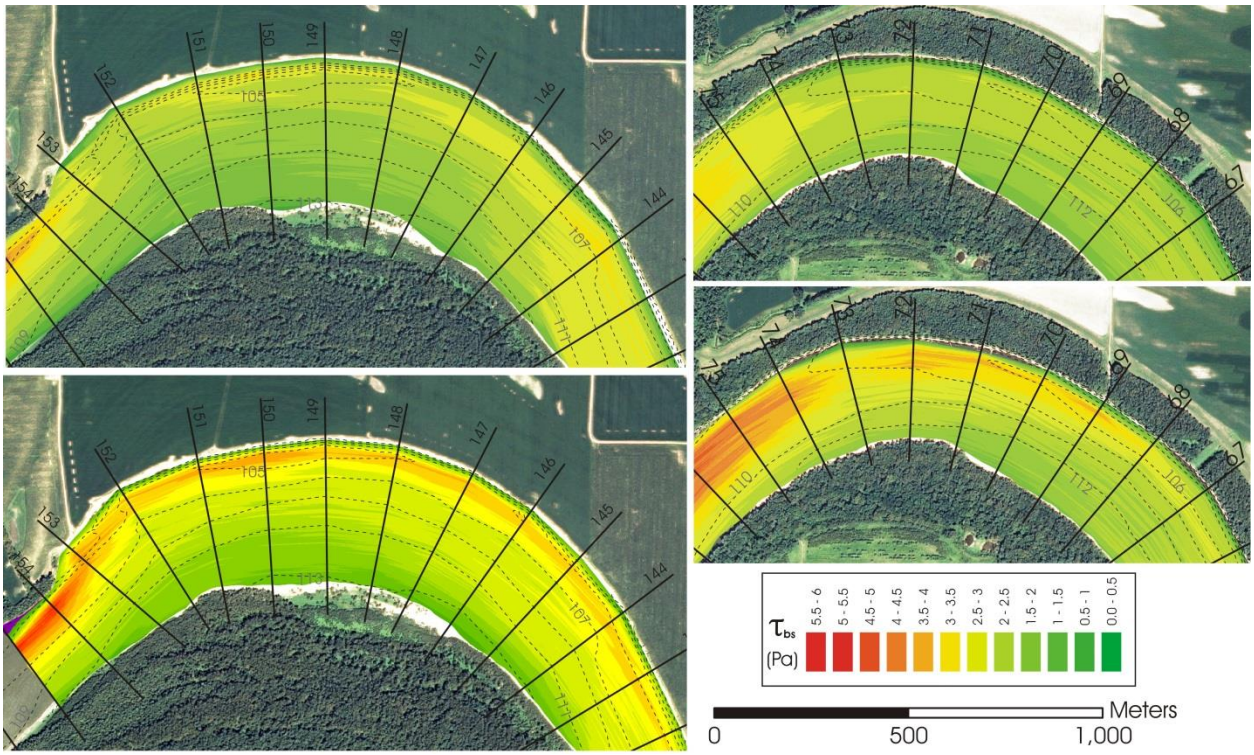

Figure 3.15: Estimated values of shear stress due to skin friction along the apex region of Maier (left) and Horseshoe (right) bends for Campaigns 1 and 2 (top and bottom, respectively). Channel bathymetry shown in dashed contours.

3.5 Discussion

The results from this study show that near-bank LWD can have a pronounced influence on near-bank streamwise velocity, patterns of secondary velocities, and shear stress in a large meandering river. The findings also provide new insights into scaling effects between LWD and channel dimensions and into variation in these effects under variable discharge conditions. Generally, the patterns of three-dimensional flow structure observed around the two elongated bends examined in this study are in agreement with previous laboratory and field investigations of flow structure through high amplitude, elongate meander bends (Jackson, 1975a,b; Whiting and Dietrich, 1993a,b; Frothingham and Rhoads, 2003; Abad and Garcia, 2009a,b; Termini and Piraino, 2011; Engel and Rhoads, 2012). On the upstream limb of the two bends, the highest velocities are located along the inner bank, reflecting both inherited flow structure from the

upstream bend of opposite curvature (Jackson, 1975a; Abad and Garcia, 2009a) as well as spatial variations in water-surface topography through sequential bends of opposing curvature that lead to high velocities along the inner bank at bend entrances (Dietrich, 1987). As flow moves through the bends, curvature-induced secondary circulation and topographic steering of the flow by the point bar shift the core of high velocity from the inner to outer bank. Patterns of secondary velocity vectors within channel cross sections display outward directed near-surface flow and inward directed near-bed flow, indicating large-scale curvature-induced helical motion through both bends. This secondary circulation redistributes momentum toward the outer bank, resulting in high near-bank velocities and boundary shear stresses in the channel thalweg. At Maier Bend, where the outer bank is not vegetated, the highest streamwise velocities along the outer bank occur immediately downstream of the bend apex (cross-section 150), consistent with findings of previous field and laboratory studies (Jackson, 1975a,b; Whiting and Dietrich, 1993a; Frothingham and Rhoads, 2003).

As illustrated by the data for Horseshoe Bend, extensive near-bank LWD can produce differences in the overall flow structure through the bend and the structure of the near-bank flow field compared to patterns of flow in meandering channels with unvegetated cutbanks (e.g. Maier Bend). In particular, the increased flow resistance offered by abundant LWD generates a nearly continuous zone of low velocities adjacent to the outer bank (Figure 3.5). This zone of low velocities ($< \sim 0.75$ ms^{-1}) typically occurs over the entire flow depth and extends approximately two to five times the height of the outer bank from this bank. As a result, the core of highest streamwise velocities is shifted away from the outer bank relative to bends without abundant near-bank LWD. The increased form drag from the LWD and associated zone of low velocities confines the high velocity core to the channel thalweg, a finding consistent with a previous report

of flow structure in meander bends with outer bank vegetation in a small river (Thorne and Furbish, 1995).

Patterns of near-bank secondary flow, as revealed by near-bank vectors of cross-stream and vertical velocities, are much more complex when abundant LWD lines a forested outer bank (Horseshoe Bend) than when the outer bank is unforested and no wood loading occurs at the base of this bank (Maier Bend) (Figures 3.10-3.12). The ADCP measurements of three-dimensional near-bank velocities obtained in this study illustrate this complexity in much greater spatial detail than previous studies of near-bank vegetation effects that relied on 2D or 3D point measurements of velocities (Thorne and Furbish, 1995; Daniels and Rhoads, 2003). Within the apex region of Horseshoe Bend, the effects of LWD generate both clockwise- and counterclockwise-rotating outer-bank secondary cells (Figure 3.12). These cells develop and dissipate over short streamwise distances (approximately $1/8^{th}$ channel width), presumably as the geometry and orientation of the LWD changes, but are fairly consistent near-bank features. Undoubtedly these secondary cells play an important role in redistributing momentum near the outer bank, especially in the exchange of momentum between the high velocities in the thalweg and the zone of low velocities along the outer bank. Despite the high level of measurement detail in this study, the exact role of these complex patterns of secondary flow in momentum exchange could not be ascertained from the velocity data. Numerical simulations capable of representing the effects of obstacles in the near-bank region on flow structure are needed to examine this problem further.

Previous investigations of near-bank flow structure in meandering channels have shown that secondary outer bank cells can reduce the lateral advection of high momentum fluid toward the outer bank, limiting the proximity of the core of high velocity to the outer bank (Blanckaert

and Graf, 2001, 2004; Termini, 2009; Termini and Piraino, 2011). Such cells can develop in the absence of near-bank vegetation, yet the effect of these cells on the distribution of streamwise velocity within a meandering channel is similar to the effects of increased form drag produced by vegetation (Thorne and Furbish, 1995). In the case of Horseshoe Bend, the low streamwise velocities and secondary circulation cells induced by LWD along the outer bank limit the spatial proximity of the high velocity core and curvature-induced helical cell to the outer bank. As high momentum fluid is advected toward the outer bank of Horseshoe Bend by helical motion and topographic steering of the flow, outward-directed, near-surface flow is directed downward along the shear layer that develops between the near-bank zone of low velocities and the adjacent core of high velocity in the thalweg.

Studies examining in detail the influence of LWD on flow structure near the outer banks of natural meandering rivers are limited and have only been conducted in small channels (Thorne and Furbish, 1995; Daniels and Rhoads, 2003). The bankfull width and depth of the channels in these studies were ~8m and ~1.2 m, respectively, ($W/D < 10$) and trees comprising the LWD were capable of spanning the entire channel width and flow depth. In such cases, LWD restricts the outward movement of the high velocity core and redirects the highest velocities toward the center of the channel (Thorne and Furbish, 1995) or even against the inner bank (Daniels and Rhoads, 2003). At Horseshoe Bend, where bankfull width and depth are ~300 m and ~8 m, respectively, ($W/D > 30$), the small relative size of the LWD compared to the flow dimensions limits deflection of flow away from the outer bank. Instead, the effects of LWD are confined to a region within about $1/10^{th}$ of the total flow width from the outer bank. These findings highlight the importance of the scale of vegetation relative to channel dimensions in influencing the structure of flow within meandering rivers.

The spatial extent of the main curvature-induced secondary circulation and the presence of secondary outer bank cells have implications for the distribution of shear stress within the near-bank region, and thus spatial patterns of bank erosion and channel evolution. Secondary outer bank cells that have an opposite sense of rotation from the main helical motion and have been shown to advect high-momentum near-surface fluid outward and downward away from the bank and low-momentum fluid below the water surface inward and upward toward the bank (Blanckaert *et al*., 2012). Thus, secondary outer bank cells have the potential to reduce shear stresses acting on the outer bank region, but these effects will depend on the strength and sense of rotation of the cells. At Horseshoe Bend, the secondary circulation cells produced by the LWD occur within the zone of low velocity and appear to be simply redistributing low-momentum fluid within this near-bank region (Figure 3.12). However, such cells exhibit opposing senses of rotation at different locations within this near-bank region and it is possible that locally these cells advect high-momentum fluid from the adjacent shear layer toward the outer bank.

This study has also documented the effect of variable discharge conditions on the flow structure through elongated bends on large rivers. For the near-bankfull conditions at Maier Bend (Campaign 2), the shift of high velocity from inner to outer bank occurred at a location roughly coincident with the intersection of the inner bank tangent with the outer bank, a finding consistent with experimental results (Whiting and Dietrich, 1993a,b). However, for discharge conditions of overbank flow (Campaign 1), the core of high velocity crosses from inner to outer bank farther downstream, close to the bend apex (Figure 3.4). The lag in the shift of the high-velocity core at flood stage is most likely related to limited topographic steering by the point bar during this overbank event, during which a large portion of the flow moved across the interior

portion of the loop in the down-valley direction. Additionally, during this overbank event, maximum depth-averaged velocities observed within the channel thalweg within the bend apex region are lower than velocities observed during the lower near-bankfull event, consistent with previous findings from Maier Bend (Jackson, 1975a). These findings are likely related to *flow bypass* (Jackson, 1975a pp. 38), where overbank flow extracts momentum from the flow, resulting in either steady or decreasing depth-averaged flow velocities as discharge increases from bankfull to overbank conditions.

Similarly, at Horseshoe Bend depth-averaged velocities within the thalweg during the near-bankfull event are higher than those during the overbank event (Figure 3.5). However, in contrast to Maier Bend, the position of the core of high velocity throughout the bend does not appear to be influenced by the change in flow conditions. Instead, the core of high velocity is positioned at a distance ~30 m from the outer bank for both campaigns, suggesting that the LWD is effective at preventing penetration of high momentum fluid, which can produce high boundary shear stresses, into the near-bank region during geomorphically active flood events.

The spatial patterns of boundary shear stress for these two elongate meander loops have implications for bank erosion and planform evolution. In particular, the contrasting patterns of near-bank flow for Maier Bend and Horseshoe Bend suggest that abundant near-bank LWD can potentially influence channel migration. At Maier Bend, the zone of high shear stress observed against the outer bank, with the highest values in this zone occurring immediately downstream of the apex (cross-section 149), results in rapid rates of erosion and lateral bank retreat within the apex region (~10-12 myr^{-1}). Downstream of the bedrock outcrop, the redirection of the primary flow streamlines toward the center of the channel results in low shear stress magnitudes against the outer bank downstream of the bedrock. These observed patterns of near-bank shear stress are

most likely responsible for elongation of the loop and the lack of downstream translation and rotation of the loop over the past 75 years (Figure 3.1).

In contrast, the near-bank LWD at Horseshoe Bend results in a zone of low shear stress against the outer bank that does not appear to be strongly affected by variable discharge events (Figure 3.14-3.15). The highest shear stress magnitudes occur on the downstream limb of the loop where highly resistant bedrock is exposed in the channel. Patterns of channel migration show that most bank retreat has occurred close to the apex of the loop (~0.75 myr^{-1}) with no measureable amount of erosion on the upstream or downstream limbs (Figure 3.1). Thus, the near-bank LWD at Horseshoe Bend is effective at reducing near-bank shear stresses, thereby limiting extension and elongation of the loop, while the bedrock within the downstream limb restricts downstream translation and rotation of the loop.

3.6 Conclusions

In this chapter, the three-dimensional flow structure through two elongate meander loops on a large meandering river was examined using detailed field measurements during different flow events with different discharges. The two elongate meander loops have different types of vegetation on the outer bank floodplains. Horseshoe Bend has an outer bank floodplain covered in riparian forests and substantial in-channel near-bank large woody debris (LWD). In contrast, the outer bank of Maier Bend is largely unvegetated, the adjacent floodplain is farmed, and no substantial LWD exists along the outer bank. Field surveys reveal bedrock outcrops within the downstream limbs of both bends. Differences in outer bank vegetation, both rooted and in the form of LWD, as well as the extent of outcropping bedrock within each bend produce substantial differences in flow structure in the two bends. The major findings are:

1) Patterns of depth-averaged velocity at Maier Bend are fairly consistent with documented patterns of flow structure through elongate meander loops documented in previous studies. On the upstream limb, the highest velocities are observed along the inner bank. The cross-over of the high velocity core from inner to outer bank is dependent upon flow discharge. At a bankfull event (Campaign 2), the cross-over occurs near the location where the upstream inner bank tangent intersects the outer bank, whereas during large discharge events (Campaign 1) the cross-over is located farther downstream. At Maier Bend, the high velocity core is positioned against the outer bank throughout the bend apex region, with highest velocities observed immediately downstream of the apex.
2) The Campaign 1 flow, an overbank event with a recurrence interval ~15 years, generated flow depths over the point bar along the inner bank of both bends of roughly 2-3 m and depth-averaged velocities as high as 1.25 ms^{-1}. Typical velocities within the thalweg reached ~1.75 ms^{-1}. In contrast, at near-bankfull discharge conditions (campaign 2), flow depths over the point bar along the inner bank of both bends ranged from 0.5 – 2 m and depth-averaged velocities were typically less than ~0.8 ms^{-1}. The concentration of the flow within the thalweg in Campaign 2 resulted in higher velocities within the thalweg in Campaign 2 compared to Campaign 1. Thus, the interaction between bed morphology and stage has an important influence on the pattern of streamwise velocity through the bend.
3) Near-bank LWD along Horseshoe Bend reduces near-bank velocities. This zone of low velocity extends from the outer bank to ~15 – 40 m toward the center of the channel and persists along the majority of the bend. The zone of low velocity is situated adjacent to the high velocity core within the channel thalweg, producing a shear layer that roughly

corresponds to the location of the LWD around the bend. Additionally, the presence of near-bank LWD appears to confine the curvature-induced secondary helical motion between the point bar and the channel thalweg, with secondary outer bank cells of opposite (counter-clockwise) orientation observed in the upper portion of the water column against the outer bank.

4) Velocity measurements at closely spaced near-bank cross sections along Maier and Horseshoe bends show the influence of near-bank roughness elements on the evolution of the near-bank flow field. The near-bank roughness elements along Maier Bend are mainly slump blocks and bankline irregularities and occur intermittently throughout the bend. As such, the influence of these types of roughness elements on the near-bank flow structure does not persist more than ~40 m downstream. In contrast, the near-bank LWD around Horseshoe Bend has a strong influence on the near-bank flow field and the effects are persistent throughout the bend apex region.
5) Estimated values of depth-averaged bed shear stress due to skin friction show higher values along the outer bank of Maier Bend than Horseshoe Bend, reflecting the importance of the near-bank LWD at Horseshoe Bend. For both bends, the highest estimated values of bed shear stress occur at the bedrock outcrop locations. Estimates of shear stress due to skin friction for Campaign 2 were higher than those estimated for Campaign 1, suggesting that near-bankfull conditions could result in more erosion and geomorphic change than overbank discharge events.

The findings from this chapter contribute to our understanding of the hydrodynamics of flow through elongate meander loops by providing detailed three-dimensional velocity measurements from a large meandering river and investigating the influence of in-channel LWD

on near-bank flow structure, a topic typically addressed through studies of relatively small rivers and laboratory experiments. While the results presented in this chapter represent some of the first detailed field measurements of the time-averaged near-bank flow structure around LWD in a large meandering river, future studies should focus on characterization of the turbulence structure through stationary measurements of velocity time series, especially the structure of turbulence near the outer bank. Emphasis on turbulence measurements will permit accurate partitioning of shear stresses and form drag as a result of in-channel vegetation.

CHAPTER 4

INVESTIGATION OF SCALES OF OUTER BANK FORM ROUGHNESS ON A LARGE MEANDERING RIVER WITH DIFFERENT FLOODPLAIN VEGETATION: IMPLICATIONS FOR NEAR-BANK FLOW STRUCTURE AND BANK EROSION

4.1 Introduction

The erosion of sediment from riverbanks and floodplains has long been of interest to geologists, geomorphologists, ecologists, and river engineers. Bank-derived sediment often accounts for a large proportion of the total sediment budget within a catchment (Rinaldi and Darby, 2007). Eroded material can directly affect water quality, turbidity, and nutrient loads, thereby indirectly influencing river ecosystems (Cordone and Kelley, 1961; Cederholm *et al.*, 1980; Kaller and Hartman, 2004; Kreutzweiser *et al.*, 2005; Rabeni *et al.*, 2005; Bilotta and Brazier, 2008). Additionally, bank erosion is a primary factor responsible for the migration of meandering rivers, which can lead to loss of riparian and agricultural lands and damage to human infrastructure. Recent research on meandering rivers has emphasized the need to better understand the complex processes that drive bank erosion to develop accurate predictive models of bank retreat and channel planform evolution (Darby and Thorne, 1996a,b; Darby *et al*., 2002; Langendoen and Alonso, 2008; Langendoen and Simon, 2008; Parker *et al*., 2011; Motta *et al*., 2012).

The process of bank erosion in alluvial rivers occurs through dynamic interactions among channel planform, three-dimensional flow structure, and sediment transport. Bank retreat most commonly occurs through the process of fluvial entrainment at the bank toe and mass failure of the overlying bank material, with subsequent removal of the failed material (Thorne, 1982, 1992;

Simon *et al*., 2000; Langendoen and Simon, 2008; Rinaldi *et al*., 2008). Rates of bank erosion are influenced by the near-bank flow field and turbulence, mechanical properties of the banks (e.g. grain size, cohesion, root tensile strength and type of riparian vegetation), and topographic irregularities of the channel banks.

Topographic irregularities of riverbanks consist of spatial variations in erosional forms produced by hydraulic action and mass failures, and of protruding bank vegetation and exposed root wads (Kean and Smith, 2006a). These irregularities enhance form drag, thereby increasing hydraulic resistance. By affecting near-bank flow structure, the irregularities influence shear stresses acting on the channel boundary, sediment transport near the bank toe, and rates of erosion of the bank itself. Thus, the capacity of the flow to erode the bank is regulated in part by the morphological characteristics of the bank.

The total shear stress acting upon the channel boundary within an open-channel flow can be expressed as the sum of the various components that contribute to flow resistance (Einstein and Barbarossa, 1952). For alluvial meandering rivers, the total shear stress can be given as,

$$\tau_{total} = \tau_{sf} + \tau_{bedform} + \tau_{bank} + \tau_{curv} \qquad (4.1)$$

where τ_{sf} is the component associated with skin friction from the sediment, $\tau_{bedform}$ is the form roughness due to alluvial bedforms, τ_{bank} is the form roughness due to bank irregularities (including in-channel bank vegetation), and τ_{curv} is the flow resistance associated with the redistribution of momentum by flow through a curving channel. The result of increased form drag from roughness elements is a decrease in values of skin friction, which is the component of shear stress responsible for the entrainment and transport of sediment. It is therefore important to estimate and partition components of form drag from the total shear stress to accurately predict sediment transport and bank erosion.

The importance of shear stress partitioning into components of form drag and skin friction has long been recognized for estimating sediment transport within the main portion of river channels. However, more recently shear stress partitioning has been used to determine the skin friction acting on channel banks, both to improve estimates of stage-discharge relations (Kean and Smith, 2004) and estimates of bank erosion (Kean and Smith, 2006a, b, Kean *et al*., 2009; Darby *et al*., 2010, 2013). In the method of Kean and Smith (2006a), the drag introduced by large-scale topographic irregularities of channel banks is approximated by Gaussian-shaped bumps allowing for relatively easy geometric characterization and estimation of the form drag forces. Darby *et al*. (2010) combined a physically-based model of bank stability and in situ measurements of bank erodibility parameters with the method of Kean and Smith (2006a) to estimate annual bank erosion on the Mekong River, providing the first predictions of hydraulic bank erosion that do not require calibration of an erosion coefficient.

Although the Kean and Smith (2006a, b) approach represents a first step toward characterization of bank roughness, the complex geometry of in-channel bank vegetation cannot readily be approximated using simple Gaussian shapes. Furthermore, successful applications of the model have been limited to riverbanks where the topographic irregularities are relatively consistent at different bank elevations and/or can be approximated by a single scale of bank form roughness. However, Kean and Smith (2006a) note that vertical and streamwise heterogeneities in bank roughness can exist, complicating the characterization of bank roughness within a particular reach.

Topographic surveys of channels banks are typically performed during conditions of low flow when a relatively large vertical section of the channel banks is exposed subaerially. However, depending upon the amount of time the banks have been exposed and the amount of

subaerial erosion that has occurred, the surveyed morphological characteristics of the bank may not reflect conditions during high stage when the banks are submerged and fluvial erosion occurs. Additionally, because long-term rates of bank erosion typically are controlled by fluvial erosion at the bank toe, scales of bank roughness evaluated in the upper portions of bank profiles might not be appropriate for accurate shear stress partitioning at the base of the bank where erosion is focused.

In this chapter, outer bank form roughness is evaluated for two meander bends of a large mixed bedrock-alluvial river with different floodplain vegetation. Detailed maps of outer bank morphology were obtained subaerially at low flow conditions using a terrestrial LiDAR scanner and subaqueously during high flow conditions using a multibeam echo sounder (MBES). These detailed maps allow for accurate characterization and comparison of form roughness at different bank elevations under different flow stage conditions. Scales of form roughness are determined by two approaches: 1) application of the spectral method Hilbert-Huang Transform (HHT) to contours of bank elevation around each meander bend and 2) estimations of variations in surface roughness within small sections of the outer bank at select locations around the two bends. The results from the analysis of bank scale roughness are used to examine the influence of form drag on near-bank flow structure as observed from data obtained using acoustic Doppler current profilers (ADCP). Additionally, repeat LiDAR surveys conducted annually for three consecutive years are drawn upon to link patterns of form roughness and structure of near-bank flow field to spatial patterns of erosion through time within each bend.

4.2 Field Site

Measurements for this study were taken within two elongate meander bends on the lower Wabash River near Grayville, Illinois (Figure 4.1). The lower Wabash River upstream from this

reach drains an area approximately 74070 km^2 and dimensions of the bankfull width and depth of the river channel range from 200-350 m and 4-8 m, respectively. Data for a USGS hydrologic gaging station located at Mt. Carmel, IL (~20 km upstream from the field site) indicate that the mean annual discharge at this location over an 85-year period of record is 881 m^3s^{-1} and the mean annual peak discharge is 4112 m^3s^{-1}. Vegetation cover within the active floodplain for the lower Wabash River varies spatially and includes riparian forest, grasses, and row crops (mainly corn and soybeans). The lower Wabash River remains the only meandering river of its size in the contiguous United States that is unregulated by major dams. The river meanders freely through its own alluvium, although at some locations it erodes into Pleistocene glaciofluvial sediments or upland bedrock (Jackson, 1975a). Recent investigations on the Wabash River have revealed that local outcrops of bedrock within the active channel are more prevalent than previously thought and can have a substantial influence on the planform dynamics of the river, suggesting that the lower Wabash River should be classified as a mixed bedrock-alluvial system.

Maier Bend is an elongate meander loop approximately 4 km long. The outer bank of this bend is eroding mainly into agricultural fields with small sections of riparian forest at the bend entrance and exit. During summer base flow conditions, nearly the full height of the outer bank (~7 m) is exposed subaerially. The lower 4 to 5 m of the outer bank consists of coarse sand and fine gravel that forms a slope of ~30°. This material is capped by 1-2 m layer of fine silty-sand loam that produces a nearly vertical bank face. In the downstream part of the bend, erosion along the outer bank has exposed a local outcrop of interbedded shales and sandstones (Pennsylvanian Bond Formation). Vegetation along the outer bank is confined mainly to the top of the bank; however, the outer bank contains many large erosional irregularities and accumulations of slump block material that contribute to form roughness. Horseshoe Bend is

located approximately 12 km upstream of Maier Bend. This elongate meander loop is approximately 3 km long and vegetation along the outer bank consists of riparian hardwood forest. At low flow, about 4 to 6 m of the nearly vertical outer bank is exposed. Bank material consists of mostly fine sediments with more than 70% silt/clay content at many locations. The nearly vertical, fine-grained portion of the outer bank is underlain by a basal layer of coarse sand and gravel that varies in thickness around the bend. The downstream portion of Horseshoe Bend has eroded into shale units of the Pennsylvanian Mattoon Formation, restricting downstream migration. In contrast to Maier Bend, the outer bank at Horseshoe Bend contains abundant roots from trees growing along the top of the channel banks. Also, erosion of the outer bank occasionally introduces large woody debris into the river channel in the near-bank region. Over time, this large woody debris, which in many cases consists of whole trees, becomes aligned roughly parallel to streamwise flow direction with remnant root wads facing upstream and the crowns of the trees positioned downstream.

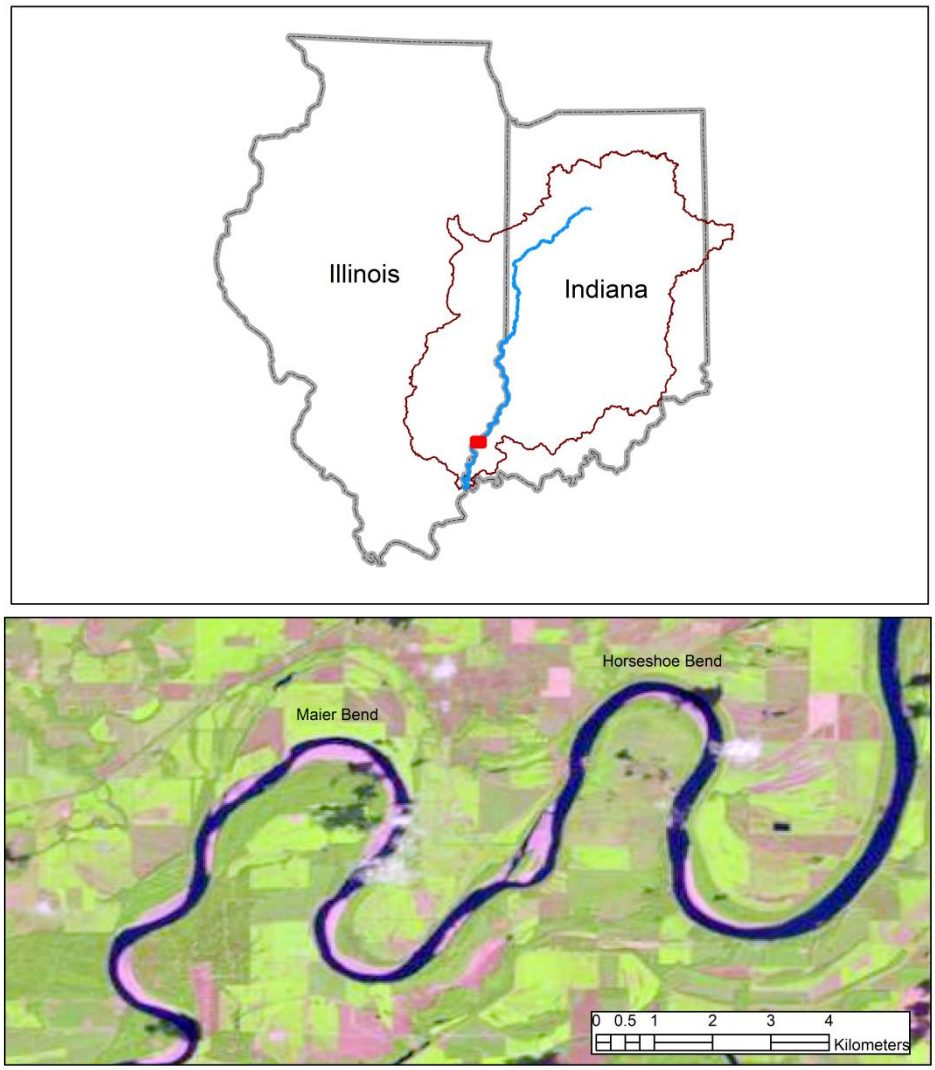

Figure 4.1: Location map for Maier and Horseshoe bends on the Wabash River near Grayville, IL.

4.3 Methods

LiDAR surveys were conducted annually during low flow conditions (summer base flow) for three consecutive years to obtain detailed subaerial morphologic data along the outer bank of each bend (Table 4.1). Terrestrial LiDAR surveys were performed using a Topcon GLS-1500 laser scanner with a maximum sampling frequency ~30 kHz, an accuracy of roughly 5 mm, and a grid spacing ~5-10 cm. The laser scanner was positioned at locations along the point bar and a TopCon GR3 RTK-GPS was used to establish temporary benchmarks during surveys (Figure

4.2). A minimum of three benchmarks was used for georeferencing individual scan positions and a transformation procedure used during post-processing defined the instrument location with subcentimetric accuracy. For each survey, approximately 12-15 scan positions per bend were required to cover more than 2 km of outer bank. Data processing and visualization of LiDAR data were performed in Fugroviewer, ArcGIS, and Caris HIPS/SIPS. Point cloud data were manually classified as ground, or low, medium, or high vegetation depending upon the location of the vegetation with respect to the elevation of the outer bank.

Table 4.1: Summary of data acquisition for data type, date collected, field location, and hydrologic conditions during survey.

Data Type	Date	Location	Discharge (m^3s^{-1})
ADCP	7/27/2008	Horseshoe	570
MBES	7/28-29/2008	Horseshoe	570
ADCP	5/9-10/2011	BOTH	5670
LiDAR	8/22-25/2011	BOTH	190
ADCP	2/2/2012	Maier	2800
MBES	2/2-4/2012	Maier	2800
LiDAR	9/24-28/2012	BOTH	200
ADCP	1/15-16/2013	BOTH	2300
MBES	1/18/2013	Horseshoe	2300
ADCP	5/3/2013	Maier	3700
MBES	5/3/2013	Maier	3700
LiDAR	08/26-27/2013	BOTH	175

For comparison of subaerial and subaqueous outer bank morphology, multibeam echo sounder (MBES) surveys were conducted during moderate to high flow stage conditions, and two surveys were conducted for each bend (Table 4.1). MBES surveys were conducted using a RESON SeaBat 7125SV, a dual frequency 200-400 kHz system with 512 beams over a 128° swath, producing 0.5 degree beams that yield an overall depth resolution of 6 mm, and a maximum update (ping) rate of 60 Hz. This system is also capable of beam steering and swath

width adjustment, allowing for the 512 beams to be focused towards regions of interest, such as outer banks. However, the combination of the configuration of the boat mount and the geometry of the steered beams typically limited subaqueous measurement of the vertical portion of the outer bank in the top 2 meters of the water column. Post-processing and visualization of all MBES data were performed in Caris HIPS/SIPS, and bathymetric grid models were exported for use in ArcGIS.

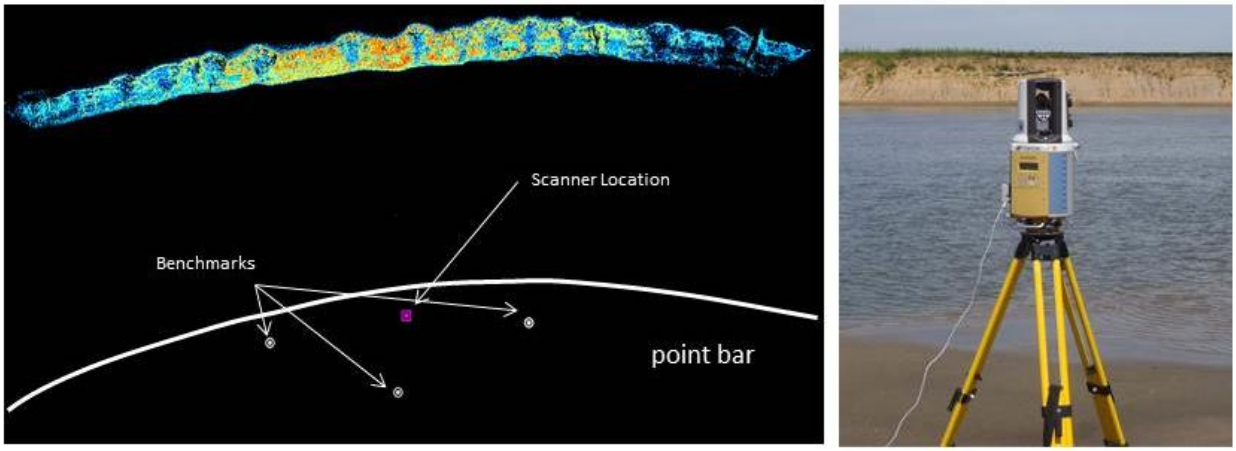

Figure 4.2: Terrestrial LiDAR field setup showing scanner position, three temporary benchmarks, and example data of outer bank along Maier Bend.

Three-dimensional velocity measurements were obtained to link the outer bank morphology to near-bank flow structure and patterns of erosion. These measurements were obtained using a boat-mounted Teledyne-RDI Workhorse Monitor 1200 kHz acoustic Doppler current profiler (ADCP). These ADCPS's use a four-beam configuration with 20° beam spread, a processing bin size in profiling mode as low as 10 cm, and a sampling frequency ~1 Hz. Repeat surveys (4-6) of transects oriented perpendicular to the channel centerline were performed to establish time-averaged maps of mean flow velocity. Analysis of velocity data was performed using Velocity Mapping Toolbox, MatLab-based software for advanced processing and visualization of ADCP data (Parsons *et al*., 2013). ADCP measurements were collected during all MBES campaigns, and additional ADCP campaigns were conducted between 2011 and 2013

to obtain detailed measurements of the three-dimensional flow field for a range of discharge conditions (Table 4.1).

Two different approaches were used to analyze the scales of form roughness along the outer banks. The first method used the LiDAR data to investigate the various scales of topographic irregularities of bank elevation contour lines located approximately at the top and middle of the bank profile and just above the water surface. The LiDAR point cloud data for each survey were interpolated using a triangulated irregular network (TIN) and points used to define contour lines were extracted using LAStools at an average streamwise spacing of 0.3 m, a collection of C++ codes designed for rapid processing and visualization of LiDAR point cloud datasets in either LAS or ASCII formats (Isenburg *et al*., 2006). The contour lines were then converted from UTM-16N coordinates into streamwise *s* and transverse *n* coordinates. This process was facilitated by digitizing the right and left bank from 2011 orthophotography of the study area and calculating a channel centerline using the Planform Statistics toolbar extension in ArcGIS (J. Lauer – NCED). The calculated 2011 channel centerline was then used as the baseline for the streamwise coordinate system with increasing *s* in the downstream direction and positive and negative *n* to the right and left of channel centerline, respectively. Thus the conversion of outer bank contour lines from Cartesian-UTM to streamwise coordinates yields the streamwise position within the bend and the orthogonal distance from the centerline to the outer bank for all vertices comprising a single contour line. These transformations were performed using custom-written MatLab functions based on previously published transformation algorithms (Legleiter and Kyriakidis, 2006).

Once the spatial series of *s* and *n* coordinates were obtained for the bank contour lines, spectral analyses were performed using the Hilbert-Huang Transform (HHT) method (Huang *et*

al., 1998). The HHT method employs the empirical mode decomposition (EMD) to extract a finite number of locally orthogonal intrinsic mode functions (IMF), and then applies a Hilbert transform to each IMF. The Hilbert transforms are then used to calculate the amplitude and frequency of *n* at each value of *s* using the following set of equations,

$$A(s) = \sqrt{Z_r^2 + Z_i^2} \tag{4.2}$$

$$\omega(s) = \frac{d\theta(s)}{ds} \tag{4.3}$$

$$f(s) = \frac{\omega(s)}{2\pi} \tag{4.4}$$

where $A(s)$ is the local amplitude, $\omega(s)$ is the local angular frequency, $f(s)$ is the local instantaneous frequency, Z_r is the original signal, Z_i is the Hilbert transform, and $\theta(s) = \tan^{-1}\left(\frac{Z_i}{Z_r}\right)$. Plots of amplitude-frequency-space can be prepared similar to wavelet analysis, and if amplitude values are binned over frequency and summed over space, a marginal Hilbert spectrum can be created similar to Fourier analysis.

The advantages of using the HHT method for spectral analysis in this study are several. First, HHT can be applied to nonlinear and non-stationary signals (Huang and Wu, 2008; Konsoer and Rhoads, 2013), such as spatial coordinate series of bank contour lines over distances at the meander bend scale. Second, inherent to the method, HHT does not require the *a priori* selection of a particular waveform to compute amplitude and frequency, constraints of both Fourier and wavelet analysis. Lastly, the EMD process can be used to examine the characteristics of individual IMFs, and thus allows for more detailed investigation of the various oscillatory components contributing to the overall variance in the original signal. This method can also extract the overall trend of the signal, which is the residual signal remaining after the EMD process, allowing for accurate nonlinear detrending of the signal. Detrending the original

signal effectively removes the influences of bankline curvature from the data series and allows data analyses to be conducted on stationary signals representing bank roughness.

The second method used to analyze surface roughness of the outer banks involved estimating root-mean-square (rms) values of vertical deviations in the bank surface for discrete sections of the outer bank. For this approach, areas of interest were selected at different locations around the bend and subsamples of the LiDAR and MBES point cloud data were extracted. The locations of the subsamples were located near the bend apex regions because of the importance of this area for the overall planform evolution of the bends. These subsamples were then imported into ArcGIS and interpolated using an inverse distance weighted technique to produce 2m x 2m smoothed grid representations of the bank morphology. This interpolated representation provided a frame of reference for the rms calculations. Each elevation value of the point cloud data was subtracted from the elevation of the smoothed surface at that particular location and the rms value of the deviations was determined. This method was used to compare subaqueous and subaerial characteristics of outer bank surface roughness. The rms approach to evaluate roughness differs from the HHT approach in that: 1) the rms analysis captures scales of roughness related primarily to relatively small slump blocks and transversely-oriented irregularities located within discrete areas of the outer bank, whereas the HHT analysis captures streamwise-oriented irregularities in roughness at specific elevations along the entire bank, and 2) the rms approach examines roughness in three-dimensional space, while the HHT approach examines roughness in two-dimensional space.

Spatial patterns of short-term rates of outer bank erosion were determined through investigation of the detrended bank contour lines in streamwise coordinates from the HHT analysis. Differences in values of *n* (transverse distance from channel centerline) at the same

streamwise distance around the bend for fixed bank elevations were determined for the three consecutive years of bank surveys. This method characterized in detail spatial patterns of erosion around each bend and allowed for patterns of erosion and deposition to be evaluated and linked to form roughness and the structure of the near-bank flow field.

4.4 Results

4.4.1 LiDAR surveys, bank contours, and bankline irregularities

Details of the outer bank morphology revealed from the 2011 LiDAR survey of Maier Bend show a range of physical scales of topographic undulations from large-scale *scallops* to small-scale gullies and rills (Figure 4.3). Herein the use of the term scallop refers to concave erosional indentations, roughly semi-circular, along the outer bank. Inspection of the LiDAR surveys shows that the geometry of these scallops varies with elevation, with a well-preserved semi-circular profile within the fine-grained top layer of bank that gradually becomes less defined as bank elevation decreases (Figure 4.3).The 2011 LiDAR survey of Horseshoe Bend clearly shows the vast amounts of vegetation both within the channel at the base of the outer bank and vegetation slumped and growing directly on the outer bank face (Figure 4.4).

Contours of outer bank elevation along Maier Bend were extracted at elevations 110.5 m, 113 m, 114 m, and 116 m, and were converted from UTM-16N to a local streamwise coordinate system (Figure 4.5). The contour lines in both coordinate systems show the variation in outer bank topography as distance increases in the downstream direction from right to left, however in the streamwise coordinate system the planform curvature is inherently removed and thus the bank roughness is more clearly visible. In particular, for contour level 110.5 m a large variation in bankline position (directed towards the center of the channel) can be seen on the downstream limb of Maier Bend and is the topographic expression of the local outcrop of bedrock in the

channel. For Horseshoe Bend, the LiDAR point returns that were manually classified as vegetation were removed from the dataset prior to surface interpolation and contouring, thus ensuring that the analysis presented in this section is limited to topographic irregularities of the bank face (classified ground returns) and does not include variations caused by vegetation. Contours along Horseshoe Bend were extracted at 112.5 m, 114 m, and 115.5 m, and the degree of variation in topographic irregularity appears to be composed of three broad large-scale undulations with smaller superimposed peaks (Figure 4.6), and differs from the degree of variation for contours at Maier Bend which appear to consist of more isolated small-scale peaks throughout the bend.

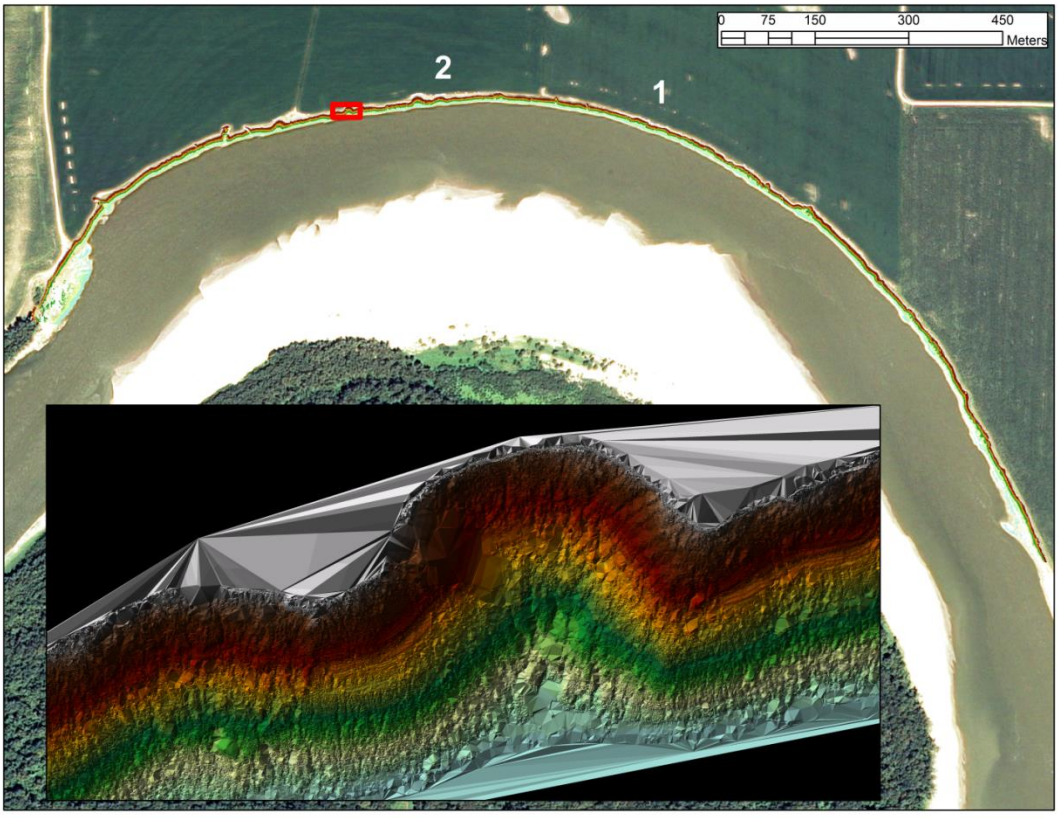

Figure 4.3: Survey extent for 2011 LiDAR survey of the outer bank of Maier Bend. Red box indicates location of inset, showing a large scallop, rills and surface roughness in a TIN representation of the LiDAR point cloud. (Numbers indicate approximate areas of interest for MBES surface roughness calculations).

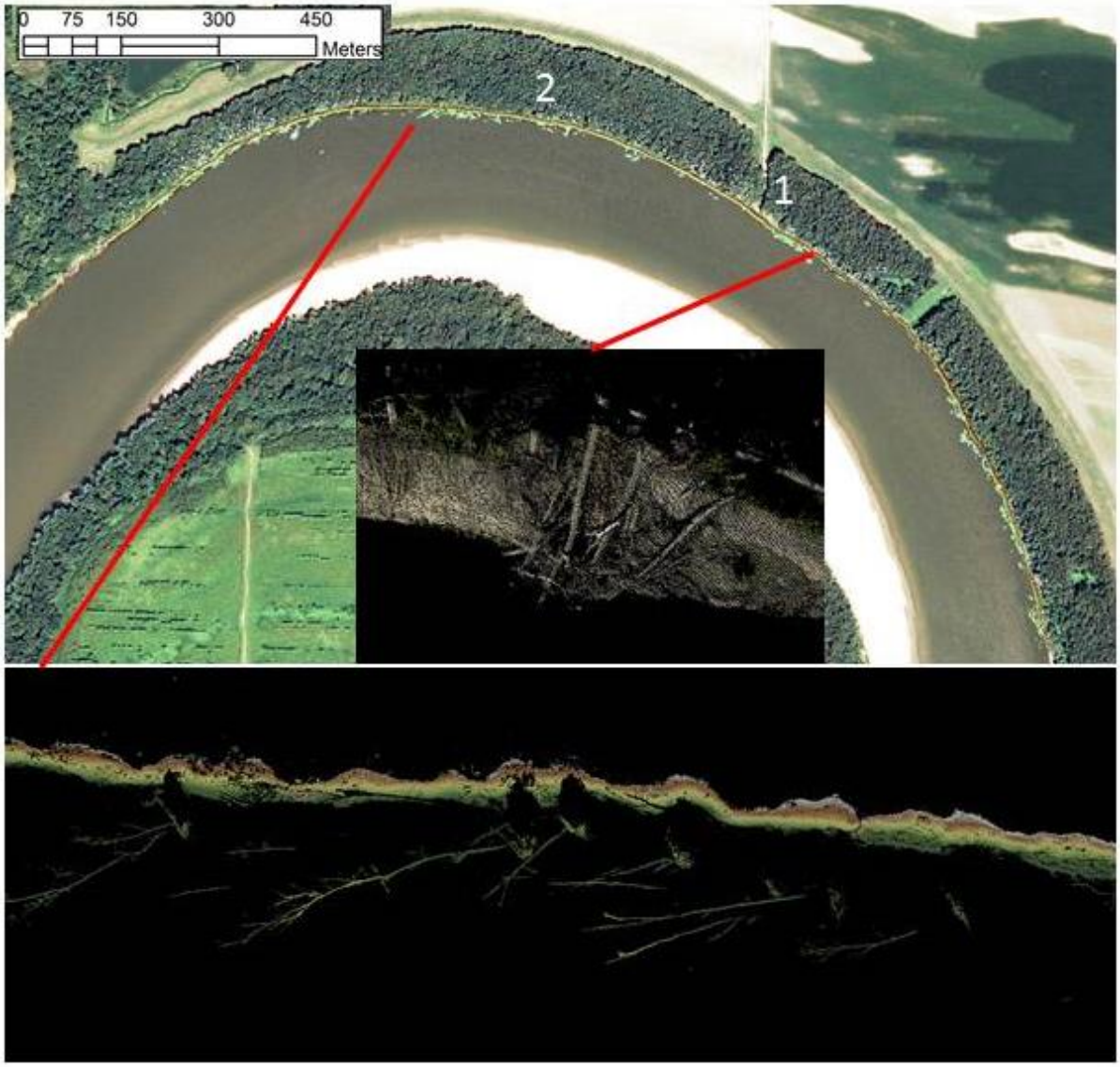

Figure 4.4: Example of 2011 LiDAR survey for Horseshoe Bend. (Numbers indicate approximate areas of interest for MBES surface roughness calculations).

HHT analyses illustrate the influence of different scales of topographic variation of the channel banks on spatial variability in the configuration of detrended contour lines at Maier Bend. This analysis also shows how the scales of bankline irregularity vary among the contours at different elevations. The local bedrock outcrop in the downstream portion of bend is the most important scale of roughness influencing spatial variability in the 110.5 m contour line (Figure 4.7). The highest amplitudes (~2.25 – 3.25) are located at the outcrop (*s* ~2350 m), where the

contour line abruptly changes transverse position. Upstream of the bedrock outcrop small variations in the contour-line signal exist, but these variations have relatively small amplitudes that typically do not exceed ~1.5 (Figure 4.7).

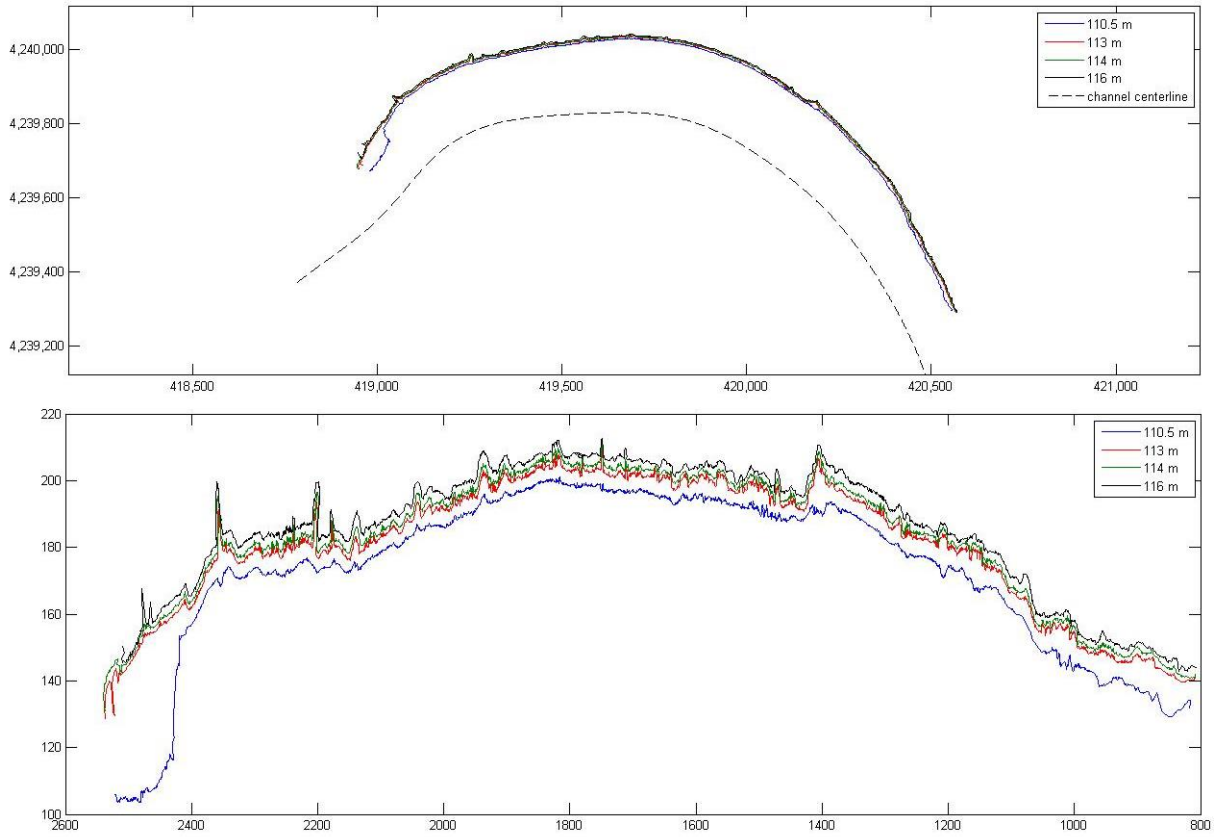

Figure 4.5: Extracted contour elevations for 2011 LiDAR survey at Maier Bend in UTM-16N coordinate system (top) and local streamwise *s* and *n* coordinate system (bottom).

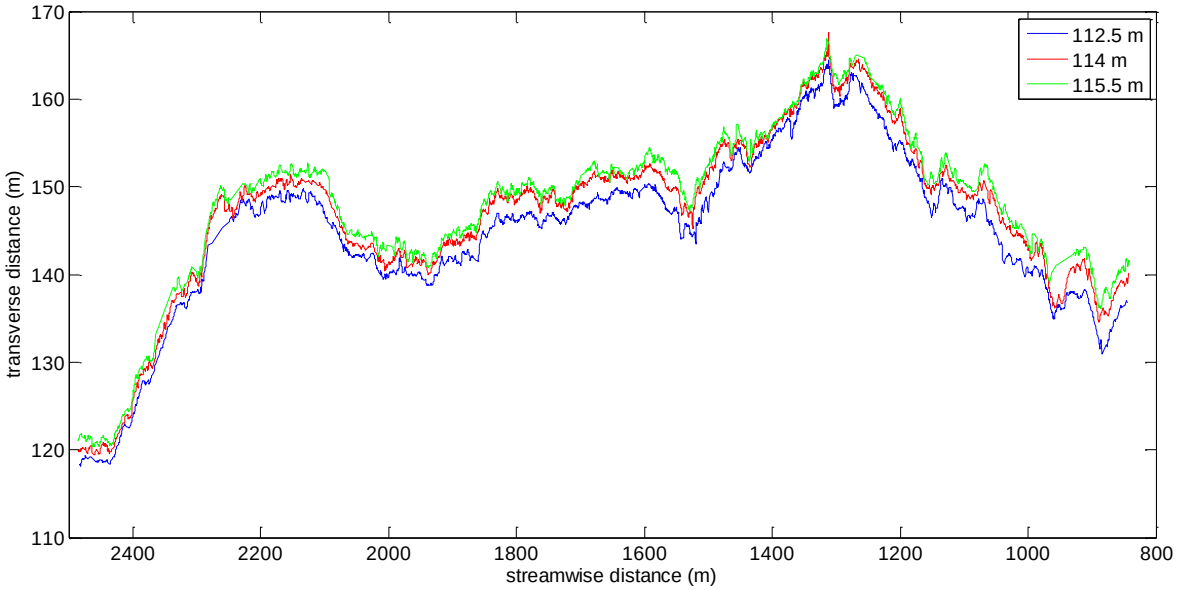

Figure 4.6: Extracted contour elevations for 2011 LiDAR survey at Horseshoe Bend in local streamwise *s* and *n* coordinate system.

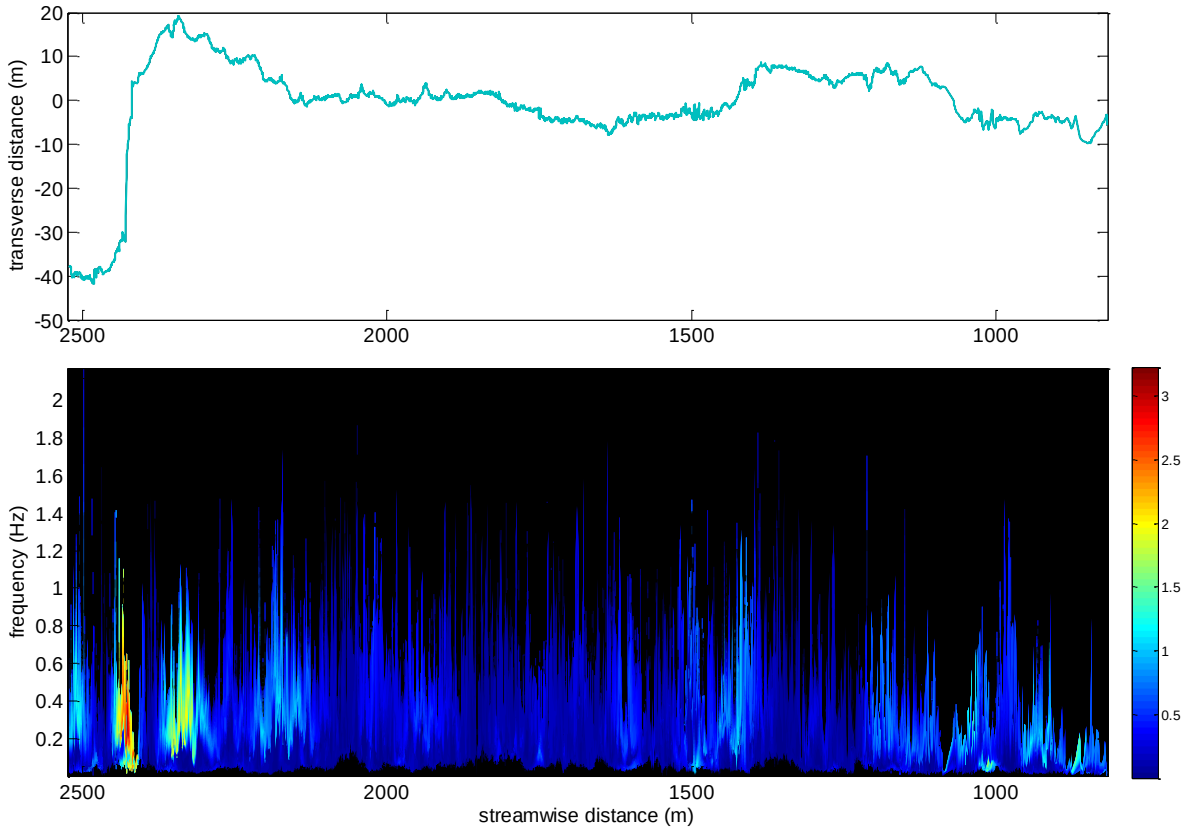

Figure 4.7: Detrended 110.5 m contour line at Maier Bend from 2011 LiDAR survey shown in local streamwise coordinates (top), and Hilbert spectrum for contour line shown in top panel (bottom).

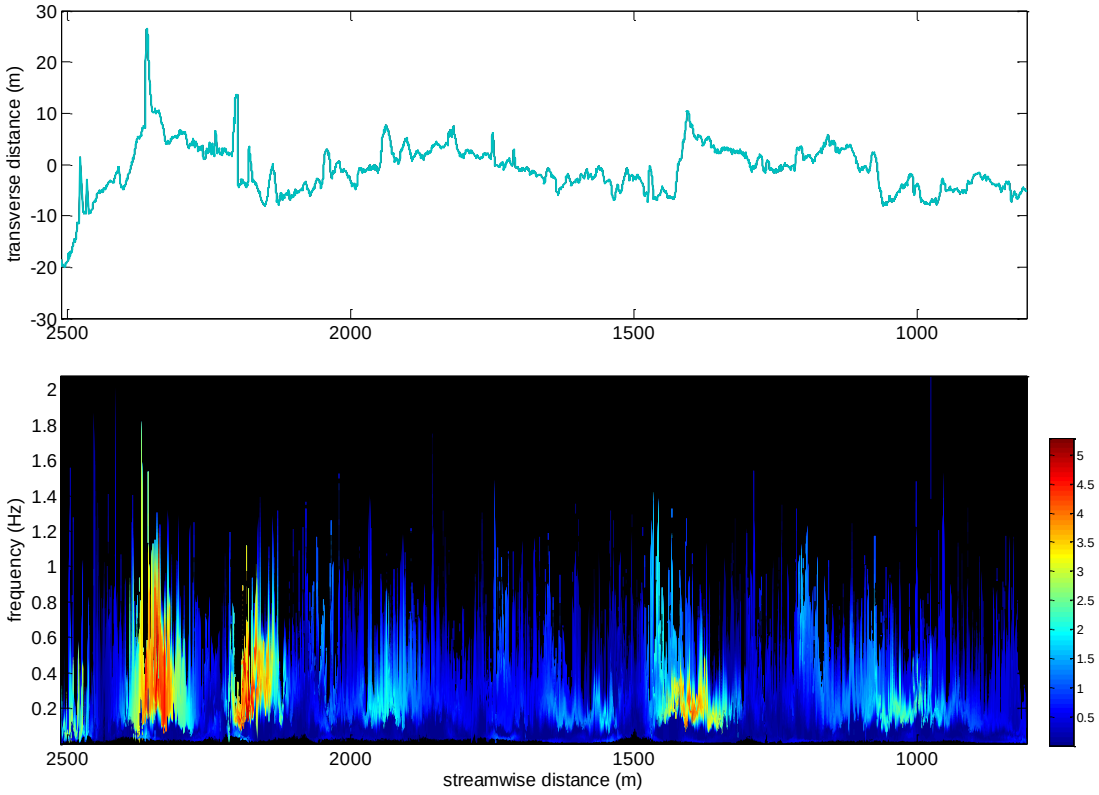

Figure 4.8: Detrended 116 m contour line at Maier Bend from 2011 LiDAR survey shown in local streamwise coordinates (top), and Hilbert spectrum for contour line shown in top panel (bottom).

In contrast, results of spectral analysis for the 116 m contour line at Maier Bend differ from those for the 110.5 m contour line. The bedrock outcrop lies below an elevation of 116 m and does not influence the shape of this contour line (Figure 4.8). Instead, the main components of topographic irregularity derive from different scales of bankline undulations. These undulations are fairly persistent with increasing distance in the streamwise direction, yet appear to have highly variable frequency and amplitude values (Figure 4.8). At this elevation, three major peaks in amplitude (> 5) occur in the Hilbert spectrum at streamwise distances of ~1400 m, ~2200 m, and ~2400 m and are associated with relatively large-scale (low frequency) variations in the bankline (Figure 4.8). In addition to these irregularities, high frequency (small-

scale) undulations produce areas of increased amplitude at streamwise distances of ~1100 m, ~1600 m, and ~1900 m.

To investigate the combined characteristics of bank roughness scales, marginal Hilbert spectra were generated for each contour line at Maier Bend (Figure 4.9). The results show that marginal Hilbert spectra differ at various bank elevations, indicating that the characteristics of roughness are not uniform over the face of the bank. For the 110.5 m contour, the marginal Hilbert spectrum does not display a dominant peak in the scale of bank roughness. However, as bank elevation increases a broad hump that peaks at frequencies ranging from ~0.02 – 0.06 Hz is evident in the spectral curves (Figure 4.9). This frequency range corresponds to physical scales of ~50 – 15 m.

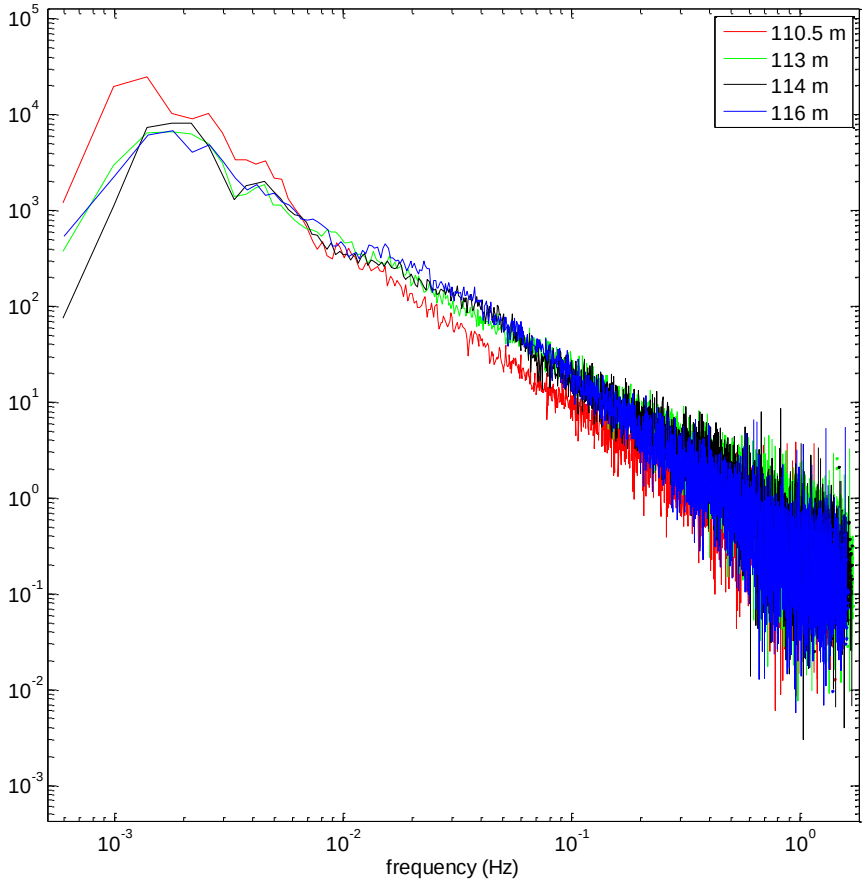

Figure 4.9: Marginal Hilbert spectra for contour lines from Maier Bend, 2011 LiDAR survey. Note increased amplitude for frequencies ~0.02 – 0.06 Hz as elevation increases.

The marginal Hilbert spectra produced for the different contour lines of the 2011 LiDAR survey at Horseshoe Bend show much different results than those for Maier Bend (Figure 4.10). Namely, the spectra for each contour line are nearly identical for frequencies higher than ~0.02 Hz, indicating no substantial differences in the spectral characteristics of bankline irregularities at different bank elevations. The spectra for bank line elevations of 112.5 m and 114 m do show a flattening of the curves of Hilbert amplitude for frequencies of about 0.005 – 0.01 Hz, which correspond to physical length scales of 100 – 200 m. These flat regions of the spectra represent frequencies that do not contribute substantially to bankline variability and thus are less important than other frequencies for influencing bank roughness. Whereas the spectra of high bank elevations at Maier Bend show a broad increase in amplitudes over the middle range of frequencies (10^{-1} to 10^{-2} Hz), the spectra of bank contours at Horseshoe Bend display no range in frequencies associated with increased amplitudes. Thus, for this bend a dominant roughness scale is difficult to identify. Nevertheless, the Hilbert spectrum for the 114 m contour (mid-bank level) shows that irregularity in the bankline still contributes to the overall variance of the signal, and that the spatial distribution of roughness is non-uniform and spatially intermittent (Figure 4.11).

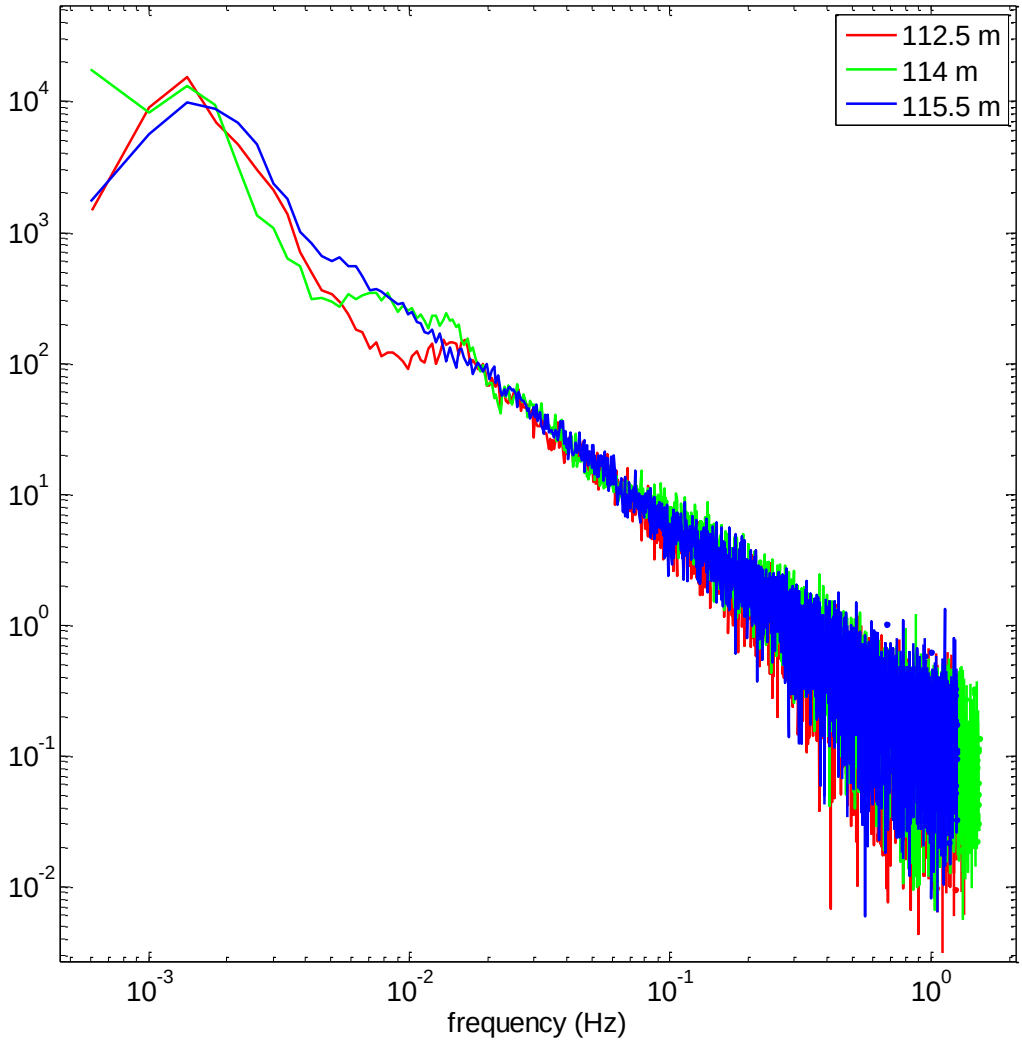

Figure 4.10: Marginal Hilbert spectra for contour lines from Horseshoe Bend 2013 LiDAR survey showing little variation between contour lines.

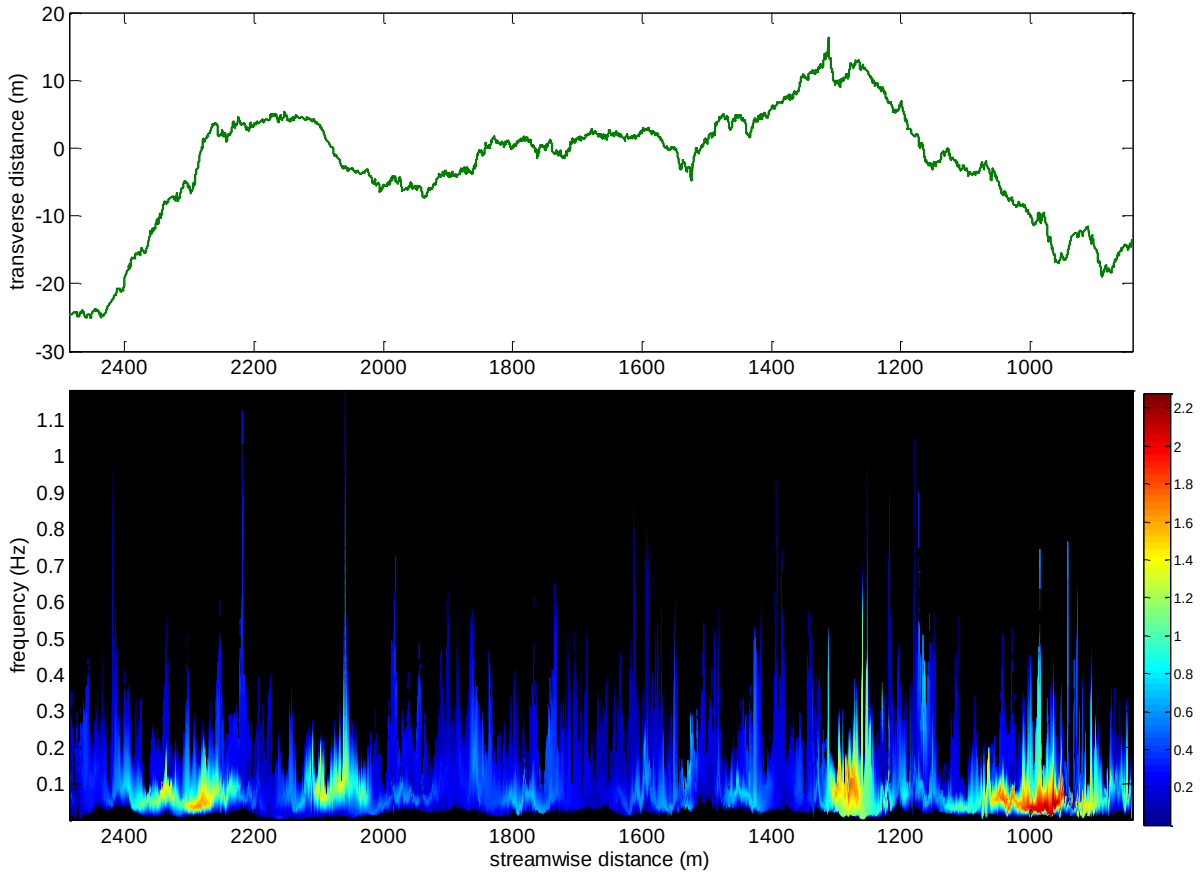

Figure 4.11: Detrended contour line for 114 m at Horseshoe Bend (top), and Hilbert spectrum showing influence and spacing of bankline irregularities through the bend (bottom).

4.4.2 Rates of outer bank erosion

The spatial patterns of erosion can be investigated in detail by examining the difference in transverse position of contour lines at constant elevations for the three LiDAR surveys. For this analysis, a single bank elevation of 114 m was chosen for both Maier and Horseshoe bends and reflects an elevation that is roughly mid-bank. The results at Maier Bend show that generally the rates of erosion are the greatest near the bend apex (at a streamwise distance roughly 1700 – 2200 m) and rates of erosion are lowest near the entrance and exit of the bend (Figure 4.12). However, rates of erosion are highly variable around the bend and for different time periods, with rates of erosion for time period 2011-2012 ranging from 0-13 myr^{-1} and rates of erosion for

time period 2012-2013 ranging 0-19 myr^{-1}. Additionally, the spatial series of erosion shows that there are locations around the bend where rates of erosion are consistently higher than surrounding rates (e.g. s = 1270, 1140), and also locations where relatively high rates of erosion for time period 2011-2012 are followed by relatively low rates of erosion for time period 2012-2013 (Figure 4.12).

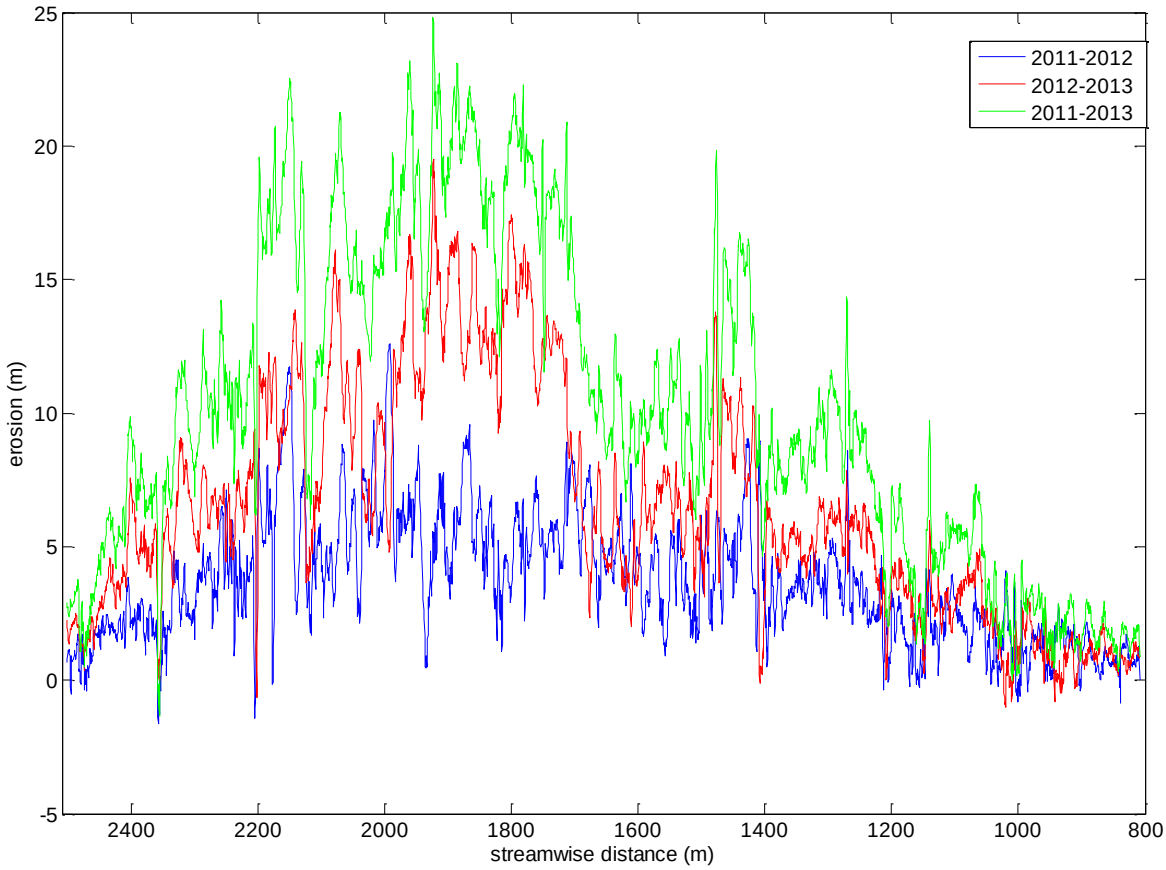

Figure 4.12: Spatial series of erosion for Maier Bend determined from repeat terrestrial LiDAR surveys at elevation of 114 m.

Rates of erosion around Horseshoe Bend are substantially lower than Maier Bend, and peak rates of erosion, which occur at a streamwise distance of about 1400 m, are only ~3 myr^{-1} (Figure 4.13). Increased erosion rates occur between streamwise distances 1200 – 1600 m, whereas average rates of erosion elsewhere around the bend are just slightly above zero. The spatial series of erosion around Horseshoe Bend also shows a few locations where rates of

erosion are negative, indicating local deposition (Figure 4.13). Similar to the results obtained for Maier Bend, the rates of lateral bank erosion for Horseshoe Bend are highly variable both around the bend and between time periods. However, in contrast to Maier Bend, the rates of erosion for time period 2012-2013 are not substantially greater than erosion rates estimated for time period 2011-2012.

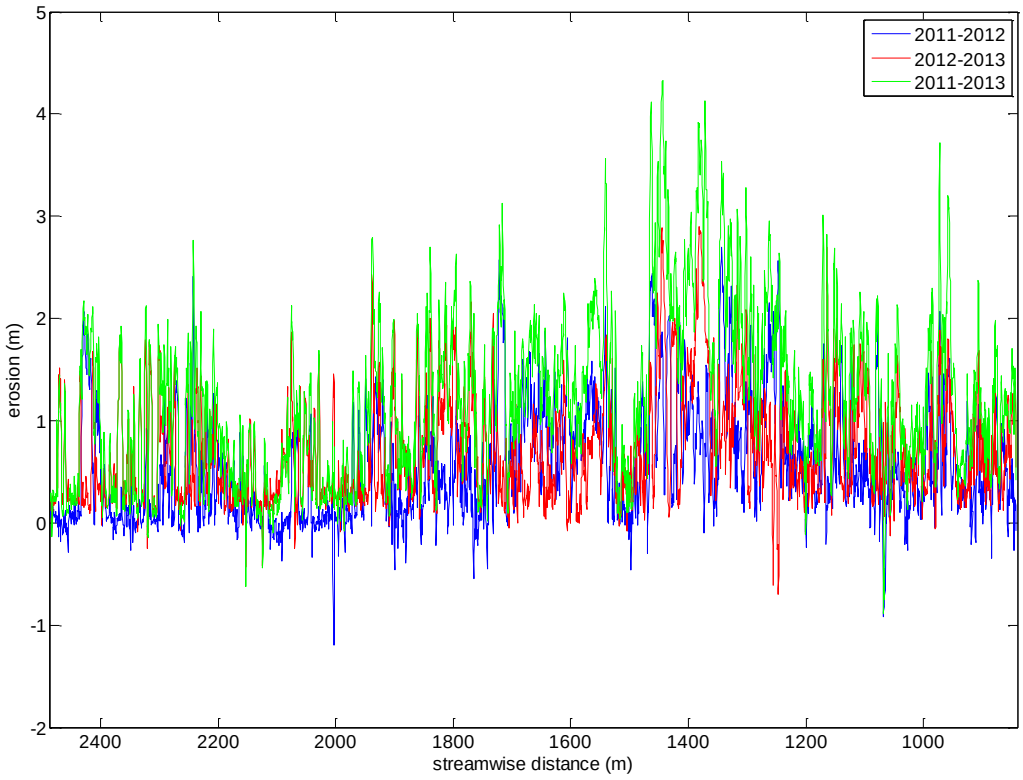

Figure 4.13: Spatial series of erosion for Horseshoe Bend determined from repeat terrestrial LiDAR surveys at elevation of 114 m.

4.4.3 Subaerial and subaqueous surface roughness

Four areas along Maier and Horseshoe bends (two on each bend) were selected to evaluate changes in surface roughness over time, based on availability of data for similar locations between different survey dates and expected importance in the overall morphodynamics of meander bends. Areas approximately 20-30 meters long and extending over

approximately 2 meters of the vertical dimension of the bank face, the extent of overlap between LiDAR and MBES data, were chosen near the bend apex (locations indicated on Figures 3-4). Because the bank face retreated between surveys, it was not possible to compare roughness estimates for the exact same areas of the bank face for each survey. Instead, estimates of roughness were compared for areas with similar positions along the bend and elevation on the bank face among the surveys (Figure 4.14).

Due to the inherent differences in the mapping resolutions between the LiDAR and MBES systems, a sensitivity analysis was performed for both instruments to determine any possible effects of spatial resolution on rms values. For this sensitivity analysis, the 2012 LiDAR survey and the 2012 MBES survey for Maier Bend area 1 were selected, and the datasets were analyzed by selecting subsets of the data at different spatial resolutions and computing the rms values for these subsets. The results indicate that varying the spatial resolution over a broad range of scales (0.01 - 0.25 m) does not substantially change the rms values for the two different methods, confirming that the rms analysis of these data is insensitive to spatial resolution (Figure 4.15). Thus, the full resolution for each dataset was used to estimate the rms surface roughness for both methods at all locations.

Table 4.2: Surface roughness rms values (m) for selected areas along Maier and Horseshoe bends for LiDAR and MBES surveys.

	Maier Bend		Horseshoe Bend	
LiDAR	Area1	Area2	Area1	Area2
2011	0.17	0.17	0.21	0.41
2012	0.24	0.16	0.18	0.51
2013	0.13	0.10	0.19	0.69
MBES				
2012	0.10	0.10		
2013			0.10	0.08

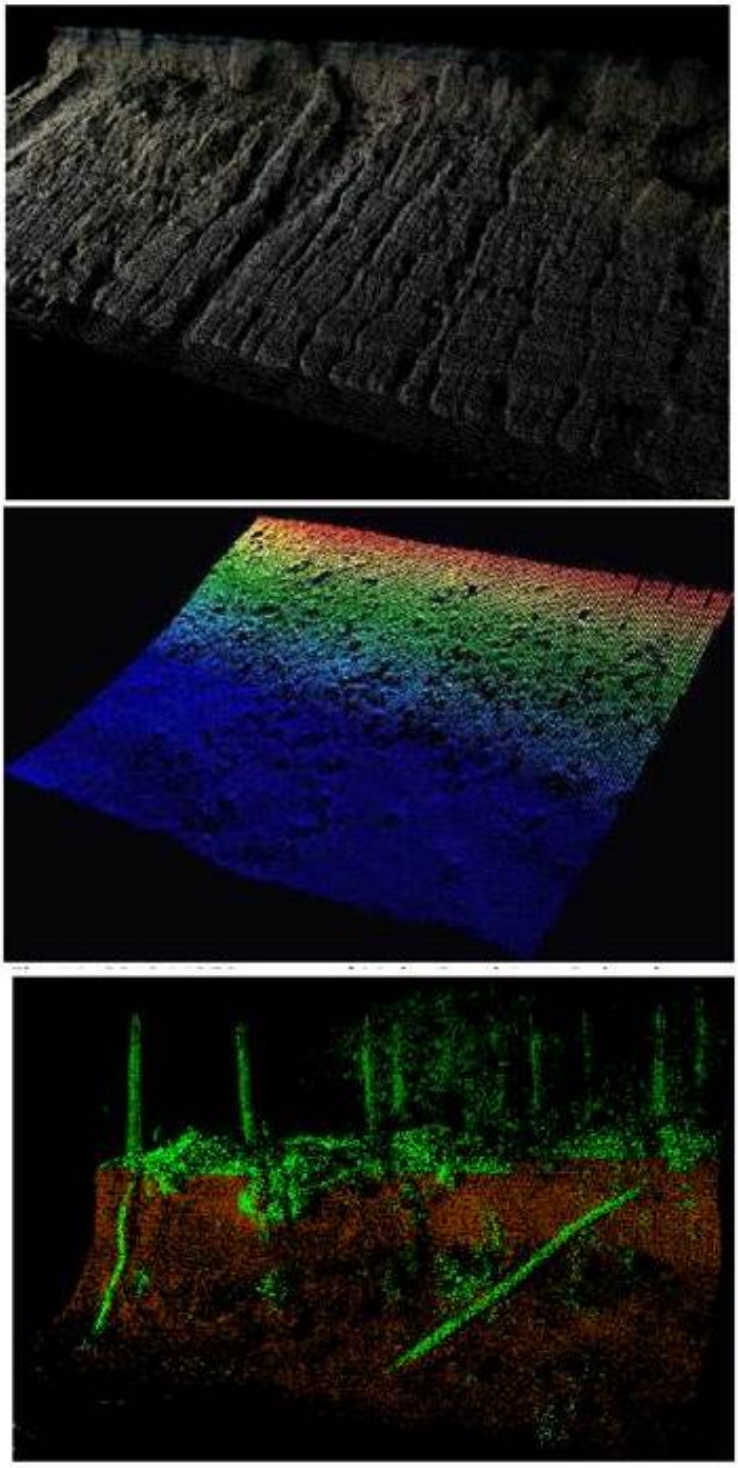

Figure 4.14: 2011 LiDAR survey of Maier Bend, area 2. Length of area ~30 m (top). 2012 MBES survey of Maier Bend, area 2 showing submerged blocks of slumped bank material (middle). 2013 LiDAR survey of Horseshoe Bend, area 2 showing vegetation (green) on outer bank. Length of areas ~18 m (bottom).

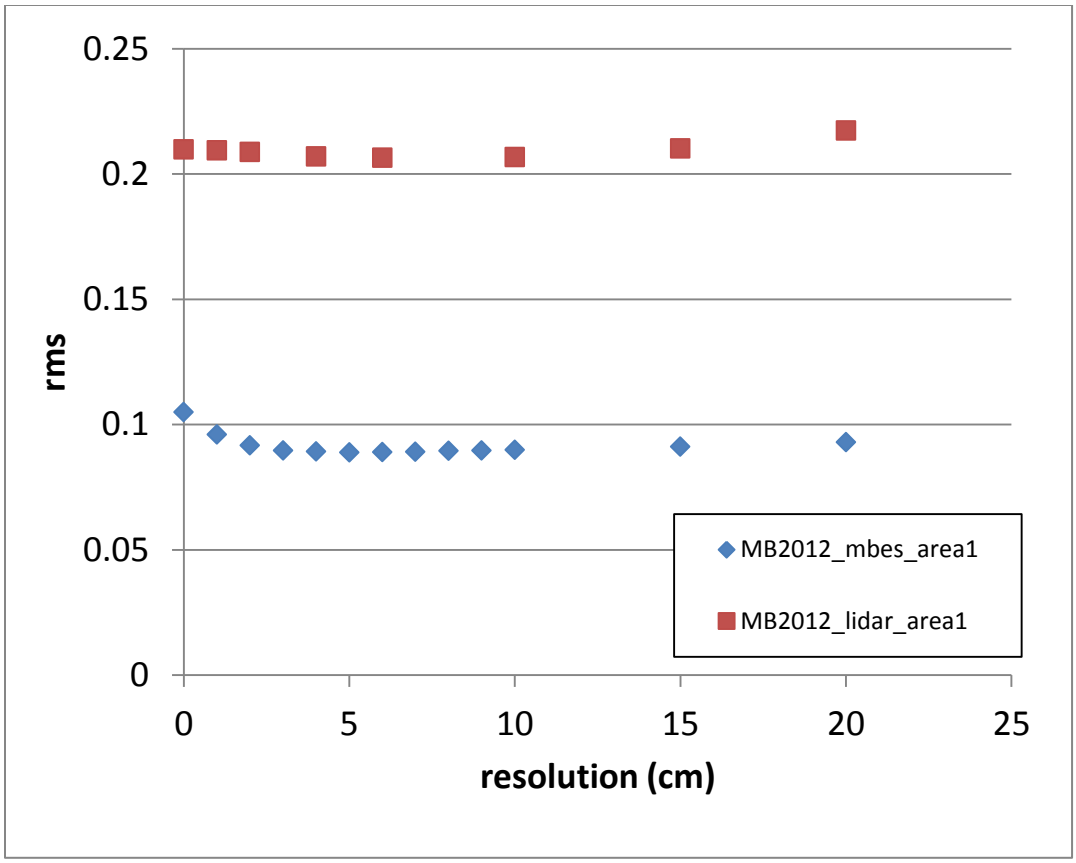

Figure 4.15 Sensitivity analysis of estimated rms surface roughness by varying the spatial resolution of subaerial (red squares) and subaqueous (blue diamonds) datasets for Maier Bend area 1, 2012.

The estimated rms values of surface roughness for Maier and Horseshoe bends show that the roughness values determined for the subaerial LiDAR surveys vary substantially between each year for both bends (Table 4.2). The highest rms value for Maier Bend area 1 was estimated from the 2012 LiDAR survey at 0.24 m, while the lowest rms value for Maier Bend area 1 was 0.13 m determined from the 2013 LiDAR survey. The rms values for Maier Bend area 2 are similar to those estimated for area 1 and also display a range in surface roughness between each year. For Horseshoe Bend, area 1 was located near a privately owned campground where the banks are locally cleared of heavy vegetation. The rms values of surface roughness at this site for all three LiDAR surveys are similar to those obtained for both sites on Maier Bend. However,

area 2 of Horseshoe Bend had a significant amount of vegetation on the bank surface for all three years (Figure 4.14), and the rms values determined from this area range from 0.41 – 0.69 m (Table 2).

The rms values of surface roughness at Maier Bend estimated using the MBES data from 2012 are 60% (area 2) and 140% (area 1) less than the estimates determined from the 2012 LiDAR data. The magnitude of subaqueous roughness (0.10 m) for the two areas of the outer bank at Maier Bend is equal to the smallest value of subaerial roughness determined for all dates at the four areas on the banks at Maier and Horseshoe bends. Values of subaqueous roughness for Horseshoe Bend estimated from MBES data in 2013 are similar to those obtained at Maier Bend in 2012 and are 90% (area 1) and 760% (area 2) less than estimates obtained from the 2013 LiDAR data. Overall, the MBES estimates of subaqueous bank roughness are substantially less than the LiDAR estimates of subaerial bank roughness.

4.4.4 Details of flow structure in relation to bank irregularities

To investigate the influence of the large-scale bank roughness elements around Maier and Horseshoe bends on near-bank flow structure, three-dimensional velocity measurements were obtained during near-bankfull discharge conditions (January 15-16, 2013: 2,380 m^3s^{-1}) along predetermined cross sections. At Maier Bend, the effects of the large-scale scallops on near-bank flow structure are best illustrated at a location near the upstream end of the bend apex region at the bankline irregularity at a streamwise distance of ~1400 m (Figure 4.8). The cross-sectional flow field at this location shows a zone of low velocity (-0.07 – 0.5 ms^{-1}) extending from the water surface to a depth ~3 m (Figure 4.16). This zone is characterized by recirculating flow within the large-scale concave bank indentation, as evidenced by the negative streamwise velocities. However, this eddy is confined to the upper portion of the outer bank profile, and

streamwise velocities near the bank toe are ~1.3 m/s. The effects of large-scale roughness elements at Maier Bend are relatively local, and the region of low velocity generally does not persist at distances downstream beyond ~40 m. In contrast to Maier Bend, the near-bank LWD present around the majority of the Horseshoe Bend protrudes into the flow and adds a substantial component of form drag, causing deceleration of streamwise velocity within a zone along the outer bank that has an average width of ~30 m and extends over the entire flow depth with velocities as low as ~0.25 ms^{-1}, as shown in the previous chapter.

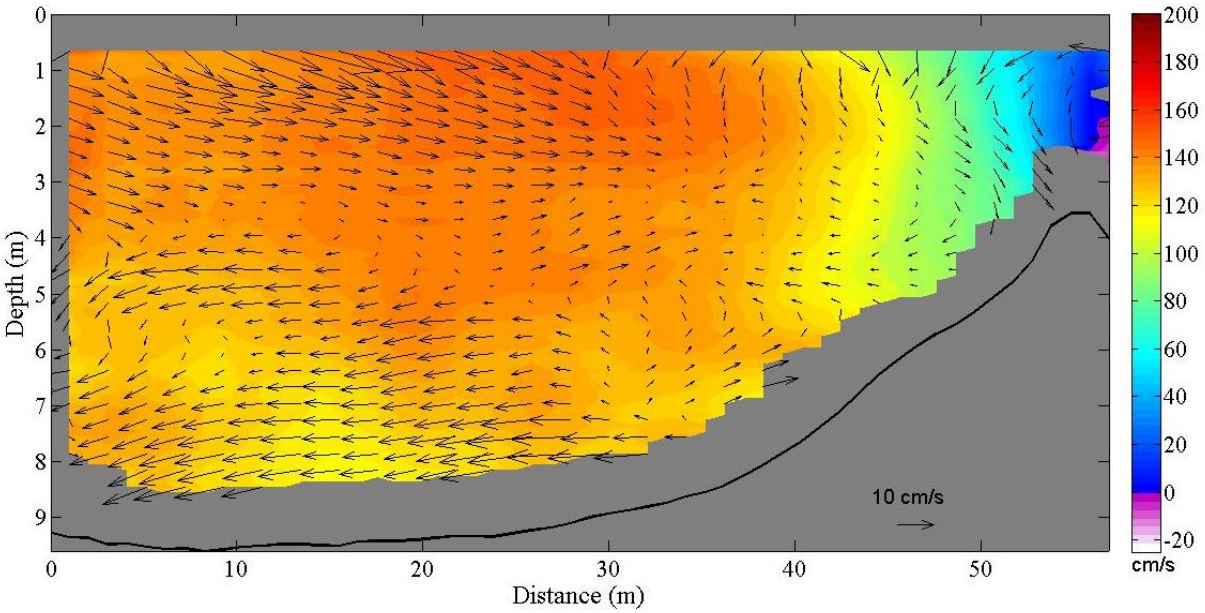

Figure 4.16: Near-bank cross-sectional flow field from Maier Bend at streamwise distance ~1400 m showing the primary (contours) and secondary (vectors) components of flow in the Rozovskii frame of reference.

4.5 Discussion

The results from this chapter show that scales of outer bank roughness differ greatly between forested and unforested elongated loops on a large meandering river, and that overall surface roughness of the outer banks is lower during subaqueous conditions compared to subaerial conditions. The large-scale bankline irregularities measured along the two bends in this investigation occurred intermittently throughout the bends, and the scales of bank roughness for

the unforested loop vary at different bank elevations. The findings from this study provide new links between scales of form roughness and patterns of bank erosion, and have implications for near-bank flow structure, decomposition of shear stress components, and numerical models of bank retreat.

Differences in the scales of roughness for Maier and Horseshoe bends can be attributed to differences in the geotechnical characteristics of the outer banks, in the bulk grain size distribution of the bank sediments, and in the characteristics of outer bank vegetation. The outer bank along Maier Bend is primarily composed on non-cohesive sand and gravel with a transverse slope of ~30°, capped by a 1 – 2 m layer of fine-grained silty sediments with a near vertical bank face. In contrast, the outer bank along Horseshoe Bend is composed of fine-grained sediments (~70% silt/clay content) ranging in thickness from 3 – 5 m and nearly vertical bank faces. The relative lack of vertical heterogeneity of the bank face around Horseshoe Bend, likely accounts for the similar marginal Hilbert spectra at different bank elevations (Figure 4.10).

These findings have important implications for linking large-scale bankline irregularities to the geotechnical properties of the banks and floodplains. The uniform HHT spectra at different bank elevations for Horseshoe Bend suggest that these forested cohesive banks have little vertical heterogeneity in bank roughness, while the lack of a dominant scale of roughness around the bend indicates that streamwise irregularity in the bankline occurs over a variety of length scales. In contrast, the HHT spectra for the unforested non-cohesive banks at Maier Bend have pronounced vertical heterogeneity in bank roughness, yet also show a tendency for the dominant bankline irregularities to occur over a narrow range of frequencies.

Differences in the patterns of erosion around each bend can be attributed to differences in the geotechnical properties of the channel banks, in bank vegetation, and in the mechanisms by

which the banks retreat. Although the highest rates of bank erosion occur near the apex on both bends, the signals of erosion are highly intermittent (Figures 4.12-4.13). The intermittency of the erosional signals can be related to the production of large-scale roughness elements (e.g. scallops and tree slumps). At Maier Bend, despite substantial bank retreat, large-scale bankline irregularities often are located at the same positions within the bend over the entire period of investigation. These persistent features are mostly transverse gullies within the outer bank and observations from the field suggest these features are related to local increased groundwater flow from agricultural tile drains. In contrast to the spatially persistent gullies, bankline irregularities produced by bank failures at Maier Bend commonly display progressive downstream migration through time (Figure 4.17). In some cases, irregularities existed only at a particular time period, and were subsequently eliminated by fluvial erosion of the surrounding bank regions.

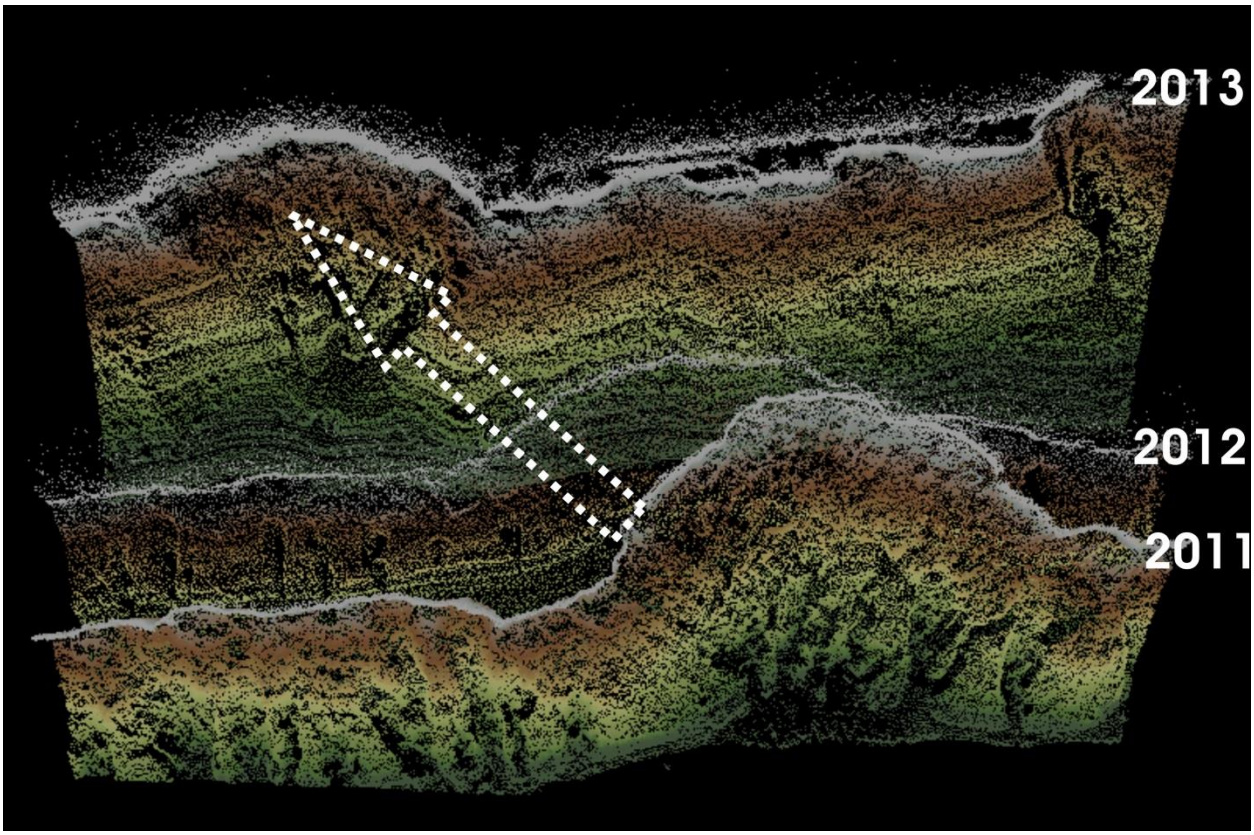

Figure 4.17: Progressive downstream migration of bank scallop at streamwise distance ~1800 m around Maier Bend.

At Horseshoe Bend, the slow rates of bank erosion restrict direct investigation of the spatial patterns of tree slumping and intermittency through time. However, the repeat annual LiDAR surveys illustrate details of a progressive tree slump at a streamwise distance ~1100 m (Figure 4.18). While the process of tree surcharge is common, it has important implications for bank roughness and near-bank flow structure. As the results of the repeat LiDAR surveys suggest, the slow and progressive process of tree slumping produces different local scales of bank roughness through time. In the 2011 survey, the roughness mainly consists of small-scale topographic irregularities in the bank face. The main roughness elements for the 2012 survey are the exposed tree roots within the top ~1.5 m of the bank, and in the 2013 survey the slumped tree becomes the dominant large-scale roughness element.

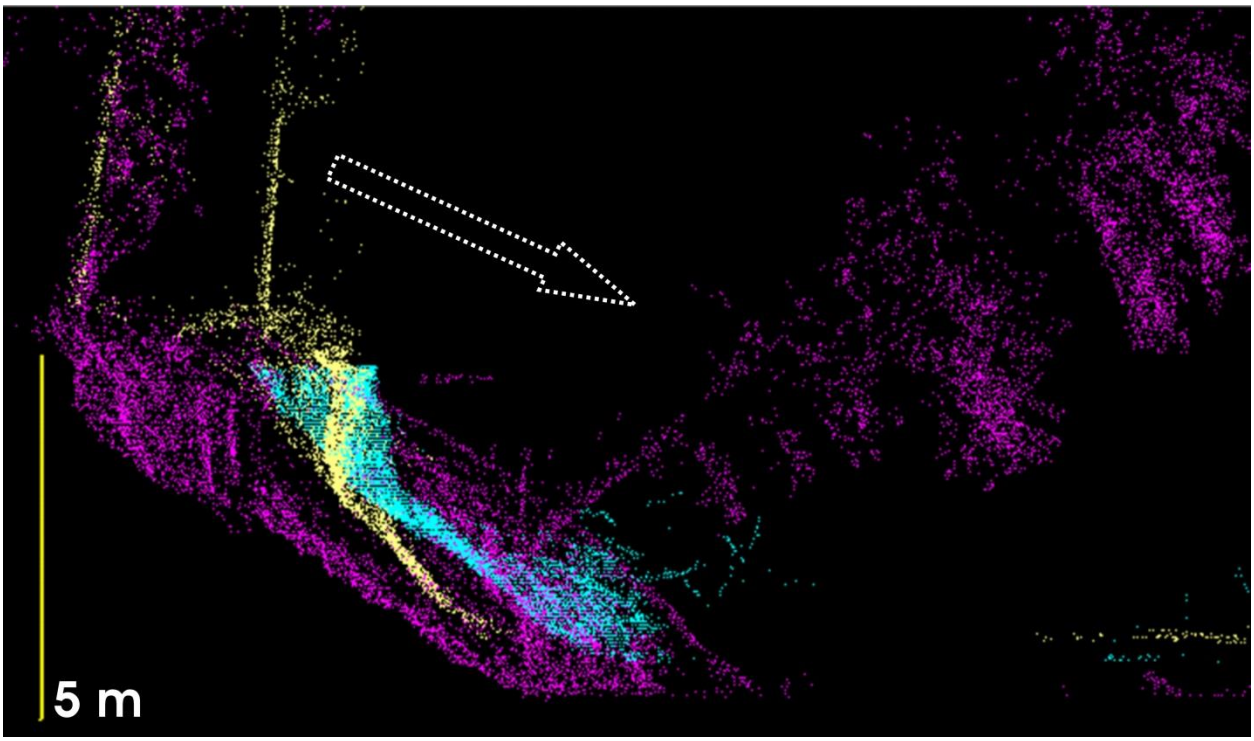

Figure 4.18: Repeat LiDAR survey point clouds showing progressive erosion and tree slumping at a streamwise distance ~1100 m at Horseshoe Bend (2011 – blue; 2012 – yellow; 2013 – pink).

An important finding of this study is that the rms surface roughness of the bank face for the subaerial LiDAR surveys is greater than the rms surface roughness for the subaqueous MBES surveys (Table 4.2). For the non-vegetated bank areas of the two bends, the subaerial roughness was much greater (> 50%) than that for the subaqueous surveys. For vegetated portions of the outer bank at Horseshoe bend, this difference was even more pronounced, with subaerial surface roughness values two to seven times larger than those for subaqueous conditions. This finding has important implications for estimating scales of bank roughness, particularly when trying to characterize form drag and shear stress partitioning for numerical models of bank erosion. Due to difficulties in obtaining detailed topographic data of riverbanks, bank roughness has most commonly been characterized during low hydrologic conditions when the banks are exposed subaerially (Kean and Smith, 2006a,b; Darby *et al*., 2010; Darby *et al*., 2013). As observed at Maier Bend, non-cohesive banks that are exposed subaerially for extended periods of time are often dissected by surface runoff and rills (Figure 4.3 and 4.14). However, during high hydrologic conditions these small-scale roughness elements are eradicated by fluvial erosion, particularly in non-cohesive sediments, as evidenced by the subaqueous rms roughness results. These findings imply that it may be necessary to characterize relatively small-scale bank roughness during subaqueous conditions to accurate simulate near-bank shear stresses and bank erosion.

Despite the relatively low values of rms roughness for the subaqueous MBES surveys, surface roughness was still estimated to be ~0.1 m, indicating some level of roughness still persists during high discharge events. At Maier Bend, these roughness elements are likely remnants of large slump blocks (Figure 4.14) composed of fine-grained cohesive silts and clays, while at Horseshoe Bend the roughness elements are primarily tree branches, woody debris, and

relatively small vegetation growing on the bank face. These roughness elements induce form drag, thereby limiting the shear stress due to skin friction and the capacity of the flow to erode bank sediment. However further research is needed to accurately estimate the form drag of isolated roughness elements near the bank toe, particularly in large meandering rivers. Additionally, in contrast to vegetation, which can be present at a certain time and then completely removed by subsequent flows, cohesive slumps can be transported as intact blocks or reduced in size through fluvial erosion. Recent morphodynamic models have incorporated the influence of near-bank slump blocks (Parker *et al*., 2011; Motta *et al*., 2012), but typically rely on an exponential decay function for the reduction in size of the block through time.

Vegetation around Horseshoe Bend produces the highest subaerial rms surface roughness, but this roughness is substantially reduced for the MBES surveys. One possible explanation for this reduction in roughness could be due to variability in hydrologic conditions and seasonality influencing the growth and removal of vegetation on the bank face, and the subsequent timing of the morphologic surveys. During extended periods of low flow conditions, it is possible for vegetation to grow on the subaerially exposed bank face, but be removed during high flow conditions. Therefore, terrestrial LiDAR surveys conducted during subaerial conditions might be capturing bank roughness associated with the temporary growth of vegetation on the bank surface, whereas subaqueous MBES surveys are capturing bank roughness once this vegetation has been removed.

To further explore the implications of the rms surface roughness on the near-bank flow field at Maier Bend, the surface roughness for subaqueous conditions can be compared to an estimate of the composite hydraulic roughness k_c, which represents the combined effects of skin friction and form drag, using the Keulegan flow resistance relationship,

$$\rho g H S = \rho C_f U^2 \tag{4.5}$$

$$C_f = \frac{1}{\kappa} \ln \left[11 \frac{H}{k_c} \right]^{-2} \tag{4.6}$$

where ρ is the density of water (kgm^{-3}), g is the gravitational acceleration (ms^{-2}), H is the local flow depth (m), S is the reach-averaged slope, C_f is fiction coefficient, U is the local depth-averaged streamwise velocity (ms^{-1}), and κ is the von Kármán constant ~0.4. Using local flow parameters obtained from ADCP measurements at cross-section MB148 (corresponding to area 1), the near-bank estimate of k_c is ~1.1 m, roughly 10 times greater than the 0.1 m roughness computed from the rms analysis. The difference in roughness is most likely due to the fact that the rms estimates represent a local physical measure of bank-face irregularity, whereas the composite roughness represents a dynamic hydraulic equivalent roughness. The Keulegan formulation for flow resistance assumes one-dimensional flow and an infinitely wide channel without the influence of sidewalls. Near the outer bank, values of k_c will be affected by more than just the local roughness of the bank face at a particular location and will reflect the overall effect of different scales of roughness on the flow. Thus, it is not surprising that the estimated composite roughness in the near bank region is much greater than the local topographic bank roughness.

The main roughness elements around Horseshoe Bend are large trees within the channel near the outer bank that were not included in the HHT or rms analyses of the bank faces due to the inherent complexity of characterizing the spatial variability of discrete, relatively linear roughness elements that vary in length and geometry. However, near-bank trees occur nearly continuously around the bend and are aligned with the streamwise flow direction with root wads oriented upstream. The consecutive annual LiDAR surveys show that many of these individual trees within the channel have not substantially moved during the three years of investigation, and

comparison with aerial photography suggests some trees have residence times greater than 5 years (Figure 4.19). As shown in the previous chapter, this in-channel LWD has a dominant effect on near-bank flow resistance that overshadows the effect of bank surface roughness.

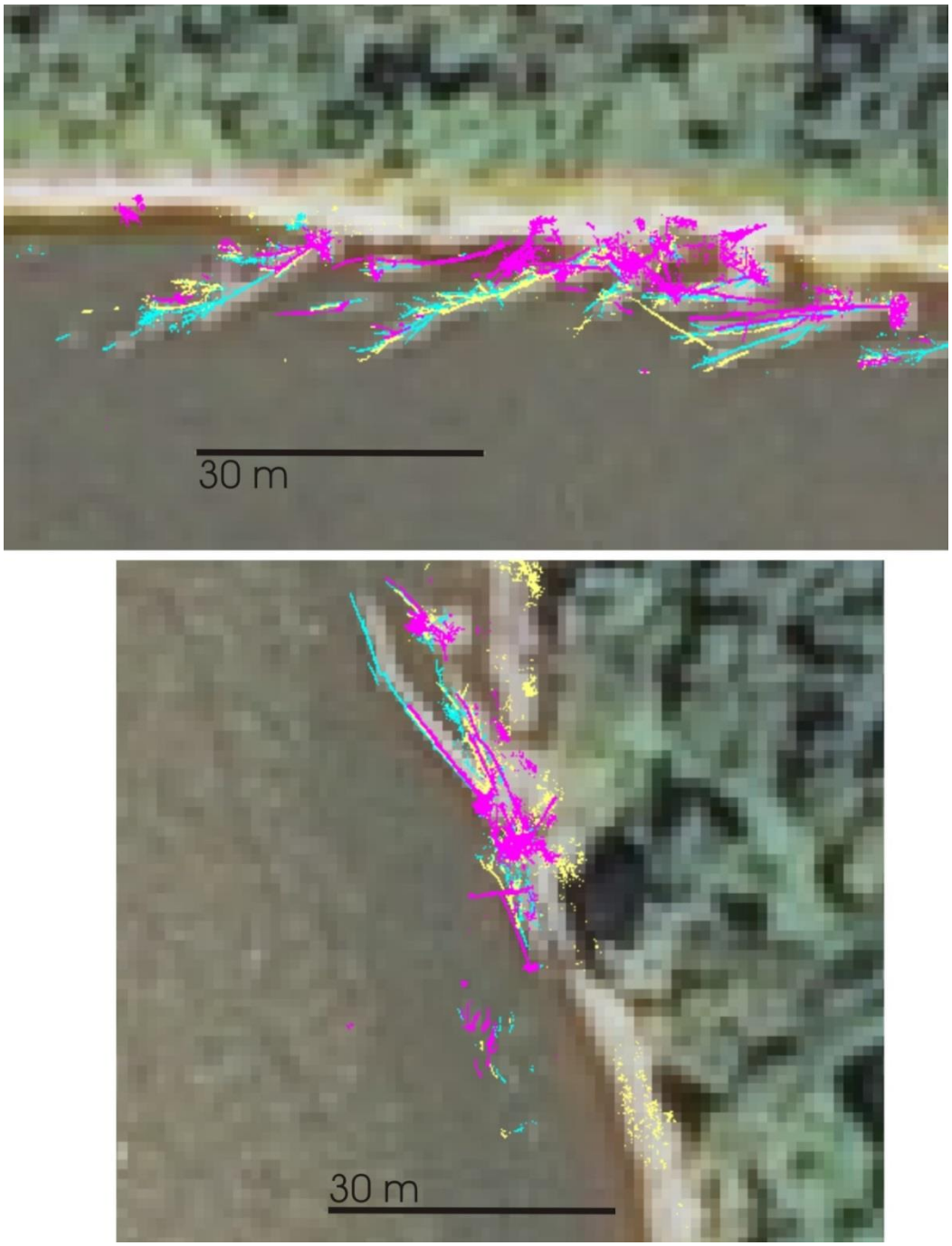

Figure 4.19: Repeat terrestrial LiDAR point cloud data plotted on 2011 orthophotograph showing near-bank LWD undergoing minimal transportation. (2011 – blue; 2012 – yellow; 2013 – pink)

The concave scallops observed at Maier Bend are different from the commonly documented convex roughness elements used in numerical models of bank erosion (Kean and Smith, 2006a, b; Darby *et al*., 2010). In these types of models, roughness elements are approximated by convex Gaussian-shaped bumps that protrude into the channel. Flow around these elements is modeled similar to flow over bed forms (Smith and McLean, 1977), with a shear layer developing from the crest of the feature and flow separation occurring on the downstream side of the feature (Kean and Smith, 1996a) (Figure 4.20A). These models have had success at improving simulations of near-bank flow structure and rates of bank erosion under appropriate conditions of bank roughness, but do not appear to be suitable for determining the roughness effects of local concavities such as the intermittent large bank scallops along Maier Bend.

The effect of roughness elements on flow structure depends on the intermittency of the elements and the baseline used as a frame of reference for flow in the absence of the elements (Figure 4.20). For the case of semi-circular, concave roughness features (e.g. scallops) with constant streamwise spacing, if the reference baseline is established so that it coincides with the exterior tangent line, then the flow will appear to be influenced by the area of bank between the scallops protruding into the channel (Figure 4.20B). Conversely, if the baseline is set to intersect the interior of the scallops, then the patterns of secondary motion will be characterized by recirculating eddies inside the scallops (Figure 4.20C), as appears for the case for Maier Bend.

In the model of Kean and Smith (2006a,b), a decomposition of the shear stress is performed to remove the component of shear stress associated with form drag. However, since drag forces arise from pressure gradient forces around an object, a requirement for the Kean and Smith (2006a,b) model is that the roughness elements protrude into the flow, with a baseline

established along the exterior of the features (Kean and Smith, 2006b). Application of the Kean and Smith (2006a,b) model to large-scale concave bankline irregularities along the Mekong River resulted in over-prediction of bank erosion rates compared to rates of bank erosion estimated from historical photography (Darby *et al*., 2010, 2013). The over-prediction in rates of bank erosion can be explained by the differences in near-bank flow structure and shear stress around convex versus concave roughness elements.

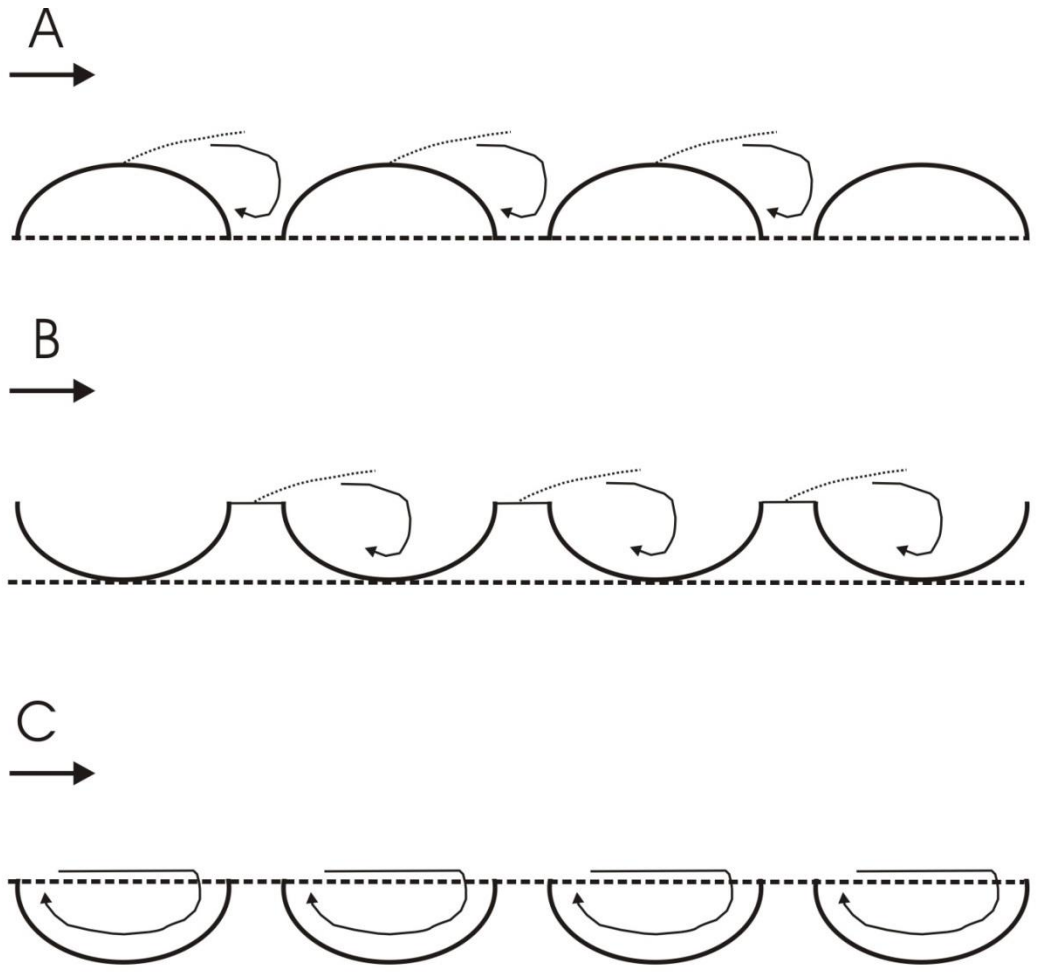

Figure 4.20: Conceptual diagrams showing bank roughness elements with similar spacing but different reference baselines and the expected secondary flow patterns. Dotted lines indicate shear layers and dashed lines represent the baseline associated with the reference flow boundary.

The geometry of the concave scallop features at Maier Bend and the patterns of flow observed around these roughness elements appear somewhat similar to the hydrodynamic conditions observed in groyne fields (Ouillon and Dartus, 1997; Uijttewaal *et al*., 2001; Uijttewaal, 2005; Sukhodolov, 2014). Flow in the presence of groyne fields is characterized by main stream flow in the center portion of the channel and the development of large eddies of recirculating fluid between the groynes (Uijttewwal *et al*., 2001). Flow dynamics within groyne fields commonly have little effect on the free stream flow, but flow conditions in the main channel can influence patterns of fluid motion within the groyne field. For the case of emergent groynes, i.e. those protruding out of the flow, boundary shear stress within groyne fields can be substantially lowered (Sukhodolov, 2014), indicating a reduced ability of the flow to erode the channel banks. Furthermore, flow structure between individual groynes usually is characterized by the occurrence of the highest velocities along the downstream groyne as flow is redirected inward and recirculates upstream. This pattern of flow within the scallops at Maier Bend could account for the progressive downstream migration of these features between successive LiDAR surveys (Figure 4.17).

4.6 Conclusions

This chapter has examined the scales of outer bank roughness along two elongate meander loops with different floodplain vegetation on a large meandering river. Repeat terrestrial LiDAR surveys conducted annually during low flow conditions and multibeam echo sounder (MBES) surveys conducted during near-bankfull discharge conditions provided detailed spatial data on the outer bank topography for subaerial and subaqueous conditions. Investigation of large-scale bankline irregularities was performed using the Hilbert-Huang Transform (HHT) method, which is valid for non-stationary and nonlinear signals. Small-scale surface roughness

for selected areas within the apex region of each bend was estimated using root-mean-square (rms) analysis on the point cloud data and a smooth interpolated bank surface. Lateral and volumetric rates of erosion were determined from the repeat LiDAR surveys and time series analysis of aerial photography dating back to 1938. The major findings from this research are:

1) Large-scale bank roughness at Maier Bend varies at different bank elevations around the bend. Near the base of the bank, a bedrock outcrop at the downstream end of the bend is the dominate form of roughness. As bank elevation increases, bankline irregularities with length scales of 15 – 50 m are the dominant roughness elements. At Horseshoe Bend, roughness is fairly uniform at different bank elevations and a dominant length scale of roughness is not evident. For both bends, large-scale bank roughness elements are highly intermittent, requiring the application of a method like HHT, which is appropriate for non-stationary, locally intermittent signals, to quantitatively characterize this roughness.
2) Scales of roughness estimated from the bank contours are related to the geotechnical properties of the banks. The bank sediment at Maier Bend is primarily non-cohesive sand and gravel with a transverse slope of ~30°, capped by a 1-2 m layer of cohesive silty material with a nearly vertical face. The geometry of the large-scale bankline irregularities at Maier Bend consists of concave indentations (scallops) produced through mass failure of the outer bank induced by localized concentrations of groundwater outflow. The morphological expression of these scallops is most pronounced within cohesive bank sediment near the top of the bank and becomes less defined toward the base of the bank. At Horseshoe Bend, the banks consist mostly of fine-grained silt and clay with near-vertical slopes over the majority of the bank height. The increased resistance of these bank materials and the added resistance from the floodplain vegetation

promote uniform roughness vertically over the bank face throughout the bend. The lack of large-scale scallops at Horseshoe Bend appears to be related to the high bank strength, the binding effects of roots associated with trees along the bank, and the absence of strong groundwater outflow induced by agricultural drainage of the floodplain, such as that at Maier Bend.

3) Comparisons between the small-scale rms results for the subaerial LiDAR surveys and subaqueous MBES surveys suggest that bank roughness diminishes greatly during flows that inundate the bank face. Riverbanks exposed to subaerial conditions for prolonged time periods, particularly banks composed of non-cohesive sediment (Maier Bend), are vulnerable to surface erosion and rill development. However, during subaqueous conditions, these relatively small-scale features are removed through fluvial erosion. In a similar way, the relatively small woody and leafy vegetation that is common on the subaerially exposed banks of Horseshoe Bend could also be removed during high discharge conditions, thereby reducing the measured roughness. Sensitiviy analysis indicates that these differences in subaerial and subaqueous bank roughness are not due to differences in the spatial resolution of the methods used to measure bank face topography (e.g. Lidar versus MBES). These findings highlight the importance of hydrologic conditions on small-scale bank surface roughness, and have implications for accurately modeling near-bank flow structure and rates of bank erosion.

4) Three-dimensional velocity data from ADCP measurements illustrate the influence of large-scale roughness elements on the near-bank flow structure. At Maier Bend, the scallops within the outer bank create zones of low velocity (-0.07 – 0.5 ms^{-1}) characterized by recirculation eddies within the upper ~3 m of the water column. These

roughness elements do not influence near-bank flow structure near the toe of the bank, and the effects typically dissipate within ~40 m downstream of the scallop. The geometry of these roughness elements and the observed pattern of three-dimensional flow structure induced by these scallops differ from current theoretical models that account for the influence of bank roughness elements on near-bank flow by treating these elements as Gaussian-bumps that protrude into the channel and produce shallow wake flow.

5) The spatial pattern of outer bank retreat determined from repeat LiDAR surveys over a two-year period shows that the highest lateral rates of retreat occur near the apex of each bend, but are highly variable throughout the bends. Rates of retreat at Maier Bend are almost two orders of magnitude larger than rates of retreat at Horseshoe Bend. Peak rates of annual lateral migration for Maier and Horseshoe bends were ~19 m and ~3 m, respectively. Lateral retreat of the outer banks resulted in variability in bank roughness over time for subaerial conditions with the greatest variability in this roughness occurring on the unvegetated outer bank of Maier Bend. However, the greatest variability in roughness over time was associated with inundation of the bank face by flowing water, which substantially decreased the roughness compared to subaerial conditions for both unvegetated and vegetated outer banks.

The findings presented in this chapter highlight the complexity and spatial variability of scales of bank roughness on a large meandering river. Major differences in bank roughness, near-bank flow structure, and rates of channel migration reflect differences in floodplain vegetation and the geotechnical properties of the banks. Future studies should focus on characterizing the influence of relatively small-scale roughness elements, such as slump blocks, woody debris and tree roots, on near-bank flow and shear stress through detailed measurements of the three-

dimensional flow structure around these elements. The residence times and rate of decay of slump blocks, as well as residence times of near-bank LWD and vegetation growing on the bank, are also in need of attention to better inform morphodynamic models.

CHAPTER 5

SPATIAL VARIABILITY IN FLOODPLAIN RESISTANCE TO EROSION ON A LARGE MEANDERING, MIXED BEDROCK-ALLUVIAL RIVER

5.1 Introduction

The erosion of sediment from riverbanks and floodplains has long been of interest to researchers in geology, geomorphology, ecology and river engineering. Bank-derived sediments can account for large fractions of the total sediment budget within a catchment (Rinaldi and Darby, 2007) and these sediments can directly affect levels of turbidity, nutrient and contaminant dynamics, and have potentially negative effects on river ecosystems. Additionally, bank erosion is a primary factor controlling channel migration and planform evolution, leading to loss of riparian and agricultural lands, and damage to infrastructure. As such, much of the recent research associated with bank erosion has sought to improve our understanding of the complex interactions driving bank erosion and develop predictive models of bank retreat and channel planform evolution.

Bank retreat most commonly occurs through the process of fluvial entrainment at the bank toe and mass failure of the overlying bank material, with subsequent removal of the failed material (Thorne, 1982, 1992). However, the properties of the channel banks and floodplains strongly influence not only rates of bank erosion, but also the mechanisms by which the banks retreat. There are two main ways that the properties of the banks and floodplains can influence erosion: 1) through the geotechnical properties that affect the resistance to erosion from fluvial action, and 2) by offering a topographic form roughness that can affect the near-bank three-dimensional flow structure, and thus the shear stresses acting upon the channel boundary.

The mechanical properties of riverbanks are dependent on a number of factors. The grain size distribution of the bank sediments will determine the necessary fluid shear stress required to entrain and transport sediment within a reach (Parker *et al*., 2008), while the relative amount of fine sediments, particularly clay-sized particles, influences the cohesion of bank materials and thus the resistance of these materials to erosion (Pizzuto, 2009). Riparian and floodplain vegetation can also have an effect on the resistance properties of the banks and floodplains by increasing tensile strength through root-reinforcement and by increasing cohesion through soil development (Van De Wiel and Darby, 2007; Pollen-Bankhead and Simon, 2009; Walker *et al*., 2010). Additionally, the presence of bedrock within a floodplain produces high resistance that locally restricts rates of bank erosion. These factors influencing the geotechnical properties of floodplains, particularly vegetation, can have a strong influence on the morphology of the outer banks. Topographic irregularities, such as bank undulations, slump blocks and large woody debris (LWD), provide additional flow resistance through increased form drag, resulting in reduced near-bank velocities, altered patterns of secondary flow and turbulence, and the redistribution of momentum within channel reaches (Lopez and Garcia, 1998; Magna and Kirchner, 200; Daniels and Rhoads, 2003; Kean and Smith, 2006a,b; Parker *et al*., 2011; Motta *et al*., 2012).

The importance of the geotechnical properties of banks and floodplains on the processes controlling bank erosion is reflected in the detailed models simulating bank retreat. Physically-based models of localized bank retreat incorporate vertical heterogeneities, complex bank geometries, effects from floodplain vegetation, and ground water pore pressures. These models are capable of thus capturing the mechanical processes that occur during bank erosion and retreat, such as basal undercutting, failure of overlying cohesive sediments including planar,

rotational, and cantilever failures, and ground water sapping (Rinaldi *et al*., 2004; Fox *et al*., 2006; Cancienne *et al*., 2008; Langendoen *et al*., 2009; Pollen-Bankhead and Simon, 2009). However, a limitation of many of these detailed physically-based models of bank retreat is that they are only capable of simulating bank erosion locally, typically within a defined channel cross section, and are therefore unable to model the spatial variability in bank erosion that leads to the planform evolution of meandering rivers.

Traditional theoretical models for long-term river migration rely on two-dimensional analytical treatments that relate the rate of migration to the near-bank excess velocity and a dimensionless erosion coefficient calibrated against field data (Hasegawa, 1977; Ikeda *et al*., 1981). Such models are limited because they operate under the assumption that channel curvature is the primary factor influencing bend migration. Furthermore, many of these models assume a constant channel width, that bank retreat is a product solely of erosion of the bank toe material, and that the resistance properties of the floodplains are spatially homogeneous. While these types of simulations have improved theoretical understanding about the long-term planform evolution of meandering rivers (Motta *et al*., 2012), such models are only able to create relatively simple planform configurations prior to channel cutoff (Güneralp and Rhoads, 2011). However, similar models that incorporate a randomly generated floodplain resistivity throughout the simulation domain are capable of producing complex channel planforms that are comparable to those observed in nature, emphasizing the importance of spatial variability in floodplain resistivity on meander evolution (Güneralp and Rhoads, 2011).

Despite widespread acknowledgment that geotechnical properties of riverbanks and floodplains influence the process dynamics of bank retreat and that spatial variability in bank geotechnical properties partly control the planform evolution of meandering rivers, few studies

have examined through detailed field measurements how spatial heterogeneities in floodplain resistance are related to spatial patterns of bank erosion and bend migration. Furthermore, many of the studies investigating the complex processes driving local bank retreat have focused on relatively small streams and two-dimensional numerical simulations (Simon and Darby, 1997; Simon *et al*., 2000; Simon and Collison, 2001; Fox and Wilson, 2006; Fox *et al*., 2007; Kean *et al*., 2009). As such, the influence of spatial variability of the geotechnical properties of riverbanks and floodplains, including riparian vegetation, on short-term patterns of bank erosion and long-term patterns of planform evolution in large meandering rivers remains poorly understood.

In this chapter, the geotechnical properties of two meander bends on a large meandering mixed bedrock-alluvial river are characterized through detailed field measurements of grain size distribution, cohesive resistance, and critical shear stress necessary for sediment entrainment. Additionally, the role of riparian vegetation on the geotechnical properties of the banks is investigated. The spatial heterogeneities of these properties are investigated and the mechanisms responsible for bank retreat are evaluated throughout each bend. The field measurements are used to inform a physically-based model of bank retreat and the results are compared to short- and long-term patterns of bank erosion to address the importance of floodplain heterogeneity on the planform dynamics of large meandering rivers.

5.2 Study Area

The field site for this research is a series of meander bends on the lower Wabash River near Grayville, IL (Figure 5.1). The lower Wabash River forms the southern boundary between Illinois and Indiana, and within the study reach drains an area of approximately 74070 km^2 with bankfull widths and depths roughly 250-350 m and 6-8 m, respectively. Historic hydrologic data

obtained from a USGS gaging station located roughly 20 km upstream at Mt. Carmel, IL indicate a mean annual discharge of ~880 m^3s^{-1} with a mean annual peak discharge of ~4110 m^3s^{-1}. However, hydrologic conditions for the Wabash River can vary substantially, and during the time period of study ranged from a low discharge of roughly 90 m^3s^{-1} and a high discharge event of roughly 7600 m^3s^{-1}.

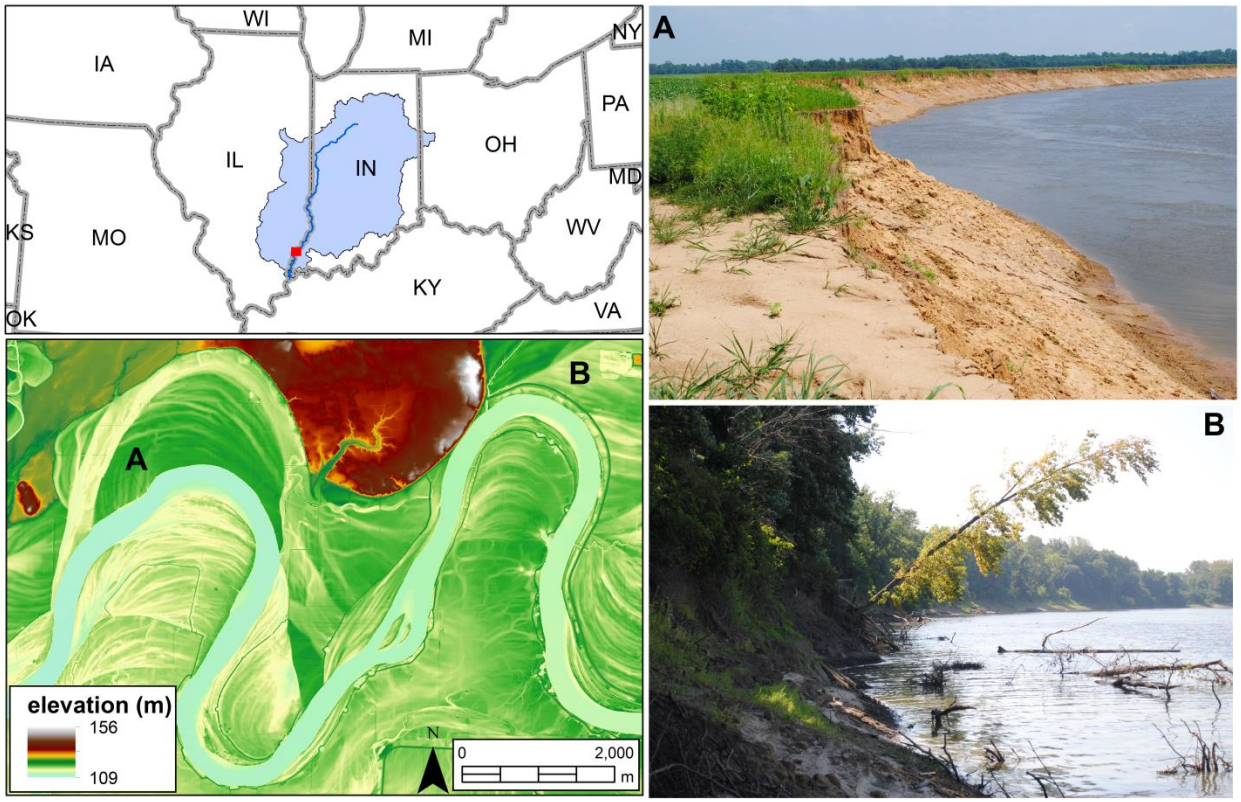

Figure 5.1: Location map of the Wabash River near Grayville, IL. Top left: Location of Wabash River drainage basin in the Midwestern United States. Red box indicates extent area of field site. Bottom left: Airborne LiDAR-derived DEM of the Wabash River near Grayville, IL, showing Maier Bend (A) and Horseshoe Bend (B).

For much of the lower Wabash, the river migrates freely across an alluvial floodplain with the exception of a few locations were the channel erodes into Pleistocene bedrock (Jackson, 1975a). These few previously reported bedrock outcrops supported the classification of the Wabash River as a mostly alluvial meandering river. However, recent extensive mapping efforts, both within the channel and the floodplain, have revealed numerous bedrock outcrops of

Pennsylvanian interbedded shales and sandstones, with a significant amount of exposed bedrock within the channel. These new findings lend support for the reclassification of the lower Wabash River as a mixed bedrock-alluvial river. The lower Wabash River is the only unregulated river of its size in the contiguous United States, making it an ideal natural laboratory for studying the influence of floodplain erosional resistance on rates and mechanisms of erosion.

Two elongate meander bends within the reach near Grayville, IL are the primary focus for the research presented herein. Horseshoe Bend, located at the upstream end of the reach, is approximately 4 km in length with forests along its entire outer bank floodplain and a fairly constant radius of curvature (Figure 5.1). In contrast, Maier Bend, located two bends downstream, is roughly 5 km in length and has agricultural fields on its outer bank floodplain and variable radius of curvature (Figure 5.1). The difference in land cover between these two bends provide a means to evaluate the influence of riparian/floodplain vegetation on the geotechnical properties of the channel banks.

5.3 Methods

The geotechnical properties of the channel banks and floodplain were characterized using a number of field and laboratory techniques. Grain size distributions were determined at several locations around each bend and at different bank elevations for each location. For these analyses, surface grab samples were collected and geo-located using a handheld GPS unit to determine horizontal positioning, while a rod and level survey was used to determine vertical positioning on the bank. Each sample was placed in an oven for a period of at least 12 hours to remove any moisture content, and then the samples were dry-sieved using half-phi scale ranging from -5.0Φ (31.5 mm – coarse gravel) to 4.0Φ (0.063 mm – fine sand). Standard statistical methods were

applied to determine cumulative distribution curves and the mean, standard deviation, and skewness for each sample.

For samples with more than 5% fines by weight (silt and clay sized particles) additional fine-grained analysis was conducted using pipette analysis at the US Department of Agriculture – National Sedimentation Laboratory (USDA-NSL) located in Oxford, MS. The fine-grained samples were added to a sedimentation flask with 200 ml of DI water and a 10 ml sodium hexametaphosphate dispersing solution, and placed in a mechanical shaking table for a minimum of 12 hours. The chemically dispersed fine-grained samples were then added to a pipette water bath set to 29 °C, with a tandem 25-ml Lowy pipette apparatus mounted on a movable carriage allowing for rapid raising and lowering of pipettes. Following 30 seconds of manual stirring, two pipette extractions were performed at 00:01:50 and 03:09:26 and transferred to separate beakers to determine respective weights, thus allowing for three fractions of fine particle size to be determined: coarse silt, fine silt, and clay.

Critical shear stresses required to entrain bank sediments were determined using a submerged hydraulic jet-test (Hanson, 1990) either on *in situ* bank materials in the field or on samples obtained from 4-inch diameter sediment cores collected at various field locations and analyzed in the laboratory. This method impinges a submerged hydraulic jet of known velocity and shear against the surface of the bank material and measurements of the depth of scour are made using a point gauge at specific time intervals. The procedure is continued until scour depth reaches an approximate asymptotic value, and the data were regressed to estimate the critical shear, τ_c (Pa), and erodibility coefficient, k (ms^{-1}), that satisfy the following equation,

$$\varepsilon = k(\tau_0 - \tau_c) \qquad (5.1)$$

where ε is the rate of erosion (ms^{-1}) and τ_0 (Pa) is the applied shear stress acting upon the sediments.

To determine the internal shear strength of the bank materials within the study area, measurements of cohesion and internal friction angle were obtained using a borehole shear tester (BST) in the field and direct shear box tests on 3-inch diameter core samples at USDA-NSL. These two standard techniques apply a given force normal to the failure plane and then apply progressively increasing shear force until failure occurs. This procedure is repeated multiple times with varying normal force until the data can be regressed to estimate the cohesion *c* (kPa) and internal friction angle φ' from the following equation,

$$\sigma_S = \sigma_N tan\varphi' + c \qquad (5.2)$$

where σ_S and ρ_N are the shear and normal stress (kPa), respectively.

Detailed morphologic surveys of the outer banks were conducted using a Topcon GLS-1500 terrestrial LiDAR scanner with maximum sampling frequency ~30 kHz, accuracy of ~5 mm and a grid spacing of 5-10 cm. Surveys were conducted during summer base flow conditions to ensure an optimum amount of subaerially-exposed outer bank face. These high-resolution topographic surveys yielded detailed mapping of vegetation within the channel, on the banks, and on the floodplains, and were capable of imaging exposed tree roots along the outer bank. The surveys also facilitated the delineation of different sedimentary layers within the channel banks through the identification of slope breaks and through variations in point return intensity. The point cloud data from each LiDAR survey were manually classified within ArcGIS into the following categories: ground, low elevation vegetation, medium elevation vegetation, high elevation vegetation, and buildings and infrastructure.

In addition to surveying the outer banks during low flow conditions, near-bank bathymetric surveys during high flow conditions were conducted using a multibeam echo sounding (MBES) system. MBES surveys were performed using a RESON SeaBat 7125SV, dual frequency 200-400 kHz system with an overall depth resolution of ~6mm and a maximum sampling frequency of 60 Hz. This system utilizes 512 beams over a swath of 128° and is capable of beam steering allowing for more focused acquisition of bathymetric data near the channel thalweg and outer bank regions. The MBES survey for Maier Bend was obtained February 2-4, 2012 with a flow discharge of ~2800 m^3s^{-1}, while the survey for Horseshoe Bend was conducted January 18, 2013 during a flood event with flow discharge ~2300 m^3s^{-1}. Post-processing and visualization of the MBES data was performed in Caris HIPS/SIPS. The processed data yielded information that was used to map in detail bedrock exposed within the channel.

The geotechnical properties of the banks and floodplains obtained through the detailed field and laboratory measurements were incorporated into a physically-based model of bank erosion to evaluate the rates and mechanisms of bank retreat spatially throughout the study area. The Bank Stability and Toe-Erosion Model (BSTEM) (US Dept. Agriculture) is a multi-layer and multi-component *factor of safety* model that estimates mechanical bank stability based on the ratio between resisting and driving forces acting on a section of channel bank as,

$$f_s = \frac{F_c + F_{pw} + F_f + F_p}{F_g} \qquad (5.3)$$

where f_s is the factor of safety, F_c is the cohesive resistance of the bank material (kPa), F_{pw} is the pore water pressure along the shear plane (kPa), F_f is the frictional force from the weight of soil acting along the failure plane (kN), F_p is the hydrostatic confining pressure from the water surface elevation of the streamflow (kNm^{-1}), and F_g is the gravitational force acting on the bank

material (kN) (Figure 5.2). This model is capable of handling up to five horizontal soil layers, vertical tension cracks and cantilever failures.

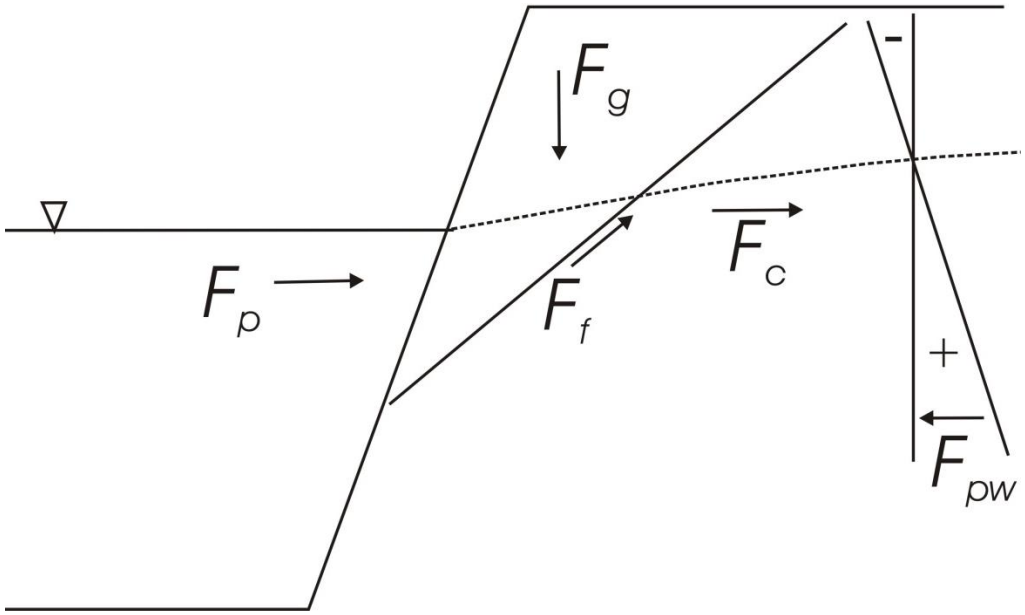

Figure 5.2 Force balance diagram for bank stability and factor of safety. Dashed line represents groundwater elevation. F_p is the hydrostatic confining pressure from the streamflow, F_g is the gravitational force acting on the bank material, F_f is the frictional force of the bank material along the failure plane, F_c is the cohesion of the bank materials, and F_{pw} is the pore water pressure.

The toe-erosion component of BSTEM is modeled using an estimate of the average boundary shear stress acting on the different layers prescribed within the simulation. Values of shear stress are estimated along the boundary using a modification of the ray-isovel approach where the near-bank flow area is subdivided into areas acting upon small segments of wetted perimeter. The estimated shear stresses are then given by the following depth-slope product,

$$\tau_{0i} = \gamma_w R_i S \qquad (5.4)$$

where τ_0 is the applied shear stress (Pa), γ_w is the unit weight of water (kNm^{-3}), R is the hydraulic radius or flow area divided by wetted perimeter, S is the reach-averaged slope, and i denotes the subdivision of bank.

A subroutine within BSTEM called RipRoot (Pollen and Simon *et al*., 2005; Pollen, 2007) is used to estimate the mechanical effects of riparian vegetation on bank stability. Modifying previous work by Wu *et al*. (1979), RipRoot employs a fiber-bundle model that accounts for the progressive breaking of different sized roots with different tensile strength and estimates the increase in shear strength due to vegetation as,

$$c_r = \frac{1}{A}\sum_{n=1}^{n=N}(A_r T_r)_n[\sin(90-\psi) + cos(90-\psi)tan\varphi'] \qquad (5.5)$$

where c_r is the additional cohesion due to vegetation (kPa), A is the area of shear surface (m^2), N is the total number of roots in the shear plane, A_r is the area of the roots in the shear plane (m^2), T_r is the tensile strength of the roots (kPa), and

$$\psi = \tan^{-1}\left(\frac{1}{\tan\theta + \cot\chi}\right) \qquad (5.6)$$

where θ is the angle of shear distortion in degrees and χ is the initial orientation angle of the fiber relative to the shear plane. The additional cohesion due to riparian vegetation depends on the type of plant species and the root characteristics of these plants. RipRoot includes values of root tensile strength and root density for a variety of common riparian species, allowing users to create a representative riparian assemblage of species based on the observed plant distributions, thus estimating the average additional cohesion due to multiple riparian plant species.

Short-term rates of outer bank erosion were determined using repeat terrestrial LiDAR surveys conducted annually for three consecutive years (2011 – 2013). Bank surfaces were interpolated using an inverse distance weighting scheme for the LiDAR point cloud data, and volumetric rates of erosion were determined between each annual survey by performing a

difference calculation in ArcGIS. These short-term rates of erosion are compared to the results from the model simulations and to long-term rates of channel migration to investigate the influence of floodplain heterogeneity on the spatial patterns of planform change. Additionally, long-term rates of channel migration were estimated through analysis of historical aerial photography from 1938, 1980, 1998, and 2012. Historic aerial photographs were georeferenced using 2009 orthophotographs in ArcGIS. The channel banks were then digitized for each time interval and the average rate of migration was determined for the entire time period of analysis.

5.4 Results:

5.4.1 Spatial extent of bedrock and vegetation

Detailed bathymetric and morphologic surveying of the study area revealed outcrops of bedrock within the channel that had previously been unmapped. On the downstream limb of Maier Bend, a relatively small outcrop of bedrock, measuring roughly 9800 m2, was mapped within the channel along the outer bank using the MBES and terrestrial LiDAR (Figure 5.3). Comparisons between the mapped bedrock within the channel and geologic bedrock maps of the study area suggest that the bedrock exposed within the channel is part of the Pennsylvanian Bond Formation, comprised of interbedded shales and sandstones. Visual inspection of the outcrop during low flow conditions confirmed the lithology of the bedrock as interbedded shales and sandstones that dip slightly to the north, and weather into cobble-sized angular slabs (Figure 5.4). While the bedrock outcrop on the downstream limb of Maier Bend most certainly extends northward into the outer bank floodplain, the elevation of the exposed bedrock does not exceed an elevation of ~113 m (Figures 5.4-5.5). Thus, the bedrock is a low platform within the channel and is covered by alluvial deposits up to four meters thick where it extends beneath the adjacent floodplain.

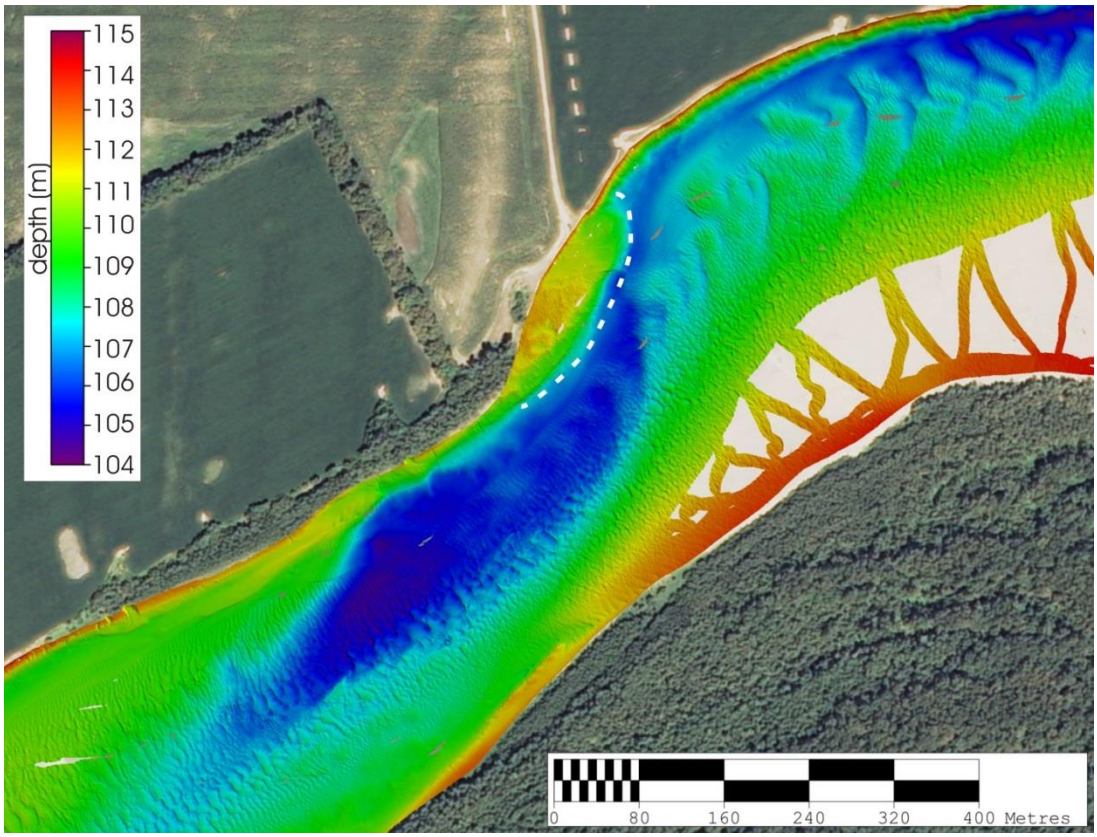

Figure 5.3: MBES bathymetric survey revealing bedrock outcrop forming a platform within the channel on the downstream limb of Maier Bend. Extent of bedrock into the channel approximated by white dashed line.

Figure 5.4: Photograph of bedrock outcrop exposed along outer bank of downstream limb of Maier Bend. Flow from left to right in photograph.

Bedrock is also exposed along the downstream limb of Horseshoe Bend along the outer bank where the bend has migrated into a prominent ridge that can be seen on both topographic maps and airborne LiDAR images (Figure 5.1). While bedrock exposure at this location has been reported previously (Jackson, 1975a), the full extent of bedrock exposure was unknown. Detailed bathymetric maps produced from the MBES surveys reveal the exposed bedrock within the channel to be quite extensive, covering an area of roughly 146,800 m^2 from the outer half of the channel and beginning just downstream of the bend apex region and continuing through the downstream inflection point of the bend (Figure 5.5). In contrast to the bedrock outcrop on Maier Bend, the bedrock at Horseshoe Bend is part of a valley sidewall, constraining the extent of floodplain and lateral channel migration locally (Figure 5.6). Comparisons with geologic maps of the area suggest that the exposed bedrock is part of the Pennsylvanian shales of the Mattoon Formation.

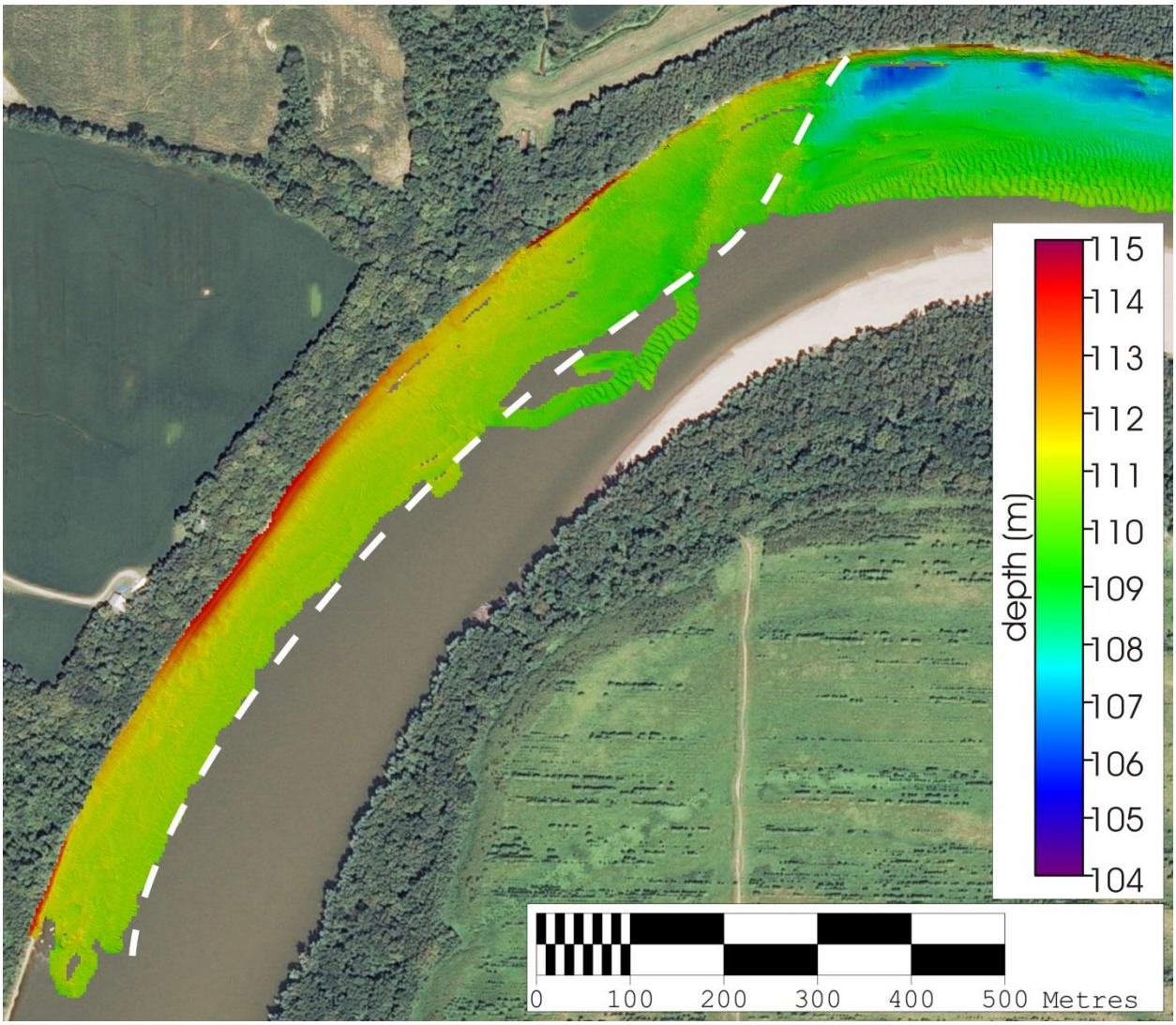

Figure 5.5: MBES bathymetric survey revealing bedrock exposed within channel on downstream limb of Horseshoe Bend. White dashed line delineates approximate extent of bedrock as mapped from MBES data.

Figure 5.6: Photograph looking downstream along outer bank of Horseshoe Bend within the downstream limb showing exposed bedrock outcrop of the valley wall.

The floodplain along the outer bank of Horseshoe Bend upstream of the bedrock ridge is covered by riparian forest consisting of sycamores, maples, and oaks. Field observations and detailed inspection of the terrestrial LiDAR surveys show that tree root wads exposed along the outer bank face extend to typically 1.5 – 2 meters below the top of bank and are dense within the top 1 meter of bank (Figure 5.7). Aerial photography dating back to 1938 confirms that the outer bank floodplain along Horseshoe Bend has been continuously covered with riparian forest. Using a minimum forest age of 80 years along with the common tree species of this forest, RipRoot was used to determine the enhancement of cohesion by root tensile strength. The results from RipRoot vary depending on the bulk grain size distribution of the bank sediments and the rooting depth of the vegetation, which are inputs to the model. Application of RipRoot to conditions at

locations HSB1, HSB4, and HSB6 yielded increased cohesion due to vegetation of 15.1, 12.4, and 15.1 kPa, respectively.

Figure 5.7: Photograph of exposed tree roots along outer bank of Horseshoe Bend showing density of root wad. Length of metered tape in photograph ~163 cm.

5.4.2 Outer bank grain size distributions and morphology

Plots of depth-averaged median grain size (D_{50}) obtained from the grain size distributions around Maier and Horseshoe bends show that, generally, the outer bank sediments along Maier Bend are coarser than the outer bank sediments along Horseshoe Bend (Figure 5.8). Spatially averaged, the mean depth-averaged grain size for Maier Bend is roughly 0.43 mm whereas for Horseshoe Bend the mean grain size is approximately 0.20 mm. However, within each bend values of D_{50} also vary spatially, ranging from 0.1 – 0.88 mm for Maier Bend and 0.03 – 0.59 for Horseshoe Bend.

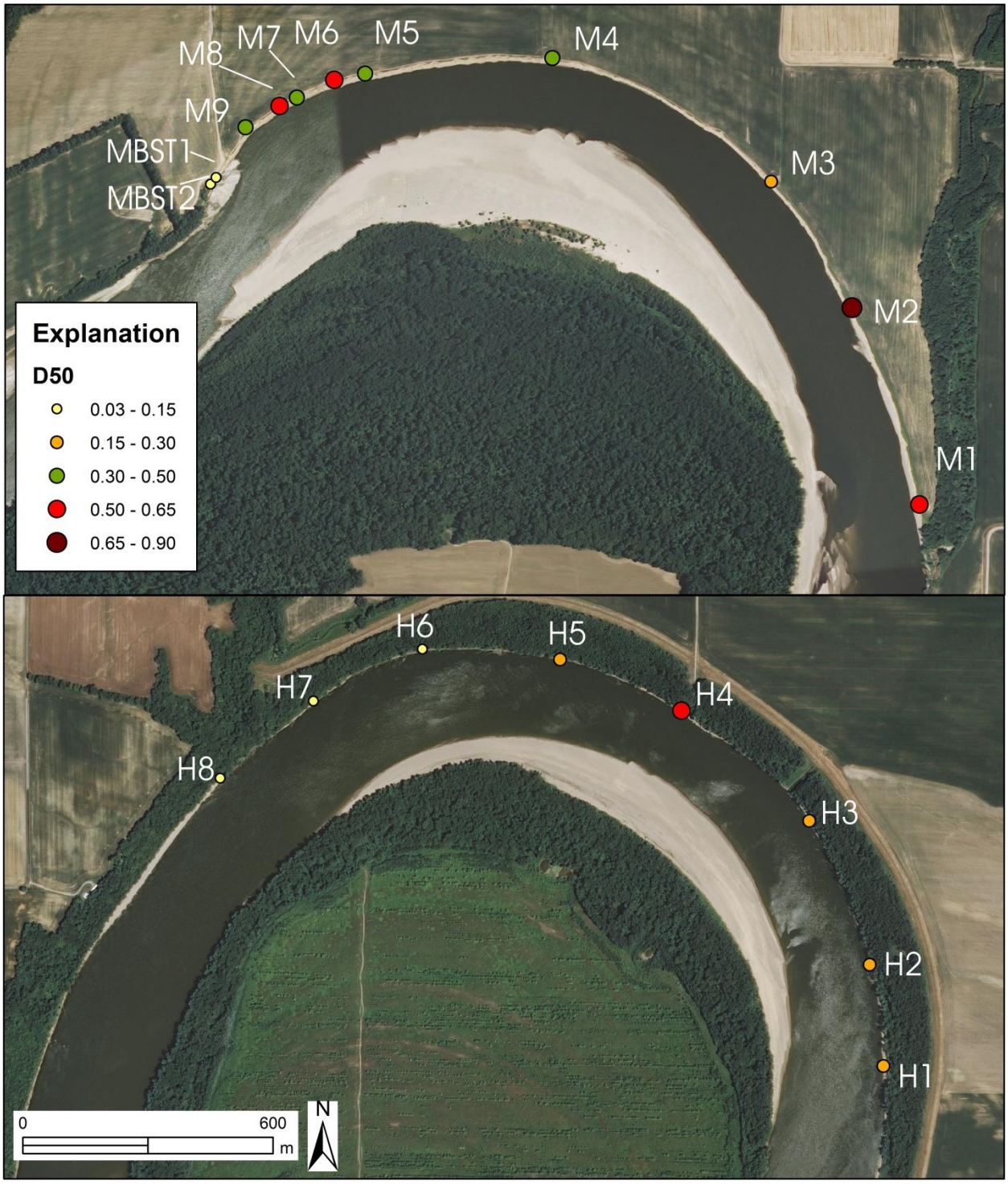

Figure 5.8: Spatial pattern of depth-averaged median grain size (*D50*) around the outer bank of Maier Bend (top) and the outer bank of Horseshoe Bend (bottom), Wabash River.

Profiles of median grain size over depth at each location around Maier and Horseshoe bends illustrate the vertical heterogeneity in outer bank sediments (Figure 5.9). The profiles for both bends show a general fining-upward trend for values of D_{50} and that sediments near the base of the bank for Maier Bend are typically coarser than those for Horseshoe Bend. For Horseshoe Bend, the first three profiles on the upstream limb of the bend (HS1-HS3) show fairly constant values of D_{50} for elevations below ~114.5 m and then grain size values quickly decrease toward the top of the bank (Figure 5.9). However, through the bend apex and entrance to the downstream limb, the profiles along Horseshoe Bend show a much quicker decrease in grain size with increasing bank elevation, and at an elevation ~114 m the median grain size is silt. In contrast, the profiles for Maier Bend are more consistent around the bend and show a more gradual decrease in median grain size as bank elevation increases (Figure 5.9).

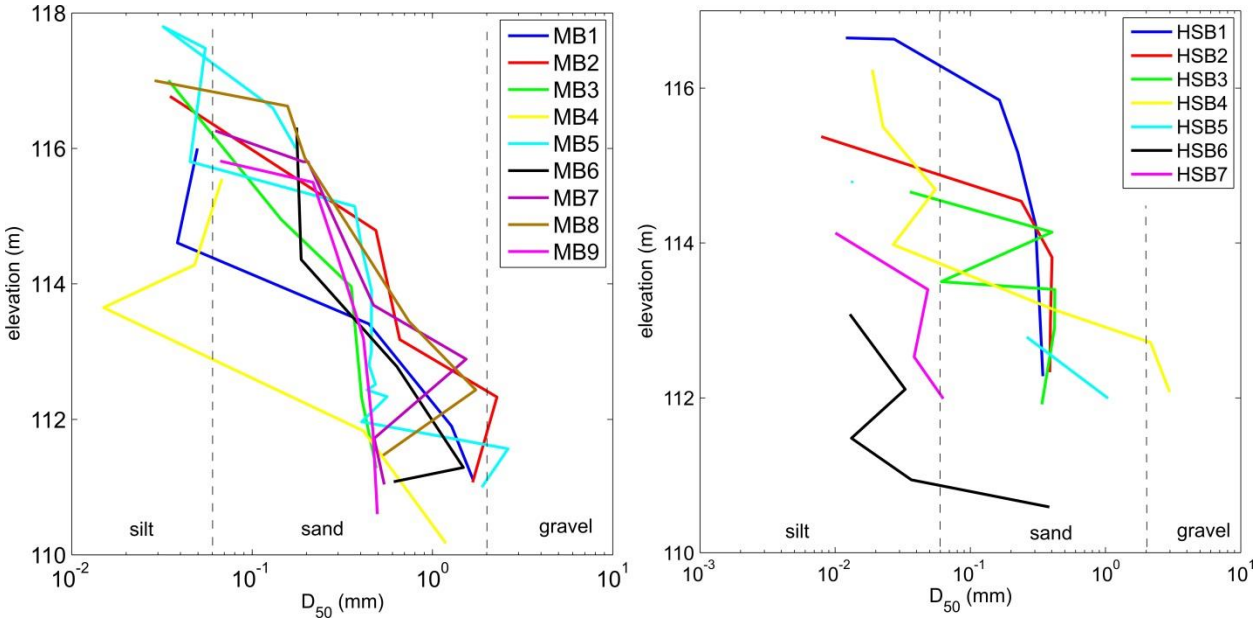

Figure 5.9: Profiles of median grain size (*D50*) for locations around Maier Bend (left) and Horseshoe Bend (right).

To investigate the spatial heterogeneity for each bend in more detail, the relative contribution of clay, silt, sand and gravel for each bank sample were plotted against the cross-

sectional bank profiles extracted from the terrestrial LiDAR surveys. The terrestrial LiDAR surveys of Maier Bend extend from near the upstream location M1 [420667E, 4238971N UTM16N] to downstream of location MBST3 [418961E, 4239741N]. Between locations M1 and M2, the bank sediments near the base of the bank are roughly an even mixture of sand and gravel (Figure 5.10a-b). This relatively coarse layer extends vertically to a bank elevation of at least 113 m and corresponds with transverse bank slopes of ~11° at MB1 and ~22° at MB2 (Figure 5.10A-B). At MB1, the sample collected at ~113.4 m, the bank sediments are composed mostly of sand (~72%) and correspond to a break in transverse slope. Above this elevation the bank sediments become progressively finer and are roughly 50% silt and ~15% clay, with bank slopes ranging from 50° - 70° (Figure 5.9A). At MB2, the bank sediments show high sand (88%) content at an elevation of 114.8 m overlain by a ~2 m vertical layer of silt (75%) and clay (20%) (Figure 5.10B).

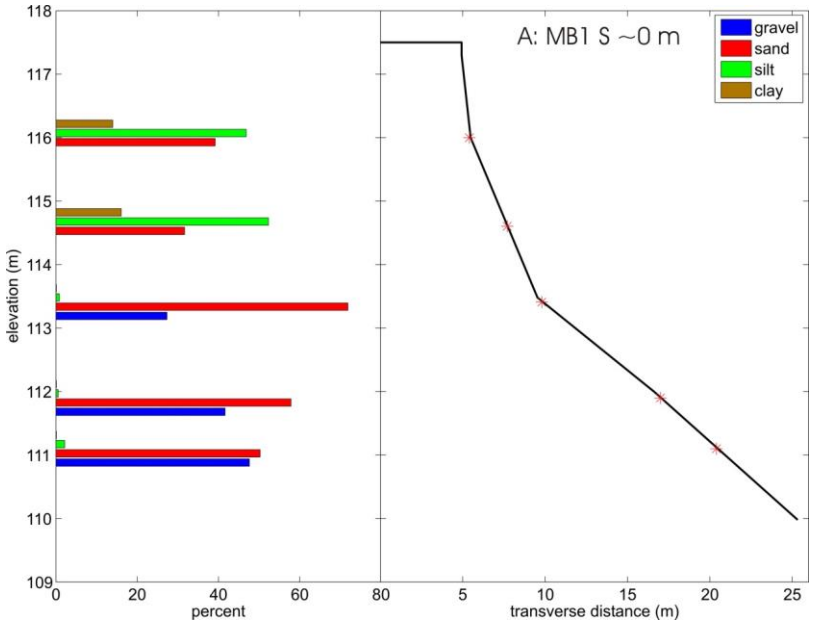

Figure 5.10: Bar charts showing percentages of clay, silt, sand and gravel at different bank heights for Maier Bend, plotted with cross-sectional bank profiles extracted from terrestrial LiDAR surveys. Streamwise distance from farthest upstream location identified.

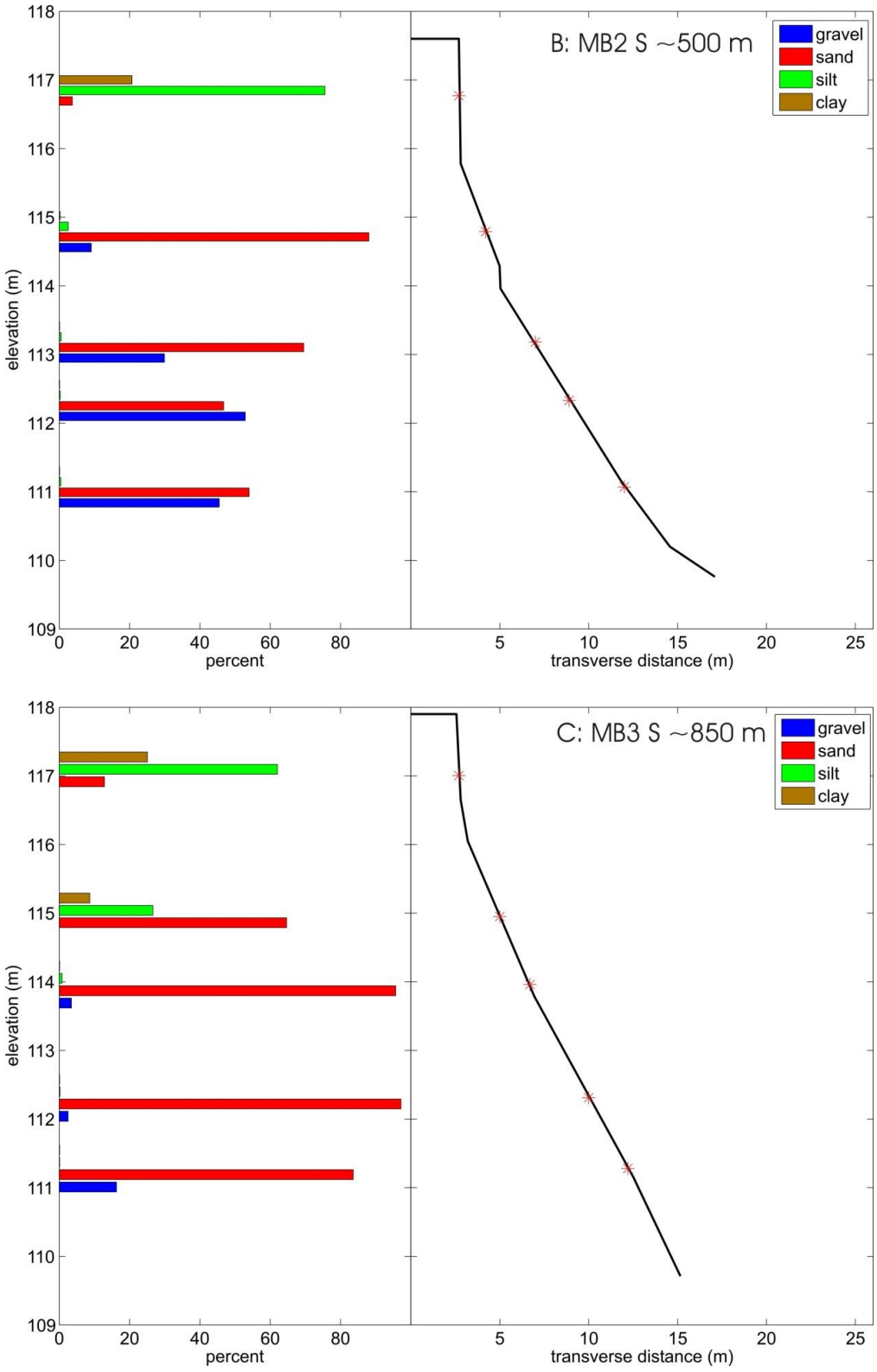

Figure 5.10: (cont.)

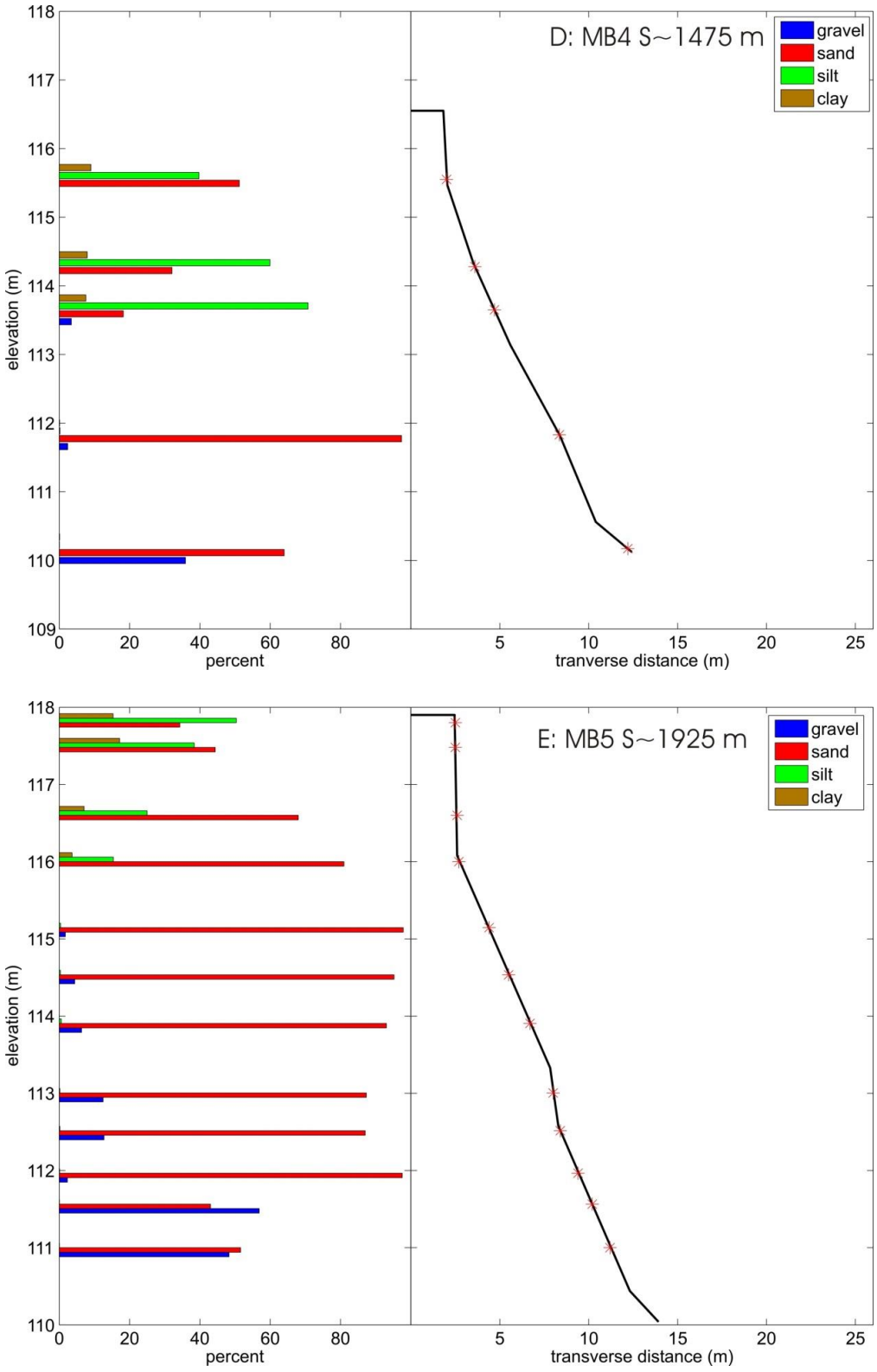

Figure 5.10: (cont.)

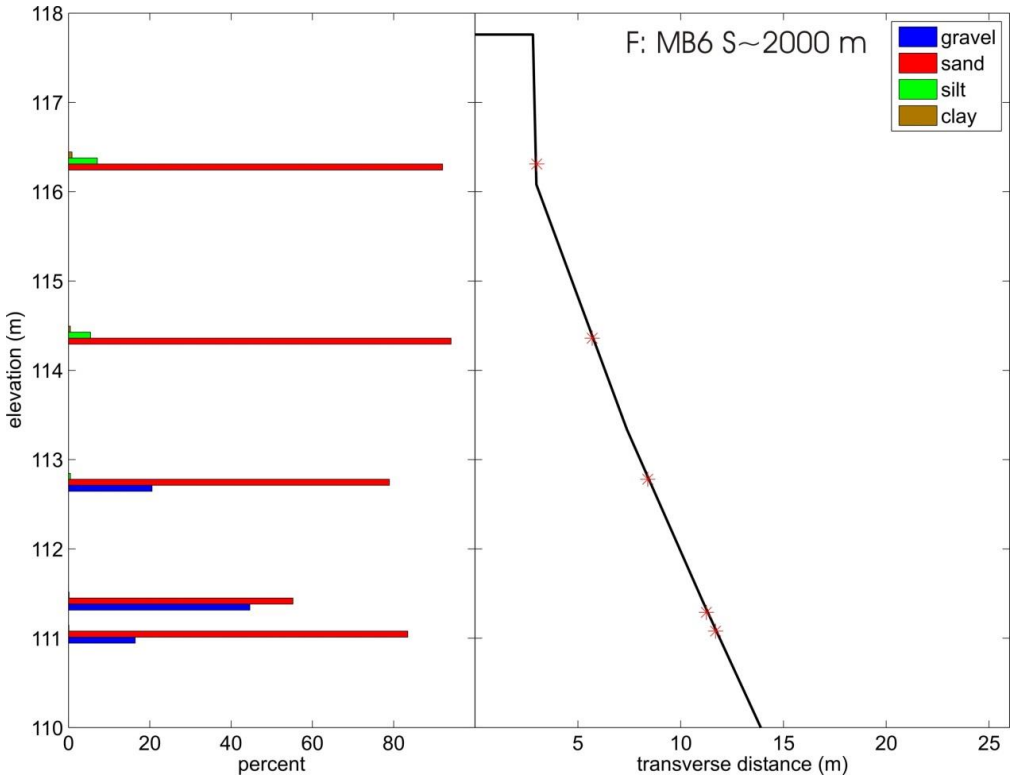

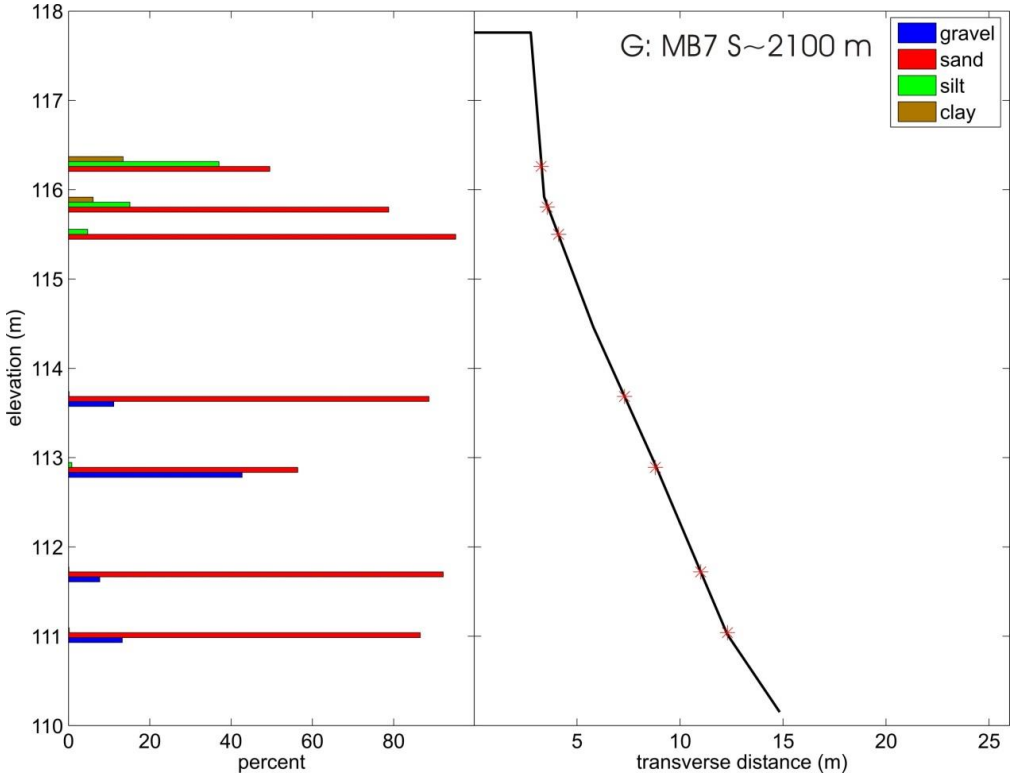

Figure 5.10: (cont.)

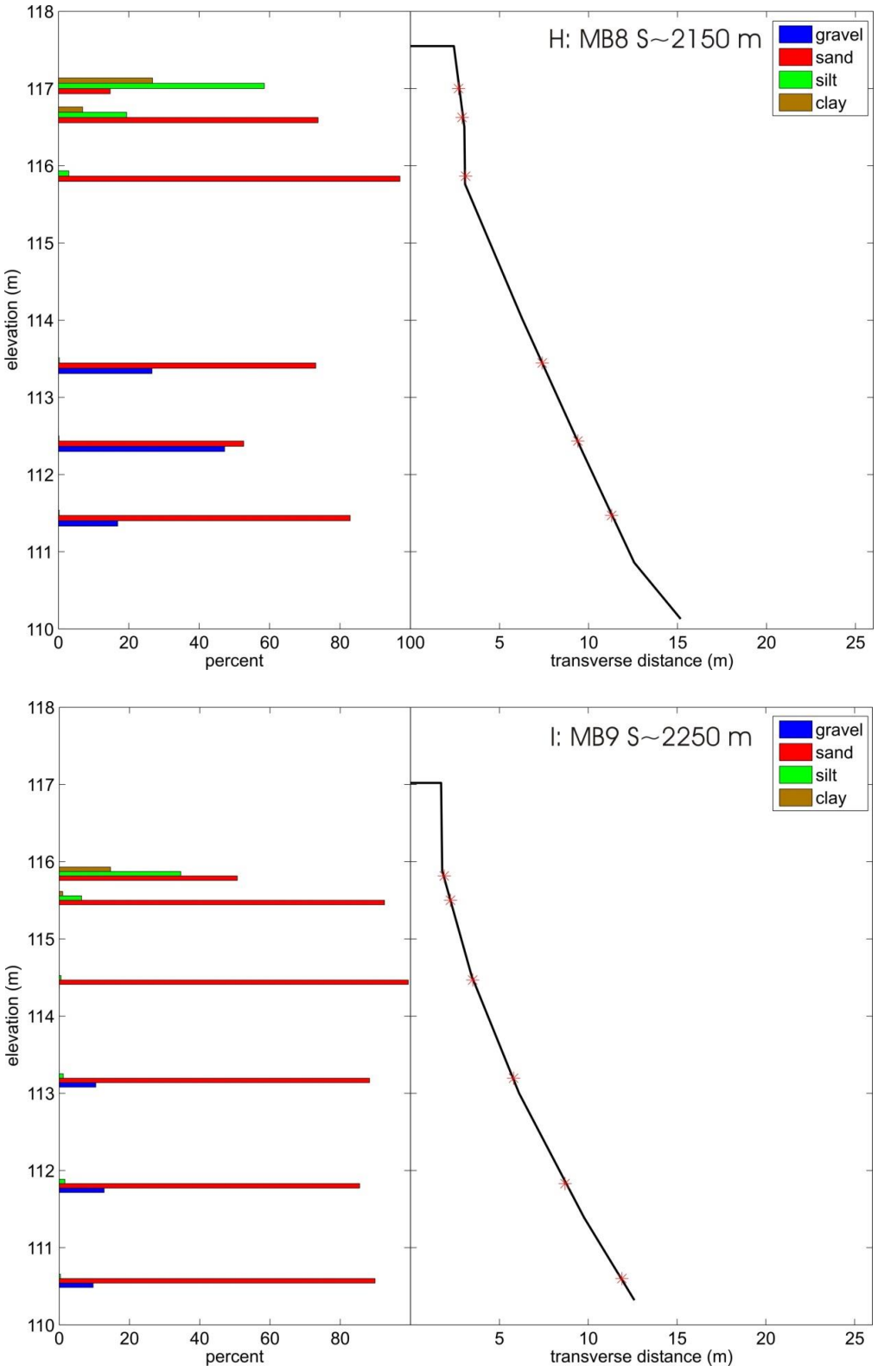

Figure 5.10: (cont.)

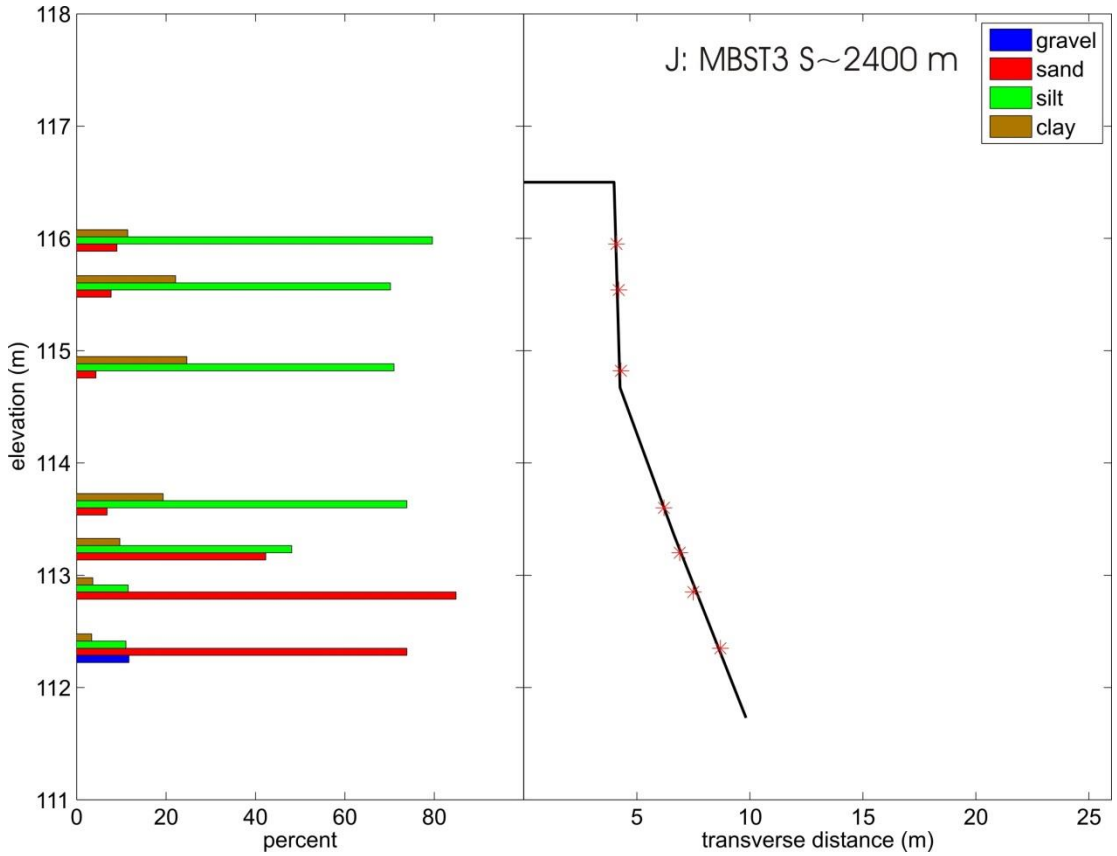

Figure 5.10: (cont.) Bar charts showing percentages of clay, silt, sand and gravel at different bank heights for Maier Bend, plotted with cross-sectional bank profiles extracted from terrestrial LiDAR surveys. Streamwise distance from farthest upstream location identified.

The bank sediments near the base of the banks at locations MB3 and MB4 have lower percentages of gravel than upstream and instead are composed primarily of sand with percentages ranging from ~60% to 97% (Figure 5.10C-D). As distance increases through the apex region from MB3 to MB5, the percentage of gravel near the base of the bank increases from ~16% to ~50% (Figure 5.10C-E). Within the apex region, the thickness of the high-sand content layer is 3-5 m and this layer has a slope angle of roughly 30°. The sand layer is overlain by 2-3 m of fine-grained sediments with silt content as high as 70% (MB4) and clay content as high as 25% (MB3). Slope angles for the overlying layer (60° – 90°) are much steeper than those for the sand layer.

Downstream of the bend apex the percentage of gravel near the base of the banks increases, reaching percentages as high as 47% (MB8) (Figure 5.10F-H). The thickness of the sand and gravel layer varies between MB6 – MB8, but gravel typically is not present in samples above a bank elevation of ~113.5 m. At locations MB7 and MB8 the break in slope at an elevation of ~116 m corresponds well with the change in bank composition from primarily sand to higher percentages of silt and clay (Figure 5.10G-H). Location MB9 shows a similar break in slope at an elevation of 116 m, however below this elevation the banks are composed almost entirely of sand with percentages reaching as high as 99% (Figure 5.10I). The sample at the location farthest downstream (MBST3) is located above the bedrock outcrop and is quite different compared to those at the other locations around Maier Bend. Here, measureable amounts of clay occur throughout the entire profile, with a clay percentage of ~3% at an elevation of ~112.3 m, an elevation just above the bedrock (Figure 5.10J). Gravel was not present in samples obtained above 112.5 m, and at bank elevations greater than 113.5 m the composition of the sediments is predominately silt (~70%) and clay (~20%) corresponding to bank slopes ~85°. Additionally, MBST3 is located above the outcrop of bedrock, and thus does not extend below an elevation of roughly 112 m (Figure 5.10J).

The bank sediment compositions and profiles for Horseshoe Bend are quite different from the composition-profiles for Maier Bend, and also exhibit contrasting spatial variability in material properties. Profiles at locations along the entrance to Horseshoe Bend contain only minor amounts of gravel with percentages less than 4% for HSB1 – HSB3 (Figure 5.11A-C). Material between 112 – 114 m for these first three locations is composed almost entirely of sand with percentages higher than 95%. At elevations above 115 m, the bank sediments consist of increasingly higher percentages of silt and clay, with clay percentages reaching 41% at HSB2

(Figure 5.11B). Transverse bank slopes for these three locations show a trend similar to the upstream locations along Maier Bend, with the lowest slope angles at the farthest upstream location HSB1 (~18°) and angles at HSB3 increasing to ~33° (Figure 5.11A-C).

Within the apex region of the bend the sediments near the base of the bank become coarser than upstream and have gravel percentages between 40% - 60% for locations HSB4 and HSB5 (Figure 5.11D-E). Although the amount of gravel increases near the base of the bank, the thickness of the exposed gravel layer is relatively small (~1 m). No appreciable amounts of gravel are found in the profiles above an elevation of 113 m, where the percentages of silt and clay increase to an average of 60% and 20%, respectively, and generally correspond to an increase in bank slope (Figure 5.11D-E). Bank heights near the apex are also the greatest within the bend, with top of bank elevations exceeding 117 m.

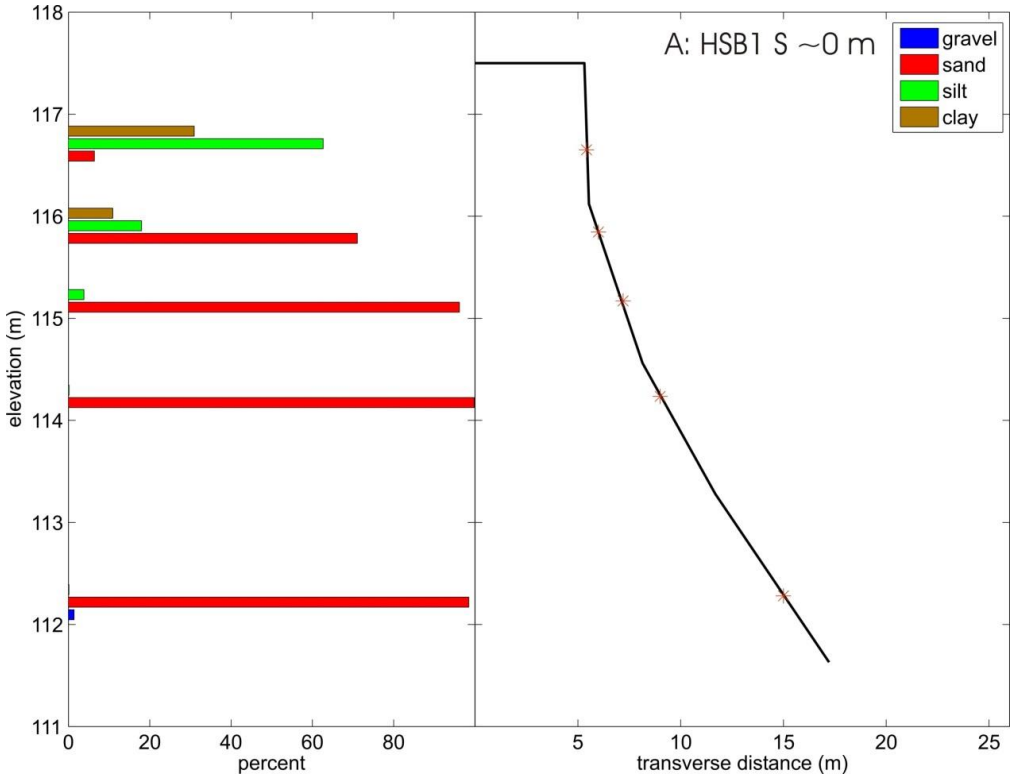

Figure 5.11: Bar charts showing percentages of clay, silt, sand and gravel at different bank heights for Horseshoe Bend, plotted with cross-sectional bank profiles extracted from terrestrial LiDAR surveys. Streamwise distance from farthest upstream location identified.

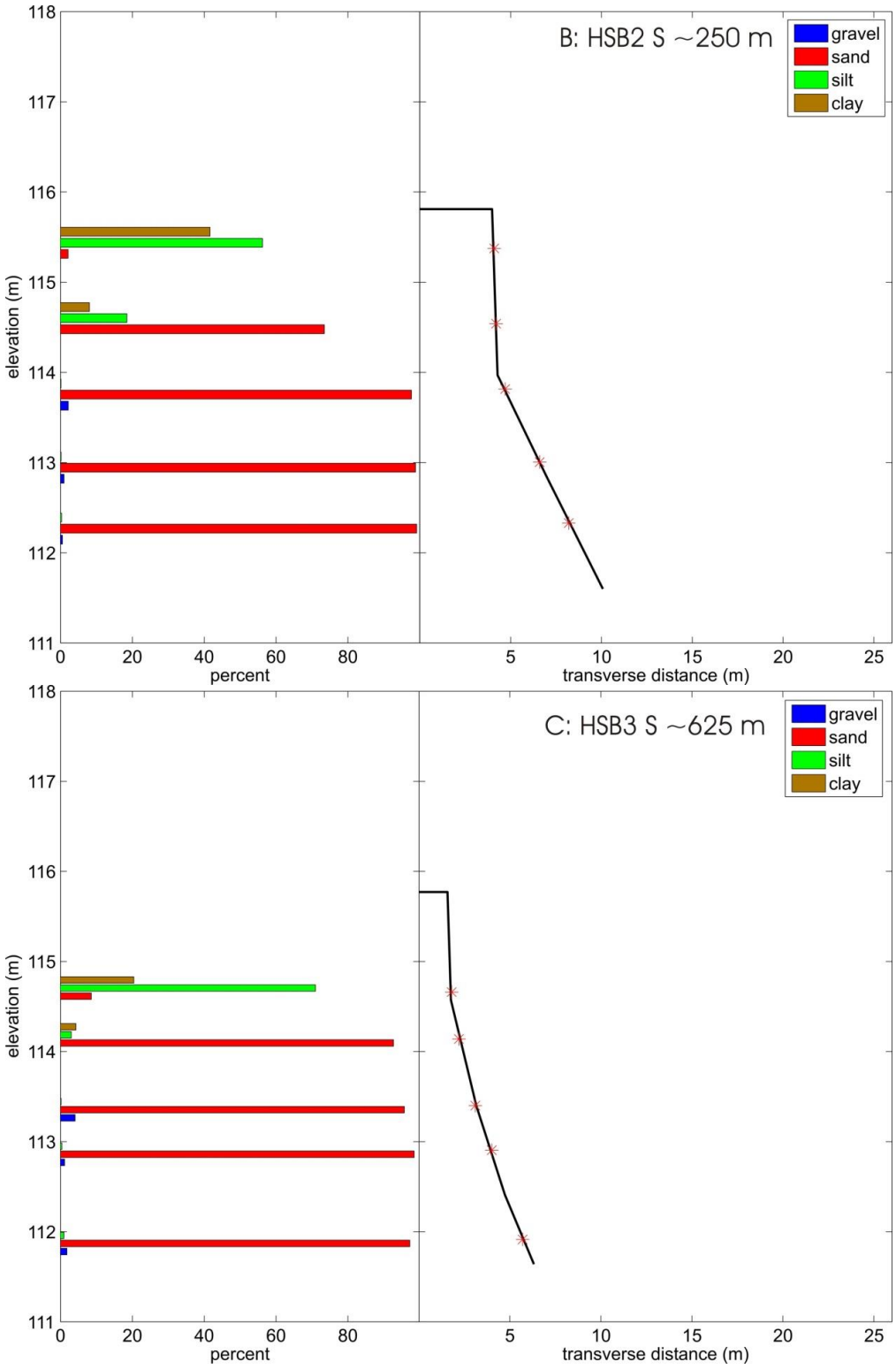

Figure 5.11: (cont.)

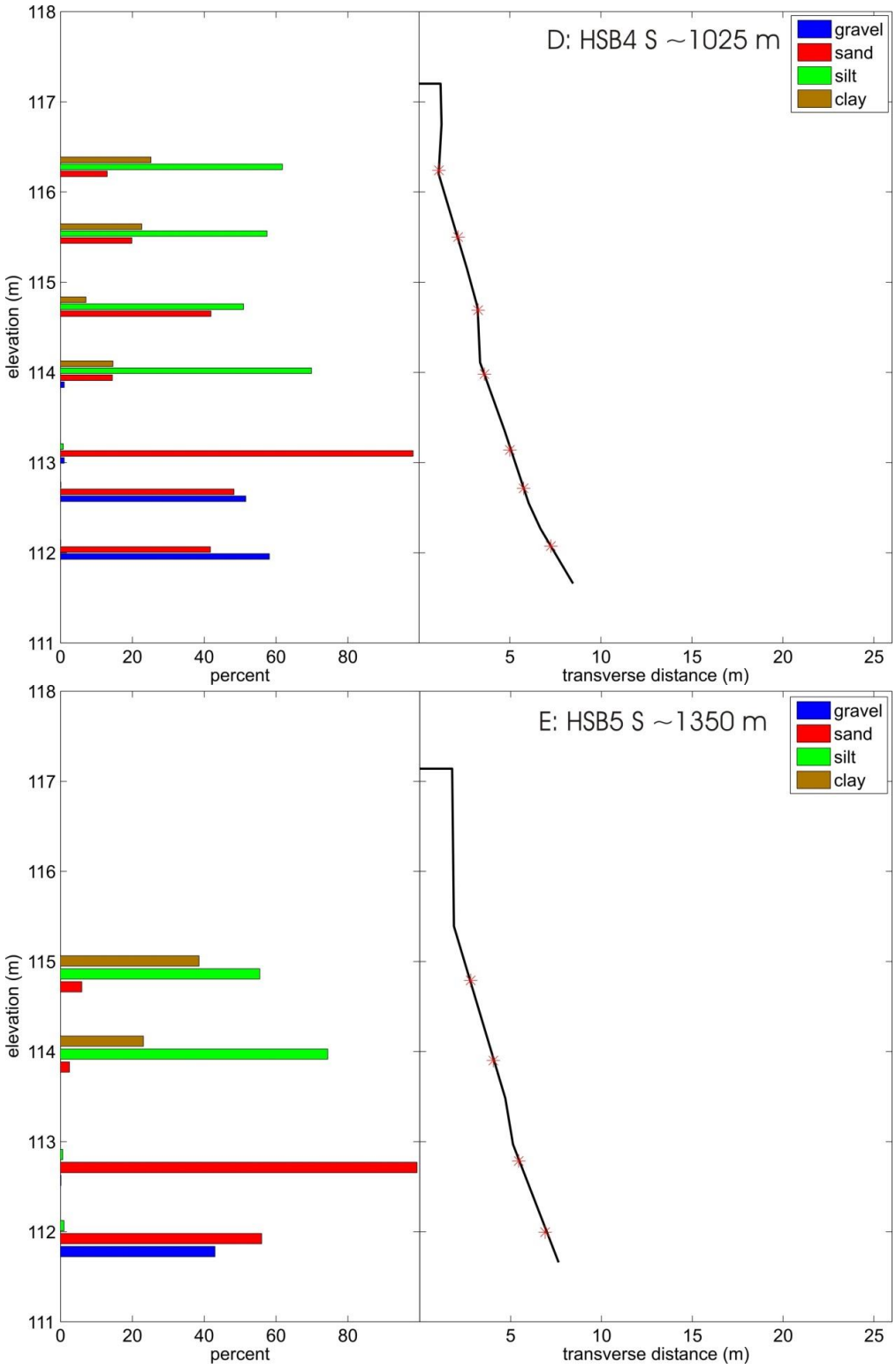

Figure 5.11: (cont.)

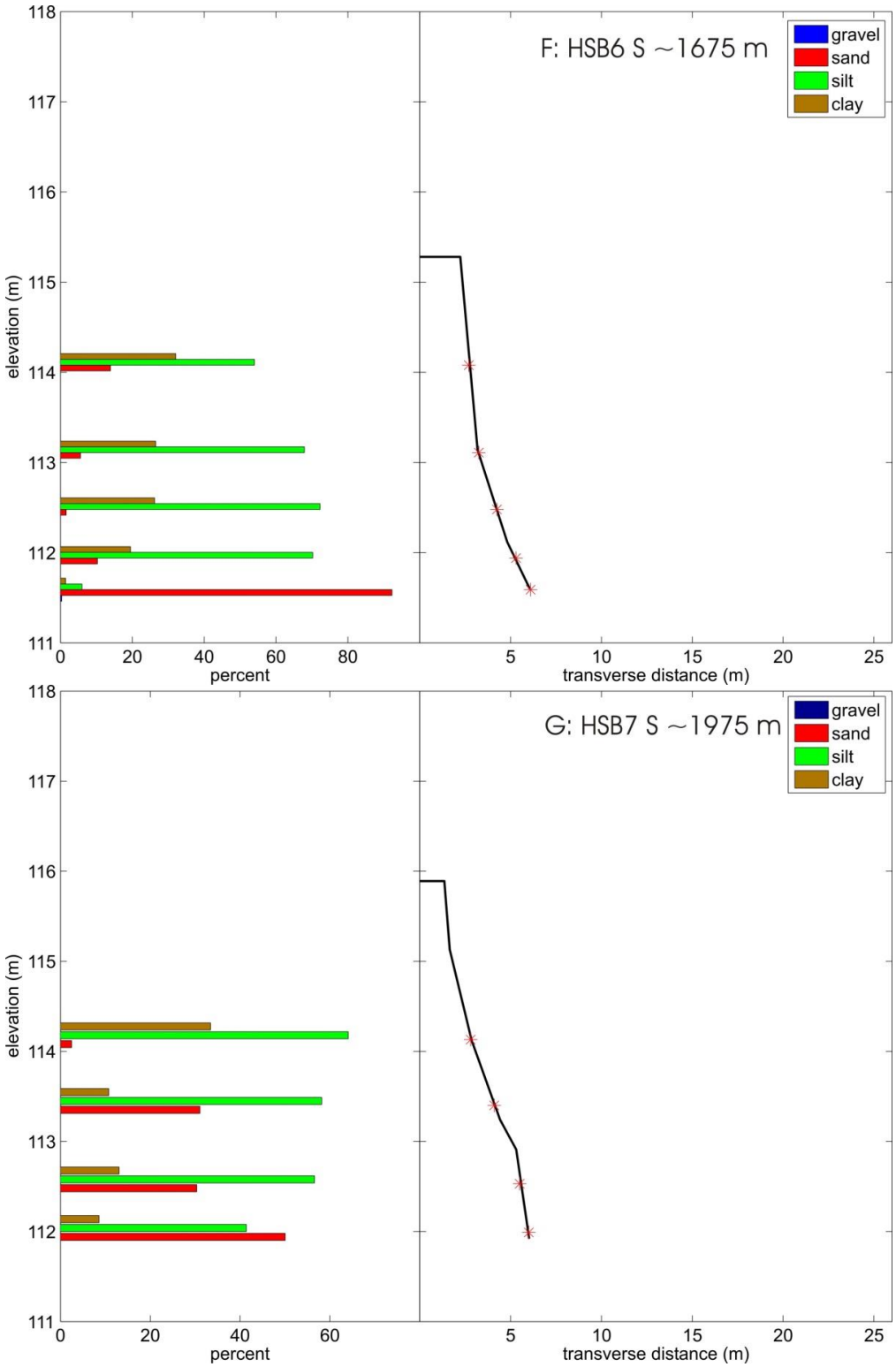

Figure 5.11: (cont.) Bar charts showing percentages of clay, silt, sand and gravel at different bank heights for Horseshoe Bend, plotted with cross-sectional bank profiles extracted from terrestrial LiDAR surveys. Streamwise distance from farthest upstream location identified.

Downstream of the bend apex region, the height of the banks decreases to elevations between 115-116 m (Figure 5.11F-G), similar to bank heights on the upstream limb of the bend. The composition of sediments near the base of the bank downstream of the apex lacks any considerable amount of gravel. At location HSB6, the base of the bank is composed of more than 90% sand and ~6% silt (Figure 5.11F), whereas at HSB7 the sediments near the base of the bank are composed of ~50% sand, ~41% silt, and ~9% clay (Figure 5.11G). At these two locations, the majority of the bank profile (~4 m) is composed of more than 50% silt with percentages of clay reaching as high as ~33%, producing a steep bank profile over the entire bank height.

5.4.3 Geotechnical characteristics of outer bank materials

The geotechnical properties of the bank sediments that are used as input model parameters in BSTEM are: 1) friction angle φ' (degrees), 2) cohesion *c*' (kPa), 3) saturated unit weight γ_s (kNm^{-3}), 4) critical shear stress τ_c (Pa), and 5) erodibility coefficient *k* (cm^{3}N^{-1}s^{-1}). Although BSTEM offers built-in estimates of these parameters based on a bulk characteristic grain size (e.g. coarse rounded sand, fine angular sand), measured estimates of the site-specific geotechnical properties of the bank sediment should result in the most accurate model simulations. In the following section, regression analyses are applied to field and laboratory measurements of the geotechnical bank properties to establish relationships that serve as inputs to the BSTEM model.

Data from the hydraulic jet tests performed in the field and in the laboratory were used to estimate the critical shear stress and erodibility coefficients by regressing values of applied shear stress against rate of erosion (Figure 5.12). The critical shear stress values obtained from this method were then plotted against the clay content (%) determined from particle size analysis. The results show clay content is positively related to critical shear stress, indicating that bank

materials with high clay content require higher critical shear stress values for entrainment than bank sediments with low clay content (Figure 5.13). Furthermore, plotting the erodibility coefficient against estimated critical shear stress shows that this coefficient is inversely related to the critical shear stress (Figure 5.14).

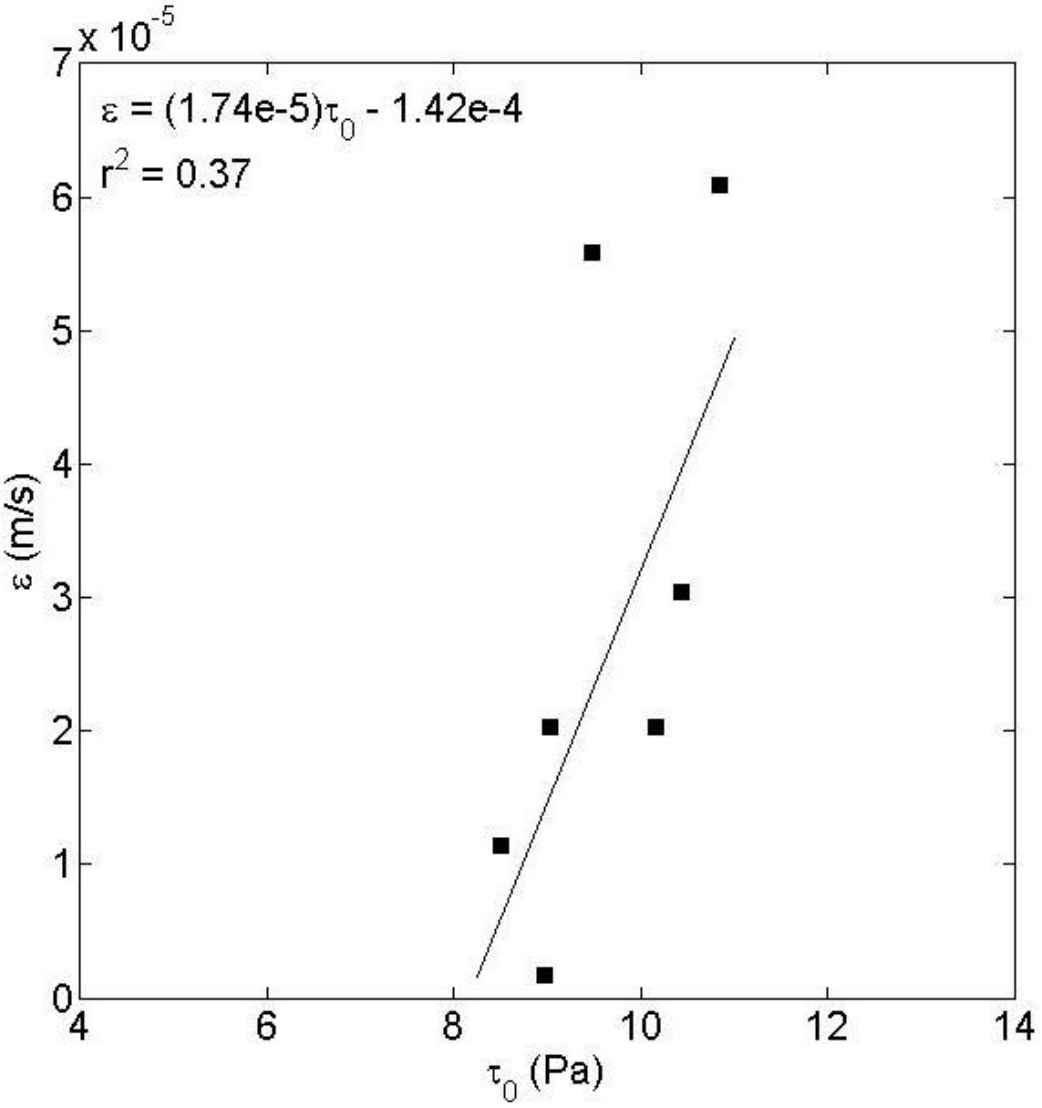

Figure 5.12: Results from hydraulic jet test for location Horseshoe Bend HS2 at a bank depth of 1.5 meters showing applied shear stress τ_0 against erosion rate ε. The slope of the linear regression line corresponds to the erodibility coefficient *K* and the x-intercept corresponds to the critical shear stress τ_c necessary for entrainment.

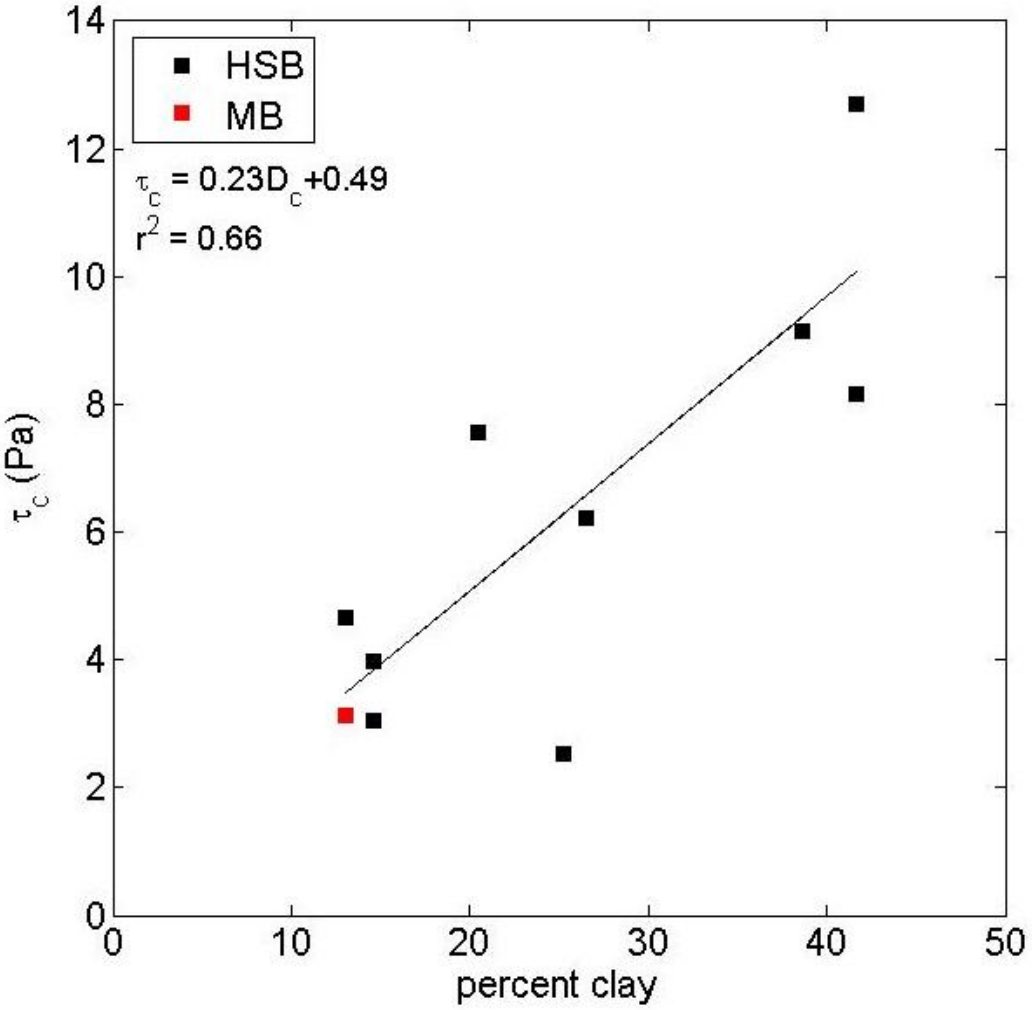

Figure 5.13: Relationship between clay content and critical shear stress τ_c estimated from hydraulic jet tests.

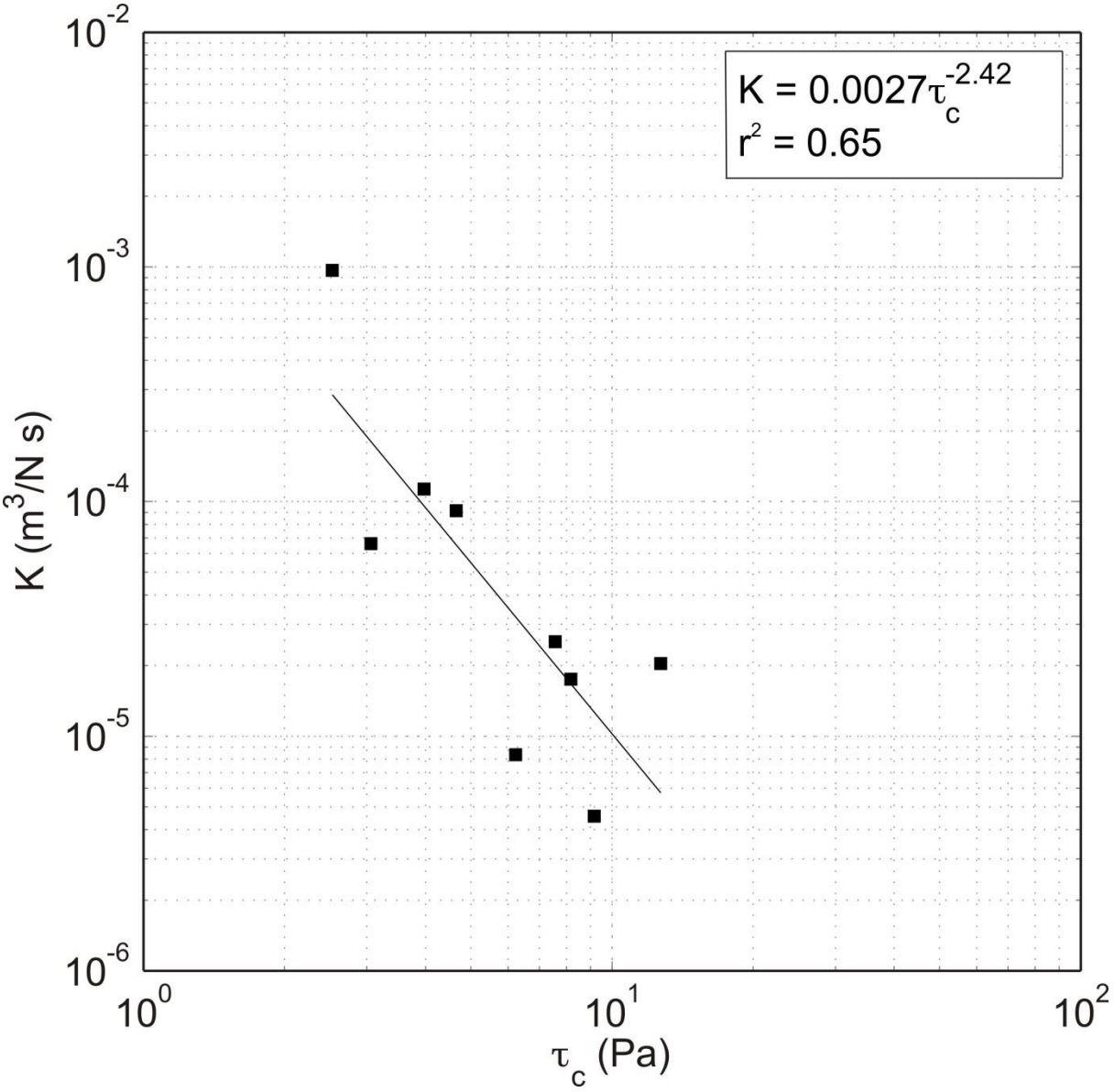

Figure 5.14: Relationship between estimated critical shear stress values τ_c and erodibility coefficient *K* for bank sediments around Horseshoe Bend.

To investigate the spatial variability in erodibility of outer bank sediments around Maier and Horseshoe bends, depth-averaged values of clay content were determined. The results show that generally values of depth-average clay content around Horseshoe Bend are higher than those for Maier Bend (Figure 5.15). However, the data also show that clay content varies within each bend as well. This variability is most evident for Maier Bend, where depth-averaged clay percent

ranges from 2.5 – 13.8 %, for locations M9 and MBST2 respectively, over a distance of only ~150 meters (Figure 5.15). Additionally, these results, combined with those for vertical heterogeneity (Figure 5.10-5.11), show the large contrast in the composition of outer bank material between Maier and Horseshoe bends.

Linear regressions of normal stress σ_N against shear stress σ_S obtained from the direct shear box tests provided an estimate of the cohesive strength (y-intercept) and internal friction angle (slope) for outer bank samples collected in the field (Figure 5.16). The results from this analysis show friction angle is inversely related to cohesion (Figure 5.17). These results are consistent with previous reports of the relation between internal friction angle and cohesion from soil mechanics investigations (Fredlund *et al*., 1978; Fredlund and Rahardjo, 1993). The results from the direct shear box tests combined with the results from the hydraulic jet tests show that outer bank materials with high erodibility coefficients typically have low values of cohesion (Figure 5.18), again emphasizing the importance of clay content on influencing rates of bank erosion.

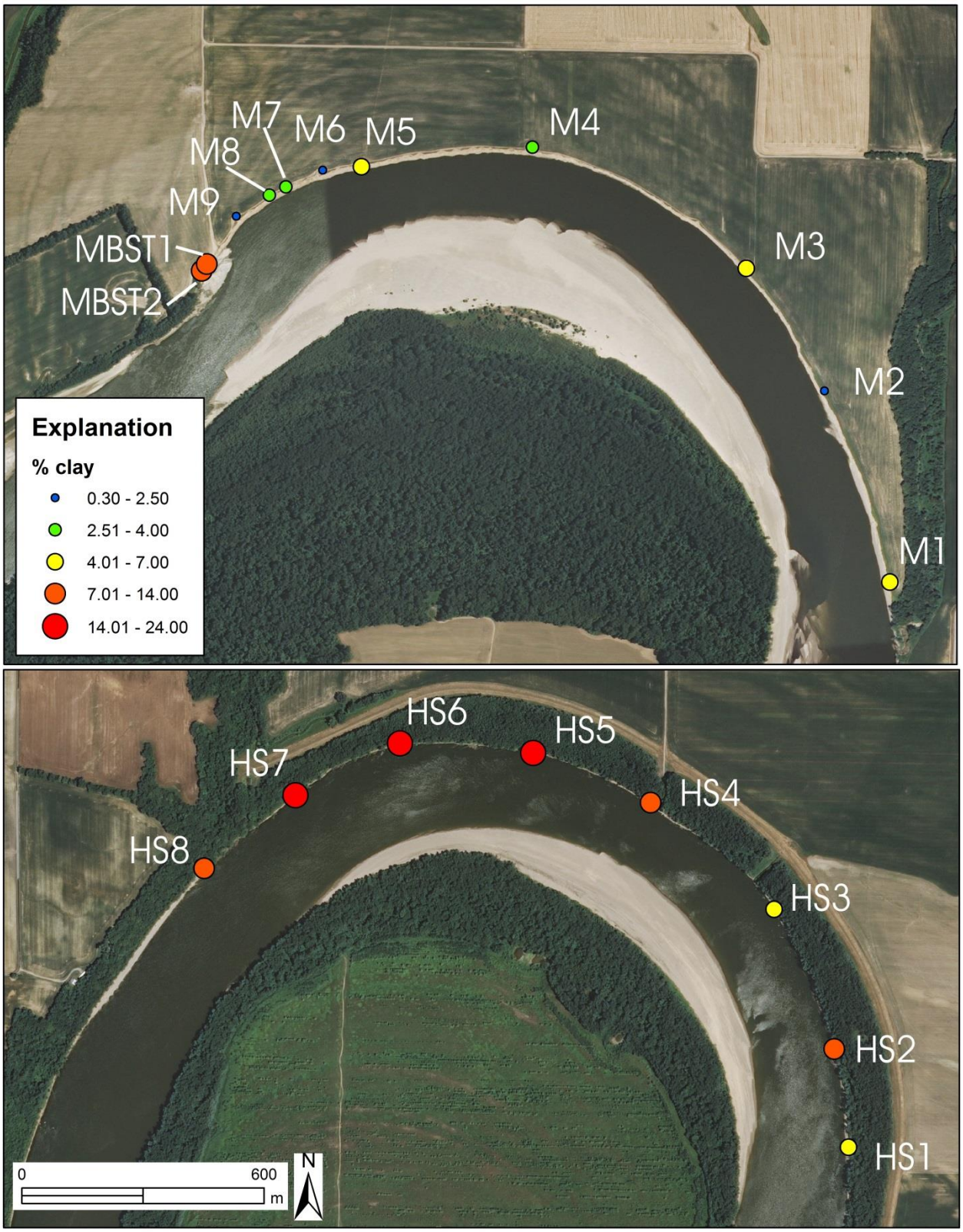

Figure 5.15: Spatial variation in depth-averaged clay content for outer bank sediments around Maier Bend (top) and Horseshoe Bend (bottom).

Although clay content influences the cohesiveness of the material and the critical shear stress, the weight of the bank materials will contribute to the gravitational shear force driving slope failures, particularly when the bank sediments are saturated with water. Results from grain size distributions around Maier and Horseshoe bends show that a positive relationship exists between the percentage of sand in a sample and the saturated unit weight (Figure 5.19). Thus, sandy bank materials have a greater tendency to fail than fine materials due to reduced resistance to erosion through low cohesion and to enhanced potential for failure through enhanced saturation.

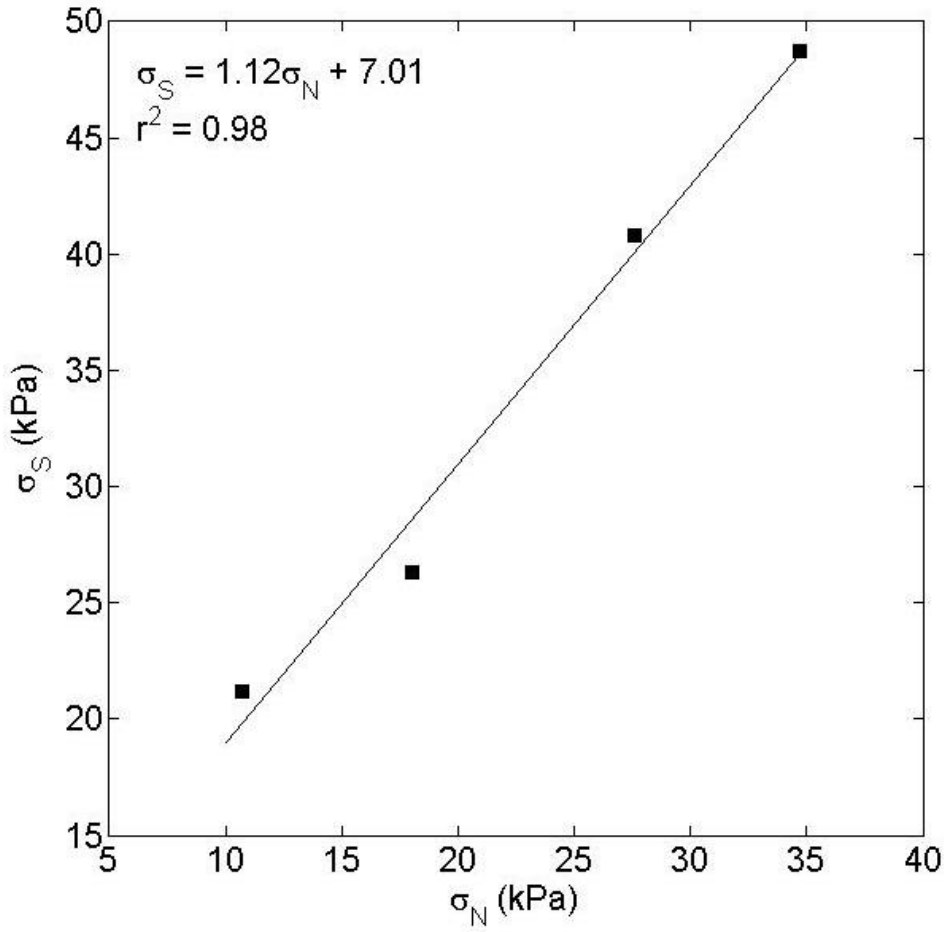

Figure 5.16: Results from direct shear box tests for location Horseshoe Bend HS7 plotting normal stress σ_N against shear stress σ_S. The linear regression line allows for the calculation of the cohesive strength of the bank material (y-intercept) and the internal friction angle (slope).

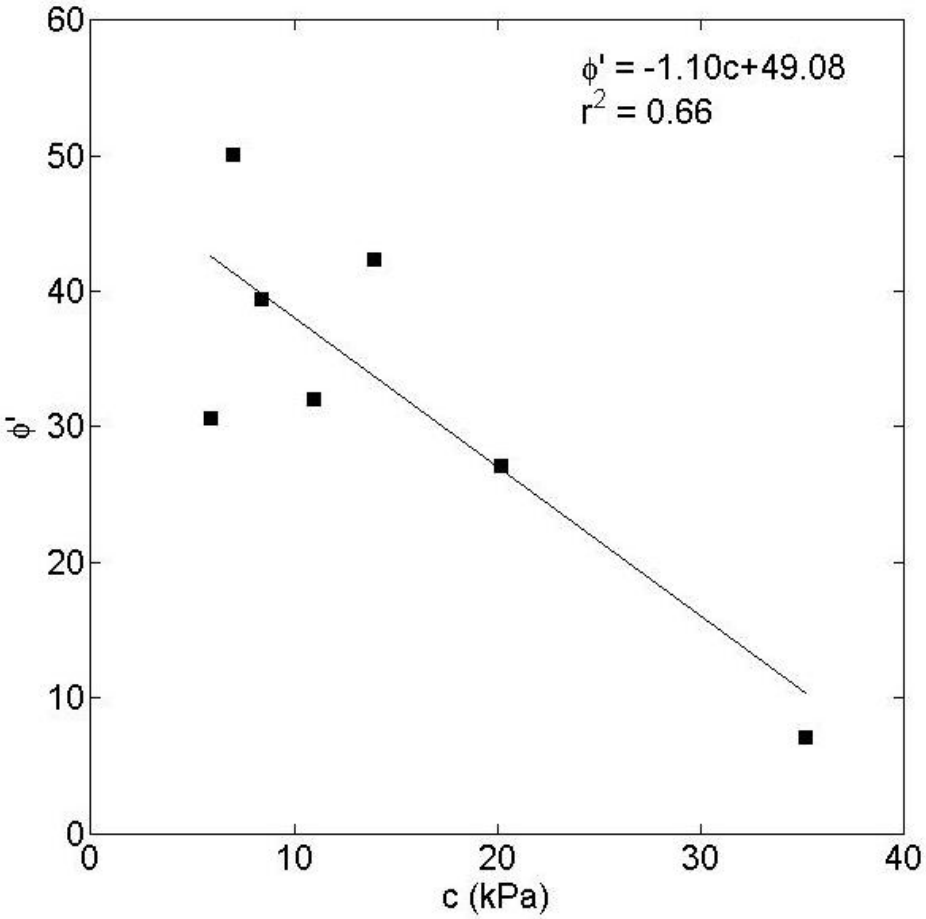

Figure 5.17: Relationship between estimated values of cohesion *c* and internal friction angle ϕ' for outer bank sediments around Horseshoe Bend.

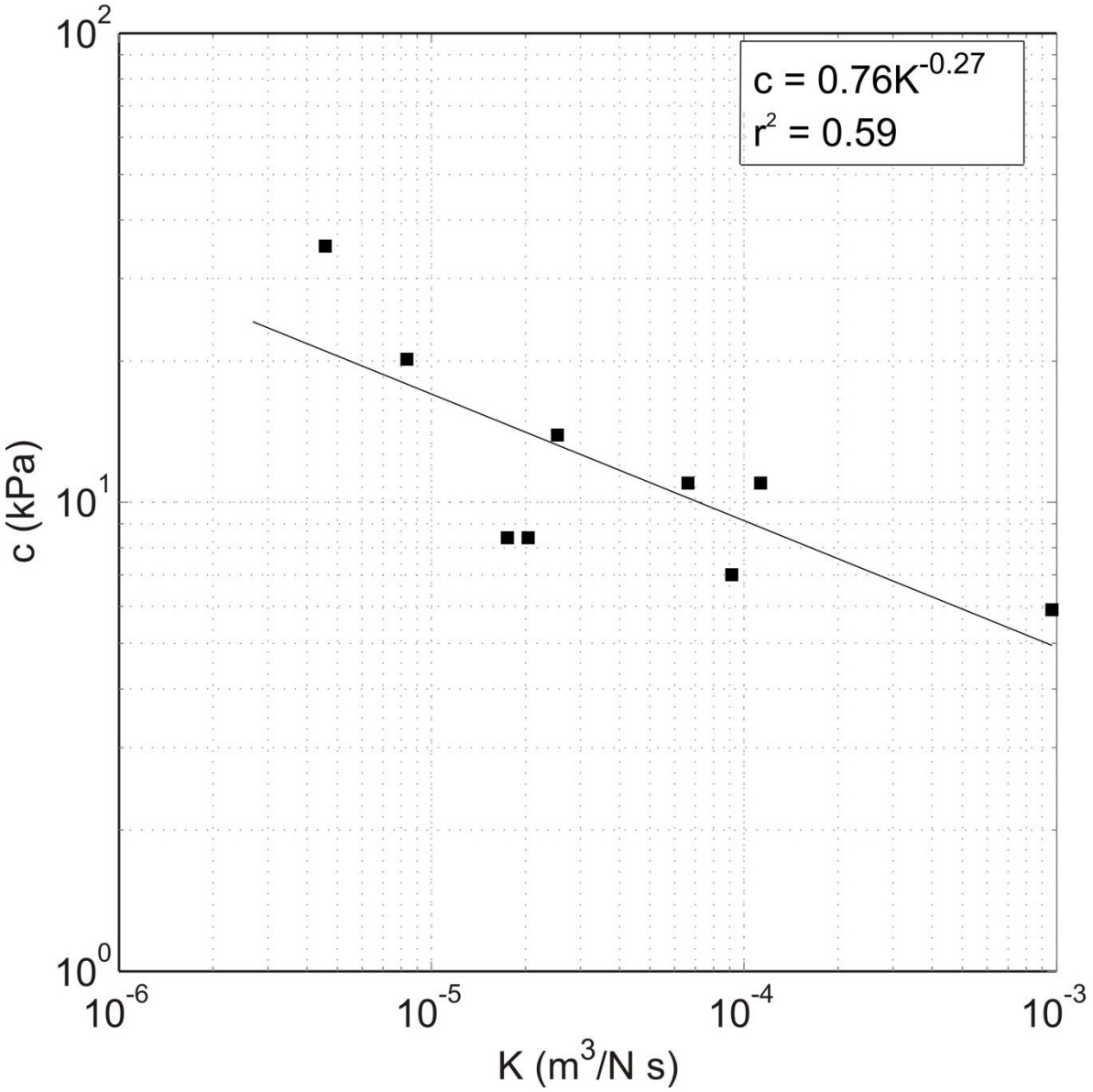

Figure 5.18: Relationship between estimated values of erodibility coefficient *K* and cohesion *c* for bank materials derived from Horseshoe Bend.

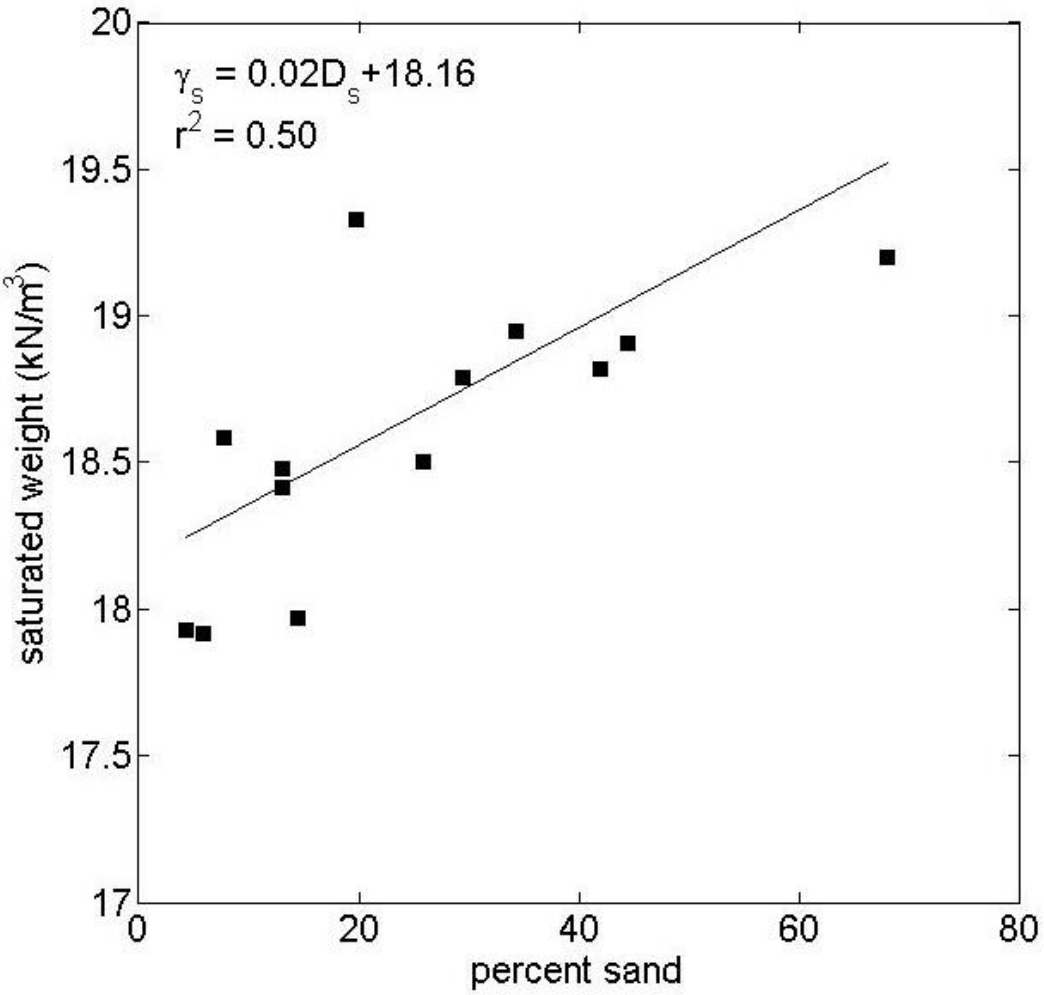

Figure 5.19: Relationship between percent sand and measured values of saturated unit weight γ_s for outer bank sediments around Maier and Horseshoe bends.

5.4.4 BSTEM model and measured rates of bank erosion

To investigate how the lateral and vertical variability in the resistance properties of the banks and floodplains influence rates and mechanisms of bank retreat, the bank stability and toe-erosion model (BSTEM) was used at various locations around Maier and Horseshoe bends. Three locations were selected from each bend and a flood hydrograph during June 25th, 2011 through July 4th, 2011 was used for the static, step-wise simulations (Figure 5.20). The results from the regression analyses of the geotechnical properties were used as inputs for the BSTEM models of bank erosion along with the bank profiles extracted from the terrestrial LiDAR

surveys, and a constant channel gradient of 0.0001 for all locations (Table 5.1). In contrast to common excess shear stress modeling approaches, where the erosion coefficient *k* is adjusted to best-fit observed rates of bank erosion, the approach adopted herein relies on direct estimates of *k* without recourse to calibration and therefore provides a more physically-based model of bank erosion (Darby *et al*., 2010). However, the geotechnical tests and regression analyses based on data derived from these tests were only valid for cohesive bank materials that have substantial amounts of clay. Therefore, the default parameters offered in BSTEM were used for bank materials with little to no clay content around Maier and Horseshoe bends.

Table 5.1: Geotechnical input parameters used in BSTEM model simulations. All other layers not shown in this table used the default values provided by BSTEM.

	regression analysis					default parameters	
Location/layer	τ_c (Pa)	K (cm^3/Ns)	ϕ' (degrees)	c' (kPa)	γ_s (kN/m^3)	τ_c (Pa)	K (cm^3/Ns)
MB1							
layer 1	3.71	1.13E-04	39.37	8.83	18.94		
layer 2	4.18	8.46E-05	38.56	9.56	18.79		
MB4							
layer 1	2.56	2.78E-04	41.45	6.94	19.19		
layer 2	2.22	3.94E-04	42.14	6.31	18.76		
MBST3							
layer 1	5.58	4.20E-05	36.38	11.55	18.31		
layer 2	6.15	3.33E-05	35.55	12.30	18.25		
layer 3	4.94	5.66E-05	37.36	10.65	18.30		
HSB1							
layer 1	7.39	2.13E-05	33.83	13.86	18.28		
HSB4							
layer 1	6.01	3.52E-05	35.76	12.11	18.46		
layer 2	2.79	2.25E-04	41.01	7.34	18.56		
HSB6							
layer 1	7.87	1.83E-05	33.18	14.45	18.44	50.00	1.41E-08
layer 2	6.59	2.82E-05	34.94	12.86	18.27	50.00	1.41E-08
layer 3	6.47	2.94E-05	35.10	12.71	18.19	5.00	4.47E-08
layer 4	4.98	5.56E-05	37.30	10.71	18.37	5.00	4.47E-08

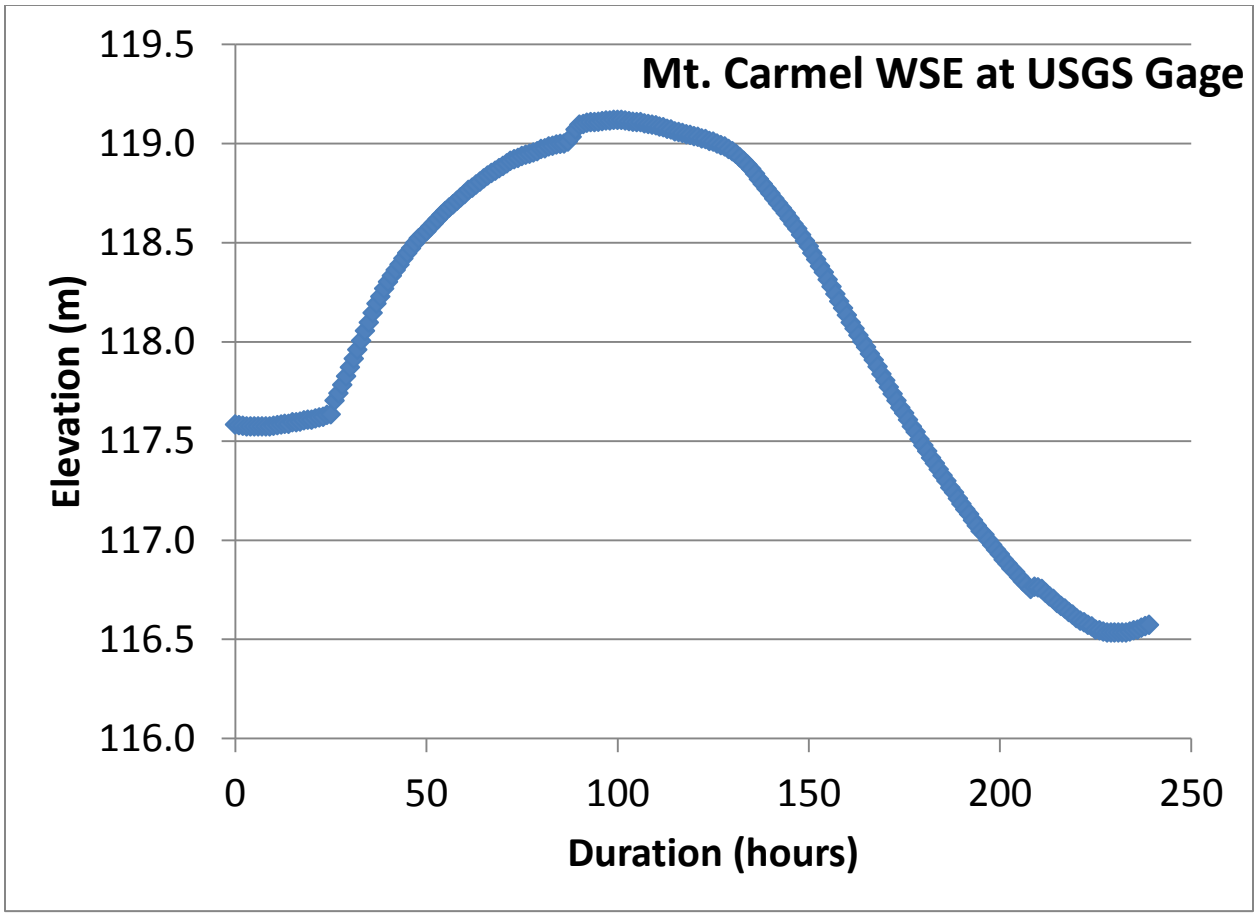

Figure 5.20: Flood hydrograph for June 25th – July 4th, 2011 recorded at Mt. Carmel, Illinois.

For Maier Bend, location MB1 was selected to represent the upstream entrance to the bend and the results from the model show ~50 cm of erosion at an elevation of 112 m for the entire flood hydrograph, with little erosion occur for the rest of the bank profile (Figure 5.21). Using a width of 1 m, the estimated volume of sediment removed during this simulation was roughly 1.05 m^3. Near the apex of the bend, at location MB4, the model results show roughly 70 cm of lateral retreat near the base of the bank with decreasing amounts of erosion to an elevation of ~114 m, roughly 2 m below the top of the bank, corresponding to ~1.7 m^3 of sediment removed (Figure 5.22). Downstream of the apex and above the outcrop of bedrock at location MBST3, approximately 90 cm of erosion was simulated near the contact with the bedrock (~111

m) with no substantial amount of erosion occurring above an elevation of ~113.5 m, resulting in ~ 0.8 m^3 of sediment eroded (Figure 5.23).

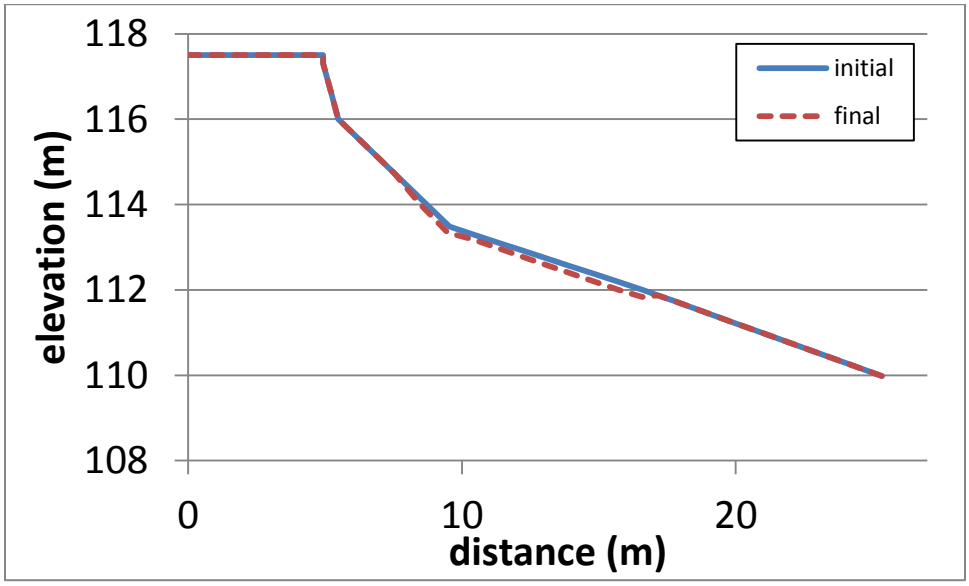

Figure 5.21: BSTEM results at MB1 for June 2011 flood hydrograph.

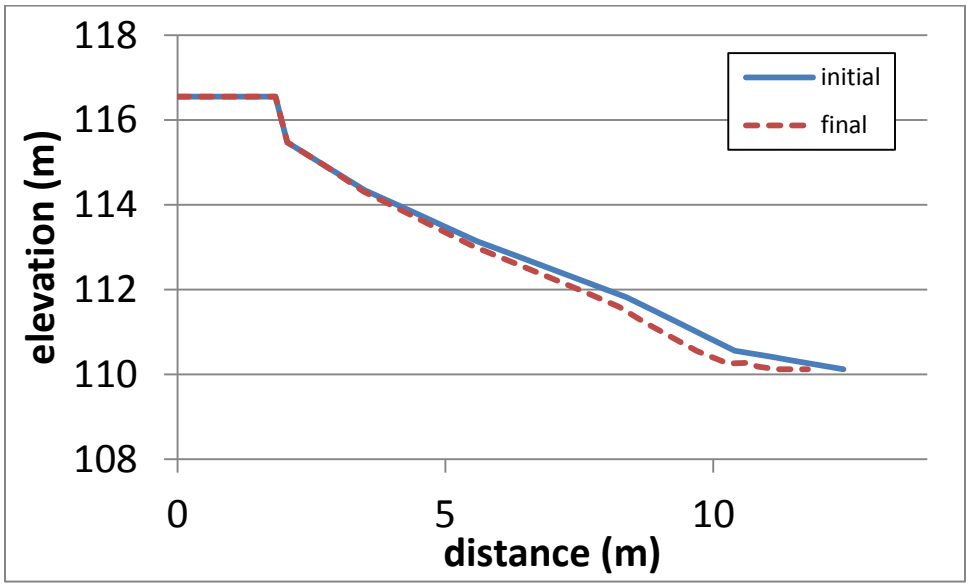

Figure 5.22: BSTEM results at MB4 for June 2011 flood hydrograph.

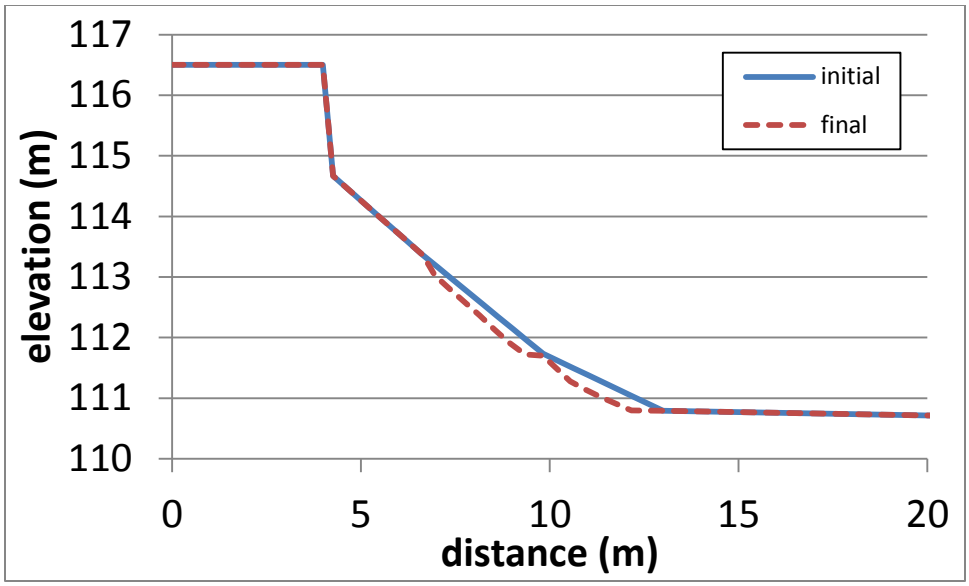

Figure 5.23: BSTEM results at MBST3 for June 2011 flood hydrograph.

A similar set of locations was chosen around Horseshoe Bend for the model simulations and included the RipRoot estimates of increased cohesion due to vegetation. At the upstream entrance to the bend at location HSB1 the model results show a maximum lateral bank retreat of ~1 m occurring at an elevation of roughly 114.2 m (roughly mid-bank) with ~1.9 m^3 of sediment eroded (Figure 5.24). Erosion at this location occurred over much of the transverse profile from an elevation of ~116 m to the base of the bank profile at ~112 m. Site HSB4 is located within the upstream end of the bend apex region, and also happens to be the location of a seasonal campground. The model results for HSB4 show that erosion was focused within the middle part of the bank between elevations 112.5 – 114.75 m, with an average lateral bank retreat of ~90 cm and a total of ~1.7 m^3 eroded (Figure 5.25). At the downstream end of the bend apex region, the model results for location HSB6 show the erosion focused near the base of the bank profile below an elevation of ~112.4 m and produced roughly ~0.45 m^3 of volumetric erosion (Figure 5.26).

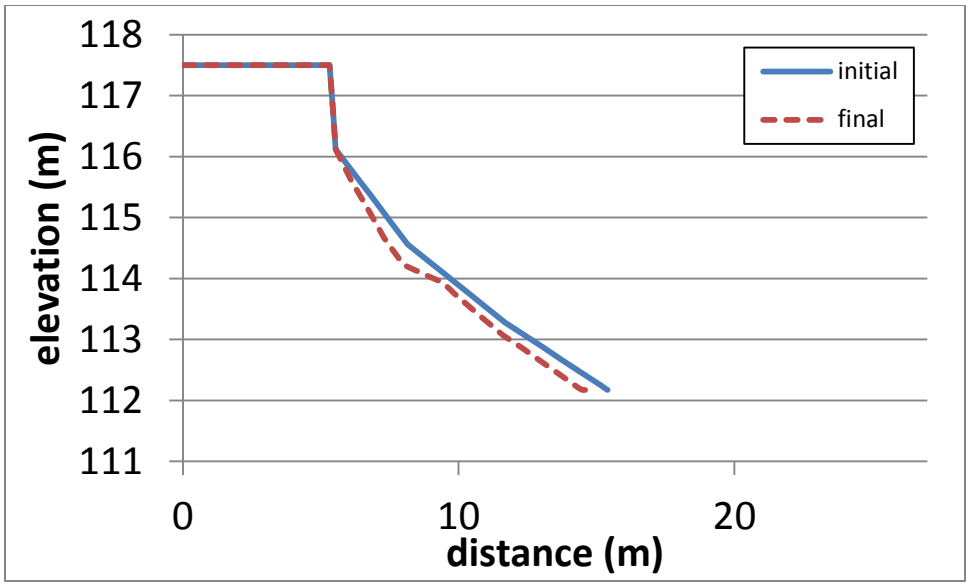

Figure 5.24: BSTEM results at HSB1 for June 2011 flood hydrograph.

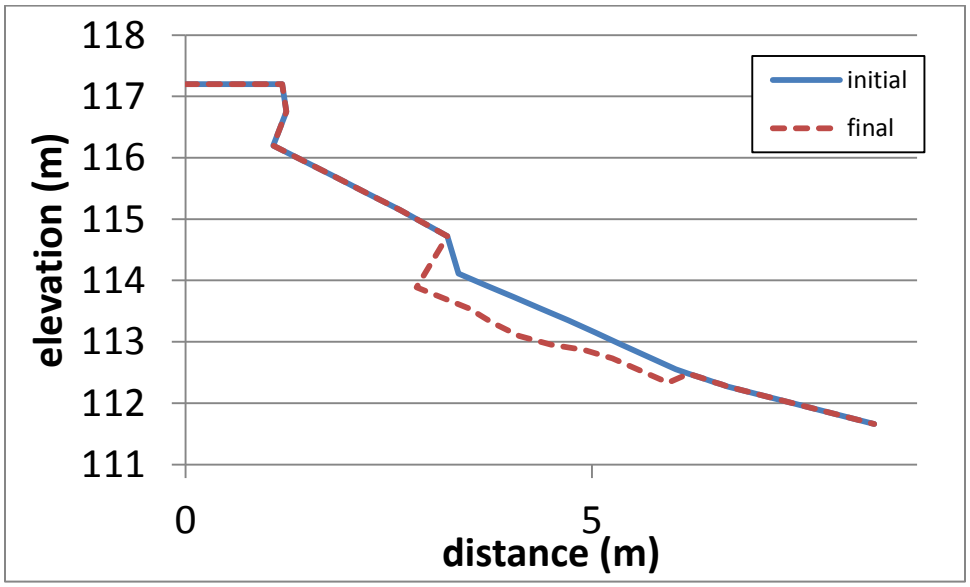

Figure 5.25: BSTEM results at HSB4 for June 2011 flood hydrograph.

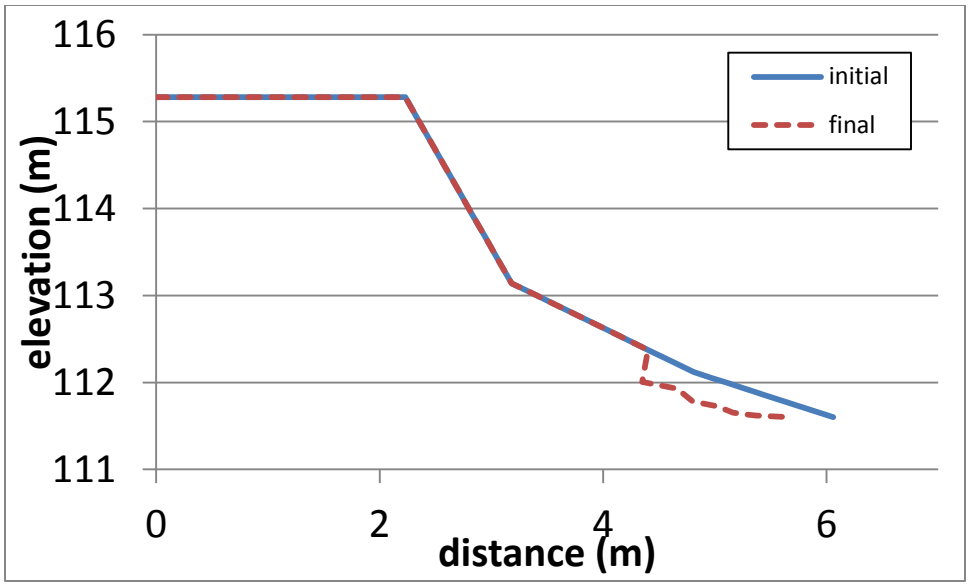

Figure 5.26: BSTEM results at HSB6 for June 2011 flood hydrograph.

The model results for Maier and Horseshoe bends for the June 2011 flood hydrograph did not produce enough erosion near the toe of the banks to promote destabilization of the top cohesive layers, and therefore no slope failures were predicted. Although the results show variation in the rates of lateral bank retreat at different locations around each bend and the patterns of erosion vertically within the transverse bank profiles, the full mechanisms of bank migration were not simulated. To investigate the style of slope failure at Maier Bend, an approximate bankfull discharge event for the lower Wabash River (~2000 m^3/s^{-1}) was simulated over a duration of ~900 hours, which roughly corresponds to the exceedance probability of this discharge.

At Maier Bend, a discharge of ~2000 m^3s^{-1} relates to a flow stage of ~115.5 m at cross-section MB4. After toe erosion was simulated by the model, the water table within the bank was held constant at 1 m below the top of bank and the flow stage within the channel was iteratively lowered until the bank became unstable and a slope failure occurred. The results for the toe erosion model at Maier Bend show roughly 5 m of lateral bank erosion over the lower 2 m of

bank profile (~110 – 112 m), with rates of erosion quickly decreasing to an elevation of ~115 m, and no erosion occurring above ~115 m (Figure 5.27). The bank stability model simulated a slope failure when the flow stage was lowered to an elevation of 113.75 m, and resulted in roughly ~1.3 m of lateral retreat at the top of bank. The final results of this simulation show a nearly parallel retreat of the bank profile, with a 1.5 – 2 m near-vertical face in the top cohesive layer and the lower portion of the bank having a slope of ~35°. The total amount of sediment removed during this simulation was roughly ~15.75 m^3.

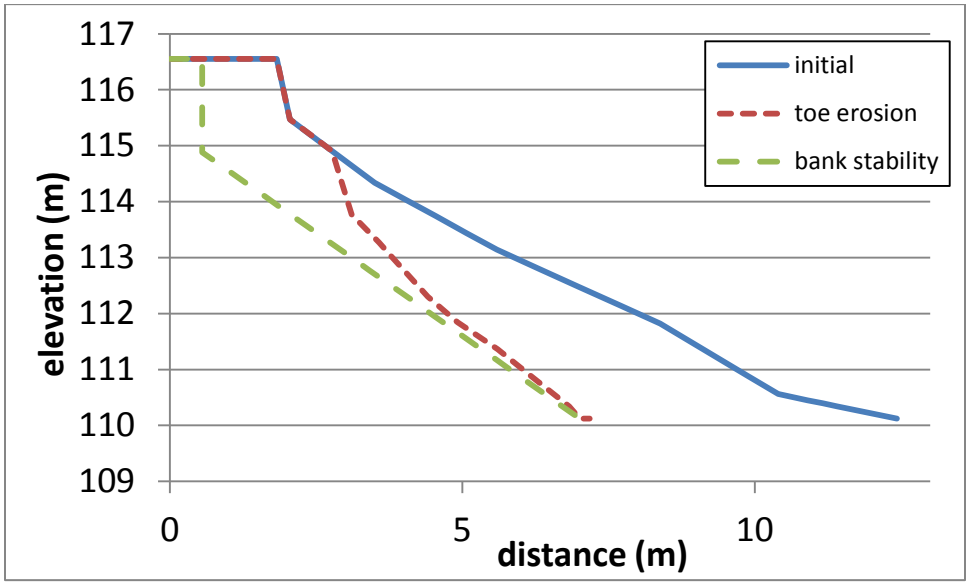

Figure 5.27: BSTEM results for MB4 simulating slope failures. Toe erosion model was performed using a flow stage of 115.5 m for duration of 900 hours, and bank stability model was performed using a water table 1 m below top of bank and a flow stage of 113.75 m.

At Horseshoe Bend, a similar discharge event was simulated for 900 hours, using a flow stage of 116.7 m for cross-section HSB6. However, the results from the toe erosion model within BSTEM resulted in erroneous bank profiles (Figure 5.28). This inaccurate model output is probably related to the relatively high erodibility coefficients that were estimated via jet tests for these cohesive bank materials. In fact, during the jet test analyses, the dominant mode of erosion for the cohesive samples was removal of small aggregate clumps to a scour distance typically no

more than ~5 cm. Once erosion by aggregates had ceased, no further scour was measured, presumably as a result of increased resistance strength of the clay material and shear stress limitations of the jet test apparatus. These jet-test observations suggest that a relatively thin weathered surface layer of the cohesive material is more erodible than the internal less-weathered materials. Thus, for long duration model simulations that remove the weathered surface layer, the jet-test estimated erodibility coefficients are not appropriate when applied to the resistant cohesive materials beneath the weathered layer.

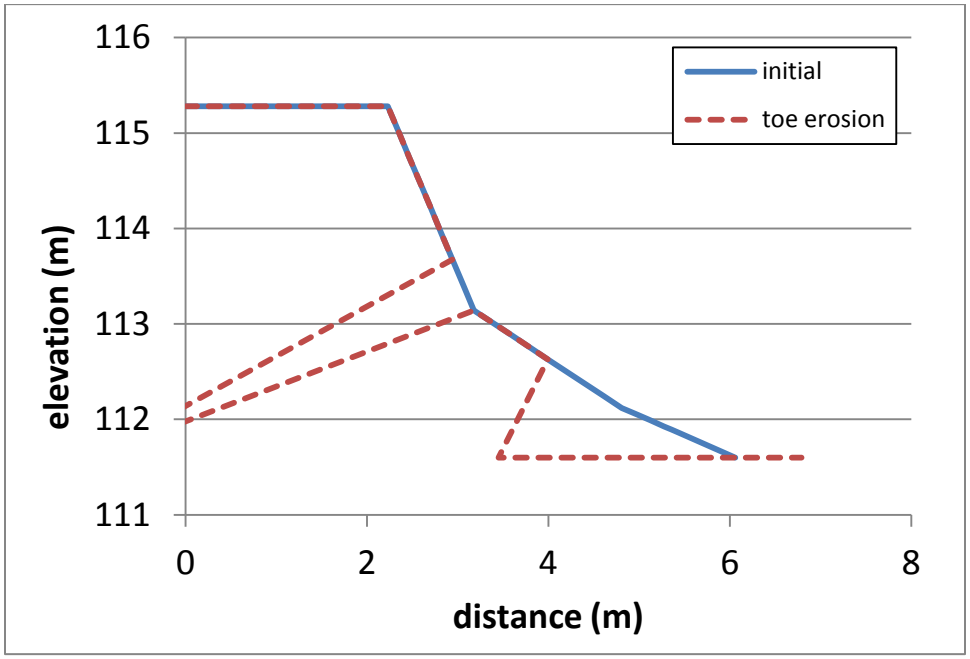

Figure 5.28: BSTEM results for HSB6 simulating slope failures using the geotechnical parameters estimated from regression analysis. Toe erosion model was performed using a flow stage of 116.7 m for duration of 900 hours.

Therefore, to compare mechanisms of bank erosion between Maier and Horseshoe bends, the soil layers within cross-section HSB6 were characterized using the default parameters supplied by BTSEM for stiff resistant cohesive sediment. For this simulation a flow stage of 116.7 m was similarly used for the toe erosion model; however, undercutting of the bank did not occur until ~15,300 hours. The model resulted in roughly 4 m of lateral erosion at the base of the

bank with no erosion occurring above ~113 m (Figure 5.29). The bank stability model was then applied using a water table elevation of ~114.75 m (0.5 m below top of bank), and a bank failure was simulated when the flow stage was lowered to an elevation of 113 m. The bank failure resulted in a ~1 m lateral retreat at the top of the bank, and produced a near-vertical profile at elevations 113.4 – 115.25 m, and transverse slopes of ~30° at elevations 111.6 – 113.4 m. The total amount of sediment removed during this simulation was ~7.9 m^3.

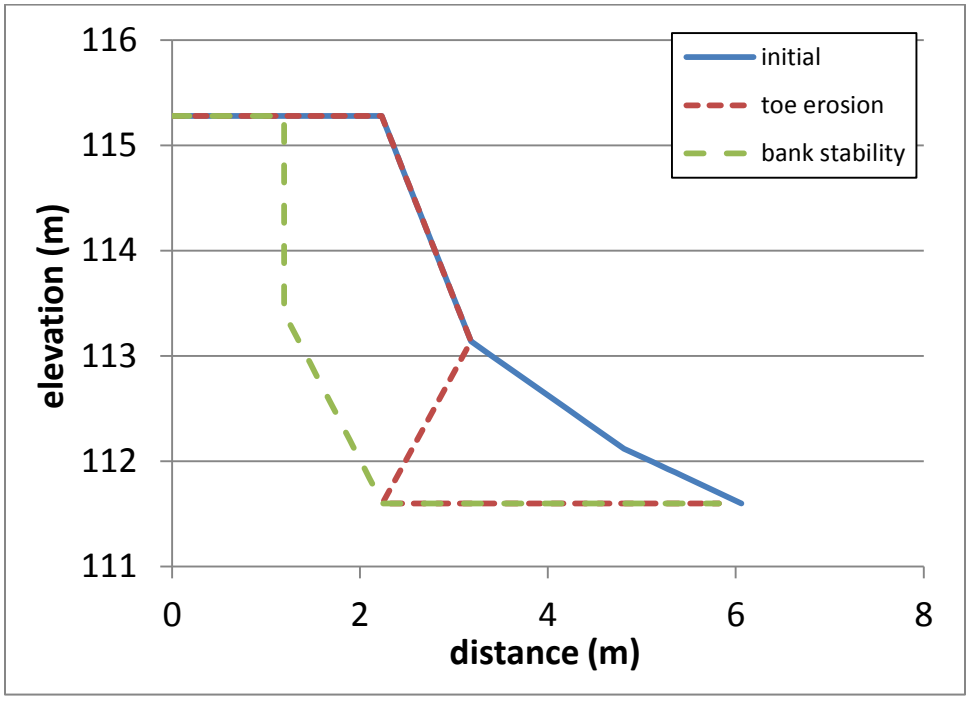

Figure 5.29: BSTEM results for HSB6 simulating slope failures using the default geotechnical parameters supplied by BSTEM. Toe erosion model was performed using a flow stage of 116.7 m for duration of 15300 hours, and bank stability model was performed using a water table 0.5 m below top of bank and a flow stage of 113 m.

Short- and long-term rates of outer bank erosion were computed from differencing of topographic data derived from annual LiDAR surveys and provide a basis for comparison with the BSTEM model simulation results. At Maier Bend, the total volumetric rate of erosion for the time period 2011-2012 estimated from the LiDAR surveys is roughly 53290 m^3yr^{-1}, with the majority of erosion occurring immediately downstream of the bend apex (Figure 5.30). The total

volumetric rate of erosion for the time period 2012-2013 is roughly ~98694 m^3yr^{-1}, about 1.85 times that of 2011-2012. The spatial pattern of erosion for this time period shows that the highest rates again occur near the bend apex, but the zone of enhanced erosion extends farther upstream than for 2011-2012 with a pronounced region of increased erosion about 400 m upstream of the apex (Figure 5.30). For Horseshoe Bend, the total volumetric rates of erosion for 2011-2012 and 2012-2013 were estimated to be 1820 m^3yr^{-1} and 3954 m^3yr^{-1}, respectively. In contrast to Maier Bend, the maximum rates of erosion occur upstream of the bend apex, between a high-water levee drainage channel and a private hunting campground (Figure 5.31).

Long-term channel migration rates for Maier and Horseshoe bends were estimated through time-series analysis of aerial photography from the following time periods: 1938, 1960, 1980, 1988, 1998, and 2009-2012. Although the amount of lateral bank migration varied spatially around both bends, migration rates for Maier Bend are substantially higher than migration rates for Horseshoe Bend (Figure 5.32). Long-term rates of lateral migration were estimated by calculating the surface area bounded by the 1938 and 2012 digitized outer banklines and dividing by the streamwise distance around the bend. The results from this analysis yield average migration rates for Maier Bend of ~11 myr^{-1}, whereas average migration rates for Horseshoe Bend are much less at approximately ~0.75 myr^{-1}. For both bends, maximum rates of lateral bank migration occur near the bend apex and rates of migration on the upstream limbs of the bends are negligible (Figure 5.32).

On the downstream limb of Horseshoe Bend, the relatively large bedrock outcrop restricts downstream channel migration (Figure 5.32). At Maier Bend, the downstream limb of the bend shows a much more complex history of channel migration and is linked to the progressive exposure of the relatively small bedrock outcrop within the channel through time.

Progressive migration of the outer bank on the downstream limb occurs for the time period 1938 – 1998. However, outer bank erosion no longer occurs near the bedrock outcrop, but instead a small region of outer bank deposition and inward channel migration is evident immediately downstream of the bedrock outcrop (Figure 5.32).

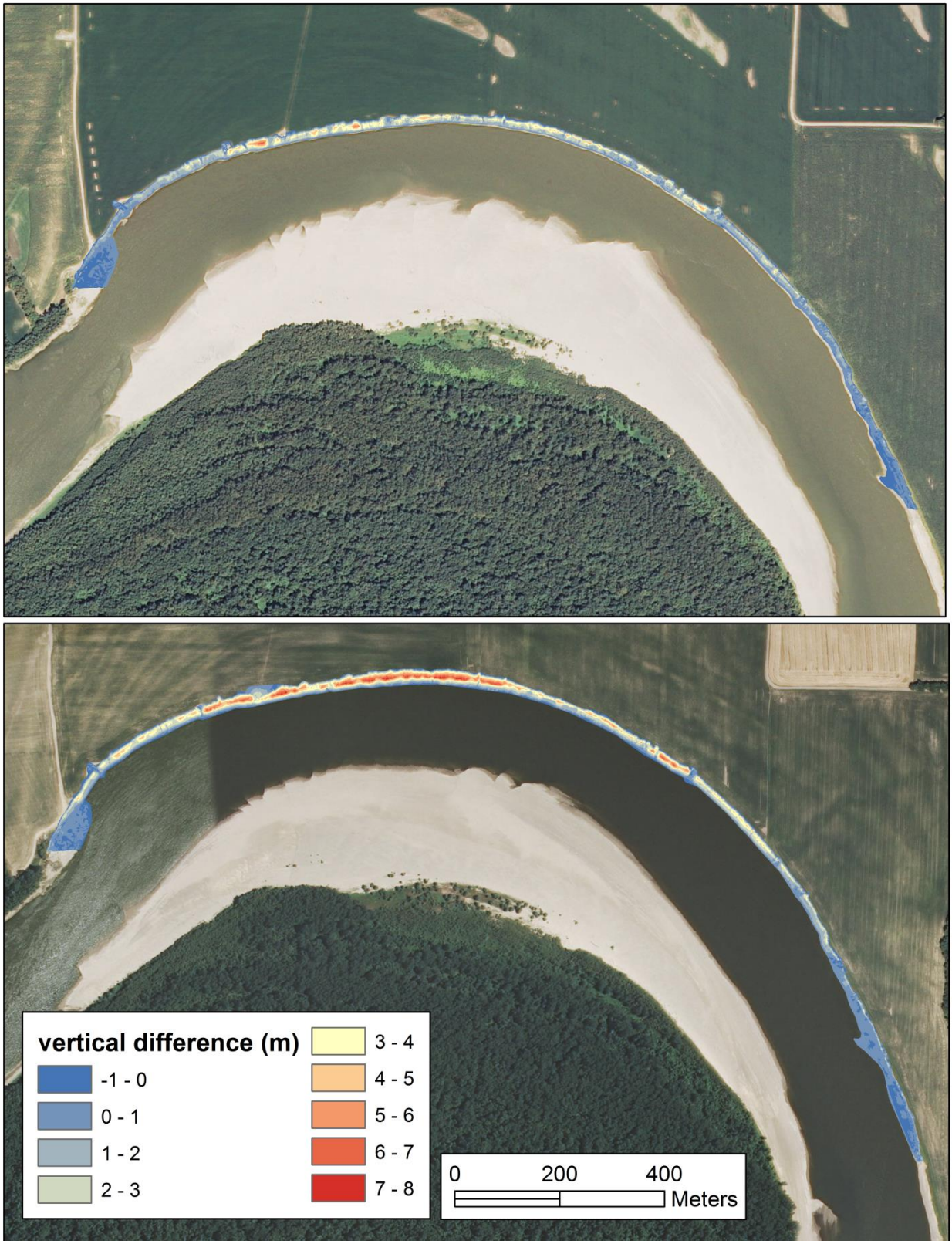

Figure 5.30: Erosional maps for Maier Bend showing the difference in vertical elevation between annual terrestrial LiDAR surveys 2011-2012 (top) and 2012-2013 (bottom).

Figure 5.31: Erosional maps for Horseshoe Bend showing the difference in vertical elevation between annual terrestrial LiDAR surveys 2011-2012 (top) and 2012-2013 (bottom).

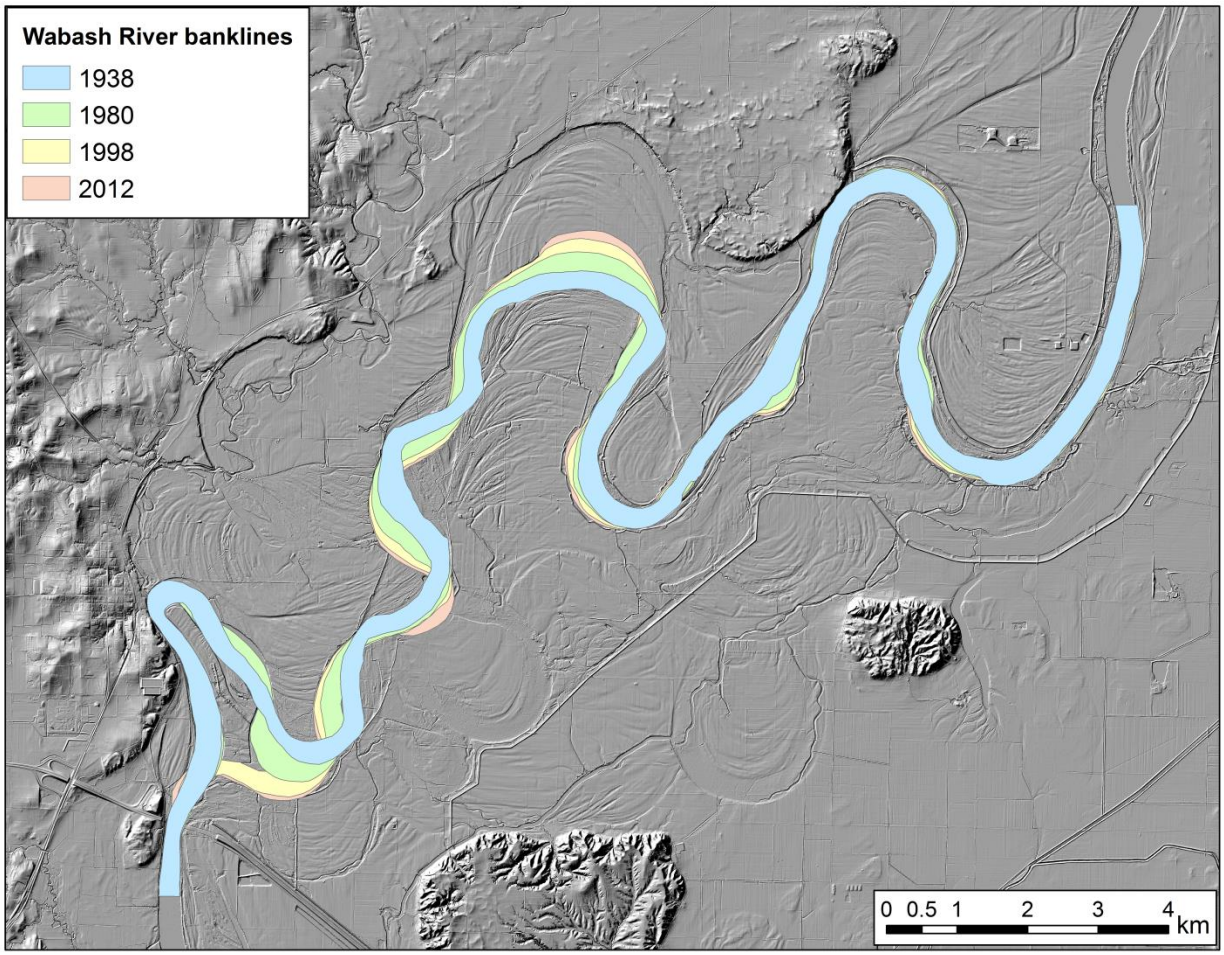

Figure 5.32: Long-term planform evolution for the Wabash River near Grayville, IL as determined from digitized banklines from aerial photography. (Base image: 2011 aerial LiDAR)

5.5 Discussion

The results from this chapter show that the geotechnical properties and transverse profiles of the channel banks of a large meandering river have high lateral and vertical heterogeneity, both between different bends and throughout a single bend, and that bank height and floodplain elevation are highly variable. The results also highlight the important influence of riparian vegetation and bedrock outcrops within the channel on the geotechnical properties of the channel banks and on the rates and spatial patterns of channel migration. These findings contribute to the

understanding of bank erosion on large meandering rivers and have important implications for modeling of the lateral migration of large meandering rivers at the landscape scale.

The results from the BSTEM model simulations show that rates of erosion and the mechanisms by which banks retreat are highly dependent upon the lateral and vertical variability in the erosional resistance properties of the banks, the local height and geometry of the bank profile, and the variability in hydrologic conditions. The model simulations were performed without recourse to calibration of an erosion coefficient or estimates of shear stress, and thus the variability in model outputs solely reflect the influence of the geotechnical properties of banks. Although the model simulations do not accurately predict absolute rates of erosion measured at Maier and Horseshoe bends, the simulations do capture the styles and mechanisms of bank retreat documented in the field. Possible explanations for the lack of correspondence between the rate of erosion predicted in the BSTEM model simulations and rates documented from the repeat LiDAR surveys and historic aerial photography include failure of the model to account for the influences of bend curvature on the distribution of shear stress within these bends and of near-bank LWD at Horseshoe Bend on shear stress along the outer bank (e.g. Chapter 3).

The model simulations for the June 2011 flood hydrograph at the selected cross sections around both bends did not result in sufficient erosion at the toe of the bank necessary to decrease bank stability and produce a bank failure. These findings do not suggest that individual flood events are incapable of producing bank failures. Terrestrial LiDAR surveys were only conducted annually during low flow conditions and thus do not provide detailed information immediately before and after individual flood events. However, observations in the field during measurements of high flow confirm that bank failures occur at Maier Bend over the time scale of individual events. The over-steepening of the transverse bank profiles produced by the model at Maier

Bend (Figures 5.21-5.23), and the variability in bank slope around the bends as observed from the LiDAR bank profiles (Figure 5.10) indicate that the occurrence of bank failures is dependent on the local bank conditions prior to an individual flood event. Thus, application of the BSTEM model to additional cross sections at Maier Bend for an individual flood event might result in simulated bank failures.

A common approach in morphodynamic models is to assume a flood intermittency factor that represents a probability of exceedance for a given discharge, typically a bankfull event (Sinha and Parker, 1996; Parker *et al*., 1998). The concept of a flood intermittency factor is introduced in this study by performing BSTEM model simulations for a bankfull discharge event with a duration of 900 hours, which yielded sufficient erosion to investigate the mechanisms of bank retreat. At Maier Bend, approximately 1 – 2 m of the outer bank is still exposed subaerially for the modeled discharge event because of the relatively high floodplain elevation at this bend. At cross-section MB4 the water surface elevation roughly coincides with the elevation of the contact between the top weakly-cohesive layer and the easily erodible non-cohesive sediment below, allowing bank erosion to occur over nearly the entire flow depth. The high rates of toe erosion, combined with the low cohesion of the top layer and lack of a strong root-reinforcement from riparian vegetation, induce bank failures with only minor lowering of the water surface elevation within the channel (confining stage pressure). Thus, bank failures occur when flow stages are still relatively high. These findings have implications for the ability of the slump blocks produced at Maier Bend to influence near-bank flow structure (e.g. Chapter 4), and suggest that these weakly cohesive blocks disintegrate upon entering the flow during the falling limb of flood events.

In contrast, the relatively low top of bank elevation at Horseshoe Bend cross-section HSB6 allowed for roughly ~1.5 m of overbank flow. However, the high cohesion of the bank materials along with the increased cohesive forces from the riparian forest produced a high resistance of the bank to erosion. These conditions required the model to be simulated for a duration 17 times longer (15300 hours) than Maier Bend to produce sufficient erosion at the bank toe. Furthermore, the bank stability model did not simulate bank failure until the water surface elevation was lowered to an elevation of ~113 m. These findings suggest that mass failure and tree loading occurs during relatively low flow conditions when velocities are not sufficient to transport mass failures containing trees, which may explain the long residence times observed for the near-bank LWD (e.g. Chapter 4).

The results from this study shed light on the role of riparian forests in stabilizing channel banks and have implications for meander planform evolution. Much attention has focused on whether trees primarily act to stabilize or destabilize riverbanks (Beeson and Doyle, 1995; Abernethy and Rutherford, 1998; Trimble, 2004; Gurnell and Petts, 2006; Eaton and Giles, 2009; Polvi *et al*., 2014). While results differ, it is generally agreed that the role of trees in stabilizing banks is dependent on the scaling between bank heights and depth of root penetration. Despite the relatively high bank heights at Horseshoe Bend (~5-6 m) and the relatively low root penetration depths of the trees (~1.5 m), the riparian forest along this bend is highly effective at increasing the resistance strength of the banks and thus reducing rates of erosion. Results from the RipRoot module in BSTEM show the trees contribute substantial additional cohesion to the bank that roughly doubles the cohesion provided by the sediment alone. These findings are consistent with a recent study that showed woody riparian vegetation substantially increases the

cohesive resistance of riverbanks (Polvi *et al*., 2014), and therefore can strongly influence rates of bank erosion and modify patterns of channel migration on large meandering rivers.

Another major finding from this study is that the critical shear stress and erodibility coefficients for the cohesive materials at Horseshoe Bend are strongly dependent on the amount of subaerial preparation of the bank. For cohesive bank materials, the process of subaerial preparation occurs through cycles of freeze-thaw and/or wetting-drying of silt and clay particles, and produces a surface layer that is desiccated and cracked, resulting in a low resistance to erosion of the bank material (Lawler, 1993; Couper, 2003). While these effects have been documented by previous studies, the findings from this study show that consideration of these effects is important for predicting the style of bank failure along meandering rivers. This issue is also important for estimating critical shear stress and erodibility coefficients for numerical models, and the influence of hydrologic variability on bank erosion.

The hydraulic jet tests performed on bank samples at Horseshoe Bend yielded erodibility coefficients that were up to four orders of magnitude higher than the default erodibility coefficients in BSTEM for cohesive materials (Figure 5.33). The BSTEM default erodibility coefficients are derived from previous field investigations that rely on the Blaisdell *et al*. (1981) method of regression (Hanson and Simon, 2001). This method of regression assumes the time required to reach an equilibrium scour depth is large and that the trend in scour over time can be described by a logarithmic-hyperbolic function. Thus, the critical shear stress and erodibility coefficient obtained from this method are estimated for the entrainment of individual particles and do not apply to the erosion of cohesive aggregates, limiting the capacity of numerical models to accurately simulate detailed rates and processes of erosion for individual flood events. For example, at Horseshoe Bend the erosion of a desiccated surface layer ~5 cm thick during an

individual flood event could result in exposure of roots at the bank face, influencing hydraulic forces acting on the bank. These findings suggest that the sequence of hydrologic events and subaerial preparation during low flow conditions can have a combined effect over time on rates of bank erosion for cohesive materials and progressive bank roughness provided by vegetation. However, the default erodibility coefficients from BSTEM applied for the bankfull simulations did produce reasonable estimates of the style of bank failure over long time scales, and therefore suggests that the use of field-derived erodibility coefficients based on jet tests for weathered surface layers is limited and careful consideration must be given to properly evaluate the erodibility of cohesive bank materials.

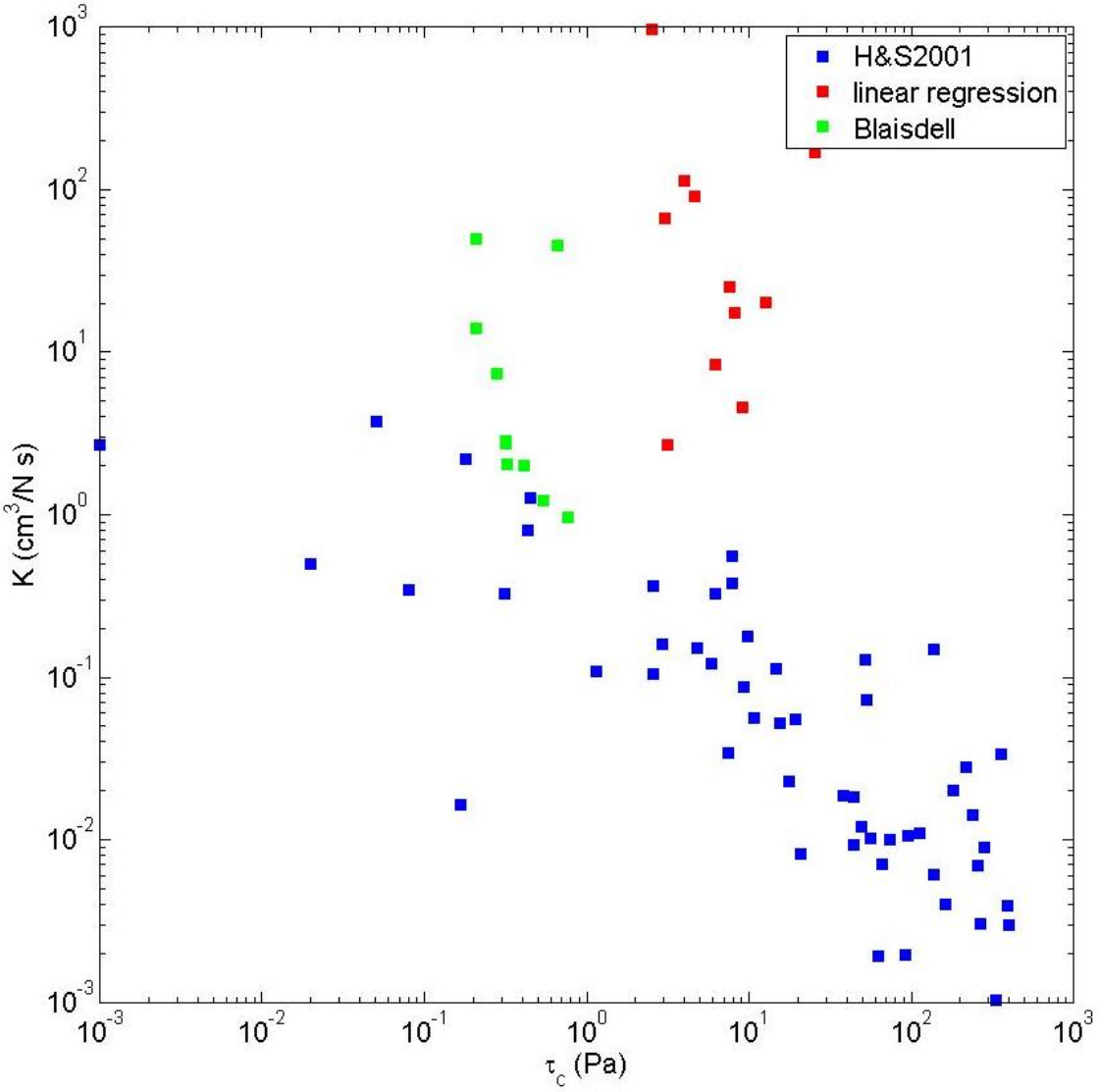

Figure 5.33: Comparison of hydraulic jet test data obtained from the Wabash River with data published in Hanson and Simon (2001). Results show difference in values of critical shear stress and erodibility between regression methods.

Lastly, previous modeling work has shown that stochastic streamwise and transverse variability in the resistant properties of floodplains can be a first-order factor influencing meander dynamics, and that such models are capable of producing complex channel planforms that are similar to planform geometries observed in natural rivers (Güneralp and Rhoads, 2011; Motta *et al*., 2012). These types of models emphasize the importance of external forcings on planform evolution; however, the variability is randomly generated using prescribed streamwise

and transverse spacing. In such models, the vertical heterogeneity within the floodplain is either ignored (Güneralp and Rhoads, 2011) or included through integration of physically-based subroutines of bank erosion (Motta *et al*., 2012). Yet, in either case, direct field measurements of the geotechnical properties are not incorporated, limiting the accuracy of the models.

The results presented for Maier and Horseshoe bends show considerable vertical variability in the geotechnical properties of the banks and that vertical heterogeneity is an important factor influencing the style and rate of bank retreat. Furthermore, the findings from this investigation show that the lateral and vertical variability for these bends is not stochastic, but rather linked to the spatial variability in riparian vegetation and floodplain materials deposited through historic channel migration.

It is important to note the close proximity of Maier and Horseshoe bends (~4.5 km down-valley distance), and yet there are considerable differences in the geotechnical properties, floodplain elevations, riparian vegetation, and rates of channel migration between these bends. Long-term rates of channel migration at Horseshoe Bend are ~0.75 myr^{-1}, while rates of lateral extension at Maier Bend are ~10 – 12 myr^{-1}, roughly 17 times greater. Interestingly, the BSTEM model simulations for the bankfull event show that Horseshoe Bend requires a duration roughly 17 times longer than Maier Bend to produce sufficient toe erosion and bank failure. Additionally, differences in the lateral and vertical extent of bedrock exposed within the downstream limbs of these two bends are producing differences in the long-term patterns of channel migration. The presence of bedrock within these two bends has considerable influence on planform evolution and should not be overlooked. These findings suggest that the external forcings due to the floodplain resistant properties of these bends are a major component influencing the observed

rates of bank erosion and patterns of channel migration, and emphasize importance of including lateral and vertical heterogeneities in morphodynamic models of meandering rivers.

5.6 Conclusions:

In this chapter, lateral and vertical heterogeneities in the geotechnical resistant properties of the outer banks and floodplains of two elongate meander bends are investigated through detailed field and laboratory analyses. The results show a high variability in the characteristic grain size of the bank sediments and bank profiles, riparian vegetation, and floodplain elevations both between the two bends and through each bend. Application of a toe erosion and bank stability model BSTEM to cross sections around each bend and observations from repeat LiDAR surveys and historic aerial photography indicate that the local bank properties strongly influence rates of erosion and mechanisms of bank retreat, and can explain much of the differences observed in long-term patterns of channel migration. Major findings from this research are:

1) The geotechnical properties of banks and floodplains in large meandering rivers can vary substantially, both laterally and vertically, over relatively short distances. The variation in grain size distribution around each bend is most likely linked to the spatial variability in riparian vegetation and floodplain development through deposition of fluvial sediment and is partly responsible for producing differences in transverse slopes throughout each bend.
2) Riparian forest around the outer bank floodplain of Horseshoe Bend substantially increases the resistance to erosion of the bank material through root-reinforcement. These trees offer an estimated additional ~15 kPa of cohesion to the top ~1.5 m of bank, resulting in a doubling of the cohesion provided by the fine-grained bank sediment. Thus,

riparian trees around this bend are capable of reducing rates of erosion and stabilizing the banks on a large meandering river.

3) A multi-component toe erosion and bank stability model (BSTEM) was used to simulate bank erosion for these two bends without calibration against an erosion coefficient. While the details of bank erosion produced by the model are specific to the two bends investigated, the results do highlight the importance of spatial heterogeneity in the geotechnical properties on rates of erosion. The results for the bankfull discharge simulation reveal the differences in bank failure mechanisms and how failures at each bend are linked to hydrologic conditions during the falling limb of a flood, and are consistent with patterns of erosion documented in repeat annual LiDAR surveys and through field observations.

4) Application of hydraulic jet tests to estimate critical shear stress and erodibility coefficients for cohesive bank materials proved challenging. The jet tests were performed on core samples collected during subaerial conditions and had a desiccated surface layer roughly ~5 cm thick that was produced through subaerial preparation. The estimated erodibility coefficients for this surface layer were up to four orders of magnitude larger than the default values used for similar bank materials in BSTEM. The results from the hydraulic jet tests were accurate for the surface layer, but did not account for the high resistance of less weathered material beneath the surface layer. Thus, the use of the erodibility coefficients for the surface layer in BSTEM did not yield appropriate predictions of bank erosion for a bankfull simulation with a long time duration. Use of the default values of the erosion coefficient, which were much lower than the values derived from the jet tests, produced more accurate predictions of bank failure when

compared to those documented in the repeat LiDAR surveys. These findings reveal the importance of subaerial preparation on the erosion of cohesive bank materials and the difficulties in obtaining accurate erosion parameters that reflect the physical processes occurring at the bank.

5) Short-term rates of erosion determined from repeat annual LiDAR surveys reveal that volumetric rates of erosion are roughly 25 times higher at Maier Bend than Horseshoe Bend, and that rates of erosion for the time period 2012-2013 were greater than the time period 2011-2012. Long-term rates of channel migration for Maier Bend are roughly 17 times greater than for Horseshoe Bend, with both bends displaying maximum rates of lateral erosion near the bend apex. Interestingly, the bankfull model simulation for Horseshoe Bend required a duration 17 times longer than Maier Bend to produce bank failure, suggesting that while the absolute rates of erosion predicted by the BSTEM models did not match measured rates of erosion for these bends, the influence of bank material properties on the model results did estimate reasonably well the differences in the relative rates of erosion between these two bends.

The findings from this chapter contribute to our understanding of how spatial heterogeneity in floodplain resistance influences styles and mechanisms of bank erosion along large meandering rivers with different bank material and vegetation properties. Application of the BSTEM model without calibration against erosion rates yielded an erodibility coefficient based on the physical properties of the bank materials and allowed independent evaluation of the effect of external forcings on styles and mechanisms of bank erosion. This study also emphasizes the importance of incorporating floodplain heterogeneity

into numerical models of channel migration. Future research should attempt to characterize the full heterogeneity of meandering river floodplains and explicitly link actual spatial variability in erosional resistance to patterns of historic planform migration. Such efforts will yield insight into the interactions between the process dynamics of meandering rivers and the geotechnical properties of floodplains, thereby improving our capacity to model large meandering rivers at the landscape scale.

CHAPTER 6

CONCLUSIONS

6.1 Summary of Findings

The primary goals of this dissertation were to investigate the influence of riparian and in-channel vegetation, as well as the geotechnical properties of outer bank materials, on the near-bank flow structure for two elongate meander loops on a large river, and to link the spatial variability of flow structure and floodplain resistance to erosion to observed patterns of short- and long-term channel change. Through detailed field measurements and analyses of the interactions between three-dimensional flow structure, bank morphology, vegetation, and bank material properties, the research presented in this dissertation provides invaluable new information on the hydrodynamics and morphodynamics of large meandering rivers, and improves our understanding and ability to model large rivers at the landscape scale.

The dissertation research consisted of three separate investigations from two elongate meander loops with different riparian vegetation on the Wabash River, a large river in Illinois and Indiana. The first study focused on the spatial patterns of three-dimensional flow structure throughout these meander loops and examined the effects of near-bank large woody debris on near-bank flow structure and boundary shear stress, and how the hydrodynamics varied during different hydrologic conditions. The second study examined the various scales of outer bank form roughness produced from large-scale bankline irregularities and small-scale surface roughness, the influence of bank material properties and vegetation on scales of roughness, interactions between roughness elements and near-bank flow structure, and how scales of roughness differ during variable discharge conditions and through time. The third study investigated the lateral and vertical heterogeneities in bank material properties and riparian

vegetation between these two bends, and a numerical model of bank retreat and observations from repeat field surveys and historic aerial photography were utilized to assess the ability of these external forcings to modify rates of erosion and patterns of channel migration. The conclusions of these three studies show that the dynamics of large meandering rivers are strongly influenced by heterogeneities in the floodplain resistance to erosion properties, and that riparian trees are capable of substantially increasing bank stability even on large rivers. Furthermore, interactions between near-bank large woody debris and the near-bank flow structure suggest that the increased form drag from these roughness elements can considerably reduce shear stresses acting on the outer bank, but bank topographic roughness elements have a limited ability to reduce bank shear stresses.

The research design was guided by key questions and objectives that are outlined in Chapter 1. The questions are restated here for clarity, and a summary of the main findings related to each question are given below.

1) What are the dominant scales of near-bank form roughness for forested and unforested bends, how do these scales of roughness vary spatially throughout these bends, and what is the effect of variable discharge and progressive bank retreat on scales of roughness?

Investigation of the spectral characteristics of bank contour lines around each bend reveal large-scale bank roughness to be highly intermittent throughout the bends (see Chapter 4). Results for the unforested bend (Maier Bend) show scales of roughness vary for different bank elevations. Near the base of the bank, a dominant scale of roughness is not evident, but as elevation increases, bankline irregularities with length scales 15 – 50 meters become the

dominant roughness elements. In contrast, at the forested bend (Horseshoe Bend), scales of roughness to vary with elevation and no dominant scale of roughness can be identified for this bend. These results are related to differences in the overall geotechnical properties of the banks for forested and unforested bends. At Maier Bend, the bank sediment is primarily non-cohesive sand and gravel with a transverse slope of ~30°, capped by a 1-2 m layer of cohesive silty material with a nearly vertical face. The large-scale bankline irregularities at this bend are produced through mass failure of the bank and the morphologic expression of these erosional features is most pronounced within the cohesive layer at top of the bank. The bank material at Horseshoe Bend is composed of mostly fine-grained silt and clay producing near-vertical slopes over the majority of the bank showing less vertical heterogeneity in grain size compared to Maier Bend. The high resistance of these bank materials, the increased cohesion from the riparian trees, and the low vertical variability in grain size promote uniform roughness vertically over the bank face throughout this bend.

Small-scale surface roughness was estimated by performing root-mean-square analysis on point cloud data collected from terrestrial LiDAR surveys and boat-mounted MBES surveys. The results from these analyses show that under subaerial conditions riverbanks with vegetation have substantially higher roughness than banks without vegetation. Comparisons between small-scale surface roughness obtained during subaerial and subaqueous conditions suggest that bank roughness is considerably reduced during high flow conditions that inundate the outer bank. The amount of reduction in surface roughness varied throughout each bend and is likely related to modification of bank roughness by erosion during subaqueous conditions, including removal of small woody and leafy vegetation and eradication of small-scale erosional features (e.g. rills) in non-cohesive bank materials. Scales of bank roughness are commonly evaluated during low flow

conditions when the majority of the bank face is exposed subaerially, and the results are used to estimate drag forces to partition shear stress and inform numerical models of bank erosion (Kean and Smith, 2006a, b; Darby *et al*., 2010; Darby *et al*., 2013). However, the findings of this research suggest that bank roughness is highly modified during high flow conditions, and to accurately estimate the amount of form drag influencing near-bank shear stress, scales of roughness should be evaluated subaqueously when the flow is interacting with the bank.

2) How do the spatial patterns of three-dimensional flow structure differ for forested and unforested elongate meander loops, and what effect do near-bank large-scale roughness elements, such as LWD and topographic irregularities, have on the near-bank flow structure and boundary shear stress in elongate meander loops?

While patterns of depth-averaged velocity at Maier Bend are fairly consistent with previous field and laboratory investigations of flow through elongate loops, patterns of depth-averaged velocity at Horseshoe Bend reveal that near-bank LWD can have a substantial influence on flow through this forested bend (see Chapter 3). Most notably, the presence of LWD nearly continuously around Horseshoe Bend produced a zone of low velocity against the outer bank that extends up to 40 m into the channel and over the entire flow depth. Additionally, the near-bank LWD also produced complex patterns of near-bank flow structure, and multiple streamwise-oriented secondary cells with both clockwise and counter-clockwise sense of rotation. The zone of reduced velocity induced by the near-bank LWD prevented the advection of high momentum fluid against the outer bank and confined curvature-induced helical motion

through the bend between the point bar and channel thalweg, thus reducing fluid shear stresses acting on the outer bank.

At Maier Bend, the large-scale bank roughness elements (scallops) produced zones of low velocity characterized by recirculation eddies within the upper ~3 m of the water column. These roughness elements did not influence flow structure near the toe of the bank and typically diminished ~40 m downstream. The geometry of these roughness elements and the observed pattern of three-dimensional flow structure around these elements differ from current theoretical models that approximate roughness elements at Gaussian-shaped bumps that protrude into the flow (Kean and Smith, 2006a, b). Instead, the flow structure induced by these concave scallop features seem to resemble the flow characteristics observed for groyne fields (Uijttewaal, 2005; Sukhodolov, 2014), but do not appear to reduce shear stresses against the toe of the bank (see Chapter 5).

3) How do the geotechnical properties (e.g. grain size, cohesion, bank height, root tensile strength) vary laterally and vertically throughout forested and unforested bends, and how much effect do riparian trees have on increasing bank stabilization on large meandering rivers?

The results from the geotechnical investigations show substantial differences in the characteristic grain size of the bank materials, soil cohesion, and critical shear stress necessary for sediment entrainment between the forested and unforested bends, and are highly variable within each bend, both laterally and vertically (see Chapter 5). The floodplain elevations and bank profiles throughout the study area are also highly variable and are likely linked to the

material properties of the banks and floodplains. Additionally, field surveys reveal bedrock outcrops within the downstream limbs of both of these bends that are highly resistant to erosion. While the influence of riparian trees on riverbank stabilization can vary with scale (Abernethy and Rutherford, 1998; Trimble, 2004; Polvi *et al*., 2014), the results from this investigation reveal that the riparian trees at Horseshoe Bend enhance stability of the banks through increased cohesion due to root-reinforcement, despite relatively high bank heights (~5-6 m) relative to root penetration depths (~1.5 m). Results from the RipRoot model component of BSTEM suggest that the riparian trees are roughly doubling the cohesion of the upper bank materials.

4) What effect does spatial heterogeneity of the bank material properties have on the dominant processes of bank erosion operating in forested and unforested bends (e.g. fluvial entrainment, mass failure, subaerial preparation)?

Observations from repeat terrestrial LiDAR surveys and BSTEM model simulations of bank retreat show substantial differences in the rates of bank erosion and the mechanisms by which these banks fail, and that these differences can be explained by the variability in bank material properties (see Chapter 5). At Maier Bend, the non-cohesive sand and gravel comprising the majority of the bank is easily eroded through fluvial entrainment, producing over-steepened bank profiles that promote the common occurrence of bank failures within the upper ~1-2 m cohesive silty layer at the top of the bank. Results from model simulations suggest that these bank failures can occur during the early stages of the falling limb of a flood hydrograph, and thus the slump blocks introduced to the channel have a high potential to break apart and be transported downstream. In contrast, at Horseshoe Bend the high resistance of the banks to

erosion and the added cohesion from the riparian trees limit the capacity of the flow to erode sediment. Yet, through continued slow erosion near the base of the bank, the root bowls of trees eventually become undercut, resulting in mass failure of the tree and upper part of the bank. BSTEM model simulations along these forested banks suggest that the banks are more susceptible to mass failure during the receding stages of a flood hydrograph when confining flow pressures are low. The occurrence of mass failures during waning stages of the flow could be an important factor contributing to the residences times of the trees. Lastly, the cohesive bank sediments at Horseshoe Bend have been highly modified through subaerial preparation, resulting in a desiccated surface layer ~5cm thick. Hydraulic jet tests on these samples yielded erodibility coefficients that were up to four orders of magnitude higher than default values used in BSTEM for similar bank materials. Thus, hydrologic variability, through its influence on the formation and removal of desiccated surface layers, is probably an important factor influencing the erodibility of cohesive banks.

5) How do the interactions between near-bank shear stress, bank material properties, and vegetation relate to patterns of short-term rates of erosion and long-term rates of channel migration in forested and unforested bends?

The spatial patterns of erosion revealed by repeat terrestrial LiDAR surveys and time series analysis of aerial photography show that rates of erosion and channel migration are substantially higher for the unforested Maier Bend than compared to the forested Horseshoe Bend (see Chapter 5). At both bends, long-term rates of channel migration are greatest near the bend apex; however, average rates of bend extension for Maier Bend are ~10 – 12 myr^{-1},

whereas the average rates of channel migration at Horseshoe Bend are ~0.75 m/yr, roughly 17 times less. Additionally, little to no erosion is occurring within the upstream and downstream limbs of both loops.

Chapters 3, 4 and 5 all present results that contribute to the process dynamics of meandering rivers, yet it is the combination of these factors that ultimately produce the complex channel planforms observed in many natural rivers. Detailed investigations of the outer banks of these two bends show that there are two main ways in which the banks can moderate rates of erosion, (1) through topographic form roughness and the introduction of vegetation to the channel that offers flow resistance and a reduction in shear stress acting on the bank, and (2) through the geotechnical properties of the bank materials influencing the resistance of the bank to erosion. Furthermore, the influence of planform curvature and bed morphology on the three-dimensional flow structure through these elongate meander loops is responsible for the redistribution of momentum within the bends and thus plays a key role in interactions between the near-bank flow field, roughness elements, and outer bank materials.

In summary, at Maier Bend, the non-cohesive bank materials, lack of riparian and in-channel vegetation, and the limited ability of the large-scale bank roughness elements all contribute to the high rates of erosion and channel migration observed near the bend apex. However, on the downstream limb of this bend, the relatively small platform of bedrock exposed within the channel is strongly influencing patterns of near-bank flow and shear stress, leading to a small zone of deposition along the outer bank downstream of the bedrock that has started to colonize with riparian trees. In contrast, at Horseshoe Bend, the combined effects of the high resistance to erosion of the bank materials, the bank stabilizing effects of riparian trees, and the reduction of near-bank shear stress resulting from increased flow resistance by abundant in-

channel LWD, substantially limit extension of this bend near the apex. Furthermore, on the downstream limb where the highest shear stresses are observed, the channel is confined by bedrock from the upland valley, restricting the downstream translation of the bend.

6.2 Future Work

This research has investigated the interactions between three-dimensional flow structure, outer bank form roughness and near-bank LWD, lateral and vertical heterogeneity in the geotechnical properties of the bank materials, and riparian vegetation on the spatial patterns of short-term erosion and long-term channel migration. Although the findings show that riparian trees contribute to the stabilization of riverbanks of large rivers, the results do not necessarily suggest that planting riparian trees along unforested riverbanks will be sufficient to stabilize the banks. Other factors, such as differences in the geotechnical properties of stream banks, are also important determinants of bank stability.

The capacity of riparian forests to increase bank stability and modify the geotechnical properties of bank materials on large rivers is of interest both scientifically and from a river management perspective. Over time scales of soil development, vegetation can affect grain size by enhancing chemical weathering rates, but differences in grain size at Maier Bend and Horseshoe bend most likely do not reflect contemporary differences in bank vegetation. Undoubtedly both bends were forested prior to the advent of agricultural land use in the region approximately 100 to 150 years ago. Thus, the differences in bank vegetation are a recent development. The differences in material properties between the two bends seem to be related to differences in the depositional history of the floodplain adjacent to the outer bank at each bend. Evidence from aerial photography and airborne LiDAR show that Maier Bend is eroding through previous point bar deposits as indicated by the scroll bar topography of the floodplain and by the

existence of a meander scar to the north of the bend – the direction the bend is currently migrating. The outer bank floodplain at Horseshoe Bend also shows evidence of scroll bar topography, but the morphologic expression of meander scrolls is more subdued than at Maier Bend and no obvious meander scars exist to the north of the bend. Further detailed work on the depositional history and alluvial architecture of the lower Wabash River floodplain is needed to determine the factors responsible for spatial variations in the erosional resistance of floodplain materials along this river.

The recruitment of local riparian trees to the near-bank region around Horseshoe Bend results in increased flow resistance through form drag and a reduction in the near-bank shear stresses. Results from the BSTEM model simulations suggest that these trees are introduced during the final stages of a flood hydrograph when confining stream flow pressures have decreased sufficiently. These findings suggest that once the trees are introduced through mass failures during these low flow conditions, the flow velocities are not capable of transporting the LWD downstream. While the results from this study show the influence of near-bank LWD on flow structure during near-bankfull and overbank discharge conditions, more work is needed to evaluate the influence of LWD on flow structure and sediment transport during low flow conditions. It is possible that during low and moderate flow conditions the LWD reduces local velocities sufficiently to promote the deposition of sediment, resulting in the partial burial of the trees. Additionally, now that the nearly continuous low-velocity zone is in place around the bend, regardless of its origin, this zone is likely self-reinforcing in the sense that as new trees fall into this near-bank region, either through mass failure or mortality, this LWD cannot be removed due to the low velocity conditions and also contributes to flow resistance in this zone. Partial burial and self-reinforcement of low velocities both would contribute to long residence times for LWD.

More detailed work is needed to determine the factors responsible for long residence times of LWD at this bend and to determine whether LWD accumulation is common along forested bends in the Wabash River and other large meandering rivers.

The comparisons between the subaerial and subaqueous bank surface roughness suggest that bank roughness decreases during flow conditions when the banks are inundated compared to roughness when banks are exposed subaerially. This reduction in roughness may be related to removal by high flows of subaerially produced roughness elements (e.g. erosional rills on steep outer banks) and of small emergent vegetation on the outer banks. More detailed analysis of the roughness characteristics of outer banks during subaerial and submerged conditions is required to comprehensively address this issue. Differences in roughness for subaerial for subaqueous conditions have important implications for understanding the near-bank hydrodynamics and for accurately modeling shear stresses and rates of bank erosion. In particular, the near-bank subaqueous MBES surveys at Maier Bend showed the presence of relatively small-scale slump blocks that account for the majority of the estimated roughness at these sites. Detailed subaqueous field observations of these types of roughness elements has not been widely documented in previous studies, and current models of channel migration that incorporate near-bank slump blocks apply an exponential rate of decay for these features. Thus, an opportunity exists to apply the advanced techniques of MBES systems to evaluate the rate of decay of subaqueous slump blocks in large rivers and to characterize the influence of these features on the near-bank flow field through time.

The findings from this research shed light into the interactions between time-averaged three-dimensional velocities and large-scale roughness elements, such as LWD and scallops, and how these features might moderate near-bank shear stresses. However, limitations in the field

measurements of velocity obtained from the ADCP do not allow for investigations of the turbulence structure around these roughness features. More work is needed to elucidate the effects of in-channel vegetation and topographic bank roughness on the spatial patterns of near-bank turbulence, and how these effects are influencing patterns of near-bank shear stress.

Lastly, this dissertation research has documented the time-averaged three-dimensional flow structure, outer bank morphology, in-channel LWD along the outer bank, and geotechnical properties of bank materials, in more detail than previous work on large meandering rivers. These data can be used to calibrate hydro- and morphodynamic models of meander dynamics to explore in greater detail than is possible in any field study, interactions among flow structure, turbulence, bank material properties, and large-scale roughness elements. Through such an approach, detailed understandings derived from analysis of field data can be extended beyond the domain of the measured conditions to explore the influence of variability in boundary conditions (bank resistance, bank vegetation) and inputs (hydrological variability, sediment loads) on the dynamics of large meandering rivers, both at the scale of individual bends and at the scale of planform evolution of multiple bends.

REFERENCES

Abad, J.D., Rhoads, B.L., Güneralp, I., and Garcia, M.H., 2008. Flow structure at different stages in a meander-bend with bendway weirs. *Journal of Hydraulic Engineering*. 134(8), 1052-1063.

Abad, J.D., and Garcia, M.H., 2009a. Experiments in a high-amplitude Kinoshita meandering channel: 1. Implications of bend orientation on mean and turbulent flow structure. *Water Resources Research,* 45 (2), W02401.

Abad, J.D., and Garcia, M.H., 2009b. Experiments in a high-amplitude Kinoshita meandering channel: 2. Implications of bend orientation on bed morphodynamics. *Water Resources Research,* 45 (2), W02402.

Abbe, T.B., Montgomery, D.R., 1996. Large woody debris jams, channel hydraulics and habitat formation in large rivers. *Regulated Rivers: Research and Management*. 12, 201-221.

Abernethy, B., and Rutherfurd, I.D., 1998. Where along a river's length will vegetation most effectively stabilise stream banks? *Geomorphology*. 23, 55-75.

Ashworth, P.J., and Lewin, J., 2012. How do big rivers come to be different? *Earth-Science Reviews*. 114, 84-107.

Bathurst, J.C., Thorne, C.R., and Hey, R.D., 1979. Secondary flow and shear-stress at river bends. *Journal of the Hydraulics Division-ASCE*. 105(10), 1277–1295.

Beeson, C.E., and Doyle, P.F., 1995. Comparison of bank erosion at vegetated and non-vegetated channel bends. *Water Resources Bulletin*. 31(6), 983-990.

Bennett, S.J., 2004. Effects of emergent riparian vegetation on spatially averaged and turbulent flow with an experimental channel. In *Riparian Vegetation and Fluvial Geomorphology*. ed S.J Bennett and A. Simon, 29-41. AGU: Washington, D.C.

Bennett, S.J., Wu, W., Alonso, C.V., and Wang, S.S.Y., 2008. Modeling fluvial response to in-stream woody vegetation: implications for stream corridor restoration. *Earth Surface Processes and Landforms*. 33, 890-909.

Beven, K., Gilman, K., and Newson, M., 1979. Flow and flow routing in upland channel networks. *Hydrological Science Journal*. 24(3), 303-325.

Bilotta, G.S., and Brazier, R.E., 2008. Understanding the influence of suspended solids on water quality and aquatic biota. *Water Research*. 42, 2849-2861.

Blaisdell, F.W., Clayton, L.A., and Hebaus, G.G., 1981. Ultimate dimension of local scour. *Journal of Hydraulics Division, American Society of Civil Engineers*. 107(HY3), 327-337.

Blanckaert, K., 2001. Bend-flow simulation using 2D depth-averaged model — Discussion. *Journal of Hydraulic Engineering-ASCE*, 127(2), 167–170.

Blanckaert, K., 2010. Topographic steering, flow recirculation, velocity redistribution, and bed topography in sharp meander bends. *Water Resources Research*, 46, W11901.

Blanckaert, K., 2011. Hydrodynamic processes in sharp meander bends and their morphological implications. *Journal of Geophysical Research-Earth Surface*, 116, F01003.

Blanckaert, K., and de Vriend, H.J., 2003. Nonlinear modeling of mean flow redistribution in curved open channels. *Water Resources Research*, 39(12), 1375.

Blanckaert, K., and de Vriend, H.J., 2004. Secondary flow in sharp open-channel bends. *Journal of Fluid Mechanics*, 498, 353–380.

Blanckaert, K., Duarte, A., Chen, Q., and Schleiss, A.J., 2012. Flow processes near smooth and rough (concave) outer banks in curved open channels. *Journal of Geophysical Research: Earth Surface,* 117, F04020.

Brice, J. C., 1974. Evolution of meander loops. *Geological Society of America Bulletin*, 85(4), 581–586.

Cancienne, R.M., Fox, G.A., and Simon, A., 2008. Influence of seepage undercutting on the stability of root-reinforced streambanks. *Earth Surface Processes and Landforms*. 33, 1769-1786.

Cederholm, C.J., Reid, L.M., and Salo, E.O., 1980. Cumulative effects of logging road sediment on salmonid populations in the Clearwater River, Jefferson County, Washington. *Water Research Center Report 39*, Conference on salmon-spawning gravel: a renewable resource in the Pacific Northwest, Washington State University, Pullman, Washington, p. 38-74.

Cordone, A.J., and Kelley, D.W., 1961. The influence of inorganic sediment on aquatic life of streams. *California Department of Fish and Game, Inland Fisheries Branch*, 47(2), 188-288.

Couper, P., 2003. Effects of silt-clay content on the susceptibility of river banks to subaerial erosion. *Geomorphology*. 56, 95-108.

Daniels, M.D., and Rhoads, B.L., 2003. Influence of a large woody debris obstruction on three dimensional flow structure in a meander bend. *Geomorphology*. 51, 159-173.

Daniels, M.D., and Rhoads, B.L., 2004. Spatial pattern of turbulence kinetic energy and shear stress in a meander bend with large woody debris. In *Riparian Vegetation and Fluvial Geomorphology*. ed S.J Bennett and A. Simon, 87–97. AGU: Washington, D.C.;

Daniels, M.D., and Rhoads, B.L., 2007. Influence of experimental removal of large woody debris on spatial patterns of three-dimensional flow in a meander bend. *Earth Surface Processes and Landforms*. 32, 460-474.

Darby, S.E., Alabyan, A.M, and Van de Wiel, M.J., 2002. Numerical simulation of bank erosion and channel migration in meandering rivers. *Water Resources Research*. 38(9), 1-23.

Darby, S.E., and Thorne, C.R., 1996a. Numerical simulation of widening and bed deformation of straight sand-bed rivers. I: Model development. *Journal of Hydraulic Engineering*. 122, 184-193.

Darby, S.E., and Thorne, C.R., 1996b. Numerical simulation of widening and bed deformation of straight sand-bed rivers. II: Model evaluation. *Journal of Hydraulic Engineering*. 122, 194-202.

Darby, S.E., Trieu, H.Q., Carling, P.A., Sarkkula, J., Koponen, J., Kummu M., Conlan, I. and Leyland, J., 2010. A physically based model to predict hydraulic erosion of fine-grained riversbanks: The role of form roughness in limiting erosion. *Journal of Geophysical Research*. 115, 1-20.

Darby, S.E., Leyland, J., Kummu, M., Rasanen, T.A., and Lauri, H., 2013. Decoding the drivers of bank erosion on the Mekong River: The roles of the Asian monsoon, tropical storms, and snowmelt. *Water Resources Research*. 49, 2146-2163.

Dietrich, W.E., 1987. Mechanics of flow and sediment transport in river bends. In *River channels environment and process*, ed. K. S. Richards, 179–224. Oxford: Basil Blackwell.

Dietrich, W.E., and Smith, J.D., 1983. Influence of the point-bar on flow through curved channels. *Water Resources Research,* 19(5), 1173–1192.

Eaton, B.C., and Giles, T.R., 2009. Assessing the effect of vegetation-related bank strength on channel morphology and stability in gravel-bed streams using numerical models. *Earth Surface Processes and Landforms*. 34, 712-724.

Einstein, H.A., 1950. The bedload function for bedload transportation in open channel flows. *Technical Bulletin No. 1026,* USDA, Soil Conservation Service, 1-71.

Einstein, H.A., and Barbarossa, N.L., 1952. River channel roughness. *Trans. American Society of Civil Engineers*. 117(1), 1121-1132.

Engel, F.L., and Rhoads, B.L., 2012. Interaction among mean flow, turbulence, bed morphology, bank failures and channel planform in an evolving compound meander loop. *Geomorphology,* 163(SI), 70–83.

Ferreira da Silva, A.M., Ahmari, H., 2009. Size and effect on the mean flow of large-scale horizontal coherent structures in open-channel flows: an experimental study. *Canadian Journal of Civil Engineering*. 36, 1643-1655.

Fox, G.A., Wilson, G.V., Periketi, R.K., and Cullum, R.F., 2006. Sediment transport model for seepage erosion of streambank sediment. *Journal of Hydrologic Engineering*. 11(6), 603-611.

Fox, G.A, Wilson, G.V., Simon, A., Langendoen, E.J., Akay, O., and Fuchs, J.W., 2007. Measuring streambank erosion due to ground water seepage: correlation to bank pore water pressure, precipitation and stream stage. *Earth Surface Processes and Landforms*. 32, 1558-1573.

Fredlund, D.G., Morgenstern, N.R., and Widger, R.A., 1978. The shear strength of unsaturated soils. *Canadian Geotechnical Journal*. 15, 313-321.

Fredlund, D.G., and Rahardjo, H., 1993. Soil mechanics of unsaturated soils. John Wiley & Sons, Inc., New York.

Frothingham, K.M., and Rhoads, B.L., 2003. Three-dimensional flow structure and channel change in an asymmetrical compound meander loop, Embarras River, Illinois. *Earth Surface Processes and Landforms*. 28, 625-644.

Garcia, M.H., Lopez, F., Dunn, C., and Alonso, C.V., 2004. Flow, turbulence, and resistance in a flume with simulated vegetation. In *Riparian Vegetation and Fluvial Geomorphology*. ed. S.J Bennett and A. Simon, 11-27. AGU: Washington, D.C.

Gorrick, S. and Rodriguez, J.F., 2012. Sediment dynamics in a sand bed stream with riparian vegetation. *Water Resources Research*. 48, 1-15.

Gregory, K.J., Gurnell, A.M., and Hill, C.T., 1985. The permanence of debris dams related to river channel processes. *Hydrological Science Journal*. 30(3), 371-381.

Griffin, E.R., Kean, J.W., Vincent, K.R., Smith, J.D., and Friedman, J.M., 2005. Modeling effects of bank friction and woody bank vegetation on channel flow and boundary shear stress in the Rio Puerco, New Mexico. *Journal of Geophysical Research*. 110, 1-15.

Gupta, A. (Ed.), 2007. Large Rivers: Geomorphology and Management. Wiley, Chichester, 689 pp.

Güneralp, İ., and Rhoads, B.L., 2008. Continuous characterization of the planform geometry and curvature of meandering rivers. *Geographical Analysis*, 40 (1), 1–25.

Güneralp, I., Rhoads, B.L., 2009. Empirical analysis of the planform curvature-migration relation of meandering rivers. *Water Resources Research*. 45, 15.

Güneralp, I., Rhoads, B.L., 2011. Influence of floodplain erosional heterogeneity on planform complexity of meandering rivers. *Geophysical Research Letters*. 38, 1-6.

Gurnell, A., and Petts, G., 2006. Trees as riparian engineers: The Tagliamento River, Italy. *Earth Surface Processes and Landforms*. 31, 1558-1574.

Hanson, G.J., 1990. Surface erodibility of earthen channels at high stresses: Part II – developing an *in situ* testing device. *Transactions of the American Society of Agricultural Engineers*. 33(1), 132-137.

Hanson, G.J., and Simon, A., 2001. Erodibility of cohesive streambeds in the loess area of the midwestern USA. *Hydrological Processes*. 15, 23-38.

Hasegawa, K., 1977. Computer simulation of the gradual migration of meandering channels. *Proceedings of the Hokkaido Branch, Japan Society of Civil Engineering*. 37-50.

Hickin, E.J. 1974., Development of meanders in natural river-channels. *American Journal of Science,* 274(4), 414–442.

Hickin, E.J., and G.C. Nanson., 1975. Character of channel migration on Beatton River, Northeast British-Columbia, Canada. *Geological Society of America Bulletin,* 86(4), 487–494.

Hopkinson, L. and Wynn, T., 2009. Vegetation impacts on near bank flow. *Ecohydrology*. 2, 404-418.

Hooke, J. M., 1995. Processes of channel planform change on meandering channels in the UK. In *Changing river channels,* eds. A. Gurnell, and G. E. Petts, 87–115. Chichester, UK: John Wiley.

Hooke, J.M., 2003. River meander behaviour and instability: A framework for analysis. *Transactions of the Institute of British Geographers,* 28(2), 238–253.

Hooke, J. M, and Harvey, A.M., 1983. Meander changes in relation to bend morphology and secondary flows. In *Modern and ancient fluvial systems,* ed. Collinson, and Lewin, 121–132. Oxford, UK: Blackwell Scientific Publications.

Hovius, N., 1998. Controls on sediment supply by large rivers. In: Shanley, K.W., and McCage, P.J. (eds.), Relative Role of Eustasy, Climate and Tectonics in Continental Rocks: SEPM Special Publication, 59, 4-15.

Huang, N.E., Shen, Z., Long, S.R., Wu, M.C., Shih, H.H., Zheng, Q., Yen, N., Tung, C.C., and Liu, H.H., 1998. The empirical mode decomposition and the Hilbert spectrum for nonlinear and non-stationary time series analysis, *Proc. R. Soc. Lond. A*, 454, 903-995.

Huang, N.E., and Wu, Z., 2008. A review on Hilbert-Huang Transform: Method and its applications to geophysical studies, *Reviews of Geophysics*, 46, 1-23.

Isenburg, M., Liu, Y., Shewchuk, J., Snoeyink, J., and Thirion, T., 2006. Generating raster DEM from mass points via TIN streaming. *GIScience'06 Conference Proceedings*. 186-198.

Ikeda, S., Parker, G., and Sawai, K., 1981. Bend theory of river meanders: Part I, linear development. *Journal of Fluid Mechanics*. 112, 363-377.

Jackson, R.G., 1975a. A depositional model of point bars in the lower Wabash River. PhD dissertation, University of Illinois – Urbana-Champaign.

Jackson, R. G. 1975b. Velocity and bed-form texture patterns of meander bends in the lower Wabash River of Illinois and Indiana. *Geological Society of America Bulletin*, 86 (11), 1511–1522.

Jackson, R., 1976. Large scale ripples of the lower Wabash River. *Sedimentology*, 23(5), 593–623.

Jamieson, E.C., Post, G., and Rennie, C.D., 2010. Spatial variability of three-dimensional Reynolds stresses in a developing channel bed. *Earth Surface Processes and Landforms*. 35, 1029-1043.

Jimenez-Hornero, F.J., Giraldez, J.V., Laguna, A.M., Bennett, S.J., and Alonso, C.V., 2007. Modelling the effects of emergent vegetation on an open-channel flow using a lattice model. *Intern. Journal for Numerical Methods in Fluids*. 55, 655-672.

Kaller, M.D., and Hartman, K.J., 2004. Evidence of a threshold level of fine sediment accumulation for altering benthic macroinvertebrate communities. *Hydrobiologia*, 518, 95-104.

Kean, J.W., and Smith, J.D., 2004. Flow and boundary shear stress in channels with woody bank vegetation. In *Riparian Vegetation and Fluvial Geomorphology*. ed Bennett and Simon, 237-252. AGU: Washington, D.C.

Kean, J.W., and Smith, J.D., 2006a. Form drag in rivers due to small-scale natural topographic features: 1. Regular sequences. *Journal of Geophysical Research*. 110, 1-13.

Kean, J.W., and Smith, J.D., 2006b. Form drag in rivers due to small-scale natural topographic features: 1. Irregular sequences. *Journal of Geophysical Research*. 111, 1-15.

Kean, J.W., Kuhnle, R.A., Smith, J.D., Alonso, C.V., and Langendoen, E.J., 2009. Test of a method to calculate near-bank velocity and boundary shear stress. *Journal of Hydraulic Engineering*. 135(7), 588-601.

Keller, E.A., and Swanson, F.J., 1979. Effects of large organic material on channel form and fluvial processes. *Earth Surface Processes*. 4, 361-380.

Kinoshita, R., 1961. *Investigation of channel deformation in Ishikari River*. Report 174. Tokyo: Bur. of Resour., Dep. of Sci. and Technology.

Konsoer, K.M., and Rhoads, B.L., 2013. Spatial-temporal structure of mixing interface turbulence at two large river confluences, *Environmental Fluid Mechanics*. 1-30.

Konsoer, K.M., Zinger, J.A., and Parker, G., 2013. Bankfull hydraulic geometry of submarine channels created by turbidity currents: Relations between bankfull channel characteristics and formative flow discharge. *Journal of Geophysical Research – Earth Surface*. 118, 1-13.

Kreutzweiser, D.P., Capell, S.S., and Good, K.P., 2005. Effects of fine sediment inputs from a logging road on stream insect communities: a large-scale experimental approach in a Canadian headwater stream. *Aquatic Ecology*, 39, 55-66.

Langendoen, E.J., and Alonso, C.V., 2008. Modeling the evolution of incised streams. I: model formulation and validation of flow and streambed evolution components. *Journal of Hydraulic Engineering*. 134(6), 749-762.

Langendoen, E.J., and Simon, A., 2008. Modeling the evolution of incised streams.II: streambank erosion. *Journal of Hydraulic Engineering*. 134(7), 905-915.

Langendoen, E.J., Lowrance, R.R., and Simon, A., 2009. Assessing the impact of riparian processes on streambank stability. *Ecohydrology*. 2, 360-369.

Latrubesse, E.M., 2008. Patterns of anabranching channels: The ultimate end-member adjustment of mega rivers. *Geomorphology*. 101, 130-145.

Lawler, D.M., 1992. Process dominance in bank erosion systems. In *Lowland Floodplain Rivers: Geomorphological Perspectives*. ed. P.A. Carling and G.E. Petts, 117-143. John Wiley & Sons, Ltd.

Lawler, D.M., 1993. Needle ice processes and sediment mobilization on river banks: the River Ilston, West Glamorgan, UK. *Journal of Hydrology*. 150, 81-114.

Leeder, M.R., 1983. On the interactions between turbulent flow, sediment transport and bedform mechanics in channelized flows. In *Modern and Ancient Fluvial Systems*. ed. Collinson and Lewin, 5-18. International Association of Sedimentologists.

Legleiter, C.J., and Kyriakidis, P.C., 2006. Forward and inverse transformations between Cartesian and channel-fitted coordinate systems for meandering rivers. *Mathematical Geology*. 38(8), 927-958.

Leopold, L.B., Wolman, M.G., and Miller, J.P., 1964. Fluvial Processes in Geomorphology. W.H. Freeman, San Francisco. 519 p.

Lewin, J., and Ashworth, P.J., 2014. Defining large river channel patterns: Alluvial exchange and plurality. *Geomorphology*. 215, 83-98.

Lopez, F., and Garcia, M.H., 1998. Open-channel flow through simulated vegetation: Turbulence modeling and sediment transport. *Water Resources Research*. 34(9), 2341-2352.

Lopez, F., and Garcia, M.H., 2001. Mean flow and turbulence structure of open-channel flow through non-emergent vegetation. *Journal of Hydraulic Engineering*. 127(5), 392-402.

Luppi, L., Rinaldi, M., Teruggi, L.B., Darby, S.E., and Nardi, L., 2009. Monitoring and numerical modelling of riverbank erosion processes: a case study along the Cecina River (central Italy). *Earth Surface Processes and Landforms*. 34, 530-546.

Majoribanks, T.I., Hardy, R.J., Lane, S.N., and Parsons, D.R., 2012. Using high-resolution CFD results to improve representation of vegetative drag and blockage effects within reach-scale flow models. *Conference Proceedings from the 3rd International Symposium on Shallow Flows*, June 4-6 2012, Iowa City, Iowa. 1-9.

Magna, M., and Kirchner, J.W., 2000. Stress partitioning in streams by large woody debris. *Water Resources Research*. 36(8), 2373-2379.

Miall, A., 2014. Fluvial Depositional Systems. Springer Geology, Springer International Publishing Switzerland, 322 pp.

Micheli, E.R., and Kirchner, J.W., 2002. Effects of wet meadow riparian vegetation on streambank erosion. 2. Measurements of vegetated bank strength and consequences for failure mechanics. *Earth Surface Processes and Landforms*. 27, 687-697.

Motta, D., Abad, J.D., Langendoen, E.J., and Garcia, M.H., 2012. A simplified 2D model for meander migration with physically-based bank evolution. *Geomorphology*. 163-164, 10-25.

Nepf, H.M., 1999. Drag, turbulence, and diffusion in flow through emergent vegetation. *Water Resources Research*. 35(2), 479-489.

Nepf, H.M., Vivoni, E.R., 2000. Flow structure in depth-limited, vegetated flow. *Journal of Geophysical Research*. 105(C12), 28,547-28,557.

Nicholas, A., 2013. Morphodynamic diversity of the world's largest rivers. *Geology*. 41(4), 475-478.

Ouillon, S., and Dartus, D., 1997. Three-dimensional computation of flow around groyne. *Journal of Hydraulic Engineering*. 123(11), 962-970.

Parker, G., Paoloa, C., Whipple, K.X., Mohrig, D., Toro-Escobar, C.M., Halverson, M., and Skoglund, T.W., 1998. Alluvial fans formed by channelized fluvial and sheet flow. II: Applications. *Journal of Hydraulic Engineering*. 24(10), 996-1004.

Parker, G., Shimizu, Y., Wilkerson, G.V., Eke, E.C., Abad, J.D., Lauer, J.W., Paola, C., Dietrich, W.E., and Voller, V.R., 2011. A new framework for modeling the migration of meandering rivers. *Earth Surface Processes and Landforms*. 36, 70-86.

Parsons, D. R., Jackson, P.R., Czuba, J.A., Engel, F.L., Rhoads, B.L., Oberg, K.A., Best, J.L., Mueller, D.S., Johnson, K.K., and Riley, J.D., 2012. Velocity Mapping Toolbox (VMT): A processing and visualization suite for moving-vessel aDcp measurements. *Earth Surface Processes and Landforms*. 38(11), 1244–1260.

Pizzuto, J., 2009. An empirical model of event scale cohesive bank profile evolution. *Earth Surface Processes and Landforms*. 34, 1234-1244.

Pizzuto, J., O'neal, M., and Stotts, S., 2010. On the retreat of forested, cohesive riverbanks. *Geomorphology*. 116, 341-352.

Phillips, J.D., 2003. Sources of nonlinearity and complexity in geomorphic systems. *Progress in Physical Geography*. 27(1), 1-23.

Pollen, N., 2007. Temporal and spatial variability in root reinforcement of streambanks: accounting for soil shear strength and moisture. *Catena*. 69, 197-205.

Pollen, N., and Simon, A., 2005. Estimating the mechanical effects of riparian vegetation on stream bank stability using a fiber bundle model. *Water Resources Research*. 41, 11.

Pollen-Bankhead, N., and Simon, A., 2009. Enhanced application of root-reinforcement algorithms for bank-stability modeling. *Earth Surface Landforms and Processes*. 34, 417-480.

Pollen-Bankhead, N., and Simon, A., 2010. Hydrologic and hydraulic effects of riparian root networks on streambank stability: Is mechanical root-reinforcement the whole story? *Geomorphology*. 116(3-4), 353-362.

Polvi, L.E., Wohl, E., and Merritt, D.M., 2014. Modeling the functional influence of vegetation type on streambank cohesion. *Earth Surface Processes and Landforms*. 1-14 (DOI: 10.1002/esp.3577).

Potter, P.E., 1978. Significance and origin of big rivers. *Journal of Geology*. 86, 13-33.

Rabeni, C.F., Doisy, K.E., and Zweig, L.D., 2005. Stream invertebrate community functional responses to deposited sediment, *Aquatic Sciences*, 67, 395-402.

Rinaldi, M., Casagli, N., Dapporto, S., and Gargini, A., 2004. Monitoring and modeling of pore water pressure changes and riverbank stability during flow events. *Earth Surface Processes and Landforms*. 29, 237-254.

Rinaldi, M., and Darby, S.E. 2007. Modelling river-bank-erosion processes and mass failure mechanisms: Progress towards fully coupled simulations. In *Gravel-Bed Rivers VI: From Process Understanding to River Restoration*, ed. Habersack, Piegay, and Rinaldi, 213-239. Elsevier, Netherlands.

Rinaldi, M., Mengoni, L., Luppi, L., Darby, S.E., and Mosselman, E., 2008. Numerical simulation of hydrodynamics and bank erosion in a river bend. *Water Resources Research*. 44, 1-17.

Rhoads, B. L., and Kenworthy, S.T., 1998. Time-averaged flow structure in the central region of a stream confluence. *Earth Surface Processes and Landforms*, 23(2), 171–191.

Rhoads, B.L., and Welford, M.R., 1991. Initiation of river meandering. *Progress in Physical Geography*. 15(2), 127-156.

Robison, E.G., and Beschta, R.L., 1990. Coarse woody debris and channel morphology interactions for undisturbed streams in southeast Alaska, U.S.A. *Earth Surface Processes and Landforms*. 15, 149-156.

Rozovskii, I. L. 1957. *Flow of water in bends of open channels*. Kiev, U.S.S.R.: Academy of Sciences of the Ukraninian S.S.R.

Schumm, S.A., and Winkley, B.R., 1994. The Variability of Large Alluvial Rivers. American Association of Civil Engineers Press, New York, 467 pp.

Shields, F.D., and Gippel, C.J., 1995. Prediction of effects of woody debris removal on flow resistance. *Journal of Hydraulic Engineering*. 121(4), 341-354.

Shields, F.D., Morin, N., and Kuhnle, R.A., 2001. Effects of large woody debris structures on stream hydraulics. In *Proceedings of the 2001 Wetlands Engineering and River Restoration Conference,* ed. D.F. Hayes, American Society of Civil Engineers, Reston, VA.

Shields, F.D., Simon, A., and Dabney, S.M., 2009. Streambank dewatering for increased stability. *Hydrological Processes*. 23, 1537-1547.

Simon, A., and Collison, A.J., 2001. Pore-water pressure effects on the detachment of cohesive streambeds: Seepage forces and matric suction. *Earth Surface Processes and Landforms*. 26, 1421-1442.

Simon, A., and Collison, A.J., 2002. Quantifying the mechanical and hydrologic effects of riparian vegetation on streambank stability. *Earth Surface Processes and Landforms*. 27, 527-546.

Simon, A., Curini, A., Darby, S.E., and Langendoen, E.J., 2000; Bank and near-bank processes in an incised channel. *Geomorphology*. 35, 193-217.

Simon, A., and Darby, S.E., 1997. Process-form interactions in unstable sand-bed river channels: A numerical modeling approach. *Geomorphology*. 21, 85-106.

Simon, A., Langendoen, E.J., Collison, A., and Layzell, A,. 2003. Incorporating bank-toe erosion by hydraulic shear into a bank-stability model: Missouri River, Eastern Montana. *Proceedings EWRL-ASCE, World Water and Environmental Resources Congress*. 1-11.

Simon, A., and Rinaldi, M., 2006. Disturbance, stream incision, and channel evolution: The roles of excess transport capacity and boundary materials in controlling channel response. *Geomorphology*. 79, 361-383.

Sinha, S.K., and Parker, G., 1996. Causes of concavity in longitudinal profiles of rivers. *Water Resources Research*. 32(5), 1417-1428.

Smith, J.D., and McLean, S.R., 1977. Spatially averaged flow over a wavy surface. *Journal of Geophysical Research*. 82, 1735-1746.

Sukhodolov, A.N., 2014. Hydrodynamics of groyne fields in a straight river reach: insight from field experiements. *Journal of Hydraulic Research*. 52(1), 105-120.

Sukhodolov, A.N., and Sukhodolova, T.A., 2010. Case Study: Effect of submerged aquatic plants on turbulence structure in a lowland river. *Journal of Hydraulic Engineering*. 136(7), 434-446.

Szupiany, R.N., Amsler, M.L., Best, J.L., and Parson, D.R., 2007. Comparison of fixed- and moving-vessel flow measurements with an aDcp in a large river. *Journal of Hydraulic Engineering*. 133(12), 1299-1309.

Tal, M., and Paola, C., 2010. Effects of vegetation on channel morphodynamics: results and insights from laboratory experiments. *Earth Surface Processes and Landforms*. 35, 1014-1028.

Termini, D., 2009. Experimental observations of flow and bed processes in large-amplitude meandering flume. *Journal of Hydraulic Engineering-ASCE*, 135(7), 575–587.

Termini, D., and Piraino, M., 2011. Experimental analysis of cross-sectional flow motion in a large amplitude meandering bend. *Earth Surface Processes and Landforms*. 36, 244-256.

Thorne, C.R., 1982. Processes and mechanisms of river bank erosion. In *Gravel-bed Rivers*. ed. R.D. Hey, J.C. Bathurst, and C.R. Thorne, 227-271. John Wiley & Sons, Ltd.

Thorne, C.R., 1992. Bend scour and bank erosion on the meandering Red River, Louisiana. In *Lowland Floodplain Rivers: Geomorphological Perspectives*. ed. P.A. Carling and G.E. Petts, 95-115. John Wiley & Sons, Ltd.

Thorne, C.R., and Hey, R.D., 1979. Direct measurements of secondary currents at a river inflection point. *Nature,* 280(5719), 226–228.

Thorne, C.R., Zevenbergen, L., Pitlick, J., Rais, S., Bradley, J.B., and Julien, P., 1985. Direct measurements of secondary currents in a meandering sand-bed river. *Nature,* 315(27), 746–747.

Thorne, S.D., and Furbish, D.J., 1995. Influences of coarse bank roughness on flow within a sharply curved river bend. *Geomorphology*. 12, 241-257.

Trimble, S.W., 2004. Effects of riparian vegetation on stream channel stability and sediment budgets. In *Riparian Vegetation and Fluvial Geomorphology*. ed S.J Bennett and A. Simon, 153-169. AGU: Washington, D.C.

Uijttewaal, W.S.J., 2005. Effects of groyne layout on the flow in groyne fields: Laboratory experiments. *Journal of Hydraulic Engineering*. 131(9), 782-791.

Uijttewaal, W.S.J., Lhemann, D., and van Mazijk, A., 2001. Exchange processes between a river and its groyne fields: Model experiments. *Journal of Hydraulic Engineering*. 127(11), 928-936.

van de Wiel, M.J., and Darby, S.E., 2007. A new model to analyse the impact of woody riparian vegetation on the geotechnical stability of riverbanks. *Earth Surface Processes and Landforms*. 32, 2185-2198.

Walker, L.R., Wardle, D.A., Bardgett, R.D., and Clarkson, B.D., 2010. The use of chronosequences in studies of ecological succession and soil development. *Journal of Ecology*. 98, 725-736.

Whiting, P.J., and Dietrich, W.E., 1993a. Experimental studies of bed topography and flow patterns in large-amplitude meanders: 1. Observations. 29(11), 3605-3614.

Whiting, P.J., and Dietrich, W.E., 1993b. Experimental studies of bed topography and flow patterns in large-amplitude meanders: 2. Mechanisms. *Water Resources Research*. 29(11), 3615-3622.

Wu, T.H., McKinnell, W.P., and Swanston, D.N., 1979. Strength of tree roots and landslides on Prince of Wales Island, Alaska. *Canadian Geotechnical Journal*. 16(1), 19-33.

Wynn, T.M., and Mostaghimi, S., 2006. Effects of riparian vegetation on stream bank subaerial processes in southwestern Virginia, USA. *Earth Surface Processes and Landforms*. 31, 399-413.

Young, W.J., 1991. Flume study of the hydraulic effects of large woody debris in lowland rivers. *Regulated Rivers: Research and Management*. 6, 203-211.

Zimmerman, R.C., Goodlett, J.C., and Comer, G.H., 1967. The influence of vegetation on channel form of small streams. In *Symposium on River Morphology*. Int. Assoc. Sci. Hydrol. Publ., 75, 255-275. Bern, West Germany.

Zong, L., and Nepf, H., 2011. Spatial distribution of deposition within a patch of vegetation. *Water Resources Research*. 47, 1-12.